Molecular Imaging of Inflammation and Extracellular Matrix Remodelling After Myocardial Infarction

Ramos, Isabel

Awarding institution:
King's College London

Molecular Imaging of Inflammation and Extracellular Matrix Remodelling After Myocardial Infarction

Isabel Maria Silva Teixeira Ramos

A DISSERTATION SUBMITTED FOR THE DEGREE OF

Doctor of Philosophy

of the

University of London

Supervised by

Professor René M. Botnar

Professor Ajay M. Shah

School of Biomedical Engineering & Imaging Sciences

Faculty of Life Sciences & Medicine

King's College London

September, 2017

ABSTRACT

Myocardial infarction (MI) and associated morbidity and mortality is one of the major health care problems in western societies. Magnetic resonance imaging (MRI) has great potential for quantification of key biological processes post MI, such as inflammatory cell recruitment and extracellular matrix (elastin and collagen deposition) remodelling with the use of novel target specific contrast agents. During the acute phase following MI, the degree and duration of the inflammatory response critically affects myocardial remodelling and cardiac function. ^{19}F perfluorocarbons (PFCs) uptaken by inflammatory cells allow direct detection and quantification of the temporal and spatial evolution of the inflammatory response in the injured myocardium. During the maturation phase, the synthesis of elastin and collagen, important ECM proteins, is upregulated. De novo elastin synthesis can be imaged by MRI using an elastin-specific contrast agent (Gd-ESMA). In this study, we explored the merits of multinuclear $^{1}H/^{19}F$ MRI for the simultaneous assessment and quantification of cardiac inflammation and elastin deposition in a murine model of MI in wild-type and knockout animals. ^{19}F containing particles, uptaken by macrophages, were used to investigate inflammatory cell recruitment into injured myocardium and Gd-ESMA was used to evaluate changes in elastin content in the ECM post-MI.

Às minhas avós, à Sara

ACKNOWLEDGMENTS

I would like to thank Professor René Botnar and Professor Ajay Shah for the opportunity to work and learn with them, for their continuous support during my PhD, providing valuable suggestions and enthusiasm. Without you this work wouldn't be possible; thanks for the inspiration, your invaluable mentorship and guidance through my whole research process.

I would like to thank Dr Ulrich Flögel for the great support fundamental for this thesis. I also need to thank all the KCL people; all of you that shared time and experience with me. Dr Alkystis Phinikaridou and Dr Markus Henningsson thanks for being outstanding teachers, your advice helped me overcome many technical challenges I faced during my work. For the help and availability, for the interest, for the conversations, for the professional collaboration, and for all the suggested corrections of this thesis I also need to thank Dr Torben Schneider, Dr Gastão Cruz, Dr Silvia Lorrio, Dr Begoña Lavin, Dr Thomas Eykyn and Dr Andrea Protti. For all the technical support, I would like to thank Dr Greta Sawyer, Dr Prakash Saha, Dr James Clark, Dr Marcelo Andia, Dr Radhouene Neji, Dr Claudia Prieto, David Thakor, Dr Kavitha Sunassee, Floyd, Thanos, Gemma, Kate and Zoe. For being there, supporting me in answering all my million questions, for the coffees, for the runs, for the amazing time over the past three years: Dr Teresa, Dr Arna, Giovanna, Dr Andrew, Dr Pierre, Dr Giulia, Dr Isabel, Dr Imran, Dr Xenios, Olivier, Aurelien, Alexandre, Camila, Dr Maryam, Dr Sara.

I am grateful to my family for everything. Thanks to all my friends and family that supported me: Mariana, Sofia, Miguel, Rita, Diogo, Laly, João, Ruchika, Marília, Clemêncio, Paulo, Cândida, Bela, Teca, Helder, Dite, and specially to you Filipe, for being there, always.

The work in this dissertation was supported by a King's College London British Heart Foundation Centre of Excellence inter-disciplinary PhD fellowship, and British Heart Foundation Program.

Contents

List of Figures

List of Tables

List of Acronyms

^{19}F	Fluorine-19 nuclei
^{1}H	Hydrogen
2D	Two-Dimensional
3D	Three-Dimensional
AAR	Area-At-Risk
ATP	Adenosine Triphosphate
B_0	Static Magnetic Field
BSA	Bovine Serum Albumin
BW	Bandwidth
c	Contrast Agent
CAD	Coronary Artery Disease
CCR2	C-C Chemokine Receptor Type 2
CLIO	Cross-Linked Iron Oxide
CMR	Cardiac Magnetic Resonance
CNR	Contrast-to-Noise Ratio
CT	Computed Tomography
CVD	Cardiovascular Disease
CVF	Collagen Volume Fraction
dNTP	Ultrapure Deoxynucleotides
ECG	Electrocardiogram
ECM	Extracellular Matrix
ECV	Extracellular Volume
EDTA	Ethylenediaminetetraacetic Acid
EF	Ejection Fraction
FACS	Fluorescent Activated Cell Sorting
FDG	Fluorodeoxyglucose
Fe^{2+}/Fe^{3+}	Iron (II)/ Iron (III)
Fe_2O_3	Maghemine
Fe_3O_4	Magnetite
FMT	Fluorescent Molecular Tomography
FOV	Filed-Of-View
FT	Fourier Transform
FXIII	Transglutaminase Clotting Factor XIII
G	Magnetic Field Gradient
Gd	Gadolinium
Gd-DTPA	Gadolinium-Diethylenetriamine Penta-Acetic Acid
Gd-ESMA	Gadolinium-based Elastin-Specific MR contrast agent
Gd^{3+}	Gadolinium (III)
G_{FE}	Frequency Encoding Gradient

GLUT4	Glucose transporter type 4
G_{PE}	Phase Encoding Gradient
GRE	Gradient-Echo
G_{ss}	Slice Selection Gradient
H&E	Hematoxylin and eosin
HF	Heart Failure
I	Spin Quantum Number
i.v.	Intravenous
IC	Intracellular
IHC	Immunohistochemistry
IL	InterLeukin
IQR	Interquartile Range
IR	Inversion Recovery
IS	Infarct Size
IV	Intravascular
LAD	Left-Anterior Descending coronary artery
LGE	Late Gadolinium Enhancement
LL	Look-Locker
LV	Left-Ventricle
LVEDV	Left-Ventricular End-Diastolic Volume
M_0	Net Magnetization before RF pulse
MAGP	Microfibril-Associated Glycoproteins
MCP-1	Monocyte Chemoattractant Protein 1
MI	Myocardial infarction
MMP	Matrix Metalloproteinase
Mn^{2+}	Manganese (II)
MOLLI	MOdified Look-Locker Inversion Recovery
MPO	Myeloperoxidase
MR	Magnetic Resonance
MRI	Magnetic Resonance Imaging
MRS	Magnetic Resonance Spectroscopy
M_{xy}	Net Transverse Magnetization
M_z	Net Longitudinal Magnetization
NFIR	Near-Infrared Fluorescent
NMR	Nuclear Magnetic Resonance
NMV	Net Magnetization Vector
PCR	Polymerase Chain Reaction
PET	Positron Emission Tomography
PFCE/PF15C	Perfluoro-15-Crown-5-Ether
PFCs	Perfluorocarbons
PFOB	Perfluorooctylbromide
PFPE	Perfluoropolyether
ppm	Parts Per Million
pQDs	Paramagnetic Quantum-Dots
R_1	T_1 Relaxation Rate
R_2	T_2 Relaxation Rate
RAFT	Regioselectively Addressable Functionalized Template
RES	Reticuloendothelial System
RF	Radiofrequency
RGD	Rayleigh-Gans-Debye

RIME	Receptor Induced Magnetization Enhancement
ROC	Receiver Operating Characteristic
RV	Right-Ventricle
SASHA	Saturation Recovery Single-Shot Acquisition
SD	Standard Deviation
SE	Spin-Echo
SEM	Standard Error of the Mean
SNR	Signal-to-Noise Ratio
SPECT	Single Photon Emission Computed Tomography
SPIO	Superparamagnetic Iron Oxide
T_1	Spin-Lattice Relaxation Time
T_2	Spin-Spin Relaxation Time
T_2^*	Spin-Spin Relaxation Time under field inhomogeneity
T_2W	T_2-Weighted
TE	Echo Time
TFA	Trifluoroacetic Acid
TGF	Transforming Growth Factor
TI	Inversion Time
TMS	Tetramethylsilane
TNF	Tumor Necrosis Factor
TR	Repetition Time
TSE	Turbo Spin Echo
TTC	2,3,5-Triphenyltetrazolium chloride
USPIO	Ultrasmall Superparamagnetic Particles of Iron Oxide
VCAM-1	Vascular Cell Adhesion Protein 1
VEGF	Vascular Endothelial Growth Factor
WT	Wild-type
μ	Magnetic Moment
ν	Absolute Resonance Frequency
ν_{REF}	Absolute Resonance Frequency of a standard reference
δ	Chemical shift
γ	Gyromagnetic Ratio
σ	Shielding/noise
ω	Larmor frequency

Chapter 1

Introduction

This PhD project was undertaken from April 2014 until September 2017 in the Division of Imaging Sciences and Biomedical Engineering Department at King's College London, UK. This thesis is a collection of contributions that have been, or will be, published in international scientific journals.

1.1 - Thesis overview

Cardiovascular diseases (CVDs) remain the leading cause of death in western counties. Among CVDs, myocardial infarction (MI) diagnosis and treatment has benefitted from several improvements in therapeutic strategies that led to significant improvements in survival rates. However, patients surviving MI, are at high risk of developing heart failure (HF) due to impaired left ventricular remodelling. Currently, it is difficult to predict which patients will develop HF making risk stratification and selection of optimal treatment options challenging often leading to overtreatment causing unwanted side effects and further increasing healthcare costs. For these reasons, there is an urgent need for

improved diagnosis to identify patients at high risk of HF and to spare those with low risk from unnecessary treatment and associated side effects.

Clinical decisions for the management of post-MI patients are based on anatomical, functional or tissue specific imaging techniques including magnetic resonance imaging (MRI) and echocardiography. With the development of cell and protein specific imaging probes the visualization of the underlying biological processes has become feasible and may facilitate risk stratification and treatment planning. It also might allow the identification and imaging based monitoring of novel therapeutic targets that augment healing and attenuate adverse remodelling.

The remodelling process after MI can be divided in three phases: the inflammatory phase where neutrophils and monocytes are recruited from the blood stream to the site of injury where they clean the area from dead cells and extracellular matrix (ECM) debris; the proliferative phase during which fibroblast proliferation and angiogenesis leads to the formation of granulation tissue and finally the maturation phase with the deposition of ECM proteins (e.g. collagen, elastin and proteoglycans) which form the fibrous scar. The ability of the heart to undergo tissue repair after MI is closely dependent upon the timing and extent of these phases.

In this thesis, two novel MR contrast agents were used for the simultaneous assessment of inflammatory cell recruitment and ECM deposition in the heart post-MI. MI was induced by the permanent occlusion of the left-anterior descending coronary artery (LAD) in wild-type (WT) and monocyte chemoattractant protein-1 knockout mice (MCP-1$^{-/-}$). ^{19}F labelled nanoparticles (^{19}F PFCs) were used for the selective imaging of inflammatory cells and a

gadolinium-based elastin-specific magnetic resonance agent (Gd-ESMA) was used for visualisation and quantification of ECM remodelling. To facilitate clinical translational, all MR scanning was performed on a clinical 3T MRI system. The organization of this thesis is described below.

Chapter 2 describes the incidence of CVDs, with a focus on MI. It describes the remodelling processes after MI, including the biological and physical changes of the heart, with special attention to inflammatory cell types and ECM proteins, which play an important role during the healing process.

Chapter 3 introduces the concept of molecular imaging and its application in assessing MI. It describes the state of the art of imaging post-MI remodelling. Examples of different imaging techniques and contrast agents for the assessment of the different phases during MI healing are described.

Chapter 4 summarizes the background knowledge related to MRI. The first part of the chapter focuses on the physical properties of MRI and the primary contrast mechanisms. The second part describes the mostly used pulse sequences used in cardiac MRI and the challenges of preclinical MRI.

Chapter 5 describes the optimization of the methodology used in this PhD project: (1) surgery optimization and reproducibility; (2) development of a MR compatible heating system for the 3T MRI and; (3) ^{19}F acquisition protocol optimization. (1) For the optimization of the surgery, a lung intubation system was designed to allow an easier and faster assessment of the trachea; it is highly

reproducible and permits faster recovery of the animals. A description of the MI induction by permanent LAD occlusion is also described. (2) A MR heating system was developed for the 3T MRI to improve the wellbeing of the animals and the reproducibility of the scans. (3) This chapter introduces the ^{19}F contrast agents. Two agents were compared and their biophysical properties were studied in phantoms using 3T MRI/MR-Spectroscopy and 9.4T nuclear magnetic resonance (NMR) spectroscopy. Based on this study, one of the two ^{19}F contrast agent was chosen and was used for the *in vivo* experiments investigating inflammatory cell recruitment after MI.

Chapter 6 investigates the feasibility of multinuclear $^{19}F/^{1}H$ MRI imaging for the simultaneous assessment of inflammation and ECM remodelling following MI non-invasively in WT mice. Inflammation was assessed after the intravenous injection of ^{19}F PFCs (which are avidly taken up by inflammatory cells), showing a peak at day 7 post-MI. ^{19}F quantification was performed with NMR spectroscopy, and was in agreement with *in vivo* MR data. *In vivo* ^{19}F MRI correlated linearly with macrophage immunohistochemistry. ECM remodelling post-MI was evaluated using Gd-ESMA, a specific contrast agent that binds to both cross-linked elastin and immature, tropoelastin, which are highly expressed after MI. Increasing Gd-ESMA uptake was observed from early to later stages of post-MI remodelling, corroborating with the deposition of tropoelastin in the infarcted tissue (tropoelastin immunohistochemistry). Furthermore, the interplay of both contrast agents and their predictive value was evaluated in a longitudinal proof-of-concept study. Fifteen animals were scanned consecutively at day 7 and 21 post-MI. ^{19}F MRI was performed at 7 days (48 hours after 400 μL ^{19}F PFCs)

to assess the peak in the inflammatory process and an elastin scan (1 hour post Gd-ESMA injection) was performed at day 7 and 21. End-diastolic volume was used as a measure of cardiac outcome.

Chapter 7 similar to the previous chapters, ^{19}F PFCs and Gd-ESMA were used to investigate inflammatory cell recruitment and ECM deposition in a MCP-$1^{-/-}$ mouse model. MCP-1 is a chemokine protein highly expressed after MI and is responsible for the recruitment of inflammatory cells into the myocardium. The objective of this study was to investigate the potential of multinuclear $^{19}F/^{1}H$ in assessing inflammatory cell influx and its impact on myocardial remodelling. The same animal model was used under similar experimental conditions for the *in vivo* experiments in chapter 6 and therefore direct comparison could be made between WT and MCP-$1^{-/-}$ animals. Inflammatory cell profiles were evaluated with Fluorescent Activated Cell Sorting (FACS).

Chapter 8 summarises the findings made in this work and provides an outlook on future projects.

Chapter 2

Cardiovascular diseases: Myocardial Infarction

Cardiovascular disease (CVD) is the leading cause of death worldwide, causing approximately one-third of deaths in 2011. It is estimated that until 2030 these rates will increase and cause 23.6 million deaths annually [1]. Despite the clinical efforts in improving survival rate by early reperfusion strategies, a large pool of patients having survived an acute myocardial infarction (MI) are at risk of developing heart failure (HF) [2]. The development of HF after MI is closely associated with severe changes in cardiac geometry, function and structure, also referred to (ventricular) **remodelling**.

Myocardial infarction is mainly caused by coronary artery occlusion due to either a rupture or an erosion of an atherosclerotic lesion and the formation of a thrombus, which obstructs blood flow to the myocardium [3]. This restriction of blood flow to the downstream tissue triggers a series of events that culminate in the death of affected cardiomyocytes. The human left ventricle (LV) has 2–4 billion cardiomyocytes, 25% of which can become necrotic in a few hours post-MI [4].

After MI, the ability of the heart to repair depends on a complex immune/inflammatory response. For those who survive MI, the heart undergoes a remodelling process within the next few weeks with progressive ventricular dilatation and fibrosis where the necrotic myocardium is replaced by collagen-rich scar tissue [5, 6]. A schematic figure of this process is shown in **Figure 2.1**.

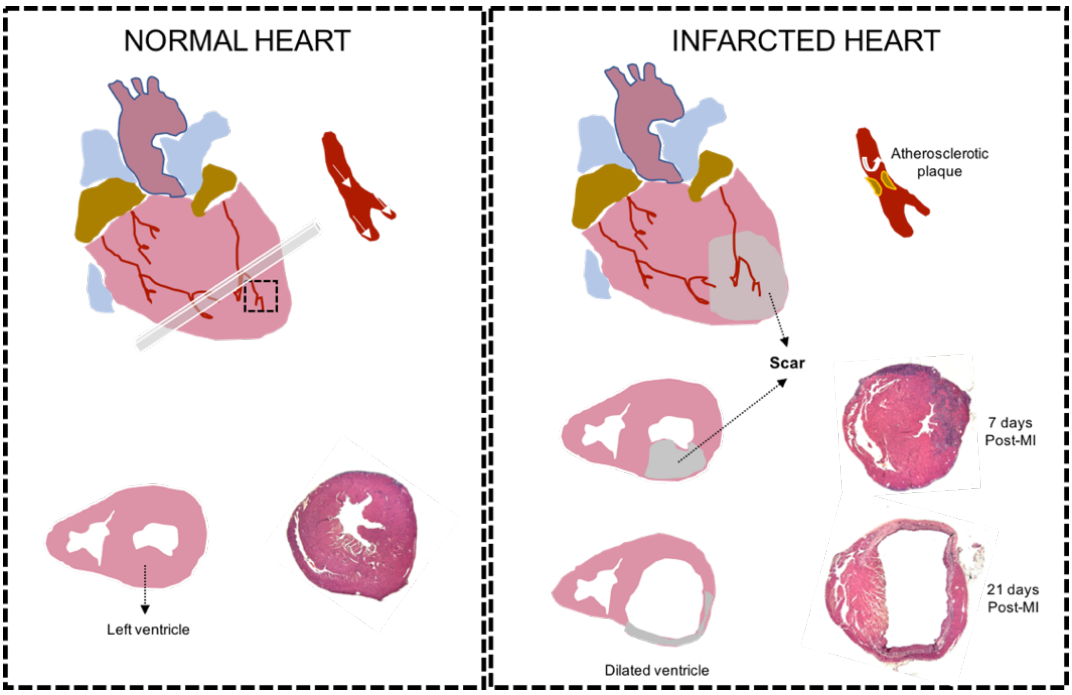

Figure 2.1. Differentiation between (A) normal and (B) infarcted myocardium. Myocardial infarcts (MI) often result from rupture of a coronary plaque, with subsequent formation of a thrombus, and consequently impaired blood flow to the downstream tissue. The process after MI, known as "ventricular remodelling" leads to death of cardiomyocytes, triggers an immune inflammatory response and at later stages leads to left-ventricle thinning as well as scar formation. Schematic short-axis views and Haematoxylin and Eosin staining at 7 and 21 days show the changes in the left-ventricle occurring between the acute event and the chronic stage.

In this chapter, an overview of the different biological processes that occur after MI will be discussed. The cellular and molecular events during MI remodelling will be considered with special focus on the time scale during which the different processes occur. In this context, the role of different cell types and of some extracellular matrix (ECM) proteins important for the understanding of

this PhD project will be discussed. This chapter is based on a number of review papers [7-21].

2.1 - Molecular and cellular processes

Coronary artery occlusion and the associated reduction of blood supply to the myocardium (ischemia) causes a decline in the availability of oxygen and glucose to an extremely metabolic active tissue, triggering a series of molecular events called ischemic cascade. Briefly, the unavailability of oxygen and glucose to the myocardium during ischemia causes depletion of ATP levels in the tissue and an immediate loss of contractility. Failure of ATP-dependent ion pumps located in the cells' membranes causes disruption of ionic homeostasis and subsequent cell swelling (oedema phase) and intracellular Ca^{2+} overload, which contributes to the production of free radical species. After MI, the tissue undergoes a remodelling process, marked by necrotic and apoptotic cell death and inflammation, where the myocardium experiences high cell and ECM turnover. Evidence suggests that although necrosis is the major form of cell death, apoptosis seems to play a crucial role during infarct healing [22-25]. The healing processes following an MI can be divided into three successive and overlapping phases: **inflammatory phase, proliferative phase/resolution of inflammation, and maturation phase** [26], in which a balance between those phases is required for an optimal healing. These different phases are active processes characterized by different cellular and molecular markers as schematically illustrated in **Figure 2.2**.

Cardiomyocyte necrotic death triggers an inflammatory response, resulting in the recruitment of leukocytes into the infarcted area to clear the debris

consisting mainly on dead cells and matrix. Once the infarcted area is cleared and inflammatory mediators are repressed, reparative cell influx commences. These cells produce ECM proteins that will help to maintain the structure and function of the LV. This phase is followed by the maturation of the scar tissue and accompanied by apoptosis of the no longer needed reparative cells.

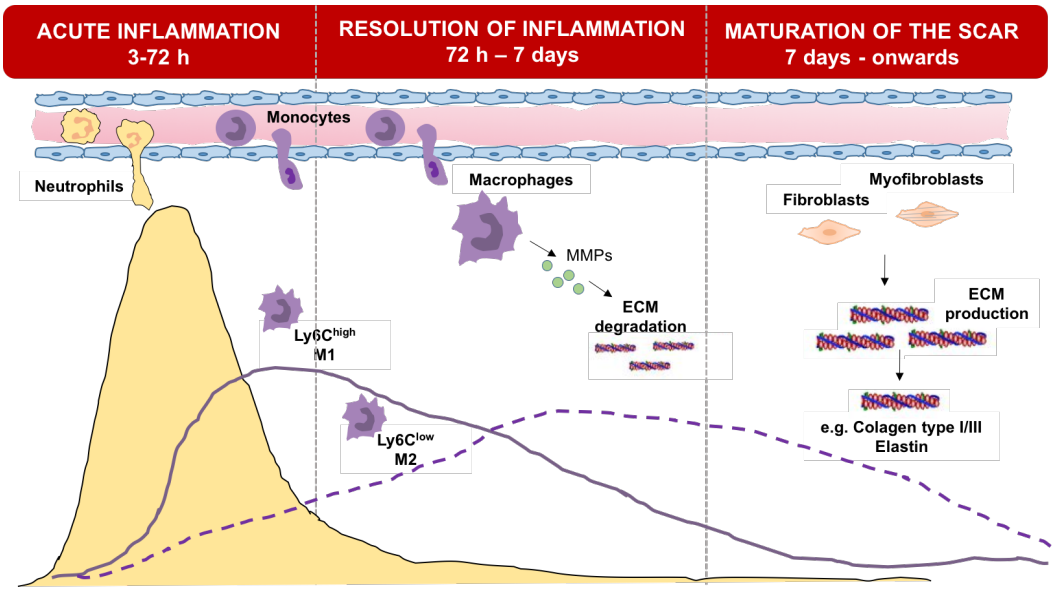

Figure 2.2. The healing process after myocardial infarction in mice can be divided in three successive and overlapping phases: acute inflammation, resolution of inflammation and maturation of the scar. The curves illustrate the time course of the different inflammatory cells involved in the healing process over time. During the inflammatory phase (3-72 hours) pro-inflammatory monocytes Ly6C^{high} and M1 macrophages and neutrophils are recruited from the blood stream to the injured area, and are responsible to clean debris and dead cardiomyocytes. Resolution of inflammation phase (72 hours-7 days) is characterized by the presence of anti-inflammatory monocytes Ly6C^{low} and M2 macrophages. These cells produce matrix metalloproteinases (MMPs) which degrade damaged extracellular matrix (ECM). This phase is also marked by an extensive formation of a vascular network. The maturation phase follows (7 days – onwards), characterized by the differentiation of myofibroblasts from fibroblasts; new ECM is formed, a scar is formed rich in collagen type I, III and elastin.

2.1.1 - Inflammatory phase

After MI, tissue necrosis is occurring in the subendothelium expanding to the epicardium during the first hours. It is during this initial phase that the most significant changes occur, affecting cells and tissues, and becoming increasingly irreversible after 12 hours. This period of time is therefore crucial and provides a

treatment window for reperfusion to occur and preserve part of the myocardium [3].

In the early hours after MI, leukocytes (neutrophils and mononuclear cells) rapidly infiltrate the infarct to remove cell debris intervened by inflammatory mediators.

2.1.1.1 - Inflammatory mediators

Ischemic myocardium produces CC chemokine ligands, complement factors and other mediators which attract neutrophils and monocytes to the site of injury. These inflammatory mediators may play an important role in the remodelling of the myocardium by promoting the removal of death cells and degradation products of the ECM by activated matrix metalloproteinases (MMP) [27, 28].

Soluble mediators such as monocyte chemotactic protein-1 (CCL2/MCP-1) and interleukin-8 (IL-8) are expressed and responsible to attract monocytes/macrophages and neutrophil populations, respectively [7, 28].

Complement activation (e.g. C5 component of complement), L-selectin and integrins (e.g. CD11/CD18) have been shown to play important roles in the recruitment of neutrophils [29, 30]. Also, TNFα and IL-1β are mediators capable of prolonged neutrophil activity during the inflammatory phase [26, 31].

MCP-1 protein is a powerful attractant for monocytes, especially during the inflammatory phase. In the absence of this protein, murine models of MI have shown a decreased and delayed infiltration of monocytes/macrophages. These animals also show an attenuation of adverse remodelling by delaying the formation of granulation tissue [32]. Monocytes/macrophages accumulate first during the inflammatory phase promoting inflammation and removal of cell debris

by producing TNFα and MMPs. Later, monocytes/macrophages produce other cytokines and growth factors, such as interleukin-10 (IL-10) and transforming growth factor β (TGFβ), which repress inflammatory signals and regulate granulation tissue formation during the proliferative/resolution of inflammation phase.

Approaches targeting molecules involved in the activation of inflammatory cells have been successful in attenuating ischaemic injury in animal studies, however the translation to patient therapy was unsuccessful [8, 9]. There is nevertheless an ongoing interest in the involvement of inflammatory mediators in repair and remodelling of the infarcted heart, but focus has turned to the understanding of functional, structural and geometrical alterations of the heart during LV remodelling.

2.1.1.2 - Neutrophils

Circulating neutrophils are recruited from the blood stream and are the first to arrive at the site of injury, through vasodilation and activation of both chemokine-dependent and chemokine-independent pathways. During the inflammatory phase, endothelial cells upregulate adhesion molecules (e.g. selectin, integrin) that trigger neutrophil adhesion and extravasation (**Fig.2.3**). Rapid accumulation leads to an early neutrophil peak after injury [10, 11]. In the ischemic tissue, neutrophils phagocyte dead cells and produce MMPs that degrade ECM. Neutrophils eventually undergo apoptosis and are removed by macrophages later on [11]. Neutrophils therefore play an important role in the resolution of inflammation and can influence the proliferative phase as well. Neutrophils however, when in abundance, can produce too much MMPs and

degrade excessively the ECM, compromising tissue stability and integrity. In patients, higher numbers of neutrophils in the heart were associated with worse prognosis [33]. The same outcome was found in mice with induced MI. Neutrophil-depleted mice have shown impaired recruitment of pro-inflammatory monocytes/macrophages (Ly6C^{high} and M1 macrophages), but not of M2 reparative macrophages, leading to increased fibrosis [34].

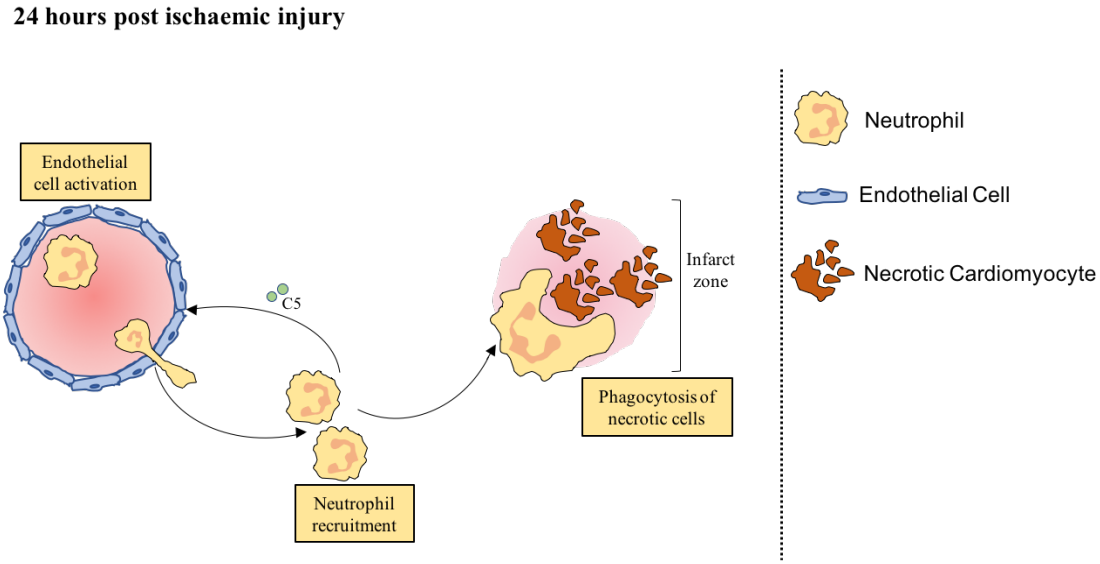

Figure 2.3. In the early hours after myocardial infarction (within 24 hours) necrotic cardiomyocyte release pro-inflammatory cytokines and chemokines into the circulation blood activating both endothelial cells and systemic neutrophils. Activated neutrophils adhere to activated endothelium and transmigrate into the cardiac tissue following a chemokine gradient. Neutrophils secrete proteases that digest tissue (and activate chemoattractants, such as complement component C5a), which further potentiates leukocyte recruitment. Neutrophils may then phagocytose dying cells, but they can also induce apoptosis in healthy cardiomyocytes themselves through the release of reactive oxygen species. Adapted from [12].

2.1.1.3 - Monocytes/Macrophages

Monocyte subpopulations infiltrate and accumulate in the myocardium sequentially (after approximately 24 hours), with pro-inflammatory monocytes arriving first, being rapidly mobilized from the bone marrow and the splenic reservoir [3, 35]. On days 1 to 4 post-MI, inflammatory Ly6C^{high} monocytes are recruited to digest the injured cells of the myocardium. During the following 5 to 10 days, a second subset of monocytes dominate, the reparative Ly6C^{low}

monocytes, supporting angiogenesis and scar synthesis, while the number of Li6C^{high} declines [10, 36].

When monocytes infiltrate from the blood stream into the tissue they mature into macrophages [11, 37, 38]. M1 macrophage subsets with pro-inflammatory properties infiltrate the infarct and might sustain a pro-inflammatory environment. M1 macrophages play a similar role as neutrophils. They clean the infarcted tissue from dead cells and debris, promote matrix breakdown and phagocytose apoptotic neutrophils. On the contrary to neutrophils, which die after phagocyting debris, macrophages survive for longer periods. M1 macrophages remove cellular debris, foreign substrates including lipids, and microbes [11]. In the final phase of the process, as the granulation tissue migrates inwards toward the core of the infarct, the remaining necrotic tissue is engulfed and digested by the M2 macrophages. M2 macrophages repress inflammation and stimulate fibroblasts growth and angiogenesis, and they also participate in the regulation of ECM deposition by the production of both MMPs and their inhibitors [20]. At this stage, the inflammation phase is repressed and the infarct is prepared for the proliferative phase. This process is schematically illustrated in **Figure 2.4**.

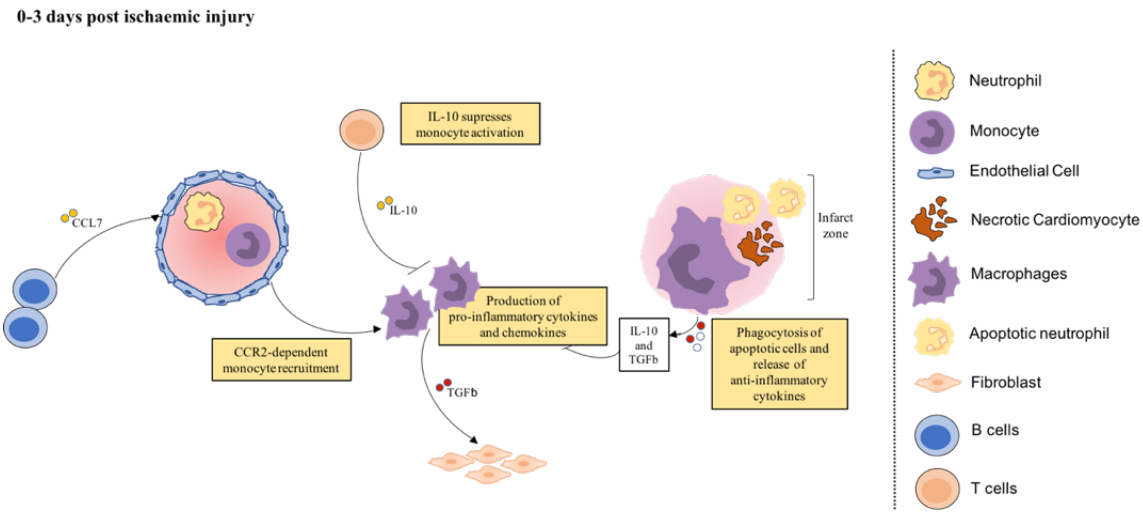

Figure 2.4. Tissue injury activates innate immune signalling and secretes chemokines (e.g. CCR2) thereby triggering leukocyte infiltration into the injured myocardium. Until day 3, Ly6C^{high} monocytes are recruited from the blood into the ischemic cardiac tissue, mobilized from the bone marrow and the splenic reservoirs. Recruited monocytes secrete pro-inflammatory cytokines and chemokines, and they further amplify inflammatory processes. A proportion of recruited monocytes ingest apoptotic cells, including neutrophils, which increases the secretion of anti-inflammatory cytokines, such as transforming growth factor-β (TGFβ) and interleukin-10 (IL-10), thereby decreasing leukocyte recruitment. Adapted from [12].

Summarizing, macrophages have several roles: they remove necrotic debris, regulate ECM turnover producing proteolytic enzymes that degrade collagen and elastin, and promote angiogenesis [13, 39, 40].

2.1.1.4 - Other cell types: B, T cells

Other cell types including B cells [41], CD^{4+} T cells [42] and dendritic cells [43] have been shown to be involved in a balanced recruitment of monocytes populations. Experiments in mouse models of permanent coronary artery ligation suggested that the depletion of B cells leads to a decrease in the Ly6C^{high} monocyte population, thus improving heart function [41]. Conversely, CD^{4+} T cell-deficient mouse strains show a negative delay in the transition from Ly6C^{high} to Ly6C^{low} monocytes, thereby impairing healing of the heart [42]. In line with this observation, a recent paper showed that CD^{4+} regulatory T cells can positively contribute to cardiac healing, promoting monocyte/macrophage differentiation

[44]. Finally, when dendritic cells were depleted the resolution of inflammation was interrupted, the recruitment of pro-inflammatory monocytes Ly6C^{high}/M1 macrophage populations was enhanced whereas the recruitment of anti-inflammatory monocytes Ly6C^{low}/M2 macrophage was decreased, impairing cardiac healing [43].

2.1.2 - Proliferative phase

The proliferative phase is characterized by an extensive neovascularization and ECM formation, regulated by reparative cells (myofibroblasts and vascular cells) some weeks after MI. The heart contains an abundant population of interstitial and perivascular fibroblasts. Bone marrow-derived fibroblast progenitors, endothelial cells, smooth muscle cells and pericytes might contribute to the myofibroblast population as well [9, 45]. A schematic of this post-inflammatory phase is shown in **Figure 2.5**.

2.1.2.1 - Fibroblasts/Myofibroblasts

Fibroblasts are, after cardiomyocytes, the most predominant cells in the heart. Fibroblasts are found throughout the cardiac tissue and surrounding myocytes, forming a complex 3D network within the connective tissue [14]. Cardiac fibroblasts in healthy tissue are not contractile and produce small amounts of ECM. However, in the presence of a pathology like MI, fibroblasts are activated and differentiate into myofibroblasts, and synthetize large amounts of ECM proteins (e.g. collagen type I, III, IV and V) [15].

Myofibroblasts are mainly differentiated fibroblasts [16, 17]. This process can be mediated by different factors such as the activation of TGFβ, deposition of matrix proteins, mechanical stress and/or pro-inflammatory mediators [9, 18].

Myofibroblasts express contractile proteins like α-smooth muscle actin and secrete large amounts of proteins important for myocardial integrity [46, 47]. They can contribute either to beneficial or adverse myocardial remodelling after MI depending on the regulation of collagen deposition [17]. Myofibroblasts have been reported to appear in the infarct as early as 3 days after MI (stimulated by macrophages and TGFβ) and remain there for months [48]. Myofibroblasts undergo apoptosis at the end of the proliferative phase, as the collagen-based scar is formed. Their persistence can be predictive of progressive fibrosis and/or organ failure.

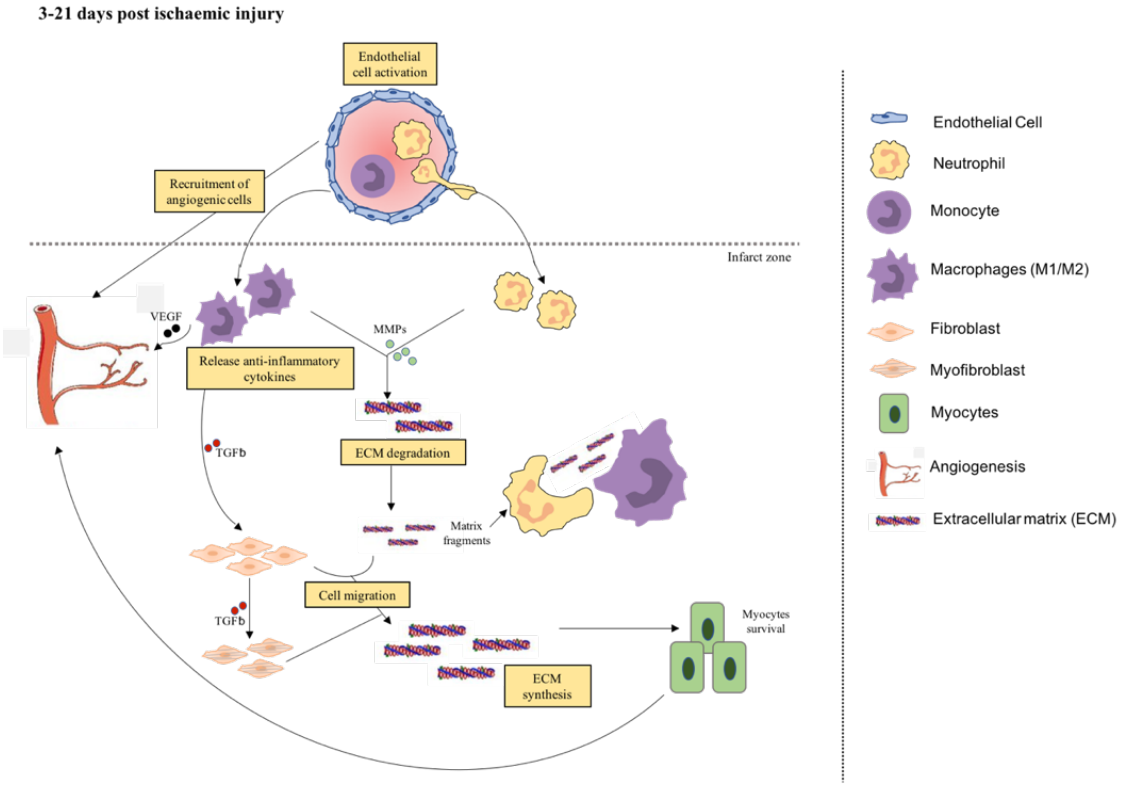

Figure 2.5. Post-inflammatory phase is marked by the production of MMPs which degrade the ECM allowing cell migration into the injured area. Neutrophils and monocytes are recruited from the blood stream, and on arrival at the injured myocardium clean dead cells and ECM fragments allowing repopulation of immune reparative cells such as fibroblasts and myofibroblasts. Pathways of repressing inflammation are activated; the number of inflammatory cells decrease and fibroblasts and myofibroblasts secrete ECM proteins. The newly synthetized ECM matrix is crucial to preserve the structure and integrity of the left ventricle. Furthermore, angiogenic signalling stimulates the proliferation and infiltration of endothelial cells and leads to the establishment of a microvascular network in the infarct area. ECM, extracellular matrix; MMPs, Matrix metalloproteinases.

2.1.3 - Maturation phase

MI is frequently associated with LV remodelling leading to progressive heart failure. The underlying mechanism of LV remodelling is multifactorial, involving changes in the chamber dimensions and geometry, namely the progressive dilation initially through infarct zone expansion, thinning of the ventricular wall and increase of the chamber [49]. A major component of adverse LV remodelling and dilatation is a profound alteration in the composition of the ECM. Other alterations are also observed, such as hemodynamic alterations resulting in overall decreased cardiac pump performance [50].

Subsequent dilation and shape change occur through myocyte hypertrophy within noninfarcted zones and are associated with increased fibrosis and cell death [50]. Infarct expansion, stretching and thinning of the infarcted wall, may occur early after MI. Over the course of several months, there is progressive dilatation, not only of the infarct zone, but also of the healthy myocardium [49].

2.1.3.1 - Role of extracellular matrix: Collagen & Elastin

The ECM is an integral component of the myocardium, and the factors that influence the integrity of the ECM have also an impact on cardiac structure and function. In vertebrates, ECM provides not only the physical and mechanical support, but it also serves as a reservoir of many biomolecules that interact and influence the cellular response after injury [51].

Remodelling of the ECM is a key component of cardiac remodelling after MI. Disruption of the ECM network structure interrupts the connection between the myocardial cells and blood vessels, thereby compromising the structural integrity and function of the heart. Conversely, excess production and accumulation of ECM structural proteins, or fibrosis, results in enhanced stiffness

of the myocardium and hinders ventricular contraction and relaxation, leading to distorted architecture and cardiac function. Excess collagen deposition and fibrosis have been clearly linked to myocardial stiffness and diastolic and systolic dysfunction [52].

During wound healing and subsequent formation of the fibrotic scar synthesis of ECM proteins is upregulated. This phase has been characterized by positive vascular remodelling with enlargement of the vessel wall [53, 54] and it has been associated with an excess production of collagen, proteoglycans and elastin [39].

Collagen: Collagen is present in all tissues and provides a structural framework and strength. In the heart collagen is synthesized and secreted by myofibroblasts., Collagen types I, III, IV, V and VI can be found in the myocardium, with structural collagen type I being the most predominant (>70%) [17, 55]. Collagen type I has been found to be a major constituent of scar formation and stabilization. In mature scar, collagen type III can be also found, however it is nonelastic and can cause LV stiffness [56]. During cardiac remodelling the balance between the synthesis and degradation of collagen of great importance.

Elastin: Elastin has been identified as a key ECM protein decisive for infarct stabilization and preservation of ventricular function [57-59] by promoting elasticity and strength of the tissues. Elastin is an insoluble and hydrophobic protein with a very low turnover rate. Elastin deposition begins with the synthesis and secretion of the 72 kDa soluble precursor molecule tropoelastin (produced

by fibroblasts) that becomes cross-linked into insoluble elastin by enzymatic reactions (lysyl oxidase) [19, 60]. Secreted tropoelastin is “chaperoned” to the extracellular space by the elastin-binding protein [61] where tropoelastin is stabilized and aligned along microfibrils [60], that contain glycoproteins (e.g., fibrillins) and microfibril-associated glycoproteins (e.g. MAGP-1) prior to enzymatic cross-linking [61].

The myocardium has normally negligible amounts of elastic/tropoelastin fibres. After MI, elastic fibres increase within the scar in the first weeks and continue to form a more dense network between the remaining viable myocytes, myofibroblasts and smooth muscle cells during maturation of the infarct scar [57]. Higher amounts of elastin in the heart might help preserve the elasticity of the scar. Mizuno and colleagues [58, 59] have shown that elastin gene injection into the infarcted area leads to increased expression of elastin in a rat model of MI. This proved to be beneficial, limiting the scar expansion and ventricular dilatation.

2.1.4 - Future perspectives

MI remodelling is a complex and dynamic process. While the duration of the healing process varies between species and genders, evidence suggests that early and aggressive immune responses and high levels of neutrophils and monocytes within the infarct may promote adverse remodelling and lead to poor prognosis [33, 62, 63]. Substantial infiltration of immune cells in the affected area and ECM breakdown can lead to infarct expansion and subsequent ventricular dilatation, aneurysm and rupture [20, 33].

Taken together, a better understanding of the underlying processes during MI remodelling is needed to design novel therapeutic strategies. Biomarker-based approaches might help with the identification of different pathophysiologic

responses. The specific identification of neutrophils or monocytes/macrophages populations by non-invasive imaging techniques could help to better understand the effect of targeted therapies. Furthermore, elucidation of the cellular and molecular mechanisms responsible for the synthesis of ECM proteins is essential to design cardioprotective and reparative strategies that could prevent or reverse fibrosis, respectively, after infarction [21, 64].

2.2 - Animal models of myocardial infarction

Animal models can closely mimic human disorders with respect to structural and functional characteristics. For that purpose, the induced disorder needs to resemble the human disease, in this case coronary heart disease. As previously mentioned in this chapter, MI occurs after the narrowing of one of the main coronary arteries in the LV.

Various strategies and methods have been developed and applied in different laboratory animal species, including mice, rats, rabbits, pigs, dogs, and primates [65]. The occurrence of MI can be induced in different ways: 1) It can be induced by feeding fat/cholesterol-rich diet, which is a risk factor for atherosclerosis and consequently MI. This model is closer to the clinical situation; however, time and site of occlusion can be random and unpredictable with this approach. 2) MI can also be surgically induced, which has the advantage of a tight control on the location, extent and time of the infarction. Controlling these parameters allows more reproducible results.

MI can be surgically induced with different methods, as shown in **Figure 2.6**: *hydraulic occlusion*, usually used in larger animals (e.g. pigs), where the constrictor is placed around the left coronary artery; *coronary artery occlusion*, where the proximal left anterior descending coronary artery (LAD) is ligated,

inducing MI. It has higher mortality rates (up to 50% in dogs and rodents [66, 67], and 20% in pigs [68]) and in the case of mice microsurgical technique and equipment is required; *myocardial ischemia* or *infarction followed by reperfusion* represents a valuable tool to elucidate pathophysiological and molecular mechanisms underlying cardiac remodelling, since reperfusion is a standard clinical procedure [69]. In comparison to the permanent occlusion model, the MI with reperfusion model leads to higher infiltration of inflammatory cells, attenuated fibrotic remodelling and enhanced neovascularisation in the infarcted area [65, 69, 70].

Mice are the preferred species for such studies because of their genetic malleability, rapid breeding cycle, and relatively economic husbandry. However, their small size is a challenge when the evaluation of an infarct is required, especially for imaging modalities.

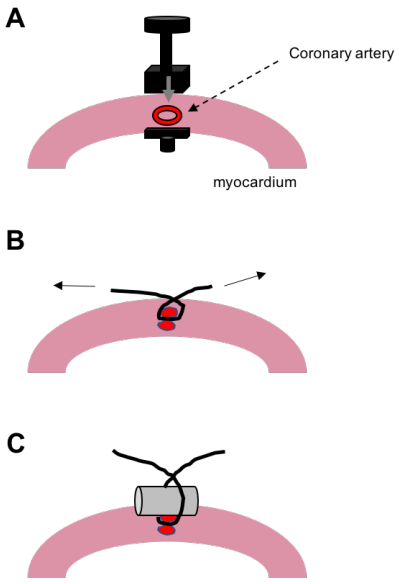

Figure 2.6. Animal model of myocardial infarction (MI). MI can be induced by (A) *hydraulic occlusion*, where a constrictor is placed around the left coronary artery; (B) *permanent coronary artery occlusion*, where a knot is placed around the left-anterior descending coronary artery (LAD); or by (C) *reperfusion model*, where a knot is placed around the LAD and a plastic tube, where the latter is removed usually after 30 minutes after the occlusion and blood flow is restored.

Chapter 3

Molecular imaging of cardiac remodelling

Conventional cardiac imaging techniques aim at detecting changes in anatomy and function of the heart, such as cardiac function, geometry, blood flow or myocardial viability. Molecular imaging in contrast, besides providing macroscopic information, allows the visualization of the underlying biological processes, at a molecular and cellular level. Molecular imaging differs from traditional imaging in that probes known as **biomarkers** are used to help image specific targets or pathways *in vivo* [71]. Molecular imaging has great potential both for the early detection of cardiovascular and other diseases.

As mentioned in **Chapter 2**, after myocardial infarction (MI) the myocardium undergoes severe alterations that involve several biological processes that could potentially be targeted with molecular imaging. Molecular imaging may enable the identification of precursors or early stages of cardiac remodelling, and allow monitoring and guidance of novel and target-orientated cardiovascular therapies. It may also provide a greater understanding of previously unknown biological processes occurring within the heart, specifically targeting molecular processes underlying the post-MI immune cell response, and

subsequent left-ventricular (LV) remodelling [72, 73]. Other clinical problems that may also benefit from molecular imaging, include early identification of patients with atherosclerotic plaques that are at high risk of causing long-term complications or patients with high risk of developing severe ventricular remodelling leading to heart failure after MI [71, 74], or even the evaluation of effectiveness of some therapies in clinical trials or for monitoring therapy response [75, 76].

In this chapter, a description of the different imaging modalities for studying cardiovascular diseases will be provided. Additionally, molecular imaging, with passive or active targeting, will be introduced and discussed in the context of cardiovascular diseases. Specific focus will be given how molecular imaging may be used to broaden our understanding of the mechanisms that underlie post MI remodelling by its ability to targeting the different stages of the remodelling process (e.g. oedema, inflammation and extracellular matrix (ECM) deposition).

3.1 - Techniques and imaging modalities

Molecular imaging provides non-invasive visualization of biological processes on a cellular and protein level, based on the use of molecular probes or biomarkers in very low concentrations and without interfering with the undergoing biological processes [71, 77]. The probe is usually composed of a signal element (e.g. gadolinium, iron oxide or a radioactive isotope) that can be visualized with an imaging modality and a ligand (e.g. antibody, peptide or small molecule) that recognizes and binds to a biological target. The probes should be non-toxic, exhibit favourable pharmacokinetics and biodistribution, e.g. fast

clearance from blood, rapid extravasation, high specificity towards the target, and provide a high target-to-background ratio. In magnetic resonance imaging (MRI), this can be further improved by a high relaxivity ratio between the bound and free probe, also called the receptor induced magnetization enhancement (RIME) effect. For efficient target-specific MRI probes this ratio varies between 2 and 5.

Figure 3.1 summarizes some non-invasive clinical imaging modalities, their applications and specifications regarding resolution and sensitivity.

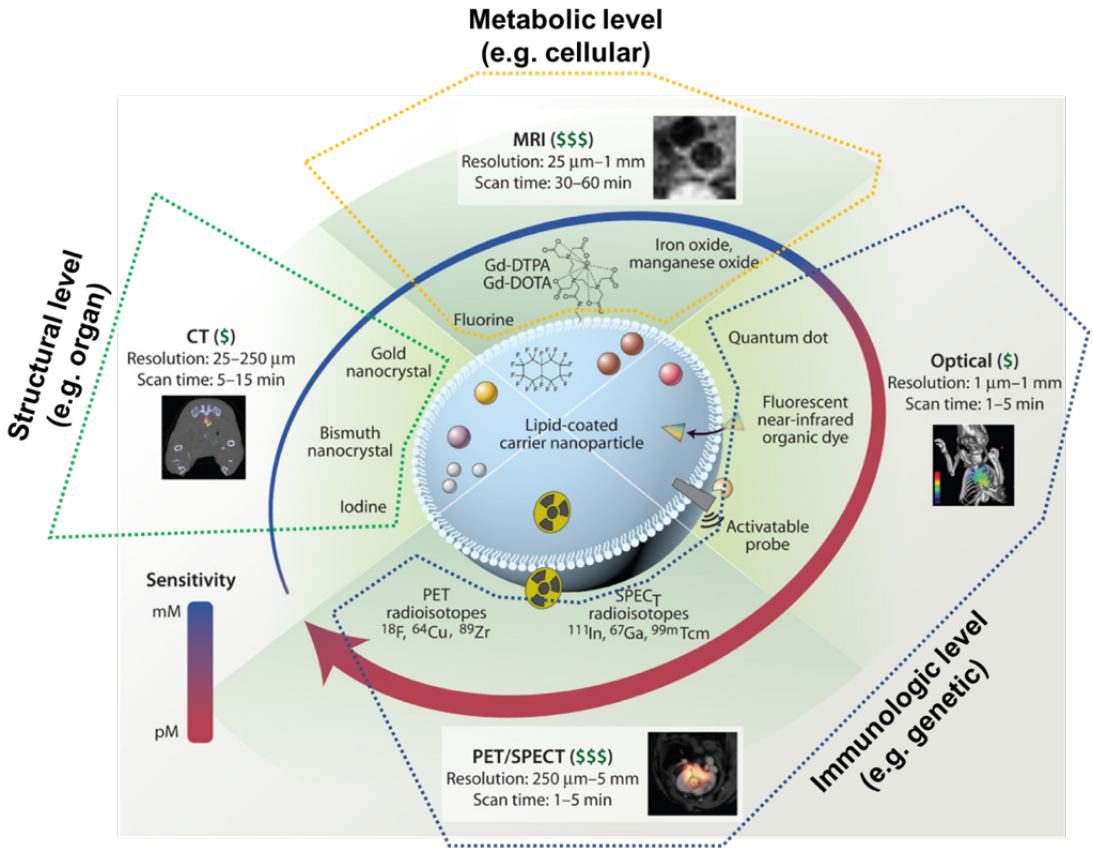

Figure 3.1. Overview of non-invasive clinical imaging modalities for anatomical, physiological, metabolic and molecular imaging. Nanoparticles can be targeted with different probes, and its functionalization can be used to assess specific cell interaction, inflammatory pathways or to monitor therapeutic responses. MRI, magnetic resonance imaging; PET, positron emission tomography; SPECT, single photon emission computed tomography; CT, computed tomography; Gd, gadolinium-based contrasts. Adapted from [78].

3.1.1 - Nuclear imaging

The most widely used molecular imaging approaches are based on nuclear imaging techniques, such as single photon emission computed tomography (SPECT) and positron emission tomography (PET) [71]. The main advantage of SPECT and PET is their high sensitivity for tracer detection. In addition, the large number of tracers together with the possibility of multinuclear imaging (SPECT) make them powerful tools for the study of metabolism and molecular targets *in vivo* [76, 79]. However, the use radioactivity may be a limitation for screening of asymptomatic patients or follow-up studies.

SPECT is usually used to assess myocardial perfusion and metabolism [80]. This technique combines the injection of a radioisotope tracer (usually thallium-201 and technetium-99m) with a gamma camera image acquisition. The camera rotates around the patient to create several images that are arranged and reconstructed to form 3D images [72]. Compared to MRI, SPECT allows the imaging of low-abundance molecules (10^{-3}/$^{-5}$ mmol/L vs 10^{-10}/$^{-11}$ mmol/L). Consequently, only low concentrations of the probe are needed (nM), and so the disruption of the biological processes or toxicity are not a concern. In a meta-analysis involving 114 studies, SPECT was shown to have a good sensitivity (88%) and moderate specificity (61%) for detecting ischaemia in patients with known or suspected coronary artery disease (CAD) [81]. A drawback of SPECT is the low spatial resolution (~8-10 mm) compared with PET (~3-5 mm) and MRI (~1-2 mm). While SPECT is highly accurate in measuring radioisotope uptake for the assessment of myocardial perfusion and metabolism, it does not provide true anatomical and functional information unlike MRI [79, 82].

PET has been the gold-standard for the non-invasive assessment of myocardial viability using 2-deoxy-2-(^{18}F)fluoro-D-glucose (^{18}F-FDG) until the introduction of late gadolinium enhancement (LGE) MRI. PET has been shown to be highly specific (81%) and sensitive (84%) for the diagnosis of CAD induced ischemia [81]. PET uses rubidium-82 chloride, nitrogen-13 ammonia and oxygen-15 radioisotopes to assess perfusion. As the radiotracers decay a positron is emitted and when it collides with an electron, it produces two gamma quants that can be measured by the scanner as a co-incidence signal (512 keV). PET provides higher image resolution than SPECT (4-5 vs 10-16 mm), and has a well-established photon attenuation correction (because of the physical behaviour of positron decay), allowing the correct localization and, in combination with validated kinetic models, the quantification of biological processes [76]. A key advantage of PET is the use of fluorine-18 deoxyglucose (^{18}F-FDG) that enables the assessment of metabolism. By combining myocardial perfusion and viability data PET can be used to determine whether the myocardium is normal, fibrotic (reduced perfusion and metabolism) or potentially salvageable [83]. A disadvantage of this modality is the very short half-life of PET tracers and the necessity of having access to a cyclotron and radiochemistry resources. In addition, PET is not widely available as it is an expensive imaging technique [71].

3.1.2 - Computed Tomography

Computed tomography (CT) combines a series of X-ray images taken from different angles to generate cross-sectional images. CT is usually used for coronary artery angiography, and to assess LV structure and systolic function. It has also been used to assess perfusion and viability. Typically, a CT imaging protocol is divided in two stages (two scans). The first scan, involves a

conventional CT angiogram for the visualization of the coronary arteries. This scan is performed after the injection of contrast agent (usually iodinated contrast), and coronary arteries appear bright due to the presence of the contrast agent. In addition, areas with reduced myocardial contrast enhancement can be associated with areas of reduced perfusion (e.g. coronary stenosis or microvascular obstruction). The second scan involves the assessment of viability, where areas of fibrous tissues appear hyperenhanced compared with normal muscle [84]. CT provides high spatial resolution, and has proven to provide good diagnostic accuracy [85]. CT could be used as an alternative to cardiac MR when patients have pacemakers or suffer from claustrophobia. Some disadvantages include high costs, exposure to ionizing radiation and the need to lower and stabilise the heart rate with beta blockers. Cardiac arrhythmias can affect image quality [73].

3.1.3 - Magnetic resonance imaging

MRI is a technique that provides excellent soft-tissue contrast with high spatial and temporal resolution allowing detailed cardiac anatomy and functional information without ionizing radiation and even without contrast agents [86]. In MRI, a big magnet is being used to align the spin of water protons in the body (H^+) parallel or anti-parallel to the magnetic field, creating a “net magnetisation vector”. Typically, only a small fraction (1 ppm) of water protons is aligned with the external magnetic field and spins are precessing with the Larmor frequency about the external magnetic field. By applying radiofrequency pulses, the net magnetization vector can be tipped into the transverse plane. The precessing transverse magnetization can then be measured in the presence of a magnetic gradient field with a receiver coil and the received time signal can be Fourier

transformed to generate an image. While the transverse magnetization decays with T_2, the longitudinal magnetization returns to the equilibrium magnetization with the tissue specific time constant T_1. More details about MRI physics are described in **Chapter 4**.

Pre-clinical and clinical studies have shown that T_2-weighted (T_2W) MRI, which is especially sensitive for water, can be used to assess oedematous area-at-risk (area of the myocardium that is supplied by the affected artery) and potentially salvageable myocardium [87-89]. To detect irreversible injured myocardium, different contrast agents have been investigated including iron-oxide nanoparticles, liposomes or emulsions (e.g. gadolinium chelates) [90-92]. Gadolinium-based contrast agents have become the gold standard for the assessment of myocardium viability, such as gadopentitic acid (Gd-DTPA). Gadolinium changes the magnetic properties of water protons and therefore the signal intensity of the surrounding tissues. It accumulates in fibrotic areas due to the increased extracellular volume and remains longer in these areas compared with normal tissue because of the dysfunctional capillary system [86, 93]. Late gadolinium enhancement (LGE) images can be used to detect small volumes of myocardial injury, which is a strong prognostic predictor of future coronary events [94]. In addition, LGE MRI allows to assess infarct extent and is important to guide coronary intervention [95, 96]. MRI also allows multimodal imaging, e.g. $^{19}F/^{1}H$ MRI. The ^{19}F signal can be measured directly by MRI because of the lack of natural fluorine in the body. ^{19}F based contrast agents, usually nanoparticles, have been used to assess hot-spots of inflammation in mouse models of MI. By combining the ^{19}F image with a ^{1}H image, exact anatomical co-localization of these particles can be achieved [97].

Compared to nuclear imaging techniques, MRI molecular imaging lacks in sensitivity. Due to the relatively slow data acquisition of MRI, cardiac and respiratory motion can cause image artefacts. To minimize motion artefacts data acquisition is synchronized with the electrocardiogram while respiratory motion is compensated using navigator techniques. Pacemakers remain challenging, and patients with claustrophobia and anxiety may need sedation prior to study, as an MRI scan can take between 45 to 90 minutes [86, 98-100].

3.1.4 - Ultrasound

Conventional ultrasound imaging (US) uses a transducer to produce pulses of sound that propagate into the tissue. US is a non-invasive technique usually used to assess the anatomy in real-time and measure blood flow in large vessels with very high temporal resolution. US systems are low cost, portable and safe for both the user and the patient, because of the lack in ionizing radiation and is the most widely used clinical cardiac imaging modality. Molecular targeted US is also available, and is based on the use of gas-filled, acoustically active microspheres or ‘microbubbles’ engineered to bind to specific endothelial targets. Development of more sophisticated ultrasound equipment may increase sensitivity and specificity, by enhancing microbubble properties, facilitating their cardiovascular molecular imaging applications [101, 102].

3.1.5 - Optical imaging

Fluorescence and bioluminescence imaging are optical molecular imaging techniques that use light-emitting agents (which generate fluorescence or bioluminescence photons) for the visualization and measurement of biological processes. Optical imaging allows high-speed and high-sensitivity detection of

multiple tracers; it can be used to target several biological events. It is relatively easy to perform and inexpensive compared with other molecular imaging techniques. The limited penetration depth (light only penetrates a few cm into the tissue, limiting a whole-body scan) is still the major limitation when translating this technology into patients [71, 103].

3.1.6 - Multi-modality imaging

Multi-modality imaging is also available and is often required when anatomical/functional information is needed or for quantification and anatomical localization of molecular probes. Some hybrid techniques include, SPECT/CT, PET/CT or PET/MRI [76, 104, 105]. These hybrid imaging modalities combine the advantages of SPECT and PET (high sensitivity for detecting molecular processes) with the high resolution morphological images provided by CT and MRI. In addition, MRI offers superior soft tissue contrast. These simultaneous acquisitions also benefit from intrinsic co-registration allowing the correction for motion, attenuation or partial volume effects thereby improving tracer quantification [71]. The drawback of these multi-modal techniques are the high equipment costs, specialised training and availability of the systems. However, the information that these hybrid modalities provide allow more complex studies and might help improving our understanding of biological processes and therapeutically targets *in vivo*.

3.2 - Molecular imaging of myocardial infarction remodelling

The remodelling process after MI involves the activation and recruitment of inflammatory cells, their maturation, the recruitment of reparative cells and

deposition of ECM proteins within the scar tissue. Understanding the MI remodelling process at a molecular and cellular level *in vivo* may improve our knowledge of post infarct healing and could aid the better selection of patient-specific treatments that aim at limiting infarct expansion and subsequent LV remodelling. In this section, practical applications of *in vivo* molecular imaging to assess MI remodelling will be described.

3.2.1 - Oedema

Myocardial oedema can refer to either myocyte swelling or accumulation of fluid in the interstitial space, that result in the retention of water in the cardiac space. Oedema can be found in many cardiac injuries including severe or acute myocardial infarction [88], reperfusion [106], inflammation [89] or cardiac transplantation [107].

T_2W MRI have been used to assess and quantify oedema *in vivo* in the heart. Due to the long T_2 relaxation time of water-bound protons, an image can be generated with higher signal intensity within the oedematous tissue by using T_2W sequences. In 1983, Higgins and colleagues [108] showed for the first time the positive correlation of T_2W signal intensity and water-tissue content in a canine model of myocardial infarction. Clinically, T_2W CMR is currently used to determine the extension of the area-at-risk in reperfused and non-reperfused myocardium [109, 110] providing prognostic information whether the myocardium is salvageable. It is also used to distinguish between acute and chronic coronary syndromes [111], which is important for diagnosis and treatment guidance.

The duration and extent of myocardial oedema depends on the disease models. In dogs, myocardial oedema has been observed after 30 minutes of ischemia [88]. In patients with MI, oedema was evident after 24 hours, remained

unchanged during the first week while a reduction in oedema size was observed by week two [93] (**Fig.3.2**).

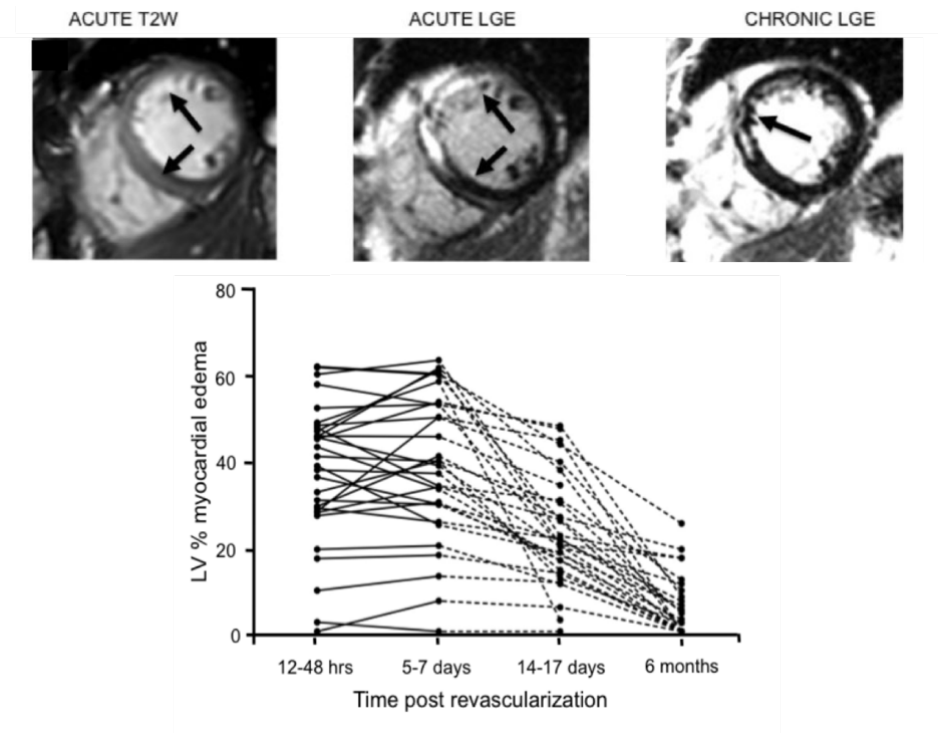

Figure 3.2. Visualization of oedema with T_2-weighted sequences (T_2W) and corresponding gadolinium enhancement (LGE) images from the scar area. Over time, the oedema area decreases significantly the left ventricular (LV) volume. Adapted from [93].

Gadolinium-based contrast agents used at an early time-point (up to 5/7 days) after MI have shown to underestimate the salvaged myocardium. On LGE images acquired during the acute phase of MI, a significant overestimation of the infarct area can be observed, which decreases considerably over time [93]. LGE observed during the acute stages not necessary implies irreversible injury, and thus may underestimate the amount of salvageable myocardium. Thus, for assessment of the area of risk a combination of LGE and T_2W imaging should be performed.

3.2.2 - Apoptosis/necrosis in MI

Within the first hours after an MI, cardiomyocytes start dying, either via apoptosis and/or necrosis. Both processes are highly regulated and their detection has been accomplished using molecular imaging approaches [112]. It is evident that cells that show early features of an apoptotic program may have the potential to be salvaged if detected early. The possibility of identifying these events *in vivo* may have profound implications on therapy and may help clinicians salvaging tissue and preventing further damage of the myocardium.

While the cell membrane remains intact during apoptosis, it ruptures and becomes permeable during necrosis; these characteristics have been taken into consideration when developing novel imaging agents. Current successful *in vivo* imaging of apoptosis has been accomplished with an Annexin-V based imaging probe. Annexin is a cellular protein and binds selectively to phosphatidylserine, a phospholipid present on the outer membrane of apoptotic cells and on the inner membrane of viable or necrotic cells [113]. Imaging of apoptosis with an Annexin-V imaging probe has been achieved with 99Tc-SPECT [114, 115], fluorescence imaging [116] and MRI [117, 118].

SPECT imaging using 99Tc/Annexin-V showed accumulation of this probe within the infarcted area, but not in the surrounding myocardium, consistent with areas of perfusion defect, suggesting the presence of programmed cell death [115]. This probe requires a waiting period of 15-20 hours for adequate blood clearance before imaging. This is a challenge when targeting apoptosis, as this process is considered more prevalent between 4-8 hours after infarct reperfusion. The time decay rate thus decreases the sensitivity of this probe [119, 120].

Annexin can also be bind to phosphatidylserine on the inner surface of necrotic cell membranes. To differentiate between apoptosis and necrosis, Sosnovik and colleagues [117, 118] used AnxCLIO-Cy5.5 to assess apoptosis and a gadolinium based contrast agent, Gd-DPTA-NBD, to identify necrosis, simultaneously in a murine model of ischemia/reperfusion. AnxCLIO-Cy5.5 nanoparticles have been developed as a multimodal probe that combined an Annexin group with a superparamagnetic cross-linked iron oxide (CLIO) providing MRI signal and an infrared fluorochrome Cy5.5 for fluorescence imaging. Similarly, Gd-DTPA was combined with NBD fluorochrome. The evolution of cardiomyocyte death was analysed, and within 4-6h of reperfusion, AnxCLIO-Cy5.5 uptake was significantly higher compared to CLIO-Cy5.5 (a control inactivated Annexin). Approximately 70% of the myocardium which showed AnxCLIO-Cy5.5 uptake did not show Gd-DTPA-NBD uptake simultaneously (**Fig.3.3A,B**). Fluorescence microscopy and immunohistochemistry confirmed that most of the cardiomyocytes in these areas were morphologically intact and therefore remained potentially salvageable within this period. The MR images showed that the signal of apoptotic areas was restricted to the mid-myocardium (where the border might have some flow restoration) whereas necrosis was confined to the sub-endocardium) (**Fig.3.3C,D**). In areas with both apoptosis and necrosis (with simultaneous uptake of AnxCLIO-Cy5.5 and Gd-DTPA-NBD) the percentage of wall thickness was significantly reduced between 4-6h of reperfusion compared to segments with apoptosis alone (**Fig.3.3E,F**) [118]. These results indicate the greater the extent of cell loss during this phase, the worse the functional outcome. These results indicate that the greater the extent of cell loss during this phase, the worse

the functional outcome. Overall, these studies have shown the potential of cardiomyocyte salvage within 4-6 hours post-MI, and that apoptosis can be imaged *in vivo*.

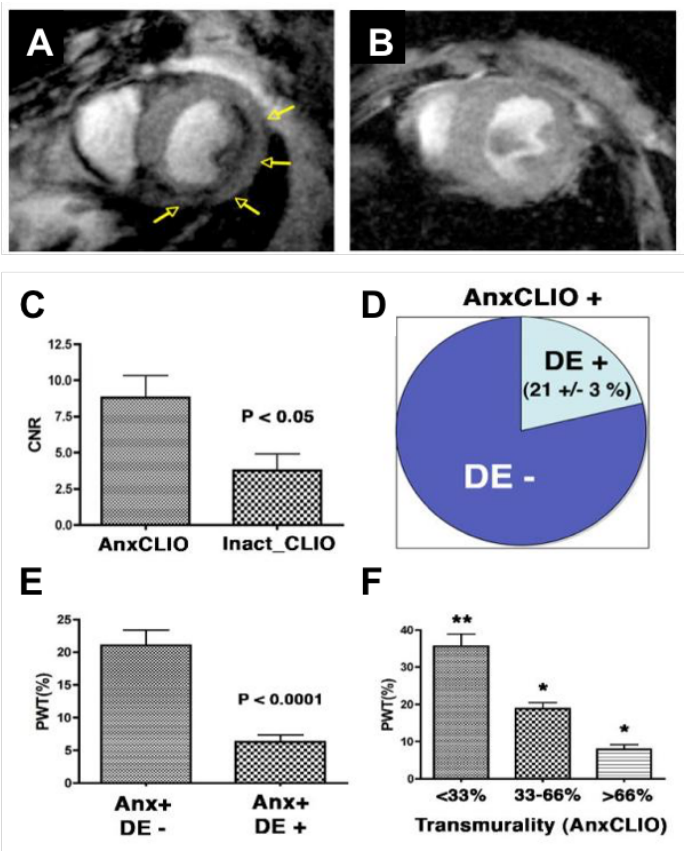

Figure 3.3. Molecular MRI of cardiomyocyte death in myocardium exposed to mild-moderate injury. Cardiomyocyte apoptosis (A) AnxCLIO-Cy5.5 showed mid-myocardial uptake (yellow arrows, hypointensity signal) and (B) control, CLIO-Cy5.5 showed no significant uptake. Cardiomyocyte necrosis (C) contrast to noise ratio (CNR) indicating uptake of AnxCLIO-Cy5.5 and the control probe inativatedCLIO-cy5.5 in injured vs non-injured myocardium (D) Percentage of AnxCLIO-Cy5.5 accumulated myocardium (anxCLIO+) with or without simultaneous Gd-DTPA-NBD uptake (DE-/+), (E) Contractile function (measured by percentage wall thickening, PWT in %) in AnxCLIO-Cy5.5 accumulated myocardium segments with or without simultaneous Gd-DTPA-NBD uptake (DE-/+). (F): Contractile function based on the transmural extent of AnxCLIO-Cy5.5 accumulation (representing infarct extent). Means±SEM **P<0.001, *P<0.01. A*dapted from [118].

3.2.3 - Inflammation (and wound healing in MI)

In patients and mice, MI triggers the recruitment of leukocytes to the injured tissue [11]. The amplitude and duration of the inflammatory response has a significant impact on the outcome of infarct healing. Both severe [20, 36, 121] and low levels [121, 122] of inflammation lead to impaired myocardial healing.

Inflammation can be assessed by targeting specific cell types and/or molecules, such as **(1) adhesion molecules critical to leukocyte recruitment, (2) enzymes released by inflammatory cells or by (3) directly assessing monocytes/macrophages.**

(1) The activation of the vascular endothelium is crucial for neutrophil and monocyte recruitment [123]. Nahrendorf and colleagues have shown the feasibility of targeting VCAM-1, expressed on endothelial cells, in a mice model of MI by PET-CT *in vivo* [124]. By using a tetrameric peptide ^{18}F-4V, which binds to VCAM-1, expression of this protein could be evaluated. ^{18}F-4V preferentially accumulated in the infarcted regions but not in the remote myocardium, which was correlated with higher VCAM-1 mRNA expression. One limitation of this particle is the potential toxicity due to cellular uptake and the waiting period of 48h before imaging.

Alternatively, iron-oxide particles have been extensively used in MRI for tracking inflammatory cells and are FDA approved for clinical use (Ferumoxytol, AMAG Pharmaceuticals, USA) [125]. They are non-toxic and allow multimodal imaging if labelled with fluorophores. As these particles are superparamagnetic they have a strong effect on T_2 and T_2* relaxation times (higher iron concentrations lead to shorter T_2 and T_2* relaxation times and higher R_2 and R_2* values). Limitations of iron oxide particles include the negative contrast (signal loss) that can create “black holes” in the images and prevent anatomical MR colocalization and consequently evaluation of the tissue of interest.

(2) Matrix metalloproteinases (MMPs) that are secreted by inflammatory cells, degrade the ECM proteins and play a significant role in myocardial healing. During remodelling, MMPs are upregulated and are actively involved in inflammatory cell infiltration, facilitating cellular debris removal, migration of cardiomyocytes and myofibroblasts, as well as promoting angiogenesis and consequently ECM protein deposition. Excessive MMPs activity can lead to increased ECM degradation and consequently lead to wall thinning, dilatation and ultimately heart failure [126, 127]. MMPs can be imaged using (1) a large range of ligands (e.g. tissue inhibitors of metalloproteinase-like peptides) or (2) exploiting their proteolytic activity [128].

^{99m}Tc-RP805 SPECT tracer has been used to label a broad spectrum of MMP inhibitors. In a porcine model of MI, a multimodality SPECT/CT imaging system was used to analyse the evolution of MMP (^{99m}Tc-RP805) activity, which was then correlated with LV deformation by cine MRI at 1, 2, and 4 weeks post-MI [129]. Within the 1st week post-MI tracer retention was maximum, and remained upregulated until 1 month post-MI; ^{99m}Tc-RP805 was in good agreement with MMP activity and correlated with the increase in LV end-diastolic volumes (**Fig.3.4**) [129].

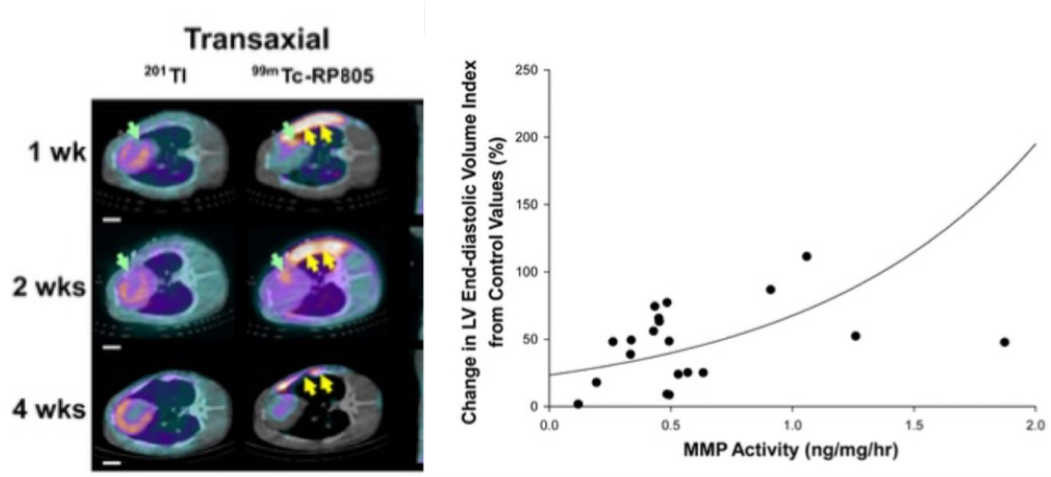

Figure 3.4. (A) *In vivo* SPECT/CT imaging using a dual-isotope 99m Tc-RP805. (B) Relationship between body mass indexed LV end-diastolic volume and MMP activity within the infarcted region. Adapted from [129].

Chen *et al* [130] developed a near-infrared fluorescent (NIRF) probe that is activated by MMP cleavage to study changes in MMP activity after MI. Two MMPs were identified; one at the beginning and another at the end of the healing process, MMP9 and MMP2, respectively. After induction of MI, the NFIR probe was injected into different groups of mice and MMP activity was evaluated *ex vivo*. Areas of infarcted regions showed an increase in NFIR signal compared to normal myocardium, with a peak at 1 week, that remained high until 4 weeks after MI. Flow cytometry demonstrated that MMPs were leukocyte-derived.

Leukocyte infiltration and protease activity after MI were further evaluated by Nahrendorf *et al* [131]. The disruption of ECM during remodelling is not just affected by proteinases, as MMPs, but also by lysosomal proteases, like cathepsins. Cathepsin is upregulated in different animal models after MI [132, 133] and in patients with dilated cardiomyopathy [134]. Fluoromagnetic iron oxide nanoparticles (CLIO-VT750), which are phagocytosed by inflammatory cells, and a fluorescent probe (Prosense-680), which is activated by the proteolytic activity of cathepsins, were investigated in the healing myocardium of wild-type and

($FXIII^{-/-}$) mice with impaired would healing. *In vivo* fluorescent molecular tomography (FMT) with Prosense-680 demonstrated a strong signal within the infarcted regions. Additionally, after co-registration of FMT and MRI images, accumulation of CLIO-VT750 was detected in the hypokinetic infarcted myocardium. Using this multichannel FMT protocol, they demonstrated that cathepsin activity (shown by Prosense-680) peaked at day 4 after MI, and phagocytosis (shown by CLIO-VT750) peaked at day 6. $FXIII^{-/-}$ mice showed lower signal for both probes ($P<0.05$).

(3) Inflammation is characterized by infiltration of the damaged tissue by monocytes/macrophages. Monocytes/macrophages phagocytose cell debris and pathogens – a property that has been used for the development of imaging strategies [97, 135-138]. Monocytes/macrophages populations have been targeted using a variety of materials, and have been imaged by PET and SPECT (using different ligands), optical imaging (using quantum dots and fluorochrome-labelled nanoparticles), CT and MRI (using iron-oxide nanoparticles and ^{19}F perfluorocarbons) [139].

^{18}FDG PET: ^{18}FDG is a marker for tissue uptake of glucose and thus ^{18}FDG PET imaging is clinically being used to assess myocardial viability as the production of glucose is supressed in the ischaemic myocardium [140]. In addition, ^{18}F-FDG, can be used to assess inflammatory cell activity (increase in glucose activity) in the myocardium post MI or in patients with myocarditis [141, 142]. Lee *et al* [142] assessed the post-infarct inflammatory response through monocyte uptake of ^{18}FDG with PET/MRI. Infarcted areas showed significantly increased ^{18}FDG-PET signal at day 5, compared with control mice (2.7±0.1 vs

1.3±0.2; *P<0.01*), and by day 14 the signal had returned normal values (**Fig.3.5**). Interestingly, the observed signal changes follow the biphasic monocyte recruitment, of Ly-6C^{high} and Ly6C^{low} monocytes. The combination of PET with MRI provided the precise co-localisation of the PET signal with the infarct and analysis of both anatomic and functional parameters. As mentioned before, myocytes also metabolize glucose, and so they can show high ^{18}FDG signal. Consequently, suppression of this uptake is required prior to inflammatory cell imaging. In this study, the authors used ketamine-xylanize anaesthesia to supress background signal. Xylanize has shown to impair insulin secretion in response to rising glucose levels, in rodents [143]. By decreasing circulating insulin, GLUT4 (an insulin-sensitive glucose transporter) is inhibited in the cardiomyocyte membrane, consequently decreasing the glucose levels and ^{18}F-FDG signal. Other strategies of food withdraw, heparin administration, or limiting the anaesthesia have been also evaluated to supress cardiomyocyte signal [144]. Fasting is the most used in clinical practise; after feeding insulin levels rise, and glucose becomes the primary substrate for oxidative metabolism (as the diet switches the myocardium from glucose to fat metabolism), and consequently, decreased FDG uptake in the myocardium.

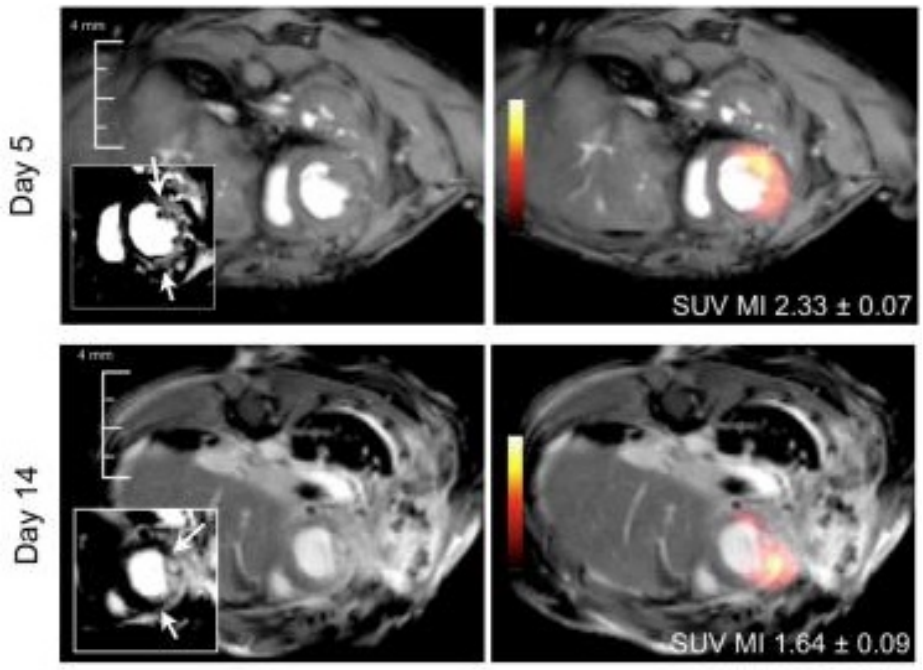

Figure 3.5. ^{18}FDG-PET detection of metabolically active macrophages in the murine myocardium 5 and 14 days post-myocardial infarction (MI). Adapted from [142].

^{1}H/^{19}F MRI ^{19}F perfluorocarbons (PFCs) nanoparticles have been also explored to target macrophages *in vivo* by ^{1}H/^{19}F MRI. ^{19}F PFCs can be imaged by ^{19}F MRI separately from the proton anatomical image. Its signal is directly proportional to the PFC concentration and background ^{19}F signal is absent resulting in high specificity for ^{19}F and consequently macrophages. Some PFC-containing nanoparticles suitable for MRI purposes are FDA approved as blood substitutes [145]. Flögel and colleagues have shown the possibility of tracking macrophages using ^{19}F PFCs *in vivo* in a mouse model of MI [97]. The authors showed that ^{19}F signal could be detected within the anterior, lateral and posterior wall of the heart, and in areas of surgical incisions, consistent with the presence of macrophages assessed by histology (**Fig.3.6A,B**).

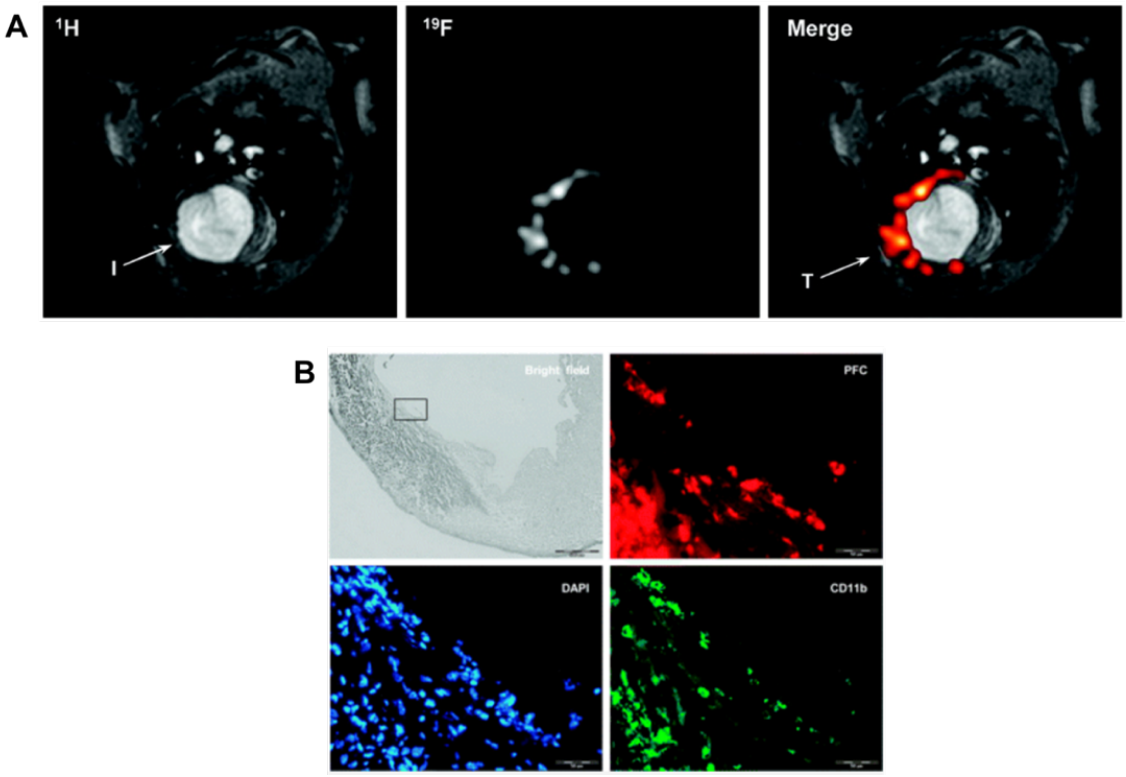

Figure 3.6. Infiltration of perfluorocarbons 4 days after induction of myocardial infarction in mice. (A) *In vivo* ^{19}F MRI: anatomically corresponding ^{1}H and ^{19}F images, showing accumulation of ^{19}F in areas of infarcted myocardium. (B) Colocalization of rhodamine-labelled PFCs and monocytes/macrophages in the heart after immunofluorescence of CD11b. Adapted from [97].

More recently, ^{19}F MRI has also been used at clinical field strength. Bönner *et al* [135] have shown the possibility of imaging ^{19}F *ex vivo* in porcine hearts at 3T. Two fluorine emulsions have been studied, perfluoro-15-crown-5-ether (PFCE) and an already clinically applied perfluorooctylbromide (PFOB) together with gadolinium enhancement. Four days after MI induction, the hearts were excised and *ex vivo* MRI showed accumulation of PFCE in the infarcted region. Detection of a low number of macrophages using the fluorine approach may remain challenging because of sensitivity issues. To allow for human application, improvements to the pharmacokinetics of the PFCs are currently researched to allow faster clearance [97, 136].

FMT/MRI Another approach to track monocytes/macrophages is by the combination of fluorescence molecular tomography (FMT-CT) and MRI. Panizzi and colleagues [36] used this hybrid technique to specifically image Ly6C^{high} monocytes and study their role in infarct healing. The authors have shown that the presence of the monocyte sub-populations was linked to high protease activity. The increment in blood circulating monocytes has been associated with disturbed resolution of inflammation and consequently poor prognosis.

SPIONs MRI Iron oxide particles have been used to detect inflammation in the heart. Similarly to ^{19}F-PFCs, iron-oxide particles have been used to track monocytes/macrophages after being injected intravenously [90, 138, 146-148]. Sosnovik and colleagues [146] have shown the potential of combining MRI and fluorescence imaging to track macrophage/monocyte populations *in vivo* after induction of MI in mice using a magnetofluorescent nanoparticle CLIO-Cy5.5. MRI and fluorescence microscopy imaging was performed 48 hours after administration, showing an increase in CNR in areas of infarcted myocardium, but not in SHAM-operated animals. Areas of accumulation of CLIO-Cy5.5 by MRI were correlated with fluorescence tomography and associated with macrophage infiltration (**Fig.3.7**).

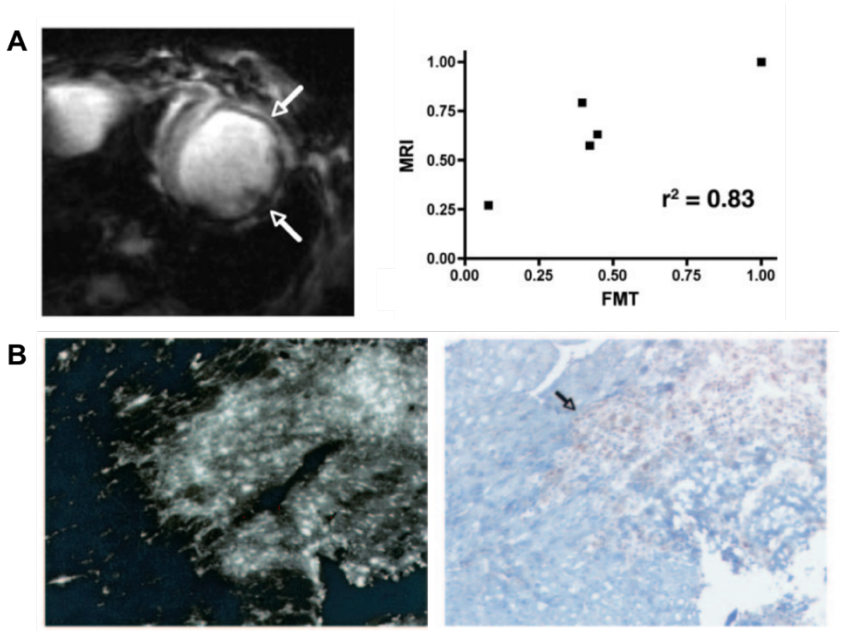

Figure 3.7. Fluorescent molecular tomography (FMT) and magnetic resonance imaging (MRI) of myocardial macrophage infiltration in the heart in a murine model of myocardial infarction. (A) Correlation of myocardial contrast-to-noise by MRI and cardiac fluorescence intensity by FMT 48h after administration of CLIO-Cy5.5 in different doses ranging from 3 to 20mg iron/kg. (B) Fluorescence microscopy colocalized well with positive signal from immunohistochemistry for MAC-3 macrophages. Adapted from [146].

Clinically, ultrasmall superparamagnetic iron oxide particles (USPIO) have been administered in patients with acute myocardial infarction. Areas of infarct showed higher R_2* relaxivity values, whereas remote areas showed less uptake. The authors suggested that the signal at the remote areas can be associated with the influx of inflammatory cells to the area of infarct. However, no histological analysis has been performed to corroborate their hypothesis [90].

Additionally, and more interesting, some studies have shown the possibility of cell tracking by *in vivo* pre-loading of monocytes/macrophages and monitor their evolution using iron-oxide particles [137, 149]. Montet-Abou and colleagues [147] showed that before induction of MI, the prior administration of fluorescent superparamagnetic iron oxide particles (SPION) can be used to track the infiltration journey of monocytes/macrophages in rats by MRI. Areas of hypointense signal could be detected in infarcted areas of MI animals but not in

the control or SHAM group. More interesting, the SPIO-MI-anti-inflammatory CCL5 group showed a significant reduction in signal in the infarct region compared with SPIO-MI rats. Immunohistochemistry against $CD68^+$ cells showed a correlation between the MRI signal and tissue macrophages. In addition, the degree of macrophage infiltration was related to the extent of myocardial fibrosis (**Fig.3.8**).

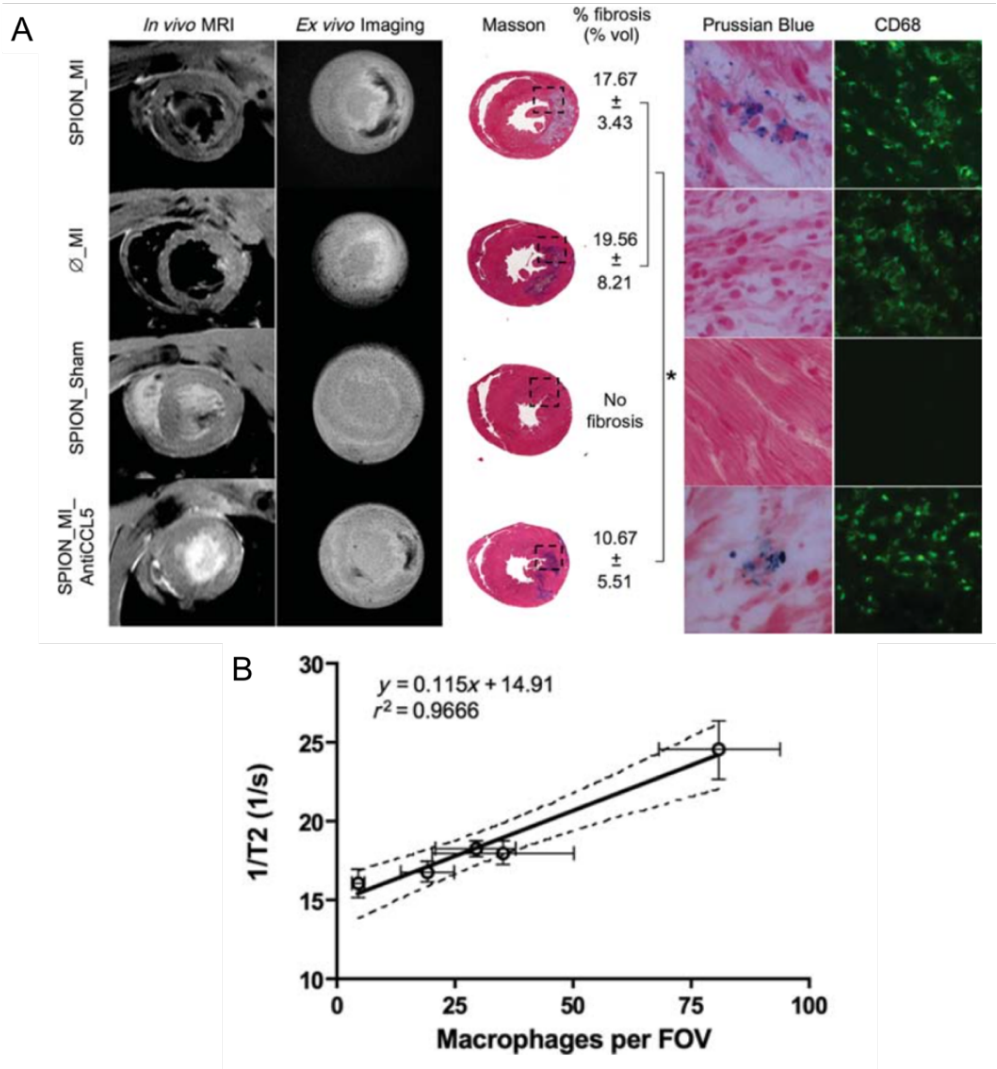

Figure 3.8. Monocytes/macrophage infiltration after myocardial infarction (MI): (A) Comparison of all groups at day 3. SPION_MI showed a hypointense signal by MRI (*in vivo* and *ex vivo*) in the MI. Fluorescent-loaded cells in the myocardial infarction corresponding to CD68 positive cells. Animals with MI but no iron injection (∅_MI) did not show hypointense signal by MRI or iron-loaded cells by histology. The SPION_SHAM group did not show an inflammatory infiltrate or myocardial infarction. The SPION_MI_AntiCCL5 showed a hypointense signal by MRI, small fibrosis and less iron-loaded CD68-poositive cells in the MI. (B) Correlation of histological data and quantification of $1/T_2$ values of monocytes/macrophage population 3 days after MI. SPION, fluorescent superparamagnetic iron oxide particles; MRI, magnetic resonance imaging. Adapted from [147].

Overall, this data supported the idea of monocytes/macrophages as a therapeutically target to regulate inflammatory response, promoting the healing process and consequently attenuating LV remodelling.

3.2.4 - Resolution of inflammation

Angiogenesis is an important part of myocardial repair following MI. The formation of new capillaries can affect the prognosis of infarct healing and therefore *in vivo* visualisation may help predict the remodelling outcome and stratify patient risk. Currently imaging approaches include probes that target the $\alpha_v ß_3$ integrin or the up-regulation of vascular endothelial growth factor (VEGF) receptors.

$\alpha_v ß_3$ integrin, expressed on the cell surface of proliferating endothelial cells, is a key signalling regulator in angiogenesis. Meoli *et al* [150] showed up to a four-fold increase in the retention of the probe in hypoperfused regions of canine myocardium where angiogenesis was stimulated using a SPECT imaging probe, ^{111}In-labeled $\alpha_v ß_3$-targeted agent. This was in agreement with the histological findings, where evidence of angiogenesis and increased expression of $\alpha_v ß_3$ was identified within the infarcted areas. A novel compound, ^{99m}Tc labelled regioselectively addressable functionalized template-RGD (^{99m}Tc-RAFT-RGD) has been used *in vivo* in a rat model of re-perfused MI by SPECT [151]. The probe has improved affinity to $\alpha_v ß_3$ integrin. ^{99m}Tc-RAFT-RGD was visible in the infarcted area but not with the negative control ^{99m}Tc-RAFT-RAD, reflecting the induction of angiogenesis in the infarct zone after reperfusion of an MI.

The time-course of angiogenesis post-MI was further studied by Higuchi et al. [152]. The ^{18}F-Galakto-RGD PET probe, which specifically binds to $\alpha_v ß_3$ integrin, was deposited at the border of the infarct by day 3, peaked between 1

and 3 weeks while expanding into the centre of the infarct, and decreased to baseline at 6 months after reperfusion. *In vivo* signal uptake was corroborated with vascular density accessed by immunohistochemistry. The translation to the clinical setting has been successfully demonstrated in one patient with recent MI, where an increase signal uptake was identified in the areas of infarction in patients 2 weeks after MI [153].

VEFG is a protein produced by cells that stimulate angiogenesis, and has also been a target for molecular imaging of angiogenesis. Rodriguez-Porcel and colleagues [154] showed the feasibility of detecting VEGF upregulation *in vivo* after MI in a rat model using ^{64}Cu-DOTA-VEGF$_{121}$ by PET. ^{64}Cu-DOTA-VEGF$_{121}$ signal increased significantly from baseline to day 3 when it peaked, and remained high for 2 weeks post-MI compared to no uptake in control animals (**Fig.3.9**).

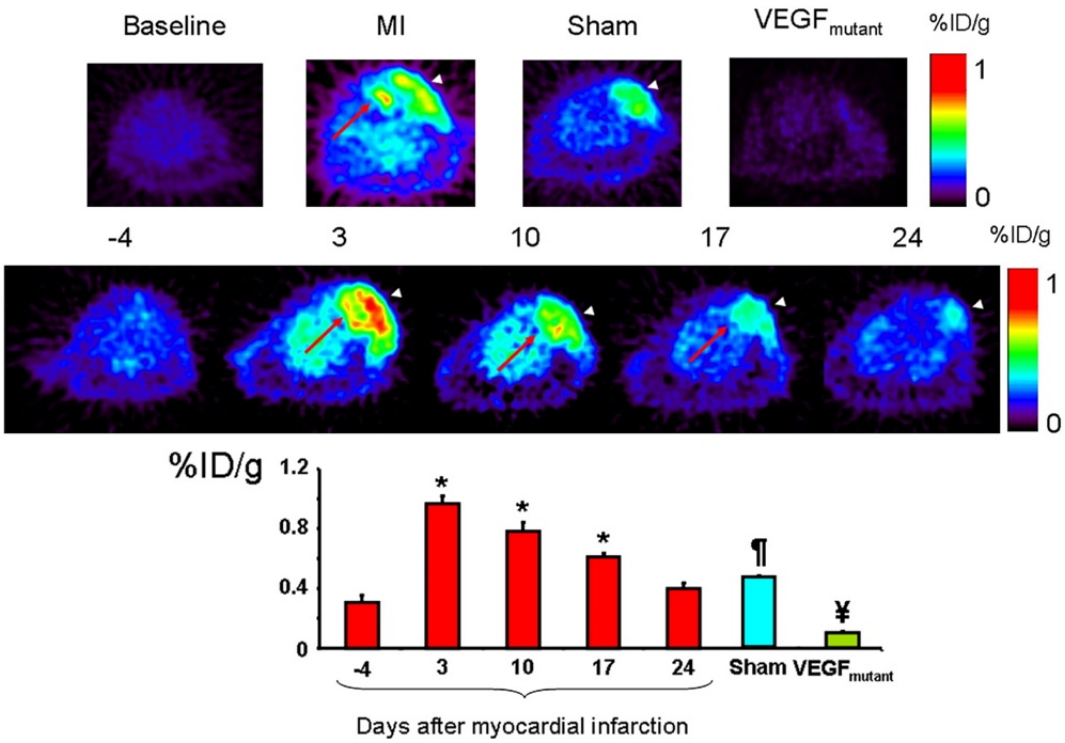

Figure 3.9. Imaging VEGF in a rat model of myocardial infarction (MI) by PET. Top representative images at baseline, animal after MI and SHAM-operated animals. Representative images of time-dependent effect on uptake of ^{64}Cu-DOTA-VEGF$_{121}$ is shown at the middle. Red arrow shows the myocardial uptake of the tracer, white shows the chest wall muscle layer uptake. At the bottom image, the quantification of ^{64}Cu-DOTA-VEGF$_{121}$ after MI over time is shown (%ID/g of tissue). *$P<0.05$ compared with baseline; ¥$P<0.05$ compared with SHAM and ^{64}Cu-DOTA-VEGF$_{121}$; ¶$P<0.05$ compared with VEGF mutant and ^{64}Cu-DOTA-VEGF$_{121}$. Adapted from [154].

Angiogenesis has also been analysed by MRI, using cyclic Asn-Gly-Arg (cNGR)-labelled paramagnetic quantum-dots (pQDs) [155]. The tripeptide cNGR homes specifically to CD13, an aminopeptidase that is strongly upregulated during myocardial angiogenesis. After seven post-operative days and after 2 hours of cNGR-pQDs injection, mice were scanned with MRI. cNGR-pQDs uptake within the infarcted area resulted in a strong negative contrast, which was significantly reduced in SHAM-operated animals and in mice which received unlabelled control contrast agent. A strong colocalization of the cNGR-pQDs with endothelial cells was confirmed *ex vivo* by 3D 2-photon laser scanning microscopy.

3.2.5 - Maturation of the scar

The ECM is a fundamental cell and tissue support component. For several years, the ECM was thought to be just a structural and static part of the heart, however its importance has been further explored, and it seems that the ECM is a dynamic and complex structure with several important biological roles such as its participation in cell signalling [51, 128, 156, 157]. The replacement of injured myocardium by fibrotic scar tissue is a compensatory mechanism that occurs in many cardiac diseases.

MRI has become the gold-standard imaging technique to assess cardiac structure and function. MRI is clinically widely used to visualize fibrosis using late-gadolinium enhancement (LGE). By shortening the T_1 of water, gadolinium accumulation within fibrotic areas makes them appear brighter on T_1W images. T_1 mapping has been used for risk stratification in patients. A study with 100 patients with heart failure and preserved ejection fraction has shown that T_1 values below median were associated with an increased risk of cardiac events compared with those above the median [158].

MRI can also be used to access differences in the extracellular volume (ECV) of the heart. This can be achieved by measuring a T_1 map before contrast injection (also known as native T_1) and after injection. Normal ECV varies between 24-28%, and changes in ECM content have been associated with disease progression, mainly as collagen deposition [128, 159]. Zeng and colleagues [160] have recently validated the use of T_1 mapping for the assessment of ECV by correlation with collagen deposition (fibrosis assessed by histology) within the myocardium in rabbits. ECV was calculated from pre and post contrast T_1 values and showed a strong correlation with pathological

collagen content (*P<0.001*; collagen volume fraction, CVF), and was better than post contrast T_1 mapping alone (*P<0.004*). In contrast, no correlation was found between pre-contrast T_1 mapping and CVF and thus this parameter cannot be used to assess diffuse myocardial fibrosis. Thus, ECV measured by MRI may provide accurate diagnostic information on the current state of the myocardium.

ECM is formed by a dense network of proteins, mostly collagen type I and III and elastin. Collagen is present in relatively high concentrations in many organs, and during fibrosis collagen concentrations further increase in response to injury. When upregulated it can be harmful by delaying diastolic function or cause arrhythmias. Different imaging techniques have been used to measure overexpression of collagen *in vivo* [161].

Helm *et al* [162] has shown the feasibility of imaging collagen using a gadolinium-based collagen-targeting contrast agent (EP-3533) in a mouse model of MI. EP-3533 retention time was longer compared with control gadolinium in the infarct zone (194.8±116.8 vs 25.5±4.2 minutes) as compared with normal myocardium (45.4±16.7 vs 25.1±9.7 minutes), revealing its specificity and higher affinity for collagen (confirmed by histology) (**Fig.3.10**).

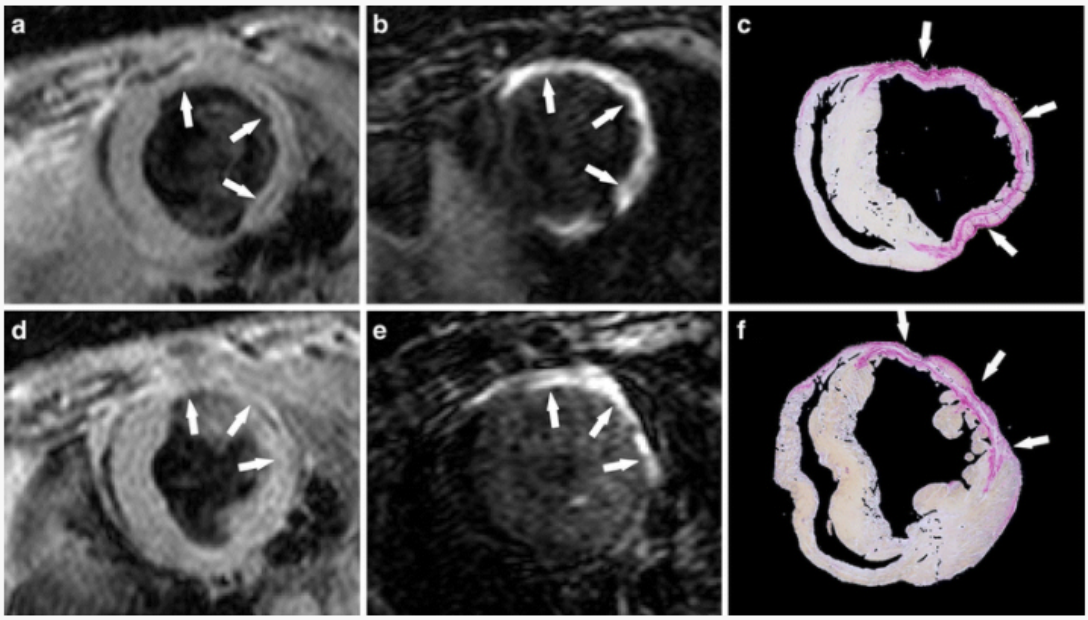

Figure 3.10. Imaging fibrosis and scar after myocardial induction in murine model using a collagen-specific contrast agent. Anatomical short-axis views (a,d), inversion-recovery (IR) MRI with scar enhancement (b,e) and corresponding histology by picrosirius red-staining of the left ventricle (c,f). Adapted from [162].

Another collagen specific peptide (collagenin) has been also reported [163]. This contrast agent is based on the glycoprotein VI platelet receptor on collagen I and III and has been used for SPECT imaging in a rat model of MI. Following injection of ^{99m}Tc-labeled-collagenin, high uptake was demonstrated in infarcted zones of MI animals but not in control animals. Tracer uptake was confirmed in regions with collagen deposition by autoradiography; the suitability and specificity of this new probe for imaging MI fibrosis has been also confirmed. This probe also benefits from fast blood clearance and lower liver uptake making it promising for clinical translation [163].

The content in elastin also increases during post-MI remodelling [58]. Using an elastin-specific MR contrast agent, Wildgruber *et al* [164] have shown the feasibility of monitoring scar elastin maturation using an elastin-specific gadolinium-based contrast agent. This contrast agent showed longer retention in

scar compared to non-targeted conventional gadolinium-based contrast agents (**Fig.3.11**).

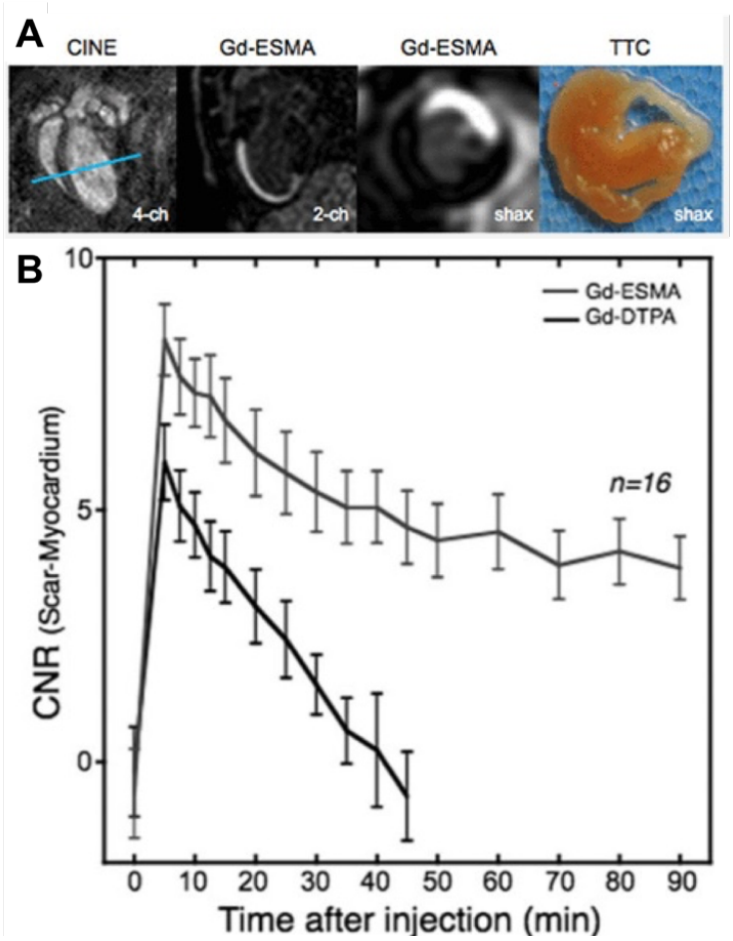

Figure 3.11. Imaging myocardial infarction remodelling using an elastin-specific MR contrast agent (Gd-ESMA) in a murine model of permanent LAD occlusion. (A) 7 days after MI induction, Gd-ESMA deposition is shown in the scar area confirmed by triphenyltetrazolium chloride (TTC) staining. (B) Prolonged enhancement of the left ventricular scar measured by contrast-to-noise (CNR) ratios [164].

Another promising contrast agent to assess and modulate ECM remodelling have been shown by Nahrendorf and colleagues [165]. Transglutaminase clotting factor XIII (FXIII) is involved in ECM turnover and in inflammatory response regulation, and consequently might play a role in infarct healing [166]. The authors have shown that FXIII tissue levels are diminished in patients with acute infarct rupture when compared with MI patients without rupture ($P<0.0045$) [165].

In a mice model of coronary ligation, the activity of FXIII was assessed using an ^{111}indium-labeled affinity peptide (^{111}In-DOTA-FXIII), allowing direct assess of the activity of this enzyme in would healing *in vivo*. Wild-type animals treated with FXIII showed attenuated LV remodelling when compared with control WT and animals treated with dalteparin (DP; an anticoagulant which inhibits FXIII activation) (**Fig.3.12A-L**). Additionally, FXIII-treated animals showed faster resolution of neutrophil response, enhanced macrophage recruitment, increased collagen content and augmented angiogenesis in the healing infarct (**Fig.3.13A-F**).

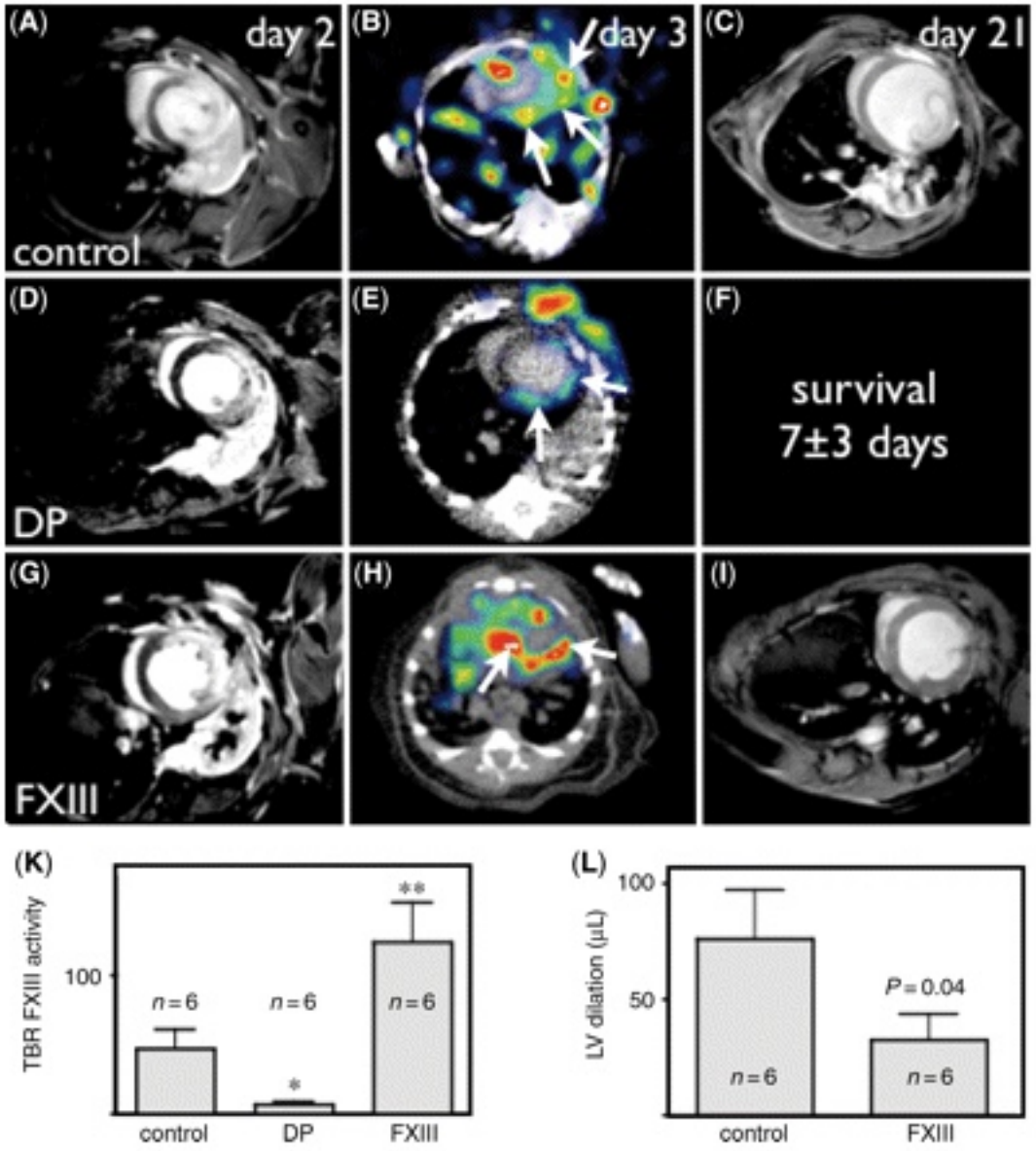

Figure 3.12. *In vivo* SPECT imaging of transglutaminase activity using an ^{111}indium-labeled affinity peptide (^{111}In-DOTA-FXIII). (*A–I*) Longitudinal imaging study (MRI day 2, SPECT-CT day 3, second MRI day 21); (A,D,G) similar infarct size at early time-point. (E,H,K) Increased SPECT signal in FXIII-treated animals compared with the dalteparin-treated (DP) mice. Attenuated left ventricular (LV) dilation was showed on the MRI (C,I,L) in FXIII-treated mice. **P<0.05*, ***P<0.001*. SPECT, single photon emission computed tomography; MRI, magnetic resonance imaging; CT, computed tomography. Adapted from [165].

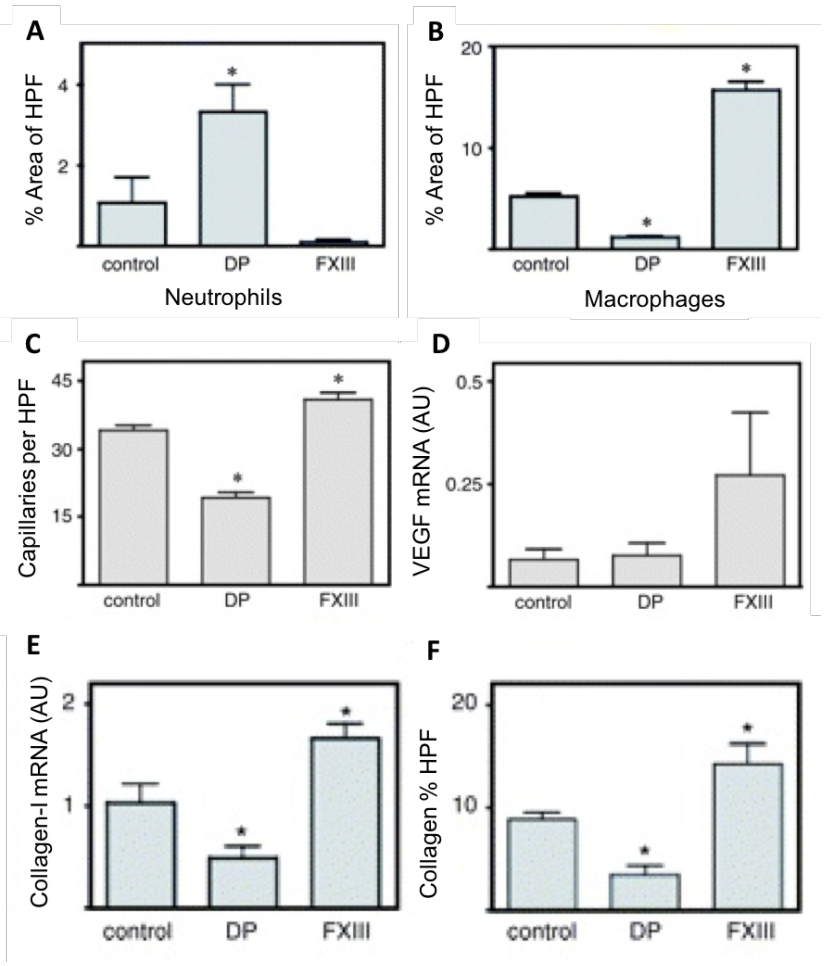

Figure 3.13. Immunoreactive staining for (A) neutrophils, (B) macrophages recruitment, (C) capillary density and (D) VEGF expression during angiogenesis, (E) collagen mRNA levels and (D) collagen content in polarized light microscopy. High power field (HPF), positive % area of high power field. *$P<0.0001$. Adapted from [165].

3.3 - Conclusion

Molecular imaging is likely to provide a new understanding of the different biological processes underlying post-MI remodelling. The demands in developing new therapeutically targets that can modulate the infarct healing process, preventing or attenuating, have been extensively studied in both preclinical and clinical settings using different imaging modalities (**Fig.3.14**). Development of novel targeted imaging agents or the improvement of the existing contrast agents is a topic of great research interest. Identifying new targets which are overexpressed during disease, or the improvement of the current imaging agents

by increasing its specificity, sensitivity, blood-clearance, safety and cost, may help not only to better understand the underlying healing process but also help the translation into the clinical setting. Additional efforts to improve image processing and acquisition protocols are also desired.

Molecular imaging is a unique area of research, where inputs from different disciplines converge to develop new strategies to detect disease at early stages, noninvasively, and quantitatively by imaging biological processes at cellular and molecular levels.

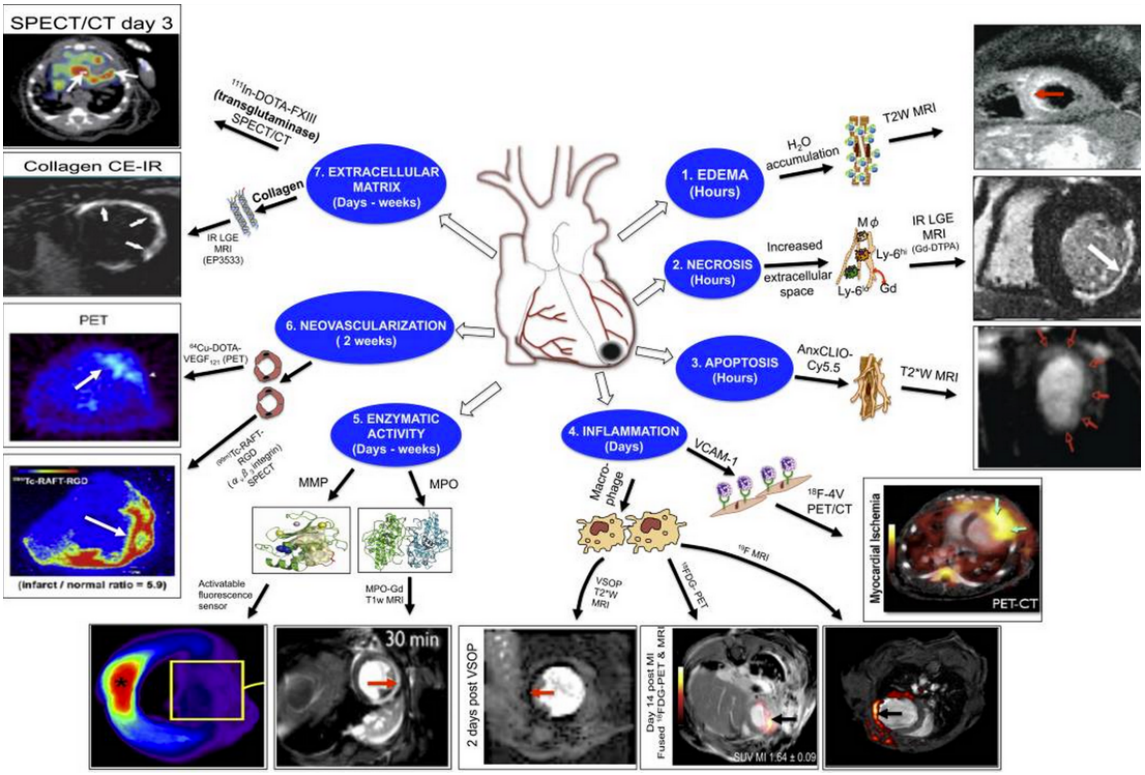

Figure 3.14. Different imaging modalities and targets for myocardial infarction (MI). Different stages of disease progression would be potentially detected: (1) Oedema by T_2W MRI, in a subject 3 days after reperfused MI; (2) Necrosis, gadolinium-contrast enhanced MRI using Gd-DTPA detects irreversible myocardial ischemic injury due to increased extracellular space; (3) Apoptosis, MRI detection of myocyte apoptosis; (4) Inflammation, imaging of endothelial cells by PET/CT or macrophages with $^{1}H/^{19}F$-MRI; (5) Enzymatic activity, MRI of MPO activity 2 days after MI in mice; (6) Neovascularization, SPECT imaging of myocardial angiogenesis; (7) Extracellular matrix, either using a collagen-specific contrast-agent by MRI or using X by SPECT/CT for the detection of myocardial scarring. For detailed information [167]. MPO: myeloperoxidase; MRI: Magnetic Resonance Imaging; PET/CT: positron emission tomography/computed tomography; SPECT: Single Photon Emission Computed Tomography.

Chapter 4

Magnetic Resonance Imaging

Magnetic resonance imaging (MRI) is a routinely used diagnostic tool to obtain high quality tomographical images with excellent soft tissue contrast. MRI is a flexible imaging technique and allows manipulating image contrast based on tissue specific properties such as the T_1 and T_2 relaxation time. However, its application extend beyond diagnostic use and MRI has become increasingly important in basic research. Preclinical MR imaging has emerged as a new tool to better understand the biological mechanisms underlying certain pathologies. Especially with the advent of experimental and clinically approved molecular contrast agents there is great potential to elucidating pathology on a molecular level. These advantageous properties of MRI can have a tremendous impact on drug screening, treatment and prognosis.

This chapter is partly based on the content from the books in references [168, 169]. In this chapter, the basic concepts of MR physics, cardiac MR sequences and the principle of MR contrast generation will be introduced. In the last section, the technical challenges of cardiac MRI in small animals using a clinical MRI system will be discussed.

4.1 - MRI signal

Magnetic resonance imaging is based on the principles of nuclear magnetic resonance (NMR), a spectroscopic technique used to obtain microscopic chemical and physical information of molecules. MRI is based on the absorption and emission of energy in the radiofrequency (RF) range of the electromagnetic spectrum. RF pulses are used to excite the spins of protons in tissue and the resulting emitted signal is detected by receiver coils and is the basis of this imaging technique. The main source of the MRI signal is hydrogen, primarily in fat and water, which constitutes about 63% of the hydrogen-based source in the human body. Hydrogen nuclei have a physical property, known as spin, that results in a magnetic moment, μ.

Without an external magnetic field the magnetic dipole moments (μ) of the protons are randomly orientated, so that the net magnetization is zero; but when placed in a strong magnetic field ($\mathbf{B_0}$), a small fraction of the hydrogen nuclei orientates themselves in two possible positions: lower-energy state (parallel to the magnetic field) or higher-energy state (anti-parallel to the magnetic field), as shown in **Figure 4.1**. Not all protons contribute equally to these states, however a small excess in this direction produces a ‘net magnetic moment’ (or net magnetization vector, NMV) that can be measured as the difference between the high and low energy state.

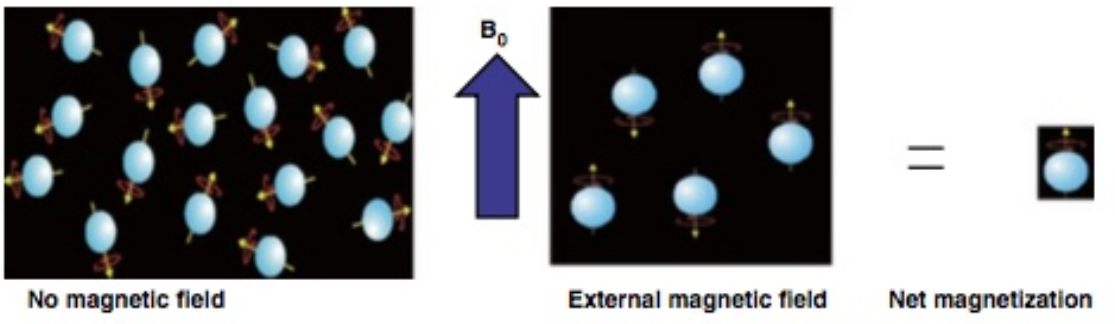

Figure 4.1. Net magnetization. When an object in placed in an external magnetic field, their nuclear spins (magnetic moments, μ) tend to orientate themselves either along (low-energy state, arrows up) or against (high-energy state, arrows down) the magnetic field (B_0). Adapted from [168].

The dipoles are not perfectly parallel or anti-parallel, but they are precessing at the Larmor frequency (ω_0, at an angle of 54 degrees), around the B_0 direction, that is determined by the equation:

$$\omega_0 = \gamma \, \boldsymbol{B_0} \qquad (1)$$

where ω_0 represents the frequency (in megahertz, MHz), B_0 represents the strength of the magnetic field (in tesla, T) and γ is the gyromagnetic ratio, which expresses the relationship between the spin and the magnetic moment of a specific nucleus ($\gamma_{hydrogen}$= 42.57 MHz/T) and represents the sensitivity of a certain nucleus.

The signal is generated by the application of short RF pulses, with a frequency equal to the Larmor frequency, where the protons from the lower energy state are excited to the higher energy state. After excitation, the longitudinal magnetization vector will relax back to level of the equilibrium magnetization. The amount of nutation that the longitudinal magnetization vector experiences after the application of the RF pulse is determined by the flip angle,

which corresponds to the strength and the duration of the RF pulse. The rate of this relaxation is described by two time constants: longitudinal or spin-lattice (T_1) and transversal or spin-spin (T_2) relaxation time that are characteristic for every tissue [170, 171].

4.2 - Contrast characteristics from Spin relaxation: T_1, T_2 and proton density

The MRI signal generated by a tissue is determined by a combination of factors, including RF pulse timing, flip angle and the density of protons and their relaxation rates.

An MRI pulse sequence describes a series of RF pulses with varying duration and strength, which allows to tip the M_z magnetization (longitudinal) into the xy plane (transverse magnetization) where the MR signal can be measured. During and after the RF pulse, two types of relaxations take place: longitudinal, spin-lattice or T_1 relaxation (M_z magnetization), and transverse, spin-spin, or T_2 relaxation (M_{xy} magnetization). Relaxation characteristics of different tissues can be expressed in terms of relaxation times T_1 and T_2 or relaxation rates R_1 and R_2 with $R_1=1/T_1$ and $R_2=1/T_2$.

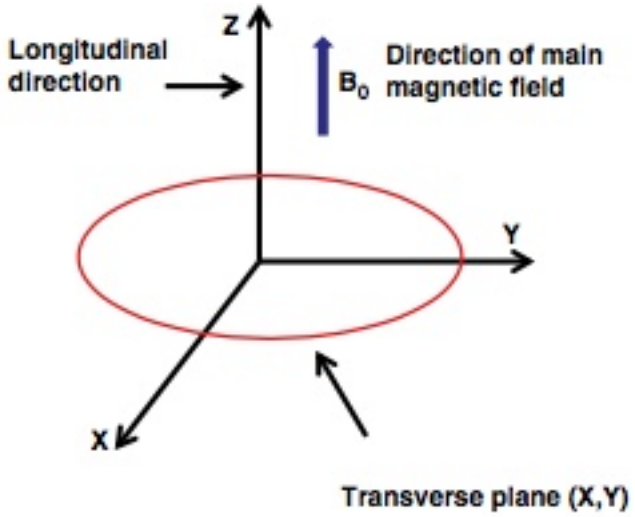

Figure 4.2. The direction of the main magnetic field and longitudinal magnetization. Adapted from [168].

4.2.1 - Longitudinal relaxation (Spin-Lattice relaxation, T_1) and image contrast

At equilibrium, the NMV aligns with the direction of the applied magnetic field B_0 and is called the equilibrium magnetization, M_0. If enough energy is put into the system, it is possible to saturate the spin system and make M_z=0. The time constant that describes how M_z returns to its equilibrium value is called the spin lattice relaxation time (T_1).

T_1 characterizes the recovery of the M_z magnetization to its equilibrium value, and is defined by:

$$\boldsymbol{M_z = M_0\left(1 - e^{\left(-\frac{t}{T1}\right)}\right)} \qquad (2)$$

Where M_z is the magnetization at time (t), after the 90^o pulse, M_0 is the equilibrium magnetisation at full recovery. T_1 is the time it takes M_z to recover to approximately 63% of M_0 (**Fig.4.3**).

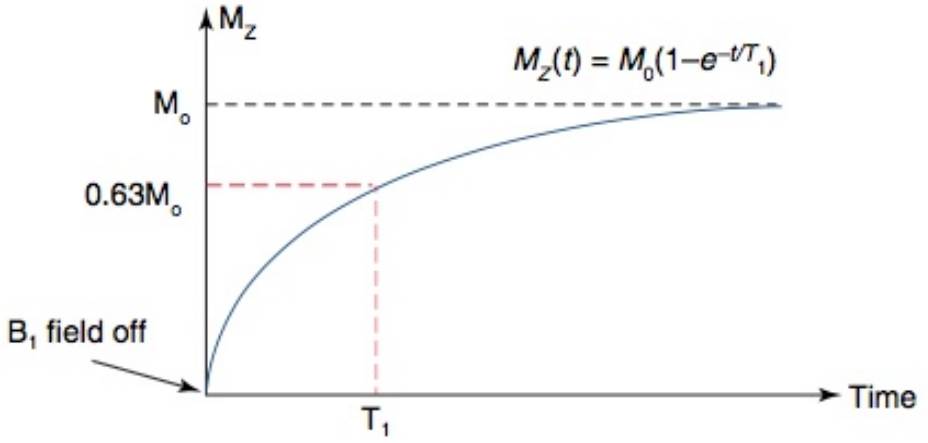

Figure 4.3. T_1 recovery curve. T_1 relaxation constant defines the time to regain 63% of longitudinal magnetization following a 90º excitation pulse. Adapted from [168].

T_1 recovery accounts for the interaction between excited spins and the surrounding lattice. T_1 values of fluids are relatively long, while fat tissues have shorter T_1 values. Thus, in a pulse sequence designed to generate image contrast sensitive to T_1 (i.e. T_1-weighted image), tissues with shorter T_1 will have higher signal than tissues with longer T_1 on T_1-weighted images (T_1W).

4.2.2 - Transverse relaxation (Spin-Spin relaxation, T_2) and image contrast

The time constant which describes the decay of the transverse magnetization (or MR signal), M_{XY}, is called the spin-spin relaxation time, T_2. The rate by which the transverse magnetization decays is given by:

$$\boldsymbol{M_{xy} = M_0 e^{-\frac{t}{T2}}} \qquad (3)$$

where T_2 is the magnetization at which time the M_{xy} magnetisation reaches approximately 37% of its initial value after the RF pulse is turned off (**Fig.4.4**). Signal decay is often significantly shortened by local field inhomogeneity and the associated relaxation time is then referred to as T_2*.

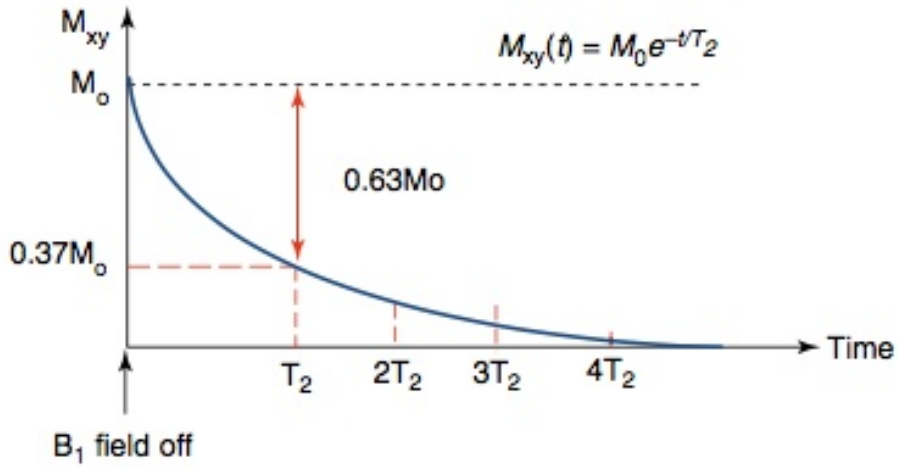

Figure 4.4. T_2 decay curve. T_2 relaxation constant defines the time for transverse magnetization to decay to 37% of its original value following a radiofrequency excitation pulse. Adapted from [168].

T_2 relaxation describes the decay of the signal due to interactions between spins, which occurs because the magnetic field created by a nucleus interacts with nearby nuclei and exchanges energy with each other. T_2 values of fluids are relatively long due to fewer spin-spin interactions, while fat tissues have shorter T_2 values. In a T_2-weighted image (T_2W), tissues with longer T_2 will appear brighter than tissues with shorter T_2.

4.2.3 - Proton density

Proton density contrast is indicative of the number of protons per volume of tissue. The higher the number of protons in a given volume of tissue, the greater is the magnetization available to provide signal. Imaging pulse sequences can be designed to provide “proton density weighting” by reducing the influence of T_1 and T_2 relaxation differences within the sample.

4.3 - Spatial localization of the signal

Spatial localization of an image is achieved by applying linear magnetic gradients. Gradients generate a linear field variation that either increases or decreases the strength of the magnetic field along a defined axis. Depending on these variations, the protons resonate either faster or slower depending on their position along this axis, i.e. their resonance frequencies vary linearly with the distance along the direction of the gradient:

$$\omega(\boldsymbol{r},\boldsymbol{t}) = \omega_{\boldsymbol{0}} + \gamma \boldsymbol{G}(\boldsymbol{t}).\boldsymbol{r} \qquad (4)$$

where $\omega(r,t)$ represents the resonance frequency at a distance along the gradient at a time (t), ω_0 is the Larmor frequency, *G* is the gradient strength, and *r* is the distance along the gradient.

These frequencies can be used to distinguish between MR signals at different positions in space. In the MR system, 3-dimensional spatial localisation is achieved by three sets of gradient coils along orthogonal axis. There are three types of spatial gradients: slice selection gradient (G_{ss}, or G_z), a phase encoding gradient (G_{PE}, or G_y) and a frequency encoding gradient (G_{FE}, or G_x). The relationship between them can be represented in a pulse sequence diagram (**Fig.4.5**).

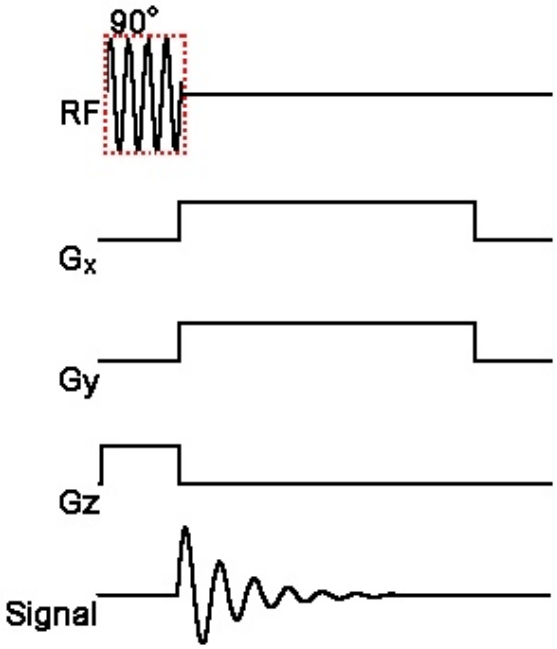

Figure 4.5. Pulse sequence diagram. A 90º radiofrequency (RF) pulse is applied in conjunction with a slice selection gradient (G_z). Subsequently, A frequency encoding gradient (G_x) and phase encoding (G_y) are turned on once the slice selection pulse is turned off. In this case, the frequency encoding gradient is composed of a G_x and G_y gradient resulting in radial k-space sampling.

For a 2D plane, the slice selection gradient (G_{ss}=G_z) is applied orthogonal to the imaging plane during the application of the RF excitation pulse. The bandwidth of the excitation pulse and the gradient strength of G_{ss} determines the slice thickness. All protons outside the slice resonate at ($\omega \neq \omega_0$) that is not excited by the RF pulse.

Next, the excited 2D slice will experience a phase encoding gradient (G_{PE}=G_y) applied in a direction orthogonal to the slice direction, allowing the localization of the signal intensity along the y-axis. The phase encoding gradient is applied between the RF excitation and the signal readout. During the application of the phase encoding gradient, protons will precess faster or slower according to their position along the y-axis. This will cause the spins to dephase for as long as the phase encoding gradient is applied. Once the gradient is turned off, the proton will precess at the Larmor frequency at their original frequency,

however, the phase shift created by the gradient (the phase angles) remains until the next gradient is applied. The whole sequence pattern has to be repeated for every line in k-space, corresponding to a different value of the phase-encode gradient until the k-space is filled.

Finally, the frequency encoding gradient (or readout gradient) is applied during the sampling of the echo, so that the echo will now comprise of a range of frequencies depending on the location of each proton along the x-axis. Once all the data is acquired, a two-dimensional Fourier transform is applied. This converts the data, already encoded as spatial frequencies (2D array called k-space) into an image (**Fig.4.6**).

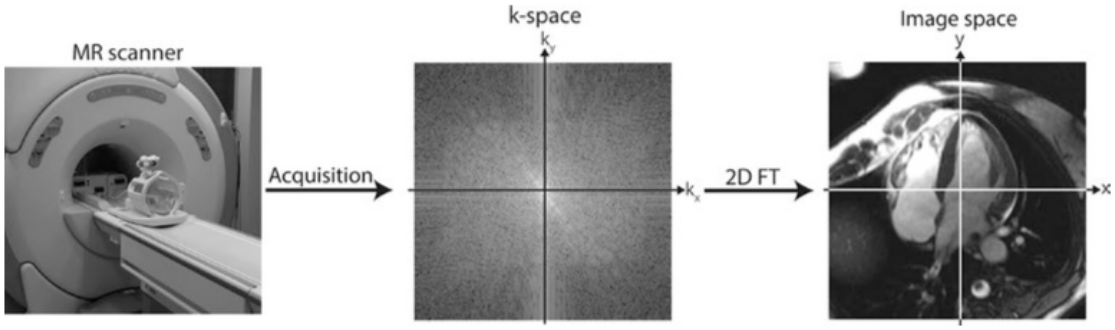

Figure 4.6. Data is collected using RF receiver coils. By using time varying gradients, the data are acquired in Fourier space (also known as k-space). Each point on the k-space contains specific frequency, phase (x,y coordinates) and signal intensity information (brightness). A Fourier transform (FT) is required to generate the final image that displays the signal distribution in spatial coordinates. Adapted from [168].

4.4 - NMR spectroscopy

Nuclear magnetic resonance spectroscopy (NMR spectroscopy) exploits the magnetic properties of certain atomic nuclei, providing detailed information about the structure, dynamics and chemical environment of molecules. The electron density around each nucleus in a molecule varies according to the types of nuclei and bonds in the molecule, causing changes in the resonance frequency, distinguishable in an NMR spectra. Therefore, different atoms

experience differently the magnetic field; and equation (1) can be re-written for a specific atom within its local chemical environment as:

$$w_0 = \gamma B_0(1 - \sigma) \qquad (5)$$

where σ is the shielding constant.

Consequently, molecules with a particular nuclei in different chemical environments may exhibit multiple resonance frequencies. This effect is called the chemical shift and will give rise to multiple peaks when measured by magnetic resonance spectroscopy (MRS). Instead of applying a linear magnetic field gradient on top of B_0, as in MRI, in spectroscopy the chemical shift experienced from the nuclei while exposed to B_0 is resolved. NMR spectra are unique, well-resolved, analytically tractable and often highly predictable for small molecules. Thus, NMR analysis is used to confirm the identity of a substance, and to identify different functional groups.

In a clinical setting, NMR can be used to study the specific resonance frequencies of a sample or tissue and can therefore be used to assess pathology, for example by detecting changes in macromolecular content. The chemical shift of a nucleus is the difference between the resonance frequency of the nucleus and a standard, relative to the standard. This quantity is reported in parts per million (ppm) and given the symbol delta, δ.

$$\delta = (\nu - \nu_{REF})\ x10^6 / \nu_{REF} \qquad (6)$$

where v is the absolute resonance frequency of the sample and v_{REF} is the absolute resonance frequency of a standard reference compound, in Hertz, measured in the same applied magnetic field B_0.

In vivo NMR spectroscopy usually used tetramethylsilane (TMS) as a reference. In the human body there is no TMS, but there are two primary hydrogen containing substances, water and fat. The chemical shift difference between these two types of hydrogens is approximately 3.5 ppm. *In vitro*, or in phantoms studies, trifluoroacetic acid (TFA) can be also used instead as it has a simple and single NMR peak.

4.5 - Contrast agents

The inherent different in T_1 and T_2 relaxation times between biological tissues, or between normal and pathologic tissue is not always large enough to obtain a detectable contrast in the MR image (more details in **section 4.8** about signal-to-noise ratio (SNR) and contrast-to-noise ratio (CNR)). Sufficient contrast is of particular importance in differentiating pathological from normal tissue.

MR contrast agents are usually not detectable themselves but they modify the relaxation properties of surrounding water protons, usually by shortening T_1 and T_2 relaxation times.

4.5.1 - Classification of MR contrast agents

Gadolinium based contrast agents are by far the most commonly used MR contrast agents [92, 168, 172, 173]; however, many other types of agents exist, such as iron-oxide particles [92, 137, 174, 175] and more recently ^{19}F

perfluorocarbons (PFCs) [176-179]. Contrast agents can be classified according to 1) the magnetic property of the agent, 2) the dominant effect of the agent on the signal intensity and 3) the biodistribution of the agent (**Table 4.1**).

Table 4.1. Classification of contrast agents based on the magnetic properties, biodistribution and image enhancement.

MAGNETIC PROPERTIES	BIODISTRIBUTION	IMAGE ENHANCEMENT
Paramagnetic	Extracellular fluid	Positive (predominant T_1-shortening)
Superparamagnetic	Intravascular Tissue specific	Negative (predominant T_2-shortening) Proton density

Magnetic properties and image enhancement:

Paramagnetic contrast agents: Most MR contrast agents are based on paramagnetic metal ions, such as (Mn^{+2}) [180], iron (Fe^{+3}) [181], or gadolinium (Gd^{+3}) [172]. Paramagnetic materials are metals with unpaired electrons giving rise to magnetic dipoles when exposed to a magnetic field. Gd^{+3} is the most commonly used metal ion as a paramagnetic contrast agents. Is ideally suited for MRI because it has an electron spin of 7/2 and hence seven unpaired electrons. The symmetry of its electronic states produces an electron spin relaxation time slow enough to interact significantly with neighbouring water protons [172]. The relaxivity (r_1 or r_2) of a contrast agent in water is defined as the change in relaxation rate R_1 or R_2 of water per concentration of contrast agent. The relationship between R_1, r_1, and the concentration of the paramagnetic material is given by the following equation.

$$R_{1\,(\mathrm{Measured})} = R_{1\,(\mathrm{Water})} + r_1\,[\mathrm{Gd}] \qquad (7)$$

The relaxivity is dependent on the magnetic field and temperature, so it is usually reported along with a B_o and temperature.

The increase in relaxation rate R_1 and R_2 is found to be directly proportional to the contrast agent concentration [c]. Therefore, [c] can be calculated by measuring the intrinsic relaxation rate before ($R1_{pre}$ or $R2_{pre}$) and after ($R1_{post}$ or $R2_{post}$) the contrast agent injection with

$$[c] = \frac{R1_{post} - R1_{pre}}{r1} \text{ or } [c] = \frac{R2_{post} - R2_{pre}}{r2} \quad (8,9)$$

where r_1 is the longitudinal relaxivity and r_2 is the transverse relaxivity of the contrast agent with the units of $(mM \times s)^{-1}$.

These equations show that the observed effect of Gd based contrast agents depends on the intrinsic relaxation times $R1_{pre}$ and $R2_{pre}$. Since $R2_{pre} > R1_{pre}$, a given increase in [c] leads to a shortening of T_1 ($\Delta R_1 > \Delta R_2$). Consequently, Gd-based contrast agents usually have a slightly stronger T_1 lowering effect compared to T_2 (r_2/r_1 ≈1-2). These contrast agents therefore lead to a positive contrast effect (detected as an increase in signal intensity or brightness) using a T_1-weighted pulse sequence. Typical r_1 and r_2 values of currently approved Gd-based contrast agents are in the range of r_1 =3-5 $mM \times s^{-1}$ and r_2=5-6 $mM \times s^{-1}$.

Superparamagnetic contrast agents: Superparamagnetic contrast agents are based on magnetite (Fe_3O_4) or maghemine (γ-Fe_2O_3) water insoluble iron oxide crystals. These crystals contain several paramagnetic Fe ions (Fe^{2+} and Fe^{3+}), which when magnetically ordered create a large net magnetic moment,

being referred to as superparamagnetic. Superparamagnetic agents can induce a strong T_1-relaxation rate enhancement, but their dominant effect is on T_2/T_2^* relaxation due to the large magnetic moment and the strong effect on transverse relaxation [175]. This strong effect in decreasing T_2 causes a negative contrast effect detected as a decrease in signal intensity or darkness ($r_2/r_1>10$) using a T_2-weighted or T_2^*-weighted pulse sequence [181]. Apart from their effect in decreasing T_2, iron oxide particles also decrease T_2^* due to their effect on the local magnetic field B_0, thus causing focal field inhomogeneities ΔB_0. This additional effect leads to an even more severe signal decay ($1/T_2^*=1/T_2 + \gamma \Delta B_0$). Iron oxide contrast agents are often images using T_2^* weighted imaging sequences. The relaxivities of iron based contrast agents are significantly higher compared to Gd-based agents with r_1=20-25 $(mM \times s)^{-1}$ and r_2=100-200 $(mM \times s)^{-1}$.

Other contrast agents: Fluorinated compounds have recently gain interest. The ^{19}F isotope is a spin ½ nucleus with a 100% natural abundance. Its gyromagnetic ratio is very close to hydrogen (40.08 vs 42.58 MHz/T of ^1H) and its MR sensitivity is therefore 83% of proton ($(\delta_F/\delta_H)^3$). Assuming linearity of increasing noise with frequency, the SNR of ^{19}F is therefore about 89% of ^1H per nucleus ($(\delta_F/\delta_H)^2$) (^{19}F properties are summarized in **Table 4.2**). Fluorinated compounds have several advantages over conventionally used gadolinium or iron-based contrast agents. Conventional contrast-agents are detected indirectly by the changes that they induce in the relaxation behaviour of nearby water protons, while ^{19}F contrast agents are detected directly by ^{19}F MRI. Since there is a low intrinsic concentration of fluorine in soft tissues of the body, ^{19}F MRI

results in no background signal and therefore works as “hot spot” imaging, directly visualising and spatially localising *only* the injected agent whilst adding independent functional and molecular information to the anatomical ^{1}H image.

Table 4.2. Nuclear properties of ^{1}H and ^{19}F. I is the spin quantum number and **δ** is the gyromagnetic ratio.

Isotope	I	δ/2π [182]	Natural Abundance	Relative Sensitivity [%]	$\frac{SNR\ ^{19}F}{SNR\ ^{1}H}$
^{1}H	1/2	42.58	99.99	1.00	$\frac{(\delta^{19}F)^2}{(\delta\ ^{1}H)^2} \approx 0.89$
^{19}F	1/2	40.05	100.00	0.83	

The most commonly used fluorine contrast agents for ^{19}F MRI applications are perfluorocarbons (PFCs). These compounds have been the focus of much interest since the 1960s, first as blood substitutes [183, 184] and afterwards as potential MRI active agents [178, 185]. PFCs are organic compounds in which all hydrogen atoms are replaced with fluorine. They are mostly biologically and chemically inert (because of the high stability of carbon-fluorine bonds) and tend to be non-toxic *in vivo* (even when high doses are administered) making them very attractive for medical applications

Biodistribution: Current contrast agents are administered intravenously (i.v.), except for the imaging of the digestive system. After the injection of a contrast agent, the circulatory system carries it throughout the body. At this point, contrast agent take a different course depending on their intended functionality: intravascular (IV), extracellular (EC), or intracellular (IC).

An intravascular contrast agent by design stays in the circulatory system until it is removed by the kidneys. All iron oxide particles are IV agents, with a half-life in blood ranging from a few minutes to several hours. Iron oxide particles

have been used as intravascular agents because of its usually slow clearance and been used for magnetic resonance angiography due to its T_1-shortening effect. Gadolinium based contrast agents are another example of IV contrast agents, usually when coupled to macromolecules or plasma proteins and thus forming macromolecules in blood, thereby increasing the blood half life time.

Extracellular contrast agents travel through the circulatory system and pass into the extracellular fluid, but do not enter the cells. Usually, tissues with denser vasculature or diseased tissue with slower contrast agent clearance receive or retain more contrast agent than healthy tissues (T_1disease<T_1healthy, **Fig.4.7**). EC contrast agents can also be functionalised by adding targeted ligands. These ligands can facilitate accumulation of the contrast agent in a specific tissue, due to increased affinity to a certain cell type or protein. Several gadolinium contrast agents have been chemically modified allowing specific imaging of proteins that are upregulated in several diseases.

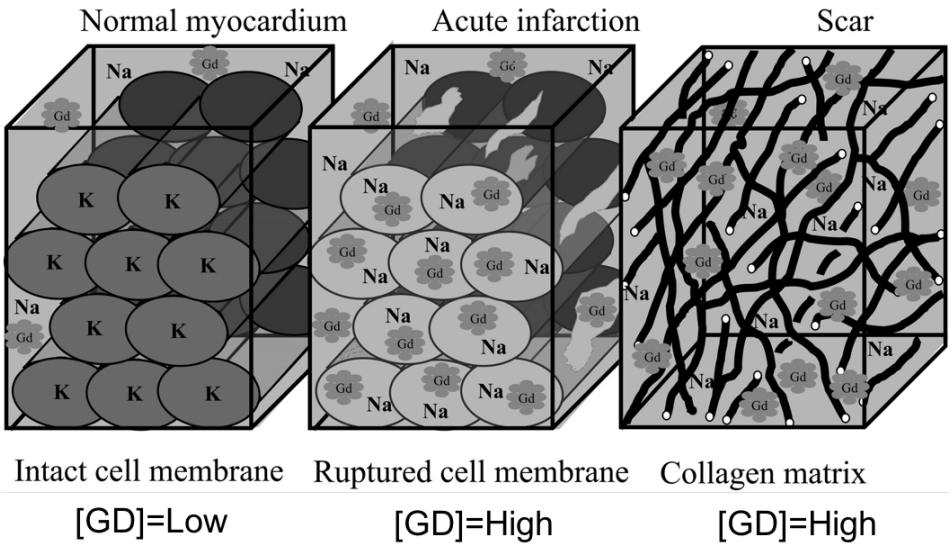

Figure 4.7. Distribution of gadolinium (Gd) based contrast agents in normal, diseased and scar tissue. With the increase in the extracellular space, a higher accumulation of Gd is observed in diseased tissues, especially myocardial infarction. Adapted from [186].

Intracellular contrast agents go one step further as they can enter a cell. Iron oxide particles as well as ^{19}F PFCs have been used to target *in vivo* inflammatory cells through phagocytosis.

4.6 - Pulse sequences

Pulse sequences used in MRI can be subdivided into spin-echo (SE) and gradient-echo (GRE) sequences. Several types of SE and GRE imaging sequences are used for optimal contrast depending on the type of clinical application, contrast agent, tissue of interest, etc.

4.6.1 - Spin-Echo sequence

SE sequences utilise a 90° excitation pulse to flip the magnetisation into the transverse plane, and a 180° refocussing pulse to refocus the magnetisation to compensate for field inhomogeneities (**Fig.4.8**). After the initial 90° pulse the individual magnetic moments dephase due to spin-spin interactions (T_2) and due to B_0 inhomogeneities (T_2*). At exactly half the echo time (TE/2) the refocusing pulse is applied, flipping the spins and changing the sign of the relative phase (a large positive phase change becoming a large negative phase e.g.). The spins continue gaining or losing phase because of the magnetic field inhomogeneities until the echo time (TE) where all the spins come back into phase again, generating an echo.

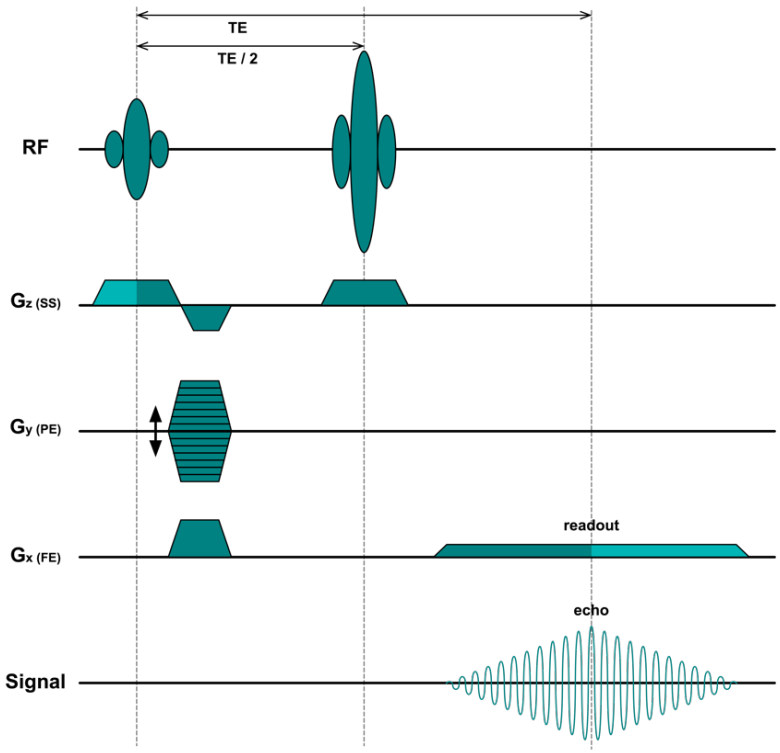

Figure 4.8. Spin-echo sequence diagram. RF, radiofrequency pulse; TE, echo time; $G_{z(SS)}$, slice selective gradient; $G_{y(PE)}$, phase encoding gradient; $G_{x(FE)}$, frequency encoding gradient.

An advantage of using a SE sequence is that it can be used to introduce strong T_2 dependence to the signal. Since some tissues and pathologies have similar T_1 values but different T_2 values it is advantageous to have an imaging sequence which produces images with strong T_2 weighting. These sequences are usually used for the assessment of morphology or tissue-water content (e.g. oedema; $T_{2\ water}$=2000ms, $T_{2\ muscle}$=50ms, $T_{2\ fat}$=70ms) [187]. T_2W SE sequences uses a relatively long TE, which has the effect of strongly reducing (or eliminating) blood signal due to the rapid decay (no refocusing) of moving transverse magnetisation.

4.6.2 - Gradient-echo sequence

GRE sequence utilises an RF excitation pulse that is typically less than 90°. As a result of the RF excitation, transverse magnetisation is created, the

magnitude of which is less than in SE, and the echo is generated using refocussing gradients. In GRE sequences the RF pulse only tips a fraction of the M_z magnetisation into the M_{xy} direction; a significant component of magnetisation remains in the M_z direction, which enables the use of much shorter TR (consequently reducing scan time). To read the signal an initial gradient in the frequency encoding direction is applied. As the spins precess at different frequencies along this gradient the transverse magnetisation will dephase. A second gradient is then applied which typically has the same amplitude as the first one but opposite direction (**Fig.4.9**).

GRE sequences typically have lower soft-tissue contrast compared with SE sequences ($T_{1\ water}$=4000msec, $T_{1\ muscle}$=900msec, $T_{1\ fat}$=250msec) [187], and provide T_2* contrast (in addition to T_2 decay because of field inhomogeneity) due to the absence of refocussing RF pulses. To minimise signal loss due to T_2*, the shortest possible TE is typically used. Compared to SE sequences, GRE are more likely to be T_1 weighted and exhibit a linear relationship between contrast agent concentration (e.g. gadolinium) and MR signal intensity [172]. GRE have usually short scan times (5-60s) making it very effective for cardiac MR and has been used to assess ventricular function and wall-motion characteristics [86, 171].

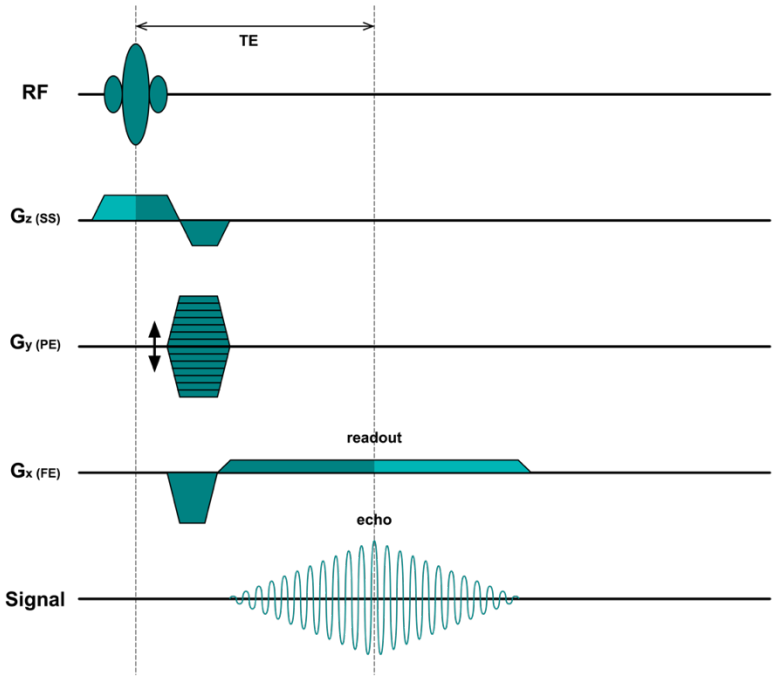

Figure 4.9. Gradient echo pulse sequence diagram. RF, radiofrequency pulse; TE, echo time; $G_{z(SS)}$, slice selective gradient; $G_{y(PE)}$, phase encoding gradient; $G_{x(FE)}$, frequency encoding gradient.

4.7 - Imaging techniques

Cardiovascular MR in the clinics and in research includes the assessment of cardiac anatomy, myocardial viability and cardiac function among others. Depending on the information desired several sequences/scans are available. Here the most relevant sequences applied in this PhD project are described: (1) *cine* for the assessment of cardiac function; (2) T_2W for the assessment of oedema; after the administration of contrast agents (usually administered intravenously) (3) *inversion recovery* and *late-gadolinium enhancement* for the assessment of scar; and (4) *T_1 mapping* for the evaluation of changes in relaxation rates and for contrast agent quantification.

4.7.1 - Cardiac cine imaging

Dynamic imaging of the heart for the assessment of cardiac morphology,

myocardial contractile function and wall motion can be achieved with cine imaging techniques. Full coverage of the cardiac cycle and high temporal resolution allow the visualization of the heart in a movie-like scan. Cine imaging relies on very short repetition times, TR, and uses GRE approaches. SE imaging is rarely used for cine cardiac imaging due to the longer TR and flow artefacts.

Cine sequences use electrocardiogram (ECG) triggering to synchronise the MRI acquisition with the motion of the heart. Using prospective ECG triggering data acquisition starts immediately after the R wave, and until the end of the cardiac cycle (**Fig.4.10**). Usually during the last 10% of the cardiac cycle no data acquisition occurs and the system waits for the next R-wave. Multiple phases of the cardiac cycle can be acquired during every heartbeat, resulting in multiple cine frame. The number of cine frames depends on the number of k-space lines collected per cardiac phase and the subject's heart rate, which determines the total acquisition window. Alternatively, ECG gating can be performed retrospectively by saving the trace of the ECG and reordering the data into cardiac phases. This allows maintaining the steady state signal thus avoiding flickering artefacts and also allows to acquire the entire cardiac cycle.

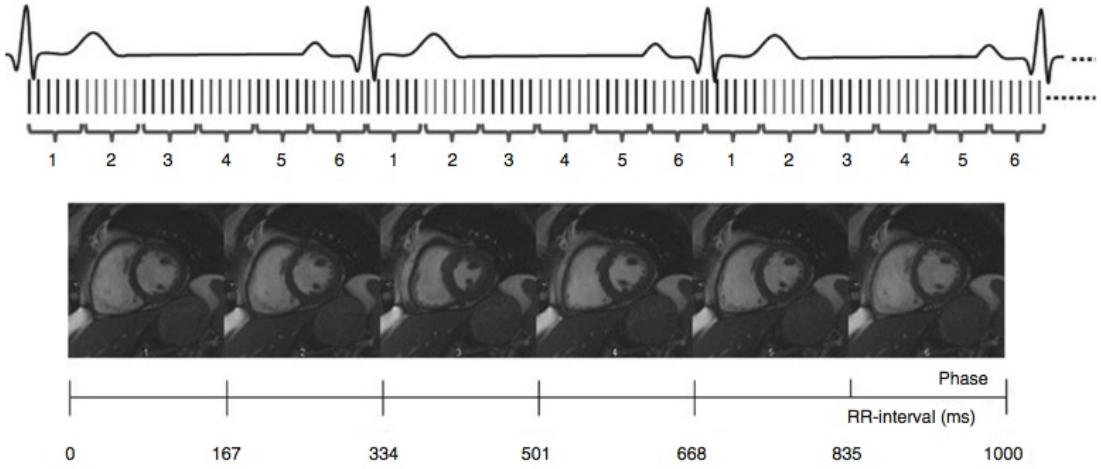

Figure 4.10. Electrocardiogram triggering cine gradient echo images. Single slices are acquired at multiple time points during the cardiac cycle and the resulting image are viewed as a movie to allow the visualization of cardiac motion and estimate different functional parameters.

4.7.2 - T_2/T_2*-weighted

Infarcted myocardium is characterized by an increase in tissue water and lipid content. Oedematous areas and area-at-risk (AAR) in reperfused and non-reperfused myocardial infarction can be highlighted by higher signal intensity on T_2W images [87, 110, 182, 188]. T_2W sequences are used to enhance the differences within the myocardium that emerge from localized changes in free-water content (oedema) but also blood oxygenation or intra- myocardial haemorrhage, among others.

T_2W images are acquired by using long TE and TR times. The longer the T_2, the greater is the contrast between regions of oedematous and normal myocardium. For very long TE, only tissues with very long T_2/T_2* relaxation times will retain signal. T_2W imaging uses a pulse sequence that produce high signal intensity in areas of oedematous tissue because of the long T_2 relaxation times that water-bound protons generate (**Fig.4.11**). T_2W sequences produce images with high SNR, however they can be time consuming due to the long TR. T_2* weighted imaging is faster, however produce less SNR and are more prone to susceptibility artefacts. Compartments filled with water appear bright and tissues with high fat appear dark.

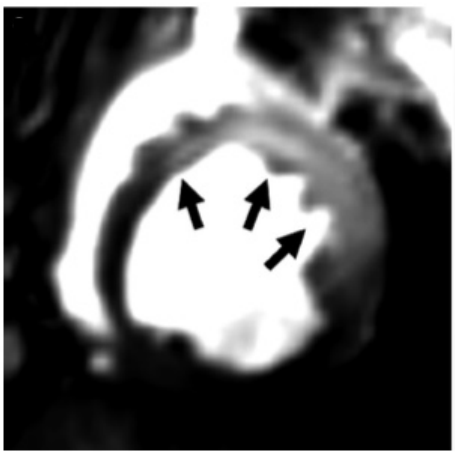

Figure 4.11. After myocardial infarction oedema is increased in the injured tissue and can be highlight with T_2-weighted sequences.

4.7.3 - Viability imaging

The application of a contrast agent (e.g. gadolinium chelates) selectively alters the native tissue relaxation times in proportion to local tissue concentration. Late gadolinium enhancement (LGE) has been used to improve the visualization of scar both in humans [189] and mice [190, 191]. Contrast agents accumulate in tissues in different ways, depending on the disease stage: viable tissue retains little amounts of contrast agent, whereas nonviable tissue retains it for longer time due to the increased extracellular space and delayed washout, resulting in shortened the T_1 values.

The most common LGE sequence used in cardiac MR is a T_1W GRE sequence employing an inversion recovery (IR) prepulse. The IR sequences provides excellent background suppression and its insensitivity to flow has shown to be particularly useful for the visualization of small amounts of contrast agent. IR techniques can be easily combined with ECG triggering and respiratory gating thereby allowing for high-resolution cardiac imaging.

IR imaging applies a 180° pulse, inverting the longitudinal magnetisation. The IR signal recovers exponentially given by:

$$\boldsymbol{S = abs(M_0(1 - 2e^{-\frac{TI}{T1}}))} \qquad (10)$$

The inversion time, TI, between the inversion pulse and the start of the imaging sequence is chosen, from a Look-locker sequence, to approximately null the signal from the healthy myocardium at the time of data collection (≈250ms). This provides the best contrast between nonviable (e.g. infarcted) and normal tissue (**Fig.4.12**).

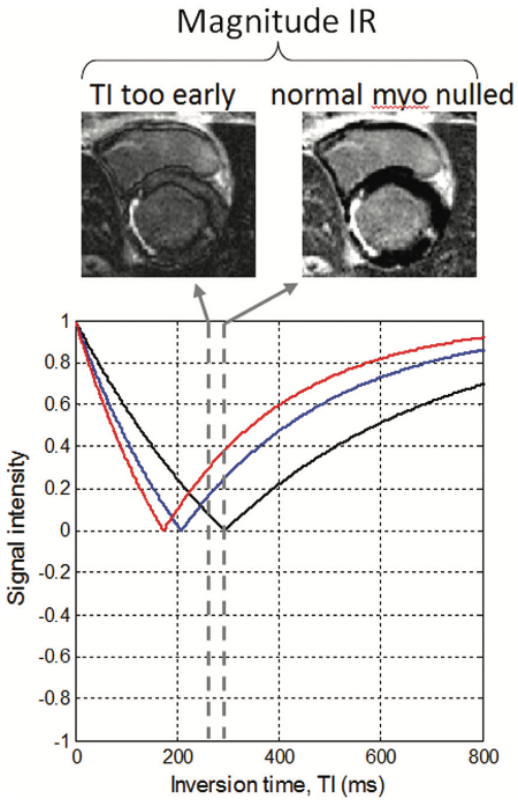

Figure 4.12. Signal intensity varies according to the chosen inversion time (TI). The time where the signals are more disperse, allowing the distinction between tissues, is the time chosen for the Inversion Recovery (IR) sequence. Adapted from [173].

4.7.4 - T_1 mapping

T_1 mapping is a technique that allows the quantification of the T_1 relaxation time using pixel-wise parametric maps. As mentioned before, T_1 varies across different tissues, allowing the differentiation between organs or, even in the same organ, altered tissues. In some diseases, T_1 values are altered depending on the local molecular environment or increased water content. In the heart, healthy and injured myocardium can be differentiated by their T_1 values, enabling the detection of different cardiomyopathies.

When contrast agents are administered, it can help investigating some pathologies on a cellular and molecular level. It has been shown that contrast agent concentration and R_1 values have a linear relationship [92, 192]. This motivates the application of T_1 mapping, which allows the quantification of

contrast agents by measuring T_1 changes between pre and post contrast MRI [193].

T_1 mapping protocols can be based on inversion or saturation recovery sequences. MOdified Look-Locker Inversion recovery (MOLLI) sequence is nowadays the most commonly used imaging method to perform T_1 mapping in cardiac MR [194]. **Figure 4.13** illustrates the T_1-mapping scheme for the MOLLI.

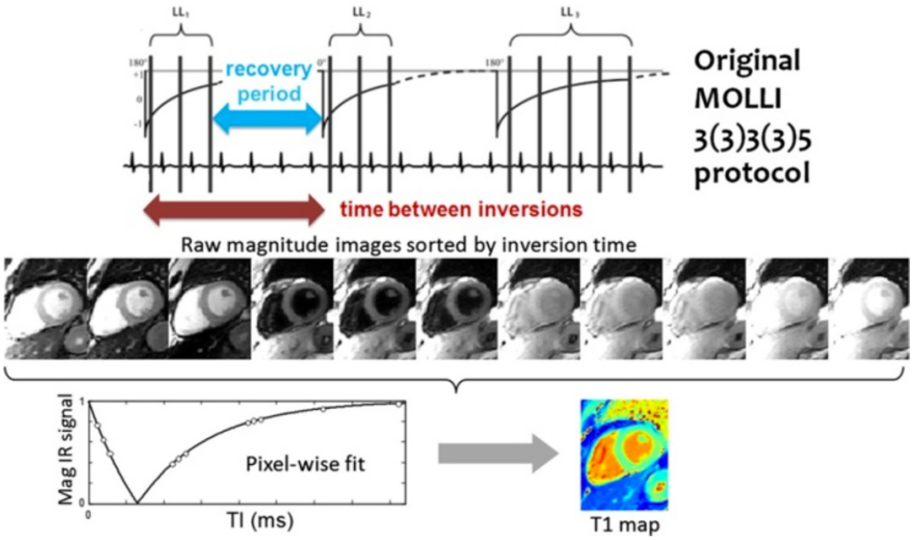

Figure 4.13. MOdified Look-Locker Inversion Recovery (MOLLI) scheme for T_1-mapping in the heart. Adapted from [194].

After the perturbation of the longitudinal magnetization using an inversion pulse, the relaxation curve is sampled at multiple time points from the inversion pulse. Pixel-wise T_1 mapping is achieved by fitting the sampled data to a model for the longitudinal signal, which is given by:

$$S = abs(M_0(1 - 2e^{-\frac{TI}{T1}})) \qquad (11)$$

In between TI, recovery periods are needed to ensure full recovery of the longitudinal magnetisation. The conventional MOLLI sequence follows a 3(3)3(3)5 protocol, meaning: 3 images are acquired, followed by a waiting period

of 3 RR intervals, then another 3 images are acquired followed by another 3 RR intervals waiting period, and finally a third inversion after which 5 images are acquired. The MOLLI sequence can be affected by high heart rates mainly because of the shortened time in between inversions and incomplete recovery of the magnetisation. To overcome this problem, the number of pauses cycles can be increased in between inversions. Despite its drawbacks, the MOLLI method is widely used, as it provides precise T_1 values and is highly reproducible.

The saturation recovery single-shot acquisition (SASHA) sequence is an alternative T_1 mapping sequence. It has the advantage that the T_1 values do not need correction (as the saturation curve recovers as T_1). However, although the T_1 quantification accuracy is higher for SASHA compared to MOLLI, the precision (reproducibility) is lower [195, 196] due to the limited dynamic range. SASHA is particularly useful for segmented acquisitions as it erases the history of the magnetisation making it heart rate independent.

T_1 mapping methods are increasingly used for diagnostic scans, and also can also be applied for more basic research questions (e.g. preclinical work) with some parameter adjustments. The size of a mouse heart is approximately 100 times smaller than that of a human heart, and the heart rate is approximately 10 times higher than in humans which creates several challenges and imposes limitations for cardiac MR. The challenges of preclinical imaging will be addressed at the end of this chapter in **section 4.9**.

4.7.5 - ^{19}F MRI

Fluorine magnetic resonance imaging using PFCs has emerged as a promising technique for molecular imaging [176, 197]. PFCs are detected using multinuclear coils, by tuning the frequency of acquisition from proton to fluorine.

^{19}F MRI is often performed using a SE sequence, with short TE and long TR to generate contrast dominated by the ^{19}F spin density and is not affected either by T_1 or T_2.

A drawback to ^{19}F MRI is the low sensitivity (reflected in low SNR). SNR increases linearly with concentration [198], however due to the large difference in tissue ^{19}F concentration that can be achieved compared to tissue water concentration, the MR signal of ^{19}F MRI is much smaller than that of conventional ^{1}H MRI. Therefore, the imaging of small areas of accumulation can be challenging (an increment in the voxel size can be an option). Although increasing the amount of injected compound will improve the SNR, high doses (more than 1-5 g/kg of PFCs) may be limited in humans because of safety concerns [199]. Several efforts have been made to improve the SNR of ^{19}F MRI, for example by increasing the magnetic field strength, improving pulse sequences or by increasing the number of equivalent fluorine atoms available [176, 179, 197, 200, 201].

4.8 - Image analysis

The analysis of the MRI images can be separated in signal intensity measurements or quantitative analysis. Examples of signal intensity measurements are SNR or CNR measurements. Quantitative analysis include relaxation mapping that estimate T_1 relaxation times.

4.8.1 - Signal-to-noise ratio (SNR)

SNR is the ration between the average signal intensity of the area of interest and the standard deviation of the noise (usually chosen from the background, or surroundings of the area of interest), given by:

$$SNR = \frac{Mean\ of\ the\ signal}{Standard\ deviation\ of\ the\ noise} \quad (12)$$

Higher field strength MRI usually benefits from higher SNR (from 1.5T to 9.4T) due to the increase in net magnetisation resulting from an increase in protons aligning with the lower energy state.

4.8.2 - Contrast-to-noise ratio (CNR)

CNR is the ratio of intensity differences between two regions and the standard deviation of the image noise, given by:

$$\boldsymbol{CNR} = \frac{\boldsymbol{Signal\ A - Signal\ B}}{\boldsymbol{Standard\ deviation\ of\ the\ noise}} \quad (13)$$

where, where *Signal A* and Signal B are signal intensities for signal producing structures *A* and *B* in the region of interest.

4.8.3 - Generation of the T_1 Map

MOLLI T_1 estimation is affected by the imaging readout, which itself perturbs the longitudinal recovery, reaching an equilibrium M_0* that is lower than the equilibrium magnetization M_0. Therefore the T_1 values from MOLLI sequence are usually underestimated and less accurate [195]. T_1* is the apparent recovery that is measured with the MOLLI T_1 map; here, the IR curve follows a 3-parameter exponential signal model:

$$\boldsymbol{S(t) = A - B\ exp^{\left(-\frac{t}{T1*}\right)}} \quad (14)$$

where, t represents the inversion time and T_1* the apparent T_1. To estimate T_1, a Look-Locker correction factor (B/A-1) is used: $T_1 \approx T_1$* (B/A-1). Nowadays, the three parameter fit model is implemented directly in the MR reconstruction software.

4.9 - Challenges of small animal MRI imaging

Preclinical imaging has become a prerequisite for imaging studies of cardiovascular diseases. From small to large animal scales, different animal models of cardiovascular diseases have been investigated. Small rodents are of huge interest because of their suitability and are relatively inexpensive. Transgenic and knock-out animals are experimental models allowing the investigation of specific genes or groups of genes associated with disease pathogenesis, permitting the study of drug efficacy and contrast agents specificity. The adequate characterization of the animal models is crucial for appropriate biological conclusions, therefore there is a need for non-invasive *in vivo* imaging which provides high spatial and temporal resolution for cardiovascular research, high reproducibility and which is suitable for longitudinal studies.

4.9.1 - Cardiac imaging in small animals in the clinical setting

Despite the availability of dedicated MR scanners for small animals, there is a strong interest in using clinical MR scanners for small animal imaging for several reasons: 1) clinical scanners may be available at lower cost during the night and weekends; 2) experimental research may be more convincing if performed with clinical imaging equipment thereby facilitating translation; 3) it is

easier to manipulate the animals because of the larger bore diameter of the clinical scanners; and, (4) many imaging sequences are readily available and imaging protocols are already implemented and can be manipulated for small animal cardiac imaging [202-205]. The main limitation of using clinical scanners is the lower gradient performance (longer TR's) and the lower strength limiting spatial resolution.

4.9.2 - Methodology for cardiac imaging

Murine MRI is extremely challenging and different aspects need to be taken into consideration. While dedicated small animal scanners or high field MR scanners have magnetic field strengths ranging from 4.7T to 17.6T, clinical scanners have typically lower magnetic field strengths, between 1.5T or 3T. As a result, high field MR have been primarily used for murine cardiac magnetic resonance because they provide high SNR and spatial resolution [206]. However, for contrast detection, lower magnetic field might be advantageous as the longitudinal relaxivity r_1 of Gd-based targeted contrast agents decreases with increasing field strength.

A mouse heart is approximately 7mm along the long axis and vascular dimensions can range between 1-2mm for the luminal diameter and 50-100μm for vessel wall thickness (for the thoracic aorta). Therefore, murine MRI requires sufficient SNR to allow for a high spatial resolution, which often requires multiple averages, lowering the bandwidth, at a price of a longer acquisition time or going from 2D to 3D acquisitions. SNR can also be improved with the use of small coils as SNR depends on the diameter of the coil. A careful selection of coils is necessary (e.g. wrist, carotid or microscopy coils) where commercially available

or even dedicated small animal coils that are adapted to the distance and size of the animal can be used.

Due to the large diameter bore of the clinical MR system, the resulting gradients strength is lower compared with dedicated small animal MR systems, which may affect the shortest available repetition time and thus temporal resolution. High temporal resolution is essential for cardiac murine imaging, which is particularly demanding because of the constant motion of the heart. In mice heart rates typically vary between 400-600 beats per minute. As such, optimal image quality requires synchronization of data acquisition with the cardiac cycle. Custom ECG is usually designed for small animals and will be described later in this chapter.

T_1 mapping techniques can be affected by high heart rates. Some T_1 mapping methods have been applied to mouse cardiac imaging on higher magnetic field scanners and more recently in our group at the 3T clinical scanner (data not published). In our group, T_1 mapping has been successfully applied using a MOLLI-based sequence on a 3T clinical MR scanner. An ECG triggered, segmented k-space 2D MOLLI based sequence was implemented with 8 sets of T_1W images and 12 pause cardiac cycles to adapt to the high heart rates in mice. To minimize cardiac motion, data acquisition was limited to the end diastolic phase. This sequence has shown to allow fast cardiac T_1 mapping in mice at clinical field strength [207].

Preclinical high field scanners are often equipped with stronger gradient systems, however clinical scanners can still achieve sufficient temporal and spatial resolution [204]. Previous studies shown that a resolution of 300μm can be obtained for cine MRI in rats at 1.5T [208] and in mice at 3T [209].

4.9.3 - Animal preparation and experimental setup

In small animal imaging, there are various animal-handling issues to be considered: strain and sex, animal wellbeing, anaesthesia, temperature and motion.

For comparative studies, the use of identical strains of rodents are mandatory. Studies have shown that parameters such as the time under anaesthesia, stress or the development of disease vary between different mice strains [210-212]. Also gender has shown to have significant effects on pharmacokinetics, metabolism and physiological parameters as well as disease progression [213], which might be due to differences in hormones or protein expression. Basic physiological functions, as heart rate, blood pressure and tissue oxygen levels can be monitored with small animal equipment commercially available, allowing the examination of the animal wellbeing and reproducible imaging conditions. Anaesthesia has shown to significantly influence results of imaging studies, especially physiologic parameters such as cardiac ejection fraction and volumes. The most used inhaled anaesthetic is isoflurane as it produces the most reliable and reproducible results [214]. Anaesthesia usually results in a reduction of core temperature (which consequently affects the heart rate), and thus it is extremely important to maintain the animals' temperature at around 37°C which can be achieved using a feed-back system which can include an MR-compatible rectal probe and a water based heating system. Despite mice being imaged under anaesthesia, respiratory and cardiac motion can create artefacts and degrade image quality in the MRI. To compensate for cardiac motion, image acquisition is usually synchronized with the R-wave of the ECG. Typical ECG systems for small rodents are based on paediatric or subcutaneous

electrodes. Signal averaging is used to compensate for respiratory artefacts in small animal imaging, since breath-holding cannot be used. For more accurate respiratory motion compensation, dedicated pneumatic pillows can be also applied.

The study design is of high importance, and control groups are necessary to compensate for these effects. The planning needs to clearly layout the strain of the animal, gender, lengths, type and dose of anaesthesia and the number of imaging sessions per animal to ensure reproducible experimental conditions. These factors should be consistent as possible within the same study.

Chapter 5

Methodology Set-up

5.1 - Personal Contribution

This chapter describes the optimization of the methodology used in this PhD thesis (and is the basis for all the experiments). It is divided in three sections: (1) development of a lung intubation system for the induction of myocardial infarction (MI) in mice and the reproducibility of the surgeries; (2) the set-up of a heating system for *in vivo* imaging on a clinical 3T magnetic resonance imaging (MRI); and (3) evaluation of the feasibility of ^{19}F MRI for the imaging of MI in a murine model.

For this project, René Botnar and Isabel Ramos (IR) conceived the main idea of the study. IR designed the mouse bed and lung intubation systems, the heating system for the 3T MRI experiments, and Pierre Gebhardt helped with the design and manufacturing of the technical equipment. IR performed all experiments including the measurements, data collection and analysis. Markus Henningsson and Torben Schneider helped with pulse sequence optimization. Thomas R. Eykyn helped with the nuclear magnetic resonance (NMR) spectroscopy acquisition.

5.2 - Lung intubation system

5.2.1 - Introduction

A method for the intubation of the mouse lung has previously been described [215, 216]. It is an important requirement when performing repeated measurements, and when open chest surgery is performed. Lung intubation can be achieved invasively by exposing the trachea with a small incision in the neck or less invasively by accessing the trachea from the vocal cords. Lung intubation protocols require training and in some cases, can be considerably expensive given the small materials required for mice. One of the main problems of performing the less invasive exposure of the trachea is that when the intubation cannula approaches the trachea it blocks the light itself, making visualization challenging. A lung intubation protocol with a self-incorporating fibre optic has been previously described [216], and has been implemented and adapted in our lab. Here, we developed an intubation bed and a portable intubation/light system for mice. It does not require expensive materials and, after some training, it is a simple technique to implement.

5.2.2 - Material and Methods

Intubation bed: A 3D model was designed with SolidWorks (Dassault Systèmes SOLIDWORKS, Massachusetts, USA) and then built in PVC (RS component, Northants, UK), providing stability with the additional advantage of being easy to clean. The intubation bed allows 90º rotation, which facilitates the mouse to be transferred from a vertical position while the intubation is being performed, to a horizontal position for the later connection to the ventilator. It had

a support for the correct placement of the animal with a rubber band positioned around the front incisors to suspend the mouse vertically (**Fig.5.1A&C**).

Portable light source: For intubation of 18-22 g mice, we used an intravenous catheter adapted with a specially designed connector to allow the assembly of the ventilator. For the light source, we used a fibre optic cable (0.5 mm diameter) connected to a mini LED illuminator (20000 millicandela). The illuminator was then connected to a 9V battery. Because the device should be portable, a switch on/off button has been implemented (**Fig.5.1B**).

Performing the intubation: After checking the pedal reflexes and shaving, animals were placed in the bed on a straight position. After placing the anaesthetised animal in the vertical position, the tong was gently pulled out and held with the forefinger (**Fig.5.1D**). Then the fibre optic together with the cannula were used to visualize the vocal cords, and the cannula was left inside the trachea while the fibre optic cable was removed. The correct positioning of the tracheal tube was confirmed by judging the symmetrical chest breathing expansion.

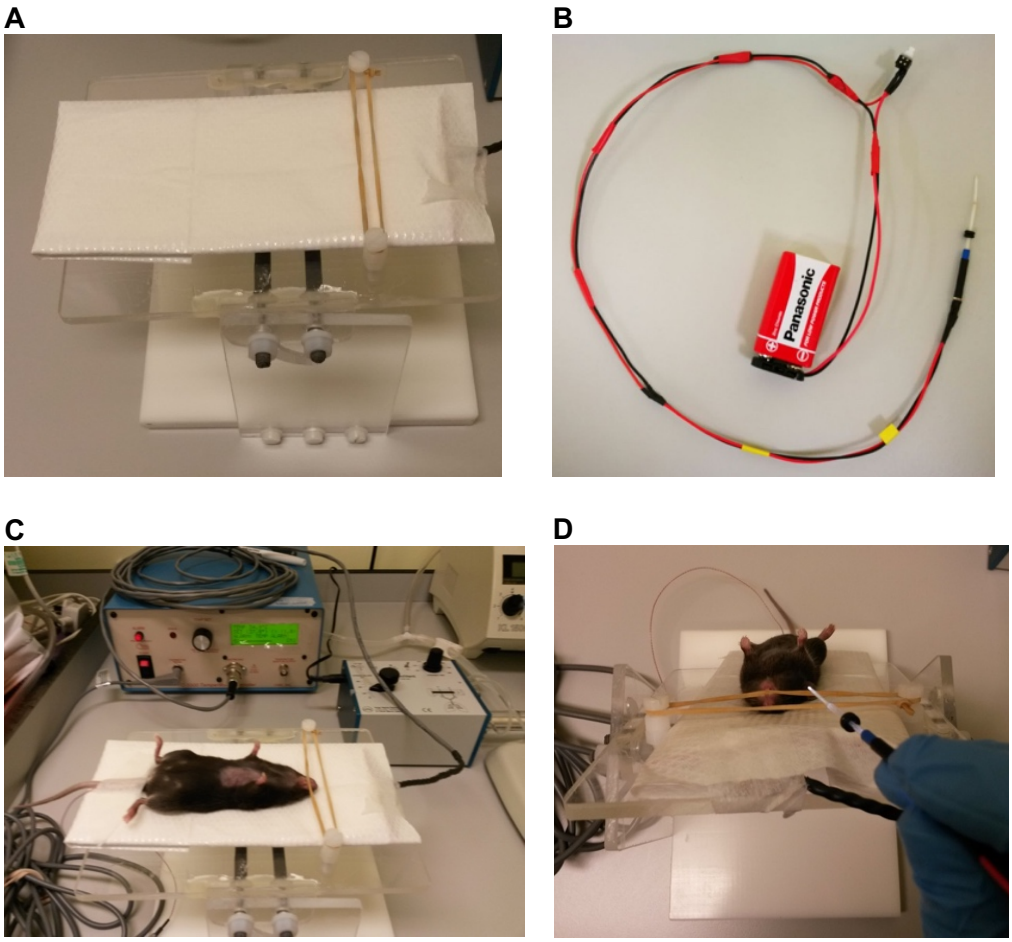

Figure 5.1. Lung intubation system. (A) PVC bed, (B) fibre optic cable with the intubation cannula, (C) mice placed in the bed with the rubber placed around the upper front tooth, (D) intubation approach, where the animal is placed vertically.

5.2.3 - Discussion

Lung intubation is a required procedure for the induction of MI. The current way of performing it implies that the trachea is directly exposed, adding an extra incision and consequently extra post-operative stress to an animal which will be subject to a severe surgery [216, 217]. The procedure is highly difficult to perform, painful and it can lead to animal death. Simpler procedures are highly recommended and preferable when several surgeries have to be done and when injectable anaesthesia is being used (40 minutes time window).

In this thesis a simple, portable and minimally invasive method for lung intubation has been adapted from previous work [216]. This technique is easy to

implement after some training and the set-up is relatively inexpensive, making it attractive for laboratory routine. It is portable, making handling easier, and does not require a microscope for the visualization of the vocal cords like other approaches [218]. Similar optical probes, with battery powered light source and optical fibre, are available from a commercial vendor (Braintree Scientific, Braintree, MA).

So far, we have used this procedure for the preparation of mice for MI induction only. However, this technique can be applied for other procedures. It can be implemented for several other surgeries that require open-chest, or when repeated measurements need to be performed (e.g. lung mechanics, imaging procedures) with minimal stress and damage to the animal. In summary, this intubation procedure is inexpensive, simple to use, and easy to implement in a lab routine, enabling investigators with relatively little experience to quickly and successfully intubate mice and perform surgeries.

5.3 - Induction of Myocardial Infarction

5.3.1 - Introduction

As previously mentioned in **sub-chapter 2.1.2**, the availability of animal models for the study of basic biology and development of new therapeutic strategies for the understanding of cardiovascular diseases are crucial. Basic research has been limited due to the complexity and difficulty to reproduce the pathophysiology of cardiovascular diseases in the laboratory. Consequently, it is extremely important to validate animal models. Myocardial infarction is often performed in murine models, as they are more suitable, efficient and less expensive than in larger animals [65].

In this project, MI was induced in mice by permanent occlusion of the left-anterior descending coronary artery (LAD). It is a well-established model for the study of acute MI pathophysiology. Following intubation, the LAD is occluded and MI is induced. In mice, given their small size, high manipulation precision during surgery is needed when performing the complex LAD ligation. Mortality rate of this procedure can be up to 50% in mice [65, 67]. Here we described how MI was induced, its reproducibility, survival rates and how infarct size was assessed.

5.3.2 - Material and Methods: validation experiments

Animal studies were performed according to UK Research Councils' and Medical Research Charities' guidelines on Responsibility in the Use of Animals in Bioscience Research, under a UK Home Office License (PPL 70/7097). MI was induced in 8-10 weeks old, female C57Bl/6 wild-type mice (N=9, 18-22 g, Charles River) by permanent occlusion of the left anterior descending coronary artery

(LAD). Mice were weighted and anaesthetised by intraperitoneal injection of 75 mg/Kg ketamine (Vetalar^{TM}V, Vetmedica, USA) and 1 mg/Kg medetomidine hydrochloride (Domitor®, Orion Corporation, Finland). Thirty minutes prior to recover, 0.15 mg/kg Buprenorphine (Vetergesic®, Alstoe, UK) was administered by intramuscular injection for analgesia. From these 9 animals, 1 died during procedure (mortality rate of 12.5%).

5.3.2.1 – Induction of myocardial infarction

After intubation (small ventilator, Hugo Sacks Electronic, Germany) described in ***subchapter 5.1.1***.), animals body temperature was maintained at 36±1°C during all surgical procedures using a heating pad equipped with a rectal probe (CWE, Biomedical Electronics, USA), in order to prevent hypothermia that may result from the anaesthesia. After disinfecting the chest, an oblique skin incision was performed from the left of the midline of the ribcage towards the left armpit (**Fig.5.2B**). The muscle layers were separated, and the top layer was retracted with a bulldog clip. The 4th intercostal space was exposed and a thoracotomy was performed (**Fig.5.2C**). With a curved forceps, the muscle layer was penetrated and then dissected with the aid of microforceps (**Fig.5.2D&E**). Retracting hooks were used to expose the heart, and the pericardium was carefully pulled apart to visualize the heart vessels (**Fig.5.2F**). An 8-0 nylon suture (Direct Medical Supplies, Alton, UK) was passed underneath the LAD ~2-3 mm below the tip of the left atria (**Fig.5.2G**). The effectiveness of the ligation was confirmed by the colour change on the left ventricle (LV) below the knot (**Fig.5.2H**). The retractor was then removed and a 5-0 Vicryl was used to suture the thoracotomy, muscle layers and the skin of the chest (**Fig.5.2 I&J**). At the end

of the procedure an antidote to reverse anaesthesia was administered. Animals were finally weaned from the ventilator and closely monitored while kept in a heating chamber at 30°C for at least 6 hours.

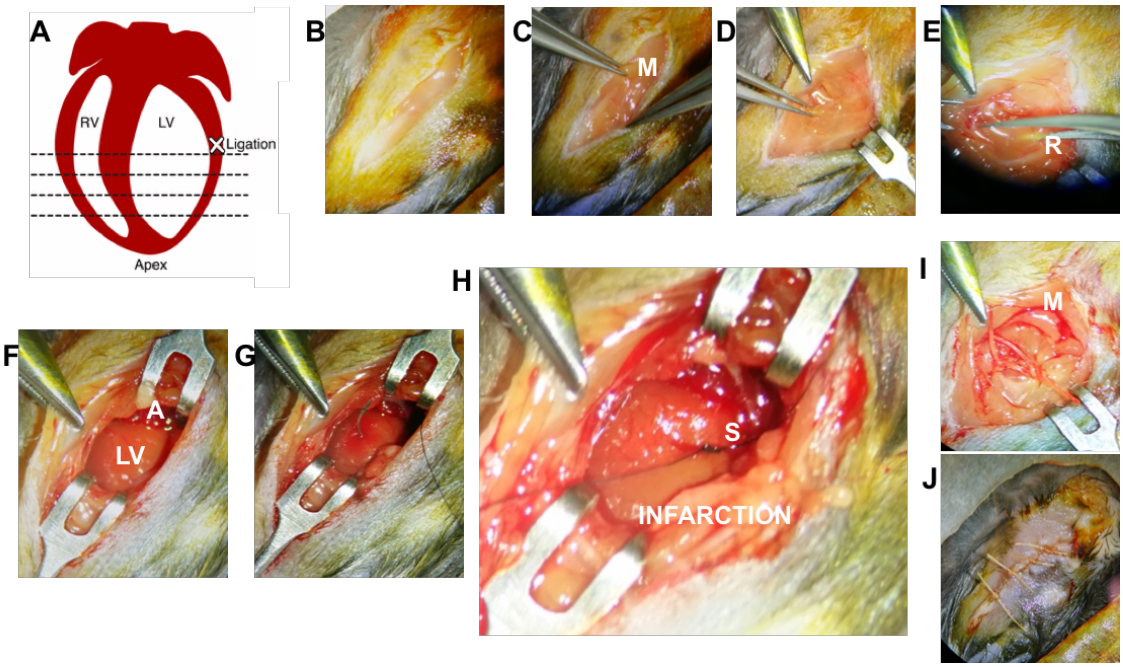

Figure 5.2. Myocardial infarction induction by permanent occlusion of the left anterior descending coronary artery (LAD) in mice. (A) Schematic representation of the location of the knot. (B) After checking pedal reflexes and disinfecting the skin, a small incision is made on the chest, (C) the muscle layers are separated (D) the ribs are localized and (E) with curved forceps the muscle layer is penetrated and (F) the heart exposed. (G) An 8-0 nylon suture is passed around the left-ventricle 2-3 mm below the atrium and (H) a knot is performed in order to induce an infarct. (I) Muscle layers and (J) skin are sutured and the animal is left to recover. RV, right ventricle; LV, left ventricle; M, muscle; R, ribs; A, atrium; S, suture.

5.3.2.2 - Analysis of infarct size

The extent of the infarct size was evaluated *in vivo* non-invasively by MRI, and *ex vivo* after tissue harvesting with 2,3,5-Triphenyltetrazolium chloride staining (TTC) or trichrome staining. After MRI imaging session, animals were culled by cervical dislocation under general anaesthesia to allow for *ex vivo* analysis. The hearts were excised, atriums were removed and the tissues were washed with PBS to remove residual blood. From the 8 animals scanned, four

tissues were frozen and processed for TTC staining, and the others were embedded in paraffin for Trichrome staining.

Magnetic resonance imaging: late gadolinium enhancement

After i.v. administration of 0.5mmol/kg of an elastin-specific MR contrast agent (Gd-ESMA, Lantheus Medical Imaging, North Billerica, USA), a 3D late gadolinium enhancement (LGE) inversion recovery (IR) sequences with 12 slices was performed. The inversion time was determined with a Look-Locker (LL) sequence to maximize the contrast between healthy and infarcted myocardium (250±30 ms). The imaging parameters included TR/TE=6.8/2.8ms, flip angle=25°, in-plane resolution=0.3×0.3 mm^2, number of slices=12, slice thickness=1 mm, TFE factor=3, scan time = 5:22 minutes. The IR pulse was performed every 5^{th} heartbeat.

2,3,5-Triphenyltetrazolium chloride (TTC) staining

For TTC staining, heart tissues were frozen at -20°C for 30 minutes and cut in 1 mm slice thickness (short-axis orientation) using a specialized mouse heart slicer (Zivic Instruments, Pittsburgh, PA). The slices were then incubated with 1.5% TTC solution for 15 minutes followed by formalin fixation (4% paraformaldehyde over night at room temperature).

Trichrome staining

Trichrome staining was performed using a Trichrome stains (Masson) kit (Sigma&Aldrich, Dorset, UK). After deparaffinising and rehydrating, sections were immersed in Bouin's Solution for 15 minutes at 56°C. Sections were then

washed in water. Then samples were incubated for 5 minutes in Working Weigert's Iron Haematoxylin Solution to stain the nuclei. Sections were then immersed for 5 minutes in Biebrich Scarlet&Acid Fucshin to identify cell cytoplasm and muscle fibres. Subsequently, slices were placed in Working Phosphotungstic/Phosphomolybdic Acid Solution for 5 minutes. Samples were then incubated for 5 minutes in Aniline Blue Solution to stain collagen fibres. Finally, samples were washed in 1% acetic acid for 2 minutes, dehydrated and mounted on slides.

Infarct Area Analysis

TTC stained sections were digitalized using a flatbed scanner (CanoScan LiDe 200, Canon). TTC sections were scanned on both sides, and the mean of the two measurements was used to calculate the total infarct area. Infarct area measured by Trichrome was quantified using ImageJ for each histology slice after manually segmenting the purple/blue area and normalizing it to the LV area. From LGE-MRI, the infarcted area was calculated by summing all areas of infarction for all slices, and dividing it by the total LV area.

5.3.3 - Representative results

When the LAD is ligated with a single stitch, an ischemic area is produced closely below the knot. The ligature is made 1-2 mm below the left atrium and, depending on the animal, it can cause a large size infarction. After permanent LAD ligation, the entire myocardial area below the knot becomes necrotic. Here we evaluated the infarct size *in vivo* by MRI and *ex vivo* using histology (**Fig.5.3**).

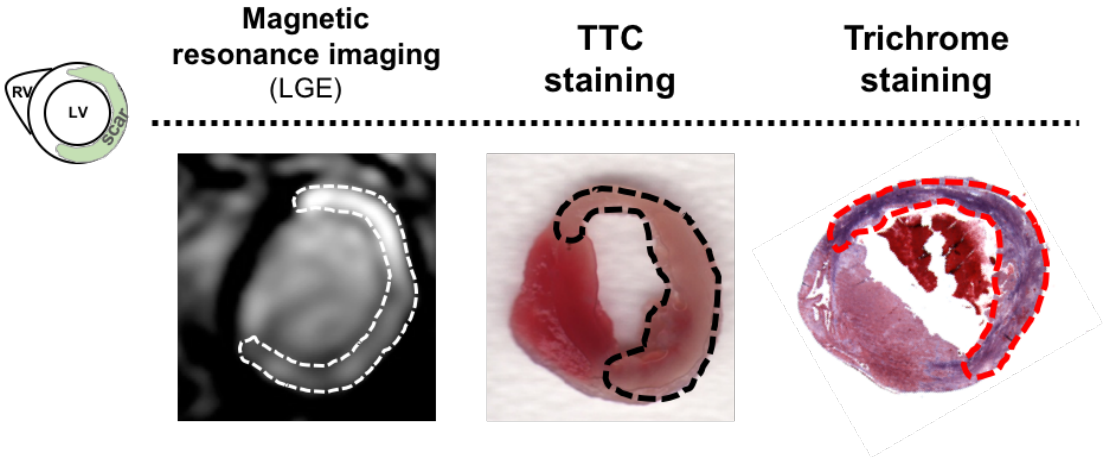

Figure 5.3. Analysis of the infarct size. Representative short-axis view of the heart (left) after gadolinium injection using late gadolinium enhancement (LGE) MRI, where area of infarct is enhanced. Representative transversal histology sections of the heart stained with (centre) 2,3,5-Triphenyltetrazolium chloride (TTC), where viable (red) and non-viable (white) areas are shown, and (right) Trichrome staining, where areas of infarct are shown in purple/blue, corresponding to the deposition of collagen. RV, right ventricle; LV, left ventricle.

MRI provides the possibility of analysing infarct size after the injection of gadolinium–based small molecular weight contrast agent non-invasively *in vivo*. After i.v. injection, the contrast agent is accumulated in the infarct region, and the damaged area appears brighter than normal myocardium. The heart is then excised and histology can be used to confirm the *in vivo* findings, either by TTC or by Trichrome staining. On fresh heart TTC-stained sections, areas of injured myocardium appear white, whereas healthy myocardium is shown in red. Trichrome staining, is commonly used for collagen fibre detection (and consequently infarct areas, where collagen deposits) which are stained in blue, nuclei are stained in black and the background is red. Quantification is shown in **Figure 5.4**. No significant differences were observed between the infarct size measurements using LGE-MRI, Trichrome or TTC (IS[%]=LGE: 50.74 [IQR, 47.75-54.26] vs Trichrome: 58.84 [IQR, 50.32-62.64] vs TTC: 47.21 [IQR, 43.20-53.91]).

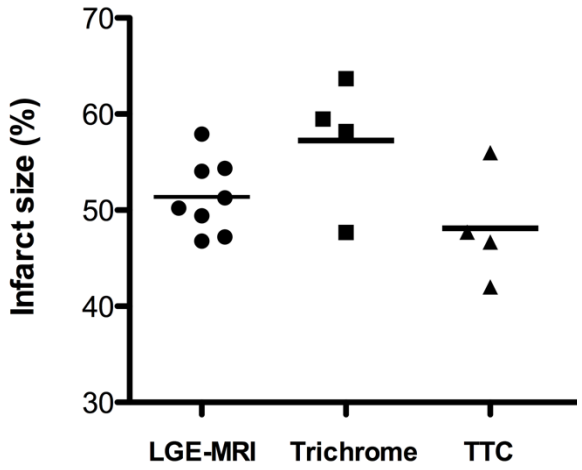

Figure 5.4. Infarct size analysis using *in vivo* LGE-MRI, and *ex vivo* Trichrome and TTC. No significant differences were seen between the different infarct size analysis methods. LGE-MRI, late-gadolinium enhancement magnetic resonance imaging; TTC, 2,3,5-Triphenyltetrazolium chloride. Data is presented as means ± S.E.M. P=ns, ANOVA, Bonferroni's Multiple comparison test pos hoc.

5.3.4 - Discussion

Similar to clinical myocardial infarctions, permanent occlusion of the LAD in mice induces an infarct by restricting the blood flow to the left ventricle [217, 219]. This is an increasingly important animal model of human disease, but remains technically challenging, due to both induction and data analysis reproducibility issues.

Here, myocardial infarction was induced by permanent ligation of the LAD in mice, a procedure known to be associated with an acute inflammatory response. Comprehensive evaluation of the extension of the infarct as well as its reproducibility are important considerations when validating the model. During these procedures, some critical aspects need to be taken in consideration: the intubation (as mentioned in subchapter ***5.1.1***), LAD ligation, and animal wellbeing mainly during the first 24 hours. The LAD ligation is the most critical step. It is susceptible to variations depending on the surgeon and animal strain. Small infarcts can show limited inflammatory response, whereas bigger infarcts can

lead to worst prognosis and ultimately lead to animal death. The LAD is difficult to visualize, and occlusion often needs to be performed blind, using some anatomical reference point. Usually the ligature is placed in the middle of the ventral side of the heart, 2-3 mm below the left atrium, and the efficiency is controlled by visualization of a grey colour in the affected areas. If the infarct appears on the anterior but does not include the posterior wall, a second suture can be placed but needs to be handled carefully to avoid bleeding or wall rupture.

In vivo MRI is the gold standard for the assessment of infarct size, however it involves high costs and expertise. Other techniques can be used instead, such as echocardiography or nuclear imaging techniques, however they do not provide the excellent reproducibility and accuracy of MRI, with the additional advantage that the latter does not involve radioactivity. *Ex vivo* histology can also be used to corroborate the *in vivo* analysis. TTC staining is the gold standard staining technique for infarct visualisation, allowing the distinction between viable and nonviable myocardium [220]. It does not require any special tissue processing, and the infarct area can be analysed on the same day of tissue collection. Trichrome staining, is used to analyse fibrotic tissue and gives not only morphological information, but also allows the quantification of collagen deposition in the heart. Here we demonstrated the feasibility of producing reproducible infarcts in mice and to quantify them using three different techniques.

5.4 - Development of an MR compatible heating system for *in vivo* imaging at 3T

5.4.1 - Introduction

Small animal experiments are usually performed under anaesthesia (e.g. isoflurane) which typically results in a decrease in body temperature [221]. This is due to their high body surface-to-mass ratio that makes mice susceptible to hypothermia, as their body temperature decreases several degrees within a few minutes of anaesthesia [222, 223]. Such a decrease in the body temperature might have severe effects on the physiological examination of the animal and may affect the pharmacokinetics and biodistribution of the contrast agent [224]. Thus, it is very important to control body temperature in small animals' experiments. Three methods of active warming are commercial available and are based on: hot air heating system, infra-red heat emitter and circulating-water blanket. The first, is usually implemented in high field MR scanners, as the MRI scanner bore is small and thus limits heat loss from the lateral walls of the MRI scanner. The infra-red system can be susceptible to the MR magnetic field, and it is usually expensive. The circulating-water blanket may have some electronics that, similarly to the infra-red systems, and thus can cause image artefacts or safety problems.

Here, we designed a simple and inexpensive heating system for controlling the body temperature in mice during the all imaging session in a 3T clinical MR scanner. The heating system is based on a circulating hot-water device and the temperature of the animals is controlled by a ECG/Temperature feedback module equipped with a rectal probe.

5.4.2 - Material and Methods: validation experiments

5.4.2.1 - Body temperature control system

The MR-compatible heating/monitoring system maintained the mouse body temperature to 36±1ºC by looping thermo-resistant tubes connected to a chiller unit with the objective to pump the water, into a closed loop tubing system (HAAKE SC100 and HAAKE A10 Thermo Fischer Scientific, US), which run warm water, next to the mouse (**Fig.5.5A**). The water temperature was regulated by the feedback received from a temperature-control unit. This unit included a rectal temperature probe, a temperature module (based on optical fibres) and a control/gating module and a computer to set the temperature (**Fig.5.5B**) (SA Instruments inc, US).

ECG needles (SA Instruments inc, US) used for pre-clinical imaging were connected to the Philips VCG device to monitor the heart rate and to synchronize the acquisition with the ECG. The two metallic needles were placed subcutaneously into the front paws (**Fig.5.6**).

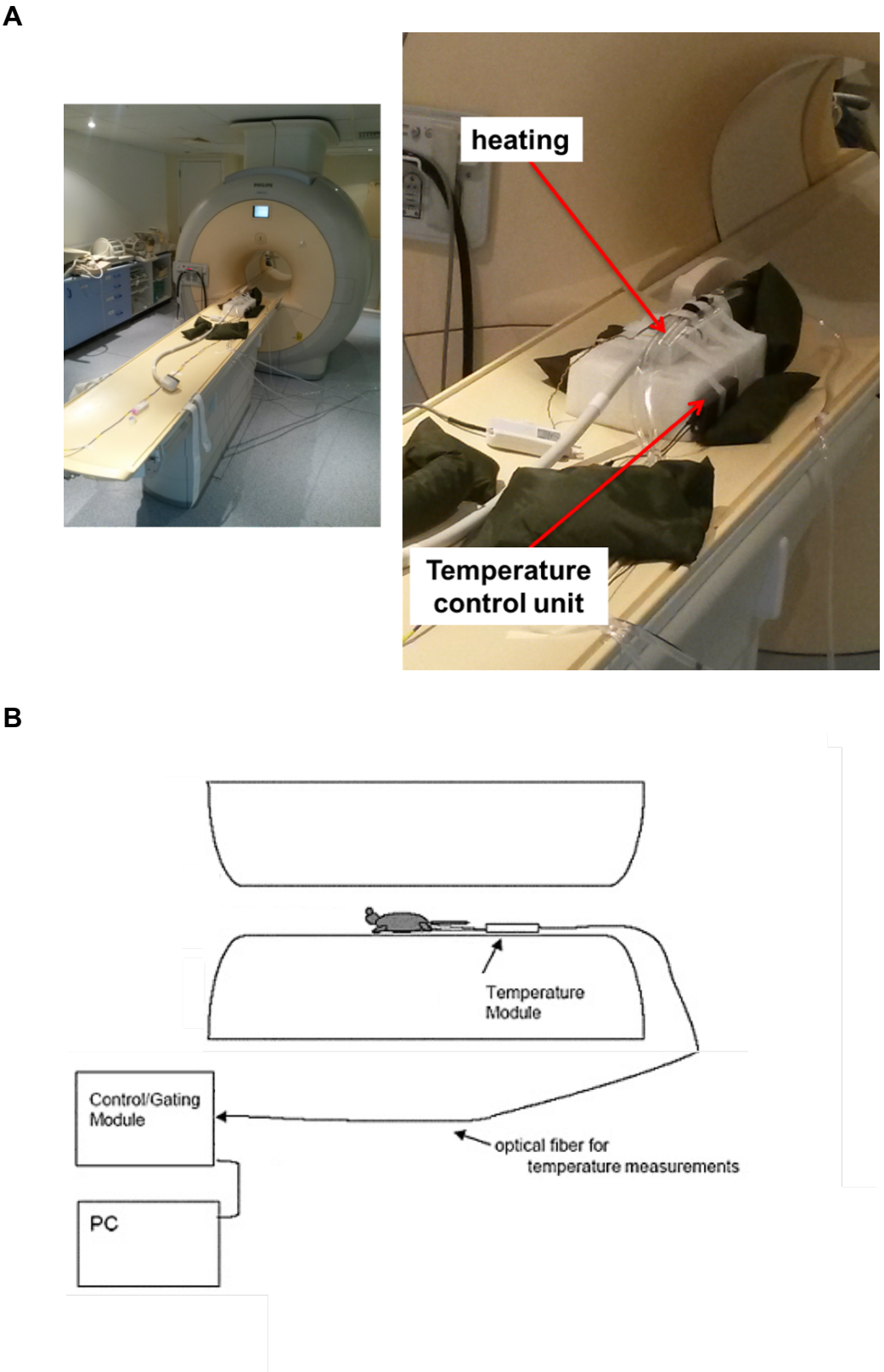

Figure 5.5. Experimental set-up of the heating system at the 3T MRI. (A) The animal was placed in prone position on top of the coil, surrounded by the plastic warm water tubes (“heating”). (B) MR compatible temperature-control unit for mice. Animal temperature is measured with a fibre optic rectal temperature probe, connected to a temperature unit which was connected outside the MRI room with a control/gating module and a computer. Adapted from [225].

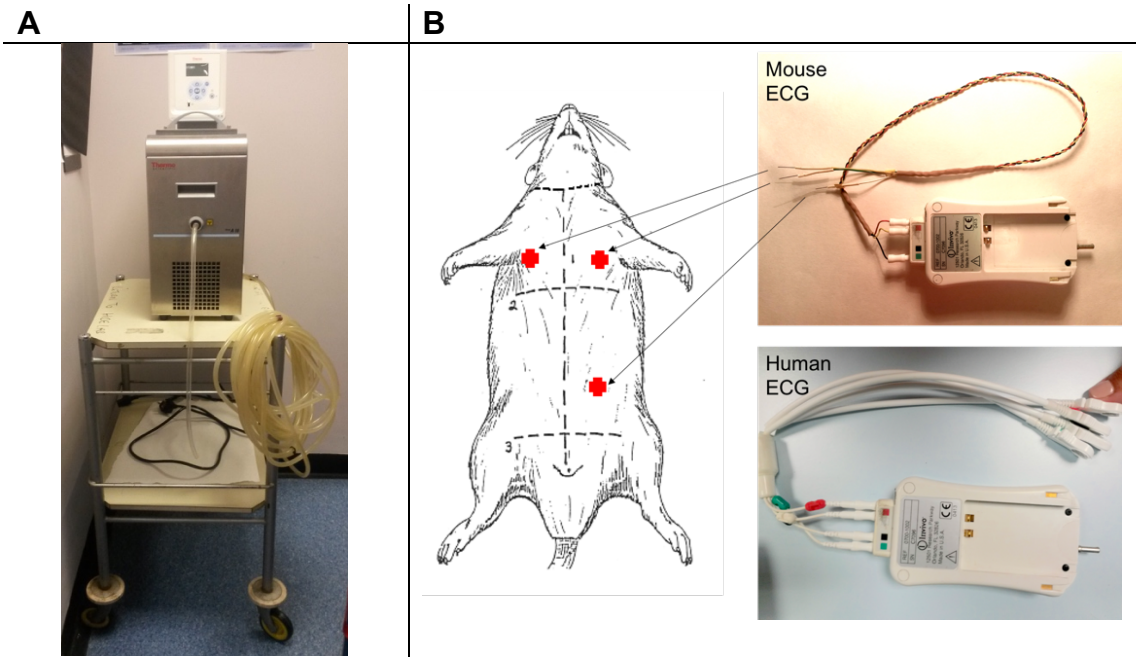

Figure 5.6 (A) MR-compatible heating system consists in a thermo-resistant tube connected to a chiller unit. (B) ECG control system used for pre-clinical (top left) and for human (down right) imaging.

5.4.2.2 - Animals

Surgical procedures were performed as described in ***section 5.3.2.1***.

5.4.2.3 - MRI methods

Ten animals were imaged using the clinical 3T MR scanner. Animals were scanned using a $^{1}H/^{19}F$ surface coil (Rapid Biomedical, Würzburg, Germany; diameter=33 mm and 23 mm). Anaesthesia was maintained with 1-2% isoflurane in medical oxygen. ECG was monitored with two metallic needles placed subcutaneously into the front paws. Following a 3D-GRE scout scan, 2D cine short-axis images were acquired covering the entire left ventricle (LV). 12 frames were acquired per cardiac cycle. Imaging parameters of the sequence included TR/TE=7.8/16.0 ms, field-of-view (FOV)=35×35 mm^2, flip angle=20°, in-plane resolution=0.3×0.3x1 mm^3 and TFE factor=1.

5.4.2.4 - Data analysis

Ejection fraction (EF) measurements were derived from the cine images using the ClinicalVolumes segmentation software (King's College London, www.clinicalvolumes.com).

5.4.3 - Results and Discussion

As reported in previous studies, when animals are anaesthetised for experimental purposes their temperature decreases and it can affect physiological measurements [221, 223]. Here, we designed a water-based heating system using a feedback loop and evaluated its effects on heart rate and ejection fraction. Without the heating system, the ECG signal was unstable; consequently, no reliable triggering could be performed affecting MR image quality or in the worst-case MR sequences could not be performed.

SHAM-operated and 3 days post-MI animals were imaged, and the effect of a small temperature increment and its effects on cardiac output (measured as EF) has been analysed. In non-diseased animals, EF usually ranges from 45-60% [212], while after MI this value tends to decrease as a consequence of a diminished cardiac function. **Figure 5.7** shows the EF measurement of the SHAM-operated and 3 days post-MI animals. At 37ºC, SHAM animals shown an EF of 47.63% [interquartile range, IQR, 46.00-53.16], while EF significantly decreased (EF[%]=3 days: 21.29 [IQR, 15.55-32.30]) in MI animals. No significant changes in EF were detected in animals 3 post-operative days after MI between when the temperature was varied between 36 and 37ºC.

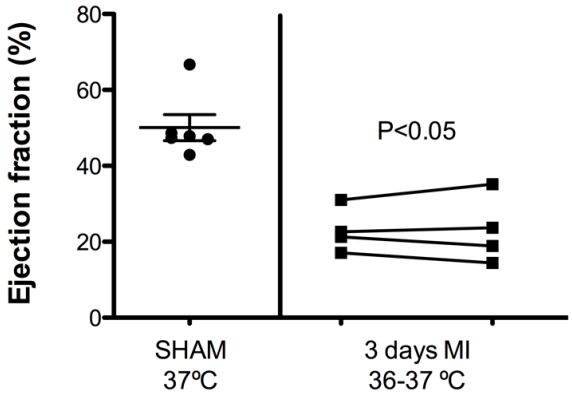

Figure 5.7. Comparison of ejection fraction (%) between SHAM-operated animals (N=6) and 3 post-operative days MI animals (N=4). Data is presented as Mean ± SEM, nonparametric Krustal-Wallis test, Dunn's Multiple Comparison test pos hoc, *P<0.008*.

A small increment of 1ºC did not lead to a significant change in the heart rate in animals with MI (Heart rate [bpm]: 36ºC=518.0 [IQR, 459.0-553.8] vs 37ºC=532.5 [IQR, 465.5-576.3]) (**Fig.5.7**).

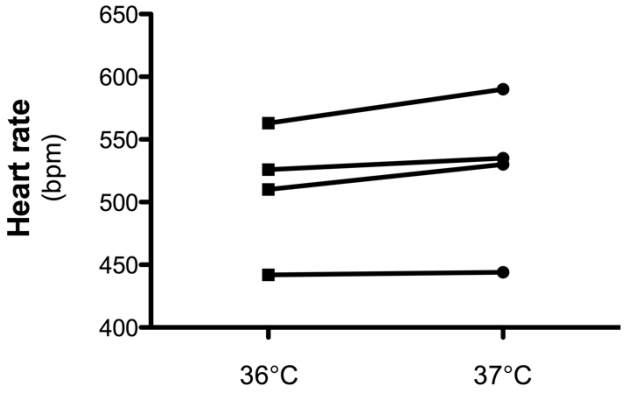

Figure 5.8. Effect of an increment of 1 degree Celsius on heart rate in animals 3 days after LAD ligation. Nonparametric, Wilcoxon rank paired test, *P=ns*.

Based on these experiments, during all the MRI imaging sessions the body temperature was maintained at 36±1ºC. In pilot experiments the temperature fluctuated between 37ºC and 33ºC and caused changes in the heart rate which has a negative impact on the ECG synchronization and image quality. This set-

up has been implemented in all my experiments, making the imaging results more consistent. Besides the normal arrhythmias that animals with disease can have, the heart rate using this setup is constant and consistent throughout the all scans, making sequences as MOLLI T_1 mapping (highly affected by changes in heart rate) easy to implement. In this project both infarcted and non-infarcted animals were analysed.

5.5 - Imaging protocol optimization of ^{19}F MRI contrast agents

^{19}F MRI has emerged as a new platform for the investigation of some biological processes, especially inflammatory cells, *in vivo*. Its advantages and applications have been described previously in **Chapters 3.2 and 4.5**, and here a comparison between different fluorinated nanoparticles were investigated.

5.5.1 - Introduction

Several fluorine probes are available and the specific choice depends on the application. Fluorine has a high electronegativity and low polarizability; and in general, PFCs are biochemically inert molecules, highly stable even at elevated temperature, or in oxidative environments, and have weak intermolecular interactions. They are also highly hydrophobic and significantly lipophobic and therefore exhibit a tendency to segregate from the surrounding environment independently of its chemical nature. Because they are insoluble in water, they are commonly administered *in vivo* in the form of lipid emulsions or encapsulated in polymer shells [226].

Molecules used as ^{19}F markers usually have multiple fluorine atoms and they often experience different chemical and magnetic environments (as described in **Chapter 3, section 4.1**). ^{19}F containing molecules have a chemical shift which covers a range of ≈ 300 ppm (compared to ≈ 12 ppm for ^{1}H) [178, 227], making ^{19}F MRI challenging for molecules with chemically different atoms [228, 229]. Ideal ^{19}F tracers should have a high fluorine content (multiple ^{19}F atoms), simple protocol, be biologically and chemically stable, exhibit no toxicity *in vitro* and *in vivo*, and yet yield a simple ^{19}F NMR spectrum with a single, sharp and intense peak with short T_1 and long T_2 relaxation times [201].

The main PFC molecular tracers used for ^{19}F MRI are perfluorooctylbromide (PFOB; a linear PFC), perfluoro-15-crown-5-ether (PF15C; a macrocyclic compound) and perfluoropolyether (PFPE; a linear PFC) (**Fig.5.9**).

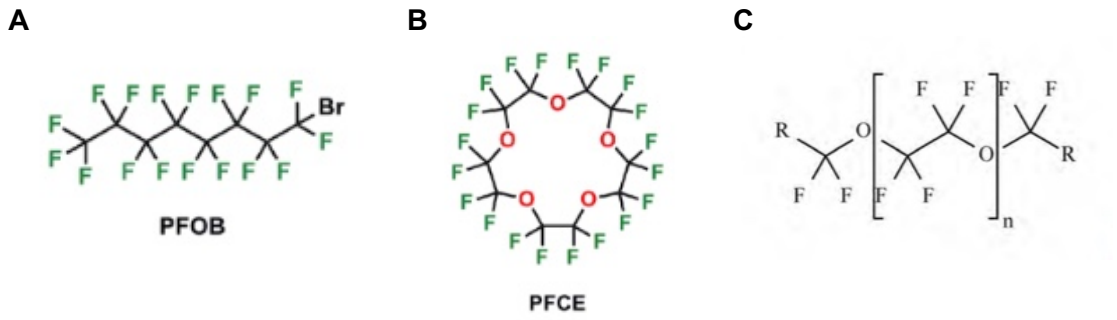

Figure 5.9. Chemical structures of (A) perfluorooctylbromide, PFOB, (B) perfluoro-15-crown-5-ether, PFCE and (C) perfluoropolyether, PFPE.

Perfluorooctylbromide (PFOB) is a commercially available PFC (also known as Fluosol). Interest in this compound for MRI started in the early 1990s [230] having been FDA approved for bowel MR imaging. However it was removed from the market because, although it did not show any toxicity, it was difficult to store the particles at -20ºC and even one year after administration it was found in lung tissue [231]. Blood-substitutes based on PFOB were considered safe, although some PFCs demonstrate long-term retention in the reticuloendothelial system (RES) [232]. However, PFOB remains a compound of interest and has been further explored in ^{19}F MRI research [228, 233].

Perfluoro-15-crown-5-ether (PF15C) shows better NMR performance than PFOB. Besides the chemical properties of the two PFCs being similar, PF15C has a higher number of equivalent fluorine atoms (**Fig.5.9B**). This eliminates the risk of chemical shift artefacts, unambiguous identification of the PFCs, and importantly, provides a single sharp resonance peak thereby maximising the

achievable SNR [176, 234]. However, except for PF15C, their behaviour is incompatible with biomedical applications. Other perfluoro-crown ethers have been shown to be unstable in blood, with a tendency to aggregate (e.g. perfluoro-12-crown-4-ether), and other PFC nanoparticles have a high molecular weight making them potentially toxic (e.g. perfluoro-18-crown-6-ether) [177]. Thus, the interest in PF15C increased and several applications have been investigated such as cell tracking, targeted drug delivery [235, 236] or cell labelling *in vivo* [97, 136, 237, 238] using ^{19}F MRI. Both strategies take advantage of the phagocytic capacity of inflammatory cells. PFCs have been investigated in several inflammatory disease models [97, 237, 238] since phagocytosis will result in accumulation of ^{19}F in the RES and in inflammatory areas.

Perfluoropolyether (PFPE), like PF15C, has a relative simple spectrum with one main resonance peak due to similar chemical groups. However, small additional peaks can be observed since the end groups are not chemically equivalent. These end groups can be replaced by fluorescence entities, thus making PFPE interesting compounds. Using fluorescence, histological correlation of *in vivo* imaging, or multi-modality imaging (e.g. MRI and fluorescence imaging) can be achieved and has been reported previously [174, 236, 239]. More information on ^{19}F MRI can be found in several review papers [174, 176, 197, 201, 240].

In this thesis, two PFC compounds were compared spectroscopically by NMR: *PFPE-VSense* (commercially known as V-Sense-1000H) and *PF15C*. Based on the pilot studies, PF15C was chosen to be used for all *in vivo* ^{19}F/^{1}H multinuclear imaging in wild type mice after MI induction on a 3T MR scanner.

5.5.2 - Materials and Methods

5.5.2.1 - Perfluorocarbons emulsion

Two PFC solutions were used for preliminary studies to establish the NMR characteristics of the agents. (A) PFPE-VSense nanoparticles (10% v/v of perfluoro-15-crown-ether, VS-1000H) were commercially available from Celsense Inc., Pittsburgh, PA, USA. (B) PF15C emulsions were prepared as reported [97], and kindly provided by Professor Flögels group (Institut für Herz und Kreislaufphysiologie, Heinrich-Heine-Universität, Düsseldorf, Germany).

5.5.2.2 - Phantom measurements

Nuclear magnetic resonance (NMR) experiments at 9.4T

NMR spectroscopic experiments were performed to determine the chemical shift of PFPE-VSense and PF15C required for the optimization of the MRI experiments. NMR spectra of the ^{19}F-PFCs were recorded at room temperature using a Bruker Avance III 9.4T scanner (^{1}H 400 MHz; ^{19}F 375.8 MHz) and a 15 mm diameter double-tuned (^{31}P/^{1}H) volumetric microimaging coil. The water resonance was used to shim the sample and the ^{1}H coil was then re-tuned to the ^{19}F frequency.

Two different vials (500 µL each) with the corresponding PFPE-VSense or PF15C PFCs were placed in NMR tubes (WILMAD NMR, Sigma) with a silicone support to position the sample within the isocentre of the coil. In addition, different dilutions of 10% and 20% PF15C PFCs were analysed. A sealed external reference capillary of 100% TFA solution was used as a reference (δTFA= -76.6 ppm as identified in the literature, and reported relative to $CFCl_3$). TFA exhibits a single resonance peak due to its three chemical equivalent fluorine atoms and is a convenient reference sample since its chemical shift is close to the resonances

of several PFC compounds. Spectra were acquired with a 90^{o} hard radiofrequency (RF) pulse (30 μs) and acquisition parameters included: number of averages= 64, total experiment duration= 4.78 minutes, time domain size= 131 K data points, pre-scan delay = 1 s, acquisition time= 3.5 s resulting in a total repetition time of TR= 4.5 s per scan and spectral bandwidth= 18797 Hz. Data were processed with an exponential line broadening factor (20 Hz), followed by Fourier transformation, zero and first order phase correction and automatic baseline correction. Peaks corresponding to the TFA reference and the PFC were integrated using Topspin 2.1 software (Bruker, Germany). NMR spectra were acquired without a deuterium lock signal. Thus, the derived NMR chemical shifts acquired at 9.4T were not referenced to the absolute frequency, which is subject to changes in shimming and field sweep of the spectrometer. However, this was used as a guide for subsequent calibration of the frequency required on the 3T MR scanner.

5.5.2.3 - 3T Magnetic resonance spectroscopy (MRS) and imaging (MRI)

Phantoms and animal scans were performed using a Philips Achieva MR scanner (Philips Healthcare, Best, The Netherlands) equipped with a clinical gradient system (30 mT m^{-1}, 200 mT m^{-1}), using a ^{19}F/^{1}H surface coil (Rapid Biomedical, Würzburg, Germany; diameter=23 mm and 33 mm, respectively). Imaging parameters were maintained between phantom and *in vivo* scans.

^{19}F PF15C phantom studies. The optimal off resonance frequency was studied by varying the off-resonance frequency between 9900 Hz and 10300 Hz. Signal-to-noise ratio (SNR) and chemical shift artefacts were studied. For localization of

the phantoms, a 3-dimensional gradient echo scout scan was performed followed by ^{19}F scans acquired perpendicular to the vials using a 3D turbo-spin echo sequence. Imaging parameters included FOV= 35x35x12 mm^3, in plane resolution= 1x1x2 mm^3, slices= 3, TSE factor = 5, offset frequency= [9800-10300] Hz (BW= 6103 Hz), 3 dynamic scans.

For signal-to-noise ratio (SNR) measurements, a region of interest was drawn on the second slice, and noise was measured on a dedicated noise scan with the RF pulses turned off (given by ***equation 10***).

The calculation of the theoretical displacement followed,

$$\Delta \boldsymbol{x}\ (\boldsymbol{mm}) = \frac{\boldsymbol{frequency\ shift\ (Hz)}}{\boldsymbol{receiver\ BW}\left(\frac{\boldsymbol{Hz}}{\boldsymbol{pixel}}\right)} \times \boldsymbol{Acq\ voxel\ size(mm)} \quad (15)$$

where, Δx is the displacement in mm; frequency shift is the difference between the expected and the studied frequency; receiver BW on the 3T was 177.7 Hz/pixel, and acquisition voxel size was 0.97 mm.

^{19}F in vivo studies. Surgical procedures were performed as described in ***section 5.3.2.1***. Pilot studies were performed to optimise the imaging protocols prior to the studies described in ***Chapters 6&7***. Mice were imaged 3 days after LAD ligation using a 3T MR scanner. 400 μL of ^{19}F-PF15C was injected i.v. 48 hours before scanning. In addition, mice were injected i.v. with 0.5mmol/kg of Gd-ESMA 1 hour prior to scanning. Anaesthesia was induced with 5% isoflurane and maintained with 1.5-2% isoflurane during MR experiments. Body temperature was maintained using a retrospective heating system and a rectal temperature probe. ECG was monitored with two metallic needles placed subcutaneously into

the front paws. ^{1}H and ^{19}F cardiac ECG-triggered images were acquired as follows. After a 3-dimensional gradient echo scout scan, a 2-dimensional Look-Locker sequence planned perpendicular to the left-ventricle was used to determine the optimal inversion time (TI) for nulling of the healthy myocardium. 3D LGE images were acquired in the short-axis for visualization of contrast agent uptake with the following parameters: FOV=35x35x12 mm^3, in-plane resolution = 0.3x0.3x1 mm^3, slices=12, TR/TE= 6.4/2.6 ms, 5 heart beats between subsequent IR pulses, and flip angle=25°. For the visualization of inflammatory cell uptake, ^{19}F scans were acquired in short-axis views using a 3D turbo-spin echo sequence. Imaging parameters included FOV=35x35x12 mm^3, in-plane resolution=1x1x2 mm^3, slices = 12, TR/TE = 4beats/8.9ms, TSE factor=5, offset frequency=10200 Hz (BW = 6103 Hz).

5.5.3 - Results

5.5.3.1 - Phantom measurements

9.4T NMR spectroscopic studies

The objective of the NMR study was to compare the magnetic properties of PFPE-VSense and PF15C stock solutions. The results of the NMR spectroscopic studies are shown in **Figure 5.10**. Both PFPE-VSense and PF15C spectra where acquired using TFA as an external reference.

PF15C contains 20 equivalent ^{19}F nuclei and showed a single peak at -90.66 ppm (-34077.52 Hz), -12.5 ppm relative to the reference TFA capillary. PFPE-VSense, a mixture of polymers with 28-36 fluorine atoms per molecule showed three main peaks: a quintuplet centred at -57.09 ppm (-21460.07 Hz); a doublet between -89.74 ppm and -89.78 ppm (-33729.88 Hz and –33745.34 Hz respectively) and a singlet at -91.81 ppm (-34507.18 Hz).

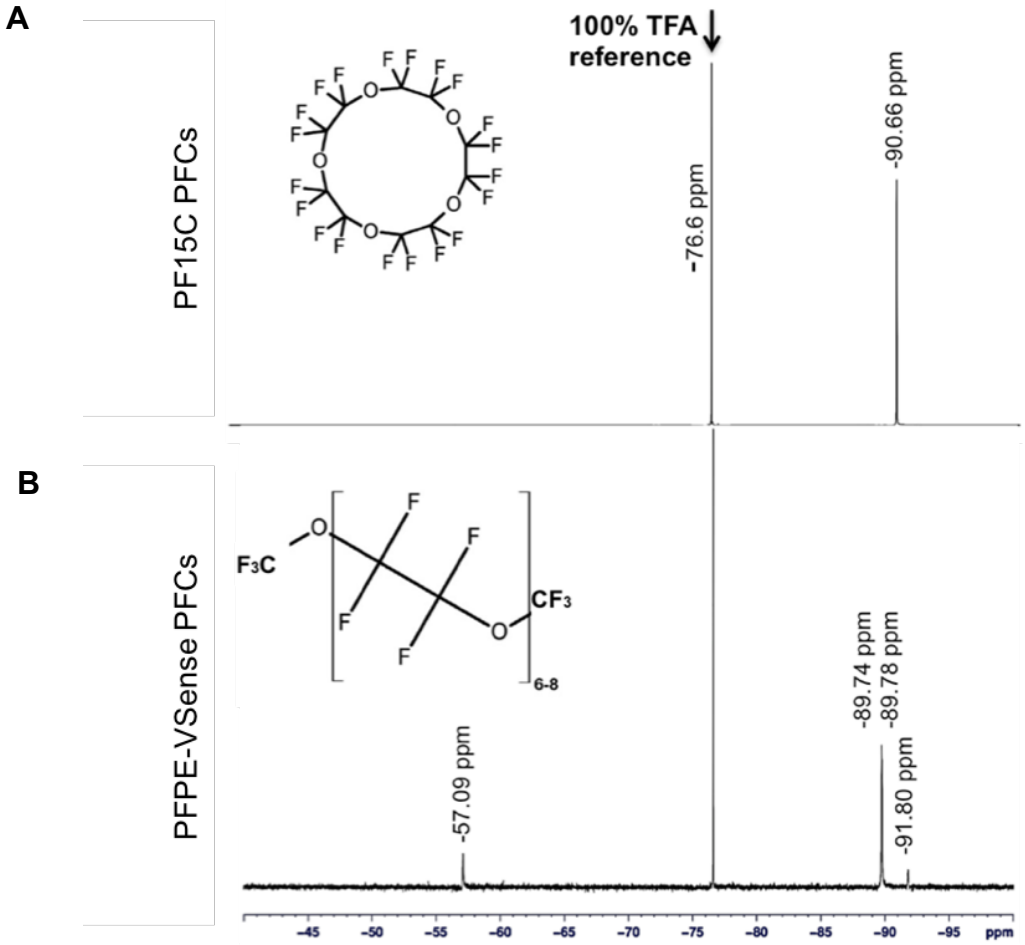

Figure 5.10 Structure and ^{19}F Nuclear Magnetic Resonance (NMR) spectra of PF15C and PFPE-VSense. (A) Structure and NMR spectra at 9.4T; PF15C PFC compound has 20 equivalent ^{19}F atoms showing a single peak at -90.66ppm. (B) PFPE-VSense PFCs (R = CF_2CF_3 or CF_3); it has about 28-36 ^{19}F atoms with three major chemical shifts at -57.09, -89.74 and -91.81 ppm.

The stability of the PF15C emulsion was further evaluated by diluting the samples in saline. The stability of the PFCs needed to be verified before *in vivo* experiments. An unstable solution would result in different spectroscopic peaks, corresponding to the different phases. Same peak was observed when different dilutions were studied (**Fig.5.11**).

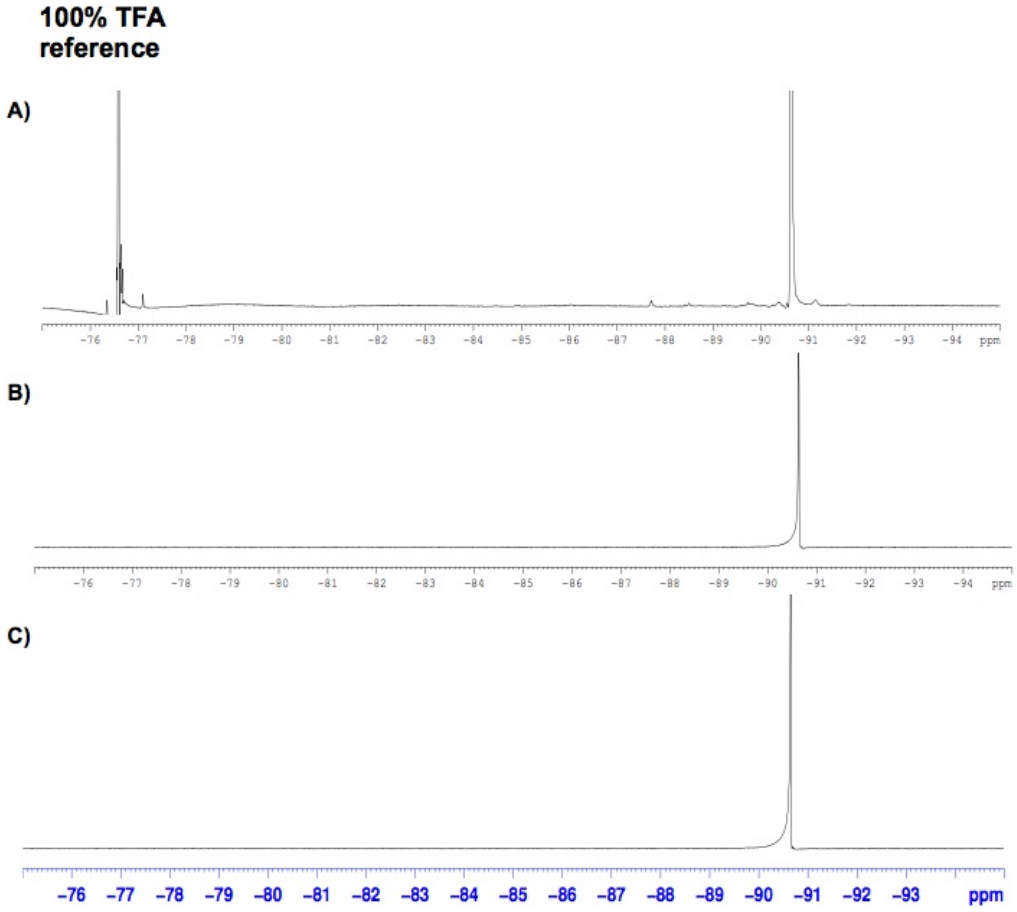

Figure 5.11. 9.4T Nuclear magnetic resonance spectroscopy studies for PF15C solution: (A) Stock solution, 100%; (B) 10% and (C) 20% dilution in saline.

Magnetic resonance spectroscopy (MRS) at the 3T

The identification of the offset frequency of PF15C was studied using 3T MRS. When the offset frequency is zero, and with a spectral bandwidth of 30000 Hz, PF15C shows a single peak centred at 10000 Hz (**Fig.5.12**).

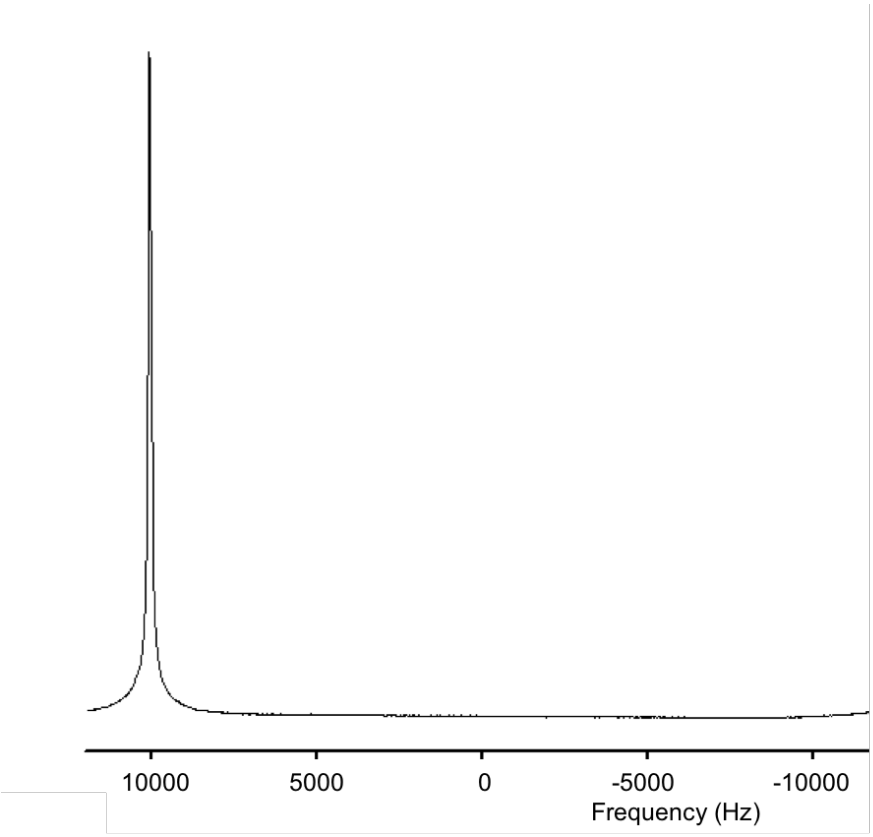

Figure 5.12. 3T Magnetic resonance spectroscopy of PF15C. With an offset frequency in 0 Hz and spectral bandwidth of 30000 Hz, a single peak was observed, centred at -10000 Hz (-10100.8065, 95.1923 Hz).

This offset frequency of 10000Hz was used for the next experiment. Using this value, the relative frequency between TFA (control) and PF15C was analysed. **Figure 5.13** shows a single peak of PF15C centred at zero (on resonance), and -12.5 ppm relative to the reference TFA capillary solution, as expected.

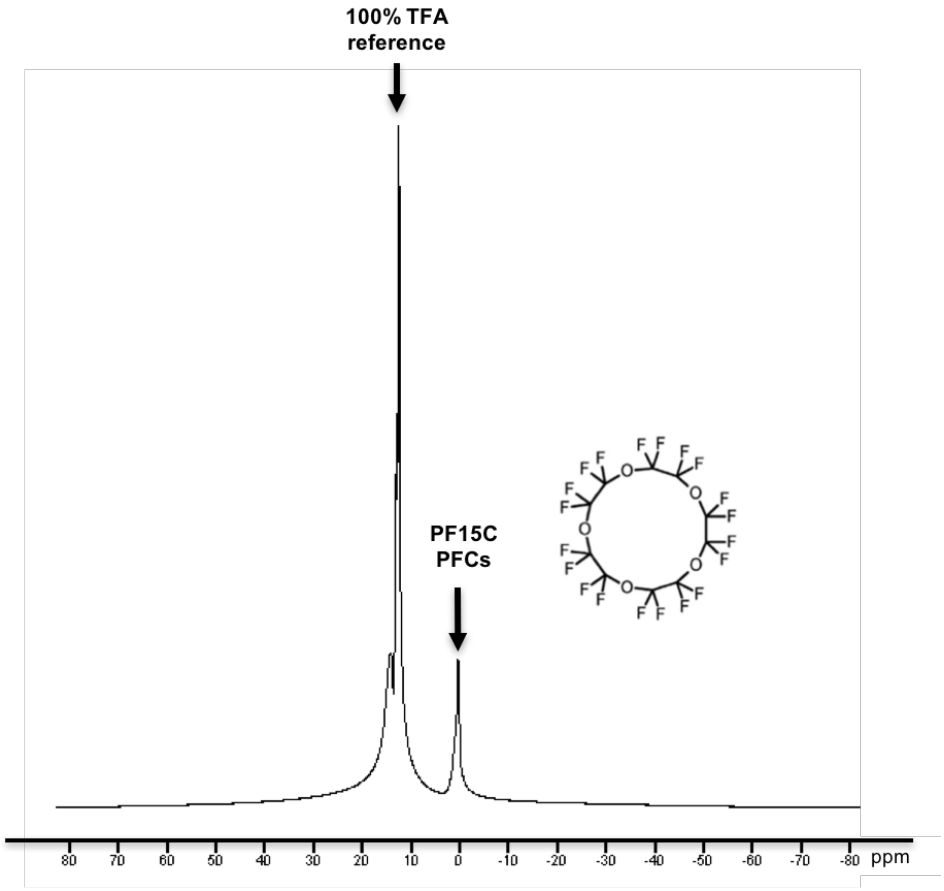

Figure 5.13. 3T Magnetic resonance spectroscopy of PF15C and TFA (reference). With an offset frequency of 10000 Hz, PF15C shows a single peak centred at 0 (on resonance), and TFA shows a peak centred at -12 ppm.

By changing the offset frequency to values different from 10000 Hz, a chemical shift artefact was observed, which results in a change of the position of the phantom in the frequency encoding direction (**Fig.5.14A**). When the transmitter frequency and therefore receiver frequency was off-resonance, a displacement (chemical shift artefact) in the foot-head direction was observed. With an offset of 10000 Hz the image of the phantom is located in the centre of the field of view, while at lower frequencies there is an “upwards” shift of the phantom in the field of view and at higher frequencies lead to a “downward” shift was observed. A displacement of 1 mm in the foot-head direction (i.e. frequency encoding direction) was observed when the offset frequency was different from

the on-resonance frequency (e.g. 10000 to 10200 Hz; measured by Osirix software) (**Fig.5.14B**).

The effects of the offset frequencies on SNR measurements were also analysed (**Fig.5.14C**); high SNR was observed between 10100-10200 Hz, a 10% difference was observed for the other frequencies studied.

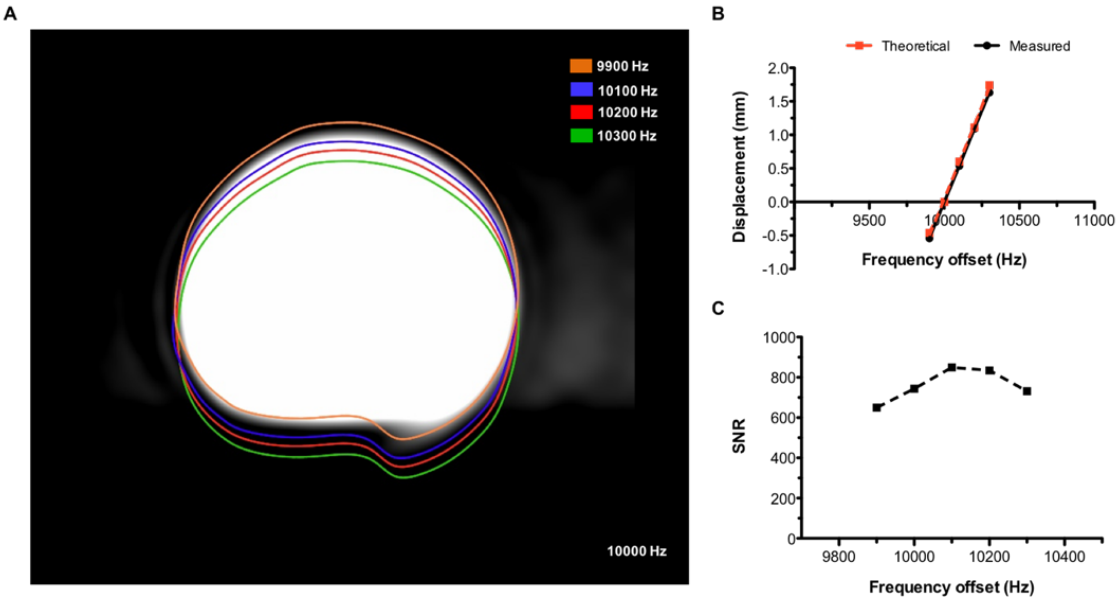

Figure 5.14. Chemical shift artefact of PF15C PFC. (A) Different frequency offsets were studied and chemical shift artefacts can be visually identified. (B) Calculated theoretical (y=0.0054x-54.30) and measured (y=0.0055x-55.05) displacement from the MRI images (C) Signal-to-noise ratio (SNR) was measured using Osirix.

Quantification of the ^{19}F signal intensity from serial dilution of the PF15C stock solution (**Fig.5.15**) showed a linear correlation between the fluorine signal intensity and ^{19}F-concentration. This suggests that the ^{19}F signal intensity can be used to quantify the concentration of ^{19}F in solutions and tissues although for *in vivo* imaging a phantom of known concentration (reference standard) would be required for absolute quantification.

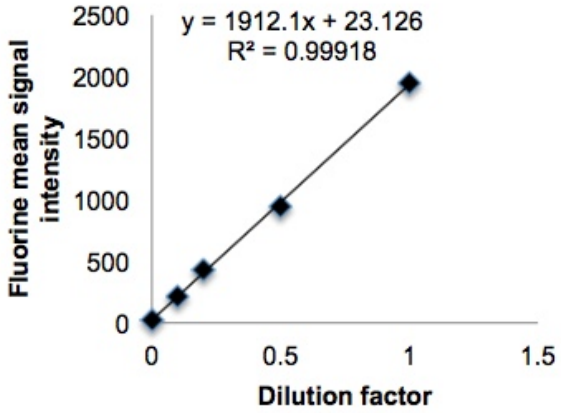

Figure 5.15. Detection threshold for ^{19}F MRI using PF15C. Emulsions were diluted (0,10,20,50,100%) and measured by $^{1}H/^{19}F$ MRI using a spin-echo sequence with the following parameters: TR=500 ms, TE=8.7 ms, Offset frequency 10330 Hz, BW= 8000 Hz.

Mice received a 400 µL injection of PF15C 48 hours prior to MRI imaging. Animals were maintained under anaesthesia during the MRI scans using isoflurane. No fluorine signal was observed in control animals without injection of PF15C (data not shown). ^{1}H and ^{19}F images are shown in **Figure 5.16**. Quasi simultaneous acquisition of morphologically matching proton (^{1}H) and fluorine (^{19}F) images enabled the exact anatomical localization of PFCs. ^{19}F signal co-localised with the infarcted area, but was also seen at the site of the surgical incision, adjacent lymph nodes and liver.

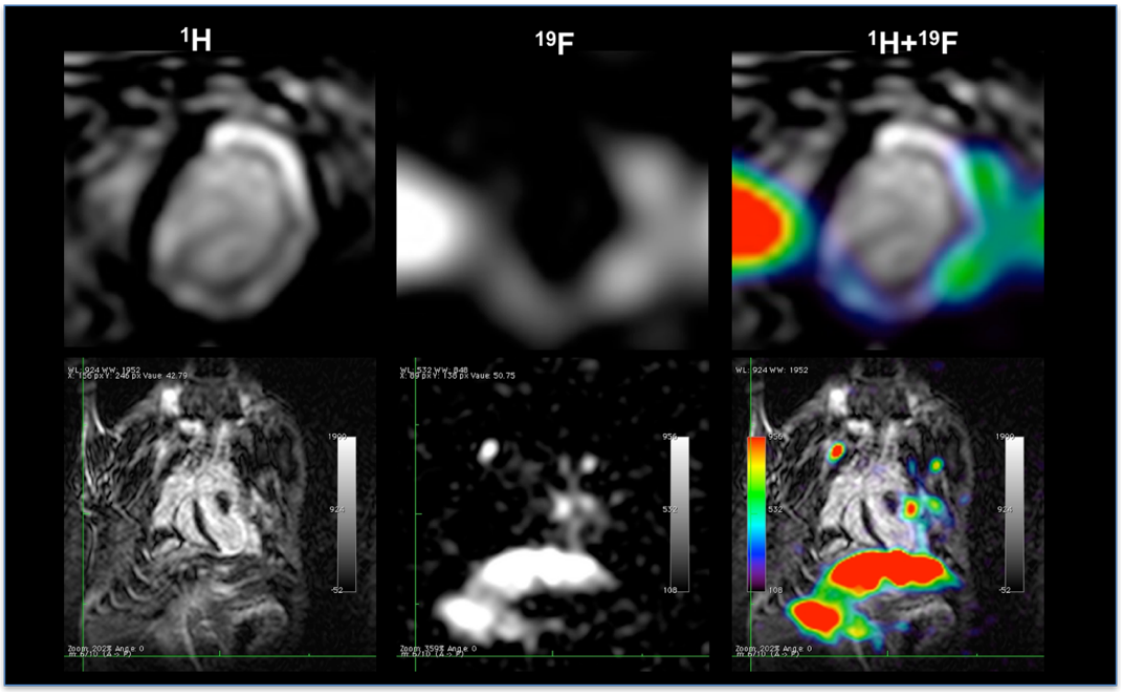

Figure 5.16. *In vivo* imaging results of ^{19}F/^{1}H MRI in a mouse model of myocardial infarction 48 hours after intravenous injection of PF15C PFCs. Three days after LAD occlusion the infarcted area was enhanced on ^{1}H, late-gadolinium enhancement scans (LGE scans, left column); ^{19}F scans showed enhanced areas of PFCs uptake; ^{1}H/^{19}F overlay images showed the co-localization of the ^{19}F signal within the infarcted myocardium, healing tissue, liver and lymph nodes; both at short-axis view (upper row) and coronal view (lower row).

5.5.4 - Discussion

In this study two goals were pursued: (1) to compare two PFCs, PFPE-VSense and PF15C emulsions by NMR spectroscopy; and (2) to investigate the feasibility of ^{1}H/^{19}F MRI for the *in vivo* imaging of inflammation in a mouse model of MI.

In phantom experiments, PFPE-VSense exhibited multiple resonance frequencies compared with the single and sharp peak of PF15C as observed using 9.4T NMR spectroscopy, making the latter the preferred agent for phantom and *in vivo* experiments using the 3T clinical MR scanner. PFPE-VSense emulsion have 28-36 fluorine atoms, which are not chemically equivalent and therefore displays several resonance peaks (-57.09 ppm, -89.74 ppm, -89.78 ppm and -91.81 ppm) [241]; this can create ghost artefacts when imaging is

performed in contrast to spectroscopy and can result in lower SNR as previously reported [234]. Due to its chemical structure and associated challenges, ^{19}F-PFPE was not chosen for further *in vivo* imaging experiments.

On the other hand, PF15C is a perfluoro-15-crown-ether which has 20 chemically equivalent fluorine atoms, which contribute to a single peak measured by spectroscopy [234]. PF15C has been shown to be chemically stable when different dilutions have been studied (single peak), and no adverse effects were observed *in vivo*.

In the 9.4T NMR study, a single peak at -90.66 ppm was observed for PF15C. Similarly, with 3T MRS a single peak was observed at 10000 Hz (82.87 ppm). These initial results suggest that there is approximately 7 ppm difference between the 9.4T and 3T. Since the ^{19}F frequency on the 3T is referenced to the H_2O signal acquired during a preparation scout scan it is likely that this disparity arose due to the lack of reference lock signal used for the 9.4T acquisition as well as differences in field homogeneity. TFA was used as a control reference in both fields, where similar offset frequency difference was observed.

When different offset frequencies were studied (on and off resonance) a chemical shift artefact was observed in the images. When the excitation frequency is not on-resonance, the images suffer a chemical shift artefact leading to a displacement of up to 1 mm (between 10000-10200 Hz), corresponding to the theoretical value. This means that image registration may be required to fuse ^{1}H and ^{19}F images. This misregistration occurs because of the difference in resonance frequency, which creates artefacts in the frequency encoding direction only. However, based on our results an off-resonance frequency of 10200 Hz showed the highest SNR and was therefore used for all *in vivo* experiments. Our

phantom study further demonstrated high signal linearity with ^{19}F concentration (R^2>0.99).

The visualization of scar tissue with the $^{1}H/^{19}F$ dual coil was feasible at 3T. The results showed that it was possible to visualize PF15C PFCs at 3T with no signal background. Previous studies in different experimental mouse models of inflammation including the early stage of MI demonstrated the feasibility of using ^{19}F PFC for the detection of inflammatory cells with high field MRI [97, 235, 238, 239, 242]. The emulsion was injected i.v. 48 hours before the scan to allow efficient phagocytosis of the PFC nanoparticles, infiltration of the labelled-immune cells into the injured myocardium [237] and sufficient blood clearance. The imaging studies demonstrated the feasibility of visualizing the infarcted regions as hot spots (fluorine (^{19}F) image) on simultaneously acquired morphologically matching proton (^{1}H) MR images. ^{19}F signal has also been observed outside the heart as LAD surgery may inflict injury to other tissues including muscle and skin that subsequently undergo an inflammatory healing process and thus take up PFC nanoparticles. In addition, liver and lymph nodes also showed fluorine signal. No signal was detected in the lungs, blood or in any SHAM-operated animals (data not shown).

A disadvantage of the direct detection of ^{19}F PFCs is the relatively high local contrast agent dose required for signal MR generation. Here a total volume of 500 µL was injected. It has been shown previously that lower volumes could be also detected in mice (50 µL of a 10% PFC-containing emulsion) using a 9.4T MR scanner [238]. However, no toxic effects were detected in the animals investigated in those studies. Furthermore, these studies have not shown any adverse effect on the proliferation, function or maturation of immune cells after

^{19}F-PFC administration [97, 235]. The PFCs used in these studies exhibit ideal MR properties but having long retention times in the body [97], making clinical translation challenging. To overcome this problem, other PFCs could be used. However, from the MRI perspective, these compounds have the disadvantage of chemical shift artefacts due to the magnetically different ^{19}F nuclei. Van Heeswijk *et al* [243] calculated the required dose for humans studies based on the contrast medium dose that was administered for animal ^{19}F MR angiography, assuming the same experimental conditions. Base on their calculations a dose of 38 mM PFC are required for human angiography studies, which has been administered previously in humans as blood substitutes [244].

Here we have shown that ^{1}H/^{19}F MRI to assess inflammatory responses in WT mice after induction of MI is feasible using a 3T clinical MRI scanner. PF15C have been shown to be ideal for these experiments because of their chemical behaviour. This methodology thus has a great potential for studying inflammatory processes in different experimental animal disease models of cardiovascular disease.

Chapter 6

Molecular imaging of inflammation and extracellular matrix remodelling in a murine model of myocardial infarction

6.1 - Personal Contribution

René Botnar, Ajay Shah and Isabel Ramos (IR) conceived the main idea of the study. IR performed the surgeries, MRI and NMR scans, histology and data analysis described in the following chapter. Maryam Nezafat, René Botnar and Markus Henningsson (MH) designed the MOLLI T_1 map sequence. MH, Begoña Lavin, Silvia Lorrio, Thomas R. Eykyn, Andrea Protti and Alkystis Phinikaridou helped with data collection. Pierre Gebhardt helped with the set-up of the heating and physiological monitoring system and Marcelo E. Andia with statistical analysis. Prof. Ulrich Flögel provided the ^{19}F nanoparticles. A manuscript has been written and reviewed by all co-authors and is ready for submission.

Part of this study was presented as an abstract at the 1st Divisional Symposium at King's College London in 2015, the 24th Scientific Meeting of the International Society of Magnetic Resonance in Medicine (ISMRM) in Singapore 2016, the King's BHF Annual Symposium in London in 2017, and at the 25th

ISMRM conference meeting in Hawaii in 2017 as an oral and poster presentations. At ISMRM 2016 and 2017 the oral presentations were awarded with Magna Cum Laude and Summa Cum Laude Merit awards, respectively.

Authors List

Isabel Ramos[1,2], Markus Henningsson[1], Maryam Nezafat[1], Begoña Lavin[1,2], Silvia Lorrio[1,2], Pierre Gebhardt[1,3], Andrea Protti[1], Thomas R. Eykyn[1], Marcelo E. Andia[4], Ulrich Flögel[5], Alkystis Phinikaridou[1,2], Ajay M. Shah[2,6], René M. Botnar[1,2,7]

Affiliations

[1]Imaging Sciences and Biomedical Engineering, King's College London British Heart Foundation Centre of Excellence, London, United Kingdom. [2]Cardiovascular Division, The British Heart Foundation Centre of Excellence, King's College London, London, United Kingdom; [3]Department of Physics of Molecular Imaging Systems, Institute for Experimental Molecular Imaging, RWTH Aachen University, Aachen, Germany. [4]Radiology Department, School of Medicine, Pontificia Universidad Catolica de Chile, Santiago, Chile. [5]Department of Molecular Cardiology, Heinrich Heine University Duesseldorf, Duesseldorf, Germany. [6]Escuela de Ingeniería, Pontificia Universidad Católica de Chile, Santiago, Chile.

6.2 - Introduction

Myocardial infarction (MI) is one of the major health care problems in western societies [245]. Optimal post-MI healing relies on a suitable degree of inflammation and its timely resolution, and a well-orchestrated deposition and degradation of extracellular matrix (ECM) proteins [9, 121, 246]. Cardiac injury activates innate immunity that triggers an inflammatory response where neutrophils and monocytes/macrophages are recruited to the myocardium [9].

Quickly after MI, neutrophils are recruited to the injured site, followed by monocytes/macrophages to remove dead cells and debris by phagocytosis [9, 26]. Studies have shown that an early and aggressive immune response and high levels of neutrophils and monocytes within the infarct may also promote adverse remodelling and lead to a poor prognosis [56, 247]. In addition to their phagocytic properties, inflammatory cells activate reparative pathways that trigger the formation and deposition of scar tissue, mainly composed of collagen and elastin/tropoelastin [26, 57, 248]. Elastin has been shown to be essential for the stabilization of the scar after MI and improving cardiac function by preserving its elasticity [58, 59]. While the remote myocardium contains elastin only to a negligible degree within the interstitium and coronary vasculature, elastic fibres increase within the myocardial scar in the first weeks following ischemic injury and continue the formation of a dense network between the remaining viable myocytes, myofibroblasts and smooth muscle cells during maturation of the infarct [57]. Tropoelastin, the soluble precursor of elastin, has been identified in increasing amounts within the remodelled myocardium and particularly towards the later stages of the healing process [249].

Magnetic resonance imaging (MRI) is a non-invasive imaging modality that provides both functional and anatomical information with high spatial resolution. Cardiac magnetic resonance imaging (CMRI) after administration of contrast agents has been used to characterize myocardial viability, perfusion, infarct size and diffuse fibrosis [148, 192, 250]. Previous studies have shown that inflammatory cells can be imaged using ^{19}F perfluorocarbons (PFCs) [97, 238].

As ^{19}F is present in extremely low concentrations in the body, the ^{19}F signal measured after administration of ^{19}F-PFCs corresponds to that phagocytosed by

inflammatory cells. Studies using a gadolinium-based elastin-specific MR contrast agent (Gd-ESMA) have allowed investigation of elastin deposition and quantification of elastin remodelling within the infarcted areas in a murine model. Additionally, Gd-ESMA enhancement allowed quantification of scar size, with higher contrast-to-noise ratio and longer retention time compared with non-specific gadolinium-based contrast agents [164, 251].

The presence of inflammatory cells and the abundance of elastin/tropoelastin within the myocardial scar makes both promising imaging biomarkers for molecular MRI. Both measurements offer a unique opportunity to detect both the temporal and spatial evolution of the inflammatory response and associated ECM remodelling (elastin) post-MI, and to correlate these biological processes with their effects on cardiac function. This approach may potentially allow a more accurate association between early or persistent inflammation and diffuse myocardial remodelling at the molecular level. It may also serve as a new biomarker for predicting outcome, monitoring treatment response or evaluation of novel cardioprotective therapies. In this study, we sought to explore the merits of multinuclear $^{1}H/^{19}F$ MRI in concert with a ^{19}F nanoparticles and Gd-ESMA for the sequential assessment and quantification of cardiac inflammation and elastin remodelling in a murine model of MI.

6.3 - Aims

Optimal healing of the myocardium following MI requires a suitable degree of inflammation and its timely resolution, together with a dynamic deposition and degradation and of ECM proteins. In this study, we explored the merits of

multinuclear $^{1}H/^{19}F$ MRI for the simultaneous assessment of cardiac inflammation and elastin remodelling in a mouse model of MI.

6.4 - Methods

6.4.1 - Animal model

MI was induced in 10 weeks old, C57BL/6J female mice (N=71) (Charles River, United Kingdom) by permanent occlusion of the left anterior descending coronary artery (LAD). SHAM-operated animals underwent the same surgical procedure apart from occlusion of the LAD. Surgery details have been described in **Chapter 5, section 1.3.2.**

6.4.2 - 3T Magnetic resonance imaging and spectroscopy

In vivo cardiac scans were performed using a 3T Philips Achieva MR scanner (Philips Healthcare, Best, The Netherlands) equipped with a clinical gradient system (30 mT m^{-1}, 200 mT m^{-1}). Mice (N=8 per time point) were imaged at 3, 7, 14 and 21 days post-MI. SHAM-operated mice (N=6 animals per time point) were imaged at the same time points and were used as controls (**Fig.6.1A**). Fifteen mice were imaged longitudinally at 7 and 21 days post-MI (**Fig.6.1B**). Animals were placed in a prone position on a $^{19}F/^{1}H$ surface coil (Rapid Biomedical, Würzburg, Germany; diameter=23 mm and 33 mm). Anaesthesia was induced with 5% and maintained with 1.5-2% isoflurane in medical oxygen during the MRI scan, and the body temperature was measured with a rectal temperature probe and maintained at 36±1ºC using a water-based heating system. The ECG was monitored with two metallic needles placed subcutaneously in the region of the chest. ^{1}H and ^{19}F cardiac ECG-triggered MR

images were acquired 48 hours after intravenous (i.v.) injection of 400 μL of ^{19}F-PFCs (as previously described [97]) and 0.5 mmol/kg of a gadolinium-based MRI contrast agent that targets elastin and tropoelastin, Gd-ESMA (Lantheus Medical Imaging, North Billerica, MA) administered 1h prior to the MRI scan. At the end of the scans, the mice were culled and the heart was excised for histological and NMR studies.

After a 3-dimensional (3D) gradient echo scout scan, 2-dimensional (2D) cine short-axis images, covering the entire left-ventricle (LV), were acquired to analyse functional and volumetric parameters. Imaging parameters included field-of-view (FOV)=35x35x12 mm^3, acquired in-plane resolution=0.3x0.3x1 mm^3, slices=12, repetition time (TR) / echo time (TE)=7.8/16.0 ms, flip angle=20°. Subsequently, a 2D Look-Locker scan planned perpendicular to the long-axis of the LV was used to determine the optimal inversion time (TI) for nulling of the healthy myocardium. 3D late-gadolinium-enhancement (LGE) gradient echo (GRE) images were acquired in the short-axis view 60-80 minutes after Gd-ESMA injection for the visualization of contrast uptake within the infarcted region. Imaging parameters included FOV=35x35x12mm^3, acquired in-plane resolution=0.3x0.3x1 mm^3, slices=12, TR/TE=6.4/2.6 ms, 5 heart beats between subsequent IR pulses, and flip angle=25°. T_1-mapping was performed using a 2D Modified Look-Locker inversion recovery (MOLLI) sequence. The inversion pulse was followed by eight segmented readouts, each spaced one RR-interval apart, for eight individual images resulting in TI's ranging from 10 ms to 2000 ms. To allow full magnetization recovery, 12 pauses/heart beats were performed before the next inversion pulse. Acquisition parameters included FOV=35x35x1.5 mm^3, acquired in-plane resolution=0.3x0.3 mm^2, slices=1,

TR/TE=7.5/3.1 ms, flip angle=16°. For the visualization of inflammatory cells, a 3D turbo-spin echo ^{19}F scan was acquired with a FOV=35x35x12 mm^3, acquired in plane resolution=1x1x2 mm^3, slices=12, TR/TE=4beats/8.9ms, TSE factor=5, offset frequency=10200 Hz (BW=6103 Hz). A saturation slice was used to suppress the liver signal. To enable SNR calculation, a noise-scan was acquired with the same imaging parameters but without any RF pulses performed. A T_2-weighted (T_2W) sequence was used to analyse oedema within the heart at 3 and 7 days post-MI, with the following parameters: FOV=35x35x1.5 mm^3, acquired in-plane resolution=0.3x0.3 mm^2, slices=3, TR/TE=126/18, flip angle=30°. To verify the ^{19}F *in vivo* results, *ex vivo imaging* experiments on the excised heart were also performed.

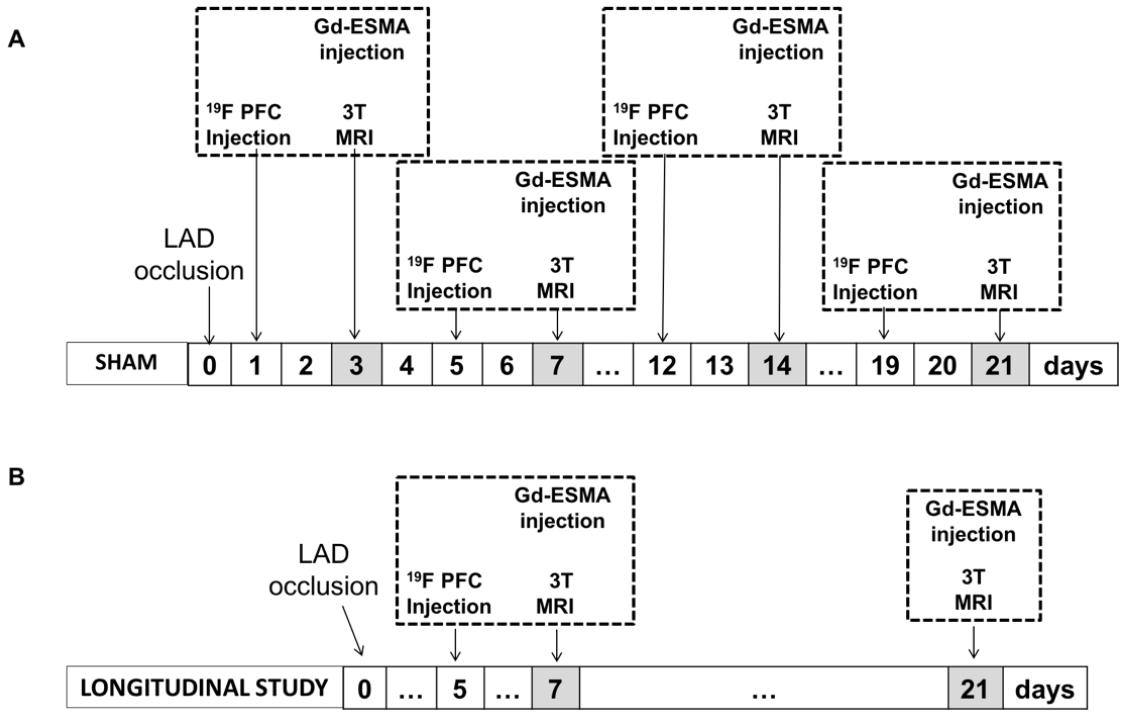

Figure 6.1. Experimental study design. Myocardial infarction was induced in C57Bl6 female mice after permanent occlusion of the left anterior descending coronary artery (LAD). 3T MRI scans were performed after intravenous injection of ^{19}F-PFCs and Gd-ESMA, 48 and 1 hour before imaging sessions, respectively. (A) Mice (N=8 per group/ time point) were imaged at 3, 7, 14 and 21 days post-MI. SHAM-operated mice (N=6 per group/ time point) were imaged at the same time points and were used as controls. At the end of the scans, mice were culled and the heart was extracted for histology and NMR (N=4/group and 3 SHAM-operated animals / time point for each technique) (B) 15 mice were imaged longitudinally at 7 and 21 days post-MI. MRI: magnetic resonance imaging; ^{19}F PFC: ^{19}F perfluoro-15-crown-ether emulsions; Gd-ESMA: elastin/tropoelastin specific MR contrast agent.

6.4.3 - Magnetic resonance image analysis

Ejection fraction (EF, %), left ventricular end-diastolic volume (LVEDV, µl) and left-ventricular mass (LV, mg) were calculated from the cine images, using an automated segmentation software (ClinicalVolumes, King's College London, www.clinicalvolumes.com) [250]. Total infarct size was calculated by adding the LGE measured on consecutive slices after the administration of Gd-ESMA. The sum of total infarcted area was multiplied by the slice thickness to generate a volume (mm^3) and was then divided by the total LV myocardium volume and expressed as a percentage. T_1 relaxation times (R_1) were calculated by manually segmenting T_1 map regions corresponding to the LGE using OsiriX (Osirix Foundation, Geneva, Switzerland). For ^{19}F measurements, regions of interest were defined as areas of enhancement seen on the ^{19}F images, which co-localized with areas of infarct as seen on the LGE images. For these areas, ^{19}F signal was calculated using the following equation: $^{19}F\ signal = \frac{\sum SNR}{scar\ volume}$, where SNR is the sum of the signal of the infarcted area divided by the standard deviation of the noise in each slice, and scar volume was calculated from the sum of the LGE area of each slice multiplied by the MRI slice thickness [238].

6.4.4 - ^{19}F Nuclear Magnetic Resonance Spectroscopy at 9.4T

Nuclear magnetic resonance (NMR) spectroscopy was used to quantify the uptake of ^{19}F PFC in the remote and infarcted myocardium, separately, at different time points following LAD ligation. A subgroup of mice injected with PFC and scanned at 3T were culled and the hearts were collected (MI: N=4 and SHAM: N=3; each per time point). Remote and infarcted regions were separated, weighed and frozen at -20ºC prior to NMR analysis. NMR spectra of the ^{19}F PFCs

were recorded at room temperature using a Bruker Avance III 9.4T scanner (^{1}H 400 MHz; ^{19}F 375.8 MHz) and a 15 mm diameter double-tuned (^{31}P/^{1}H) volumetric micro-imaging coil. The water resonance was used to shim the sample and the ^{1}H coil was then re-tuned to the ^{19}F frequency. Both remote and infarcted areas were placed in NMR tubes (Fisher Scientific, Leicestershire, UK) with a silicone support to position the sample within the isocentre of the coil. A sealed external reference capillary of 100% TFA solution (δTFA=-76.6 ppm as identified in the literature, and reported relative to $CFCl_3$) was placed adjacent to the heart. The ^{19}F NMR chemical shift of the PFC peak was -12.5 ppm relative to the reference capillary. A 90^{o} pulse (30 μs hard pulse) was used together with 64 signal averages, total experiment duration=4.78 minutes, time domain size=131k data points, pre-scan delay=1s, acquisition time=3.5s resulting in a total repetition time of TR=4.5s per scan and spectral bandwidth=18797 Hz. Data were processed with an exponential line broadening factor (20 Hz), followed by Fourier transformation, zero and first order phase correction and automatic baseline correction. Peaks corresponding to the TFA reference and the PFC were integrated using Topspin 2.1 software (Bruker Biospin GmbH, Rheinstetten Germany) and normalized to the reference capillary. The number of moles of ^{19}F were calculated using the equation: $[PFC] = \frac{N_{TFA} \times I_{PFC} \times [TFA]}{N_{PFC} \times I_{TFA} \times g_{tissue}}$ where [PFC] is the concentration/g tissue (wet weight)), N_{TFA} is the number of ^{19}F nuclei giving rise to the TFA signal, N_{PFC} is the number of ^{19}F nuclei giving rise to the PFC signal, I_{PFC} is the peak integral of the PFC peak, I_{TFA} is the peak integral of the TFA peak (I_{TFA} = 1, normalised), [TFA] is the number of moles of TFA.

6.4.5 - Histology

Following the MRI scans, anesthetized mice were culled by neck dislocation and hearts were collected for *ex vivo* analysis (N=4 MI mice per time point, and N=3 SHAM-operated animals per time point). Hearts were harvested, the atriums were removed and the ventricles were washed in saline solution followed by immersion in 10% formaldehyde solution for 24 hours at room temperature. Hearts were then dehydrated, paraffin-embedded and transversely sectioned (5 μm thick). Masson's trichrome (Sigma-Aldrich, Dorset, United Kingdom) staining was performed to assess cardiac morphology and collagen content, respectively.

Immunohistochemistry (IHC) was used to quantify the amount of tropoelastin and macrophages in the myocardium. Tropoelastin was detected with an anti-mouse rabbit polyclonal antibody (21600, Abcam; dilution 1:100) using an avidin-biotin-peroxidase method (Vector® SG Peroxidase substrate; Vector Laboratories, Burlingame, CA). A monoclonal rat anti-mouse antibody (550292, BD Pharmingen) (CD107b; MAC-3; dilution 1:100) was used for macrophage detection. The antibody was revealed with streptavidin-peroxidase (Dako, Ely, UK) (ABC kit, 1:100). Digital images were analysed using ImageJ (National Institute of Health, Bethesda, MD). Tropoelastin and MAC-3 were quantified and expressed as percentage of the infarcted myocardium using ImageJ, and were manually segmented and compared with the total area of infarction for each histology slice calculated from Masson's trichrome staining.

6.4.6 - Statistical analysis

GraphPad Prism 5.00 (GraphPad Software, Inc., La Jolla, California, USA) was used for statistical analysis. Normality was assessed by histogram, Q-

Q plots, and the Shapiro-Wilk test, and equal variances was assessed with the Bartlet's test and Levene's test. For normally distributed variables with equal variances, an ANOVA test followed by Bonferroni post hoc analysis for multiple group comparisons (e.g. R_1 of infarct) was performed. For normally distributed variables with unequal variances a Welch test followed by a Games-Howell post hoc test was used for multiple group comparisons (e.g. LVEDV, LV mass, ^{19}F MRI, R_1 of SHAM). For non- normally distributed variables, a Kruskal-Wallis test was used for multiple group comparisons (e.g. data from a specific time-point and/or data obtained at mouse termination) following by Dunn's post-hoc test (e.g. EF, ^{19}F NMR, IHC, R_1 remote). Correlations were assessed using Pearson correlation. Receiver operating characteristic (ROC) curve analysis was performed to identify the cut-off point of imaging biomarkers to predict the evolution of functional cardiac parameters. *P<0.05* was considered statistically significant. Data are presented as median ± interquartile range.

6.5 - Results

6.5.1 - Assessment of Cardiac Function by 3T MRI

Representative cardiac short-axis cine images acquired at different time points post-MI are shown in **Figure 6.2A**. Visual enlargement of the left ventricle and thinning of the ventricular wall, at the site of the infarction, was observed post-MI and became more evident at day 21. The left-ventricular end-diastolic volume (LVEDV) increased significantly at 14 and 21 days post MI compared to SHAM-operated animals (LVEDV[µL]=14 days: 96.59 [IQR, 71.34-109.9] *P<0.01*; LVEDV[µL]=21 days: 96.27 [IQR, 81.88-130.90], *P<0.01* vs LVEDV[µL]=SHAM: 46.73 [IQR, 43.26-57.56]). LVEDV was also significantly

increased at 14 and 21 days compared with 3 days post-MI (LVEDV[µL]=3 days: 65.02 [IQR, 53.18-69.11], *P<0.05*) (**Fig.6.2B**)]. Ejection fraction (EF) was significantly reduced at 7 and 21 days after MI compared to SHAM-operated animals (EF[%]=7 days: 22.64 [IQR, 17.70-43.30], *P<0.05*; EF[%]=21 days: 21.79 [IQR, 14.69-28.84], *P<0.01*, EF[%]=SHAM: 53.64 [IQR, 53.26-59.80]) (**Fig.6.2C**). Left-ventricular (LV) mass increased significantly over time after MI compared with SHAM-operated animals (LV[mg]=3 days: 84.02 [IQR, 77.87-90.50], *P<0.05*; LV[mg]=7 days: 85.72 [IQR, 76.29-123.9], *P<0.05*; LV[mg]=14 days: 106.20 [IQR, 88.34-123.90], *P<0.05*; LV[mg]=21 days: 111.4 [IQR, 106.0-124.0], *P<0.001*; LV[mg]=SHAM: 63.77 [IQR, 51.24-68.21]), and from 3 to 21 days post-MI (*P<0.01*) (**Fig.6.2D**). These results are consistent with previous studies in this animal model.

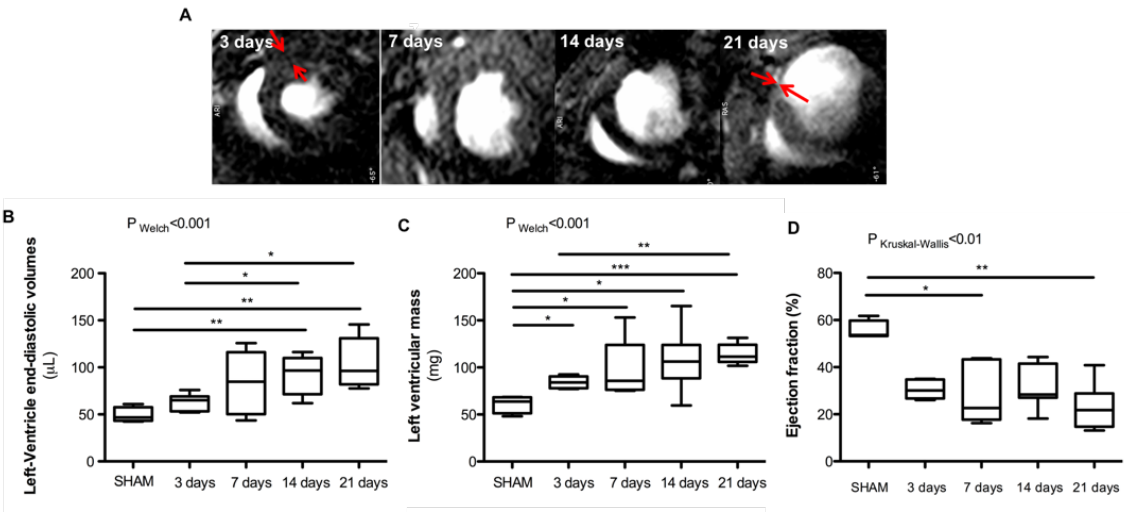

Figure 6.2. Functional and volumetric parameters of MI animals at 3,7,14 and 21 days and SHAM operated mice. (A) Representative anatomical short-axis images of the heart. (B) The left ventricle dilates from acute to late stages of MI. (C) An increment in Left ventricular mass and (D) a decrease in Ejection fraction were observed over time. N=8 MI animals per time-point, N=4 SHAM-operated animals per time-point. MI: myocardial infarction. **P<0.05, **P<0.01, ***P<0.001.*

6.5.2 - Assessment of the inflammatory response with ^{19}F PFCs: imaging during post-MI remodelling and histological findings

Myocardial remodelling post-MI is associated with an acute inflammatory response. Acquisition of morphologically matching proton (^{1}H) and fluorine (^{19}F) images enables anatomical localisation of the PFCs. Merged images confirmed the co-localization of the ^{19}F PFC within the infarcted area at both 3 and 7 days, in agreement with the inflammatory response described for this animal model [9] (**Fig.6.3A**).

Quantitative *in vivo* ^{19}F MRI signal intensity measurements are shown in **Figure 6.3B**. A significant increase of ^{19}F signal within the infarcted area was detected at 3, 7 and 14 days post-MI compared with SHAM-operated animals (^{19}F MRI=SHAM: 0.19 [IQR, 0.13-0.20] vs 3 days: 0.44 [IQR, 0.39-0.67], *P<0.05*; SHAM vs 7 days: 1.27 [IQR, 0.84-1.58], *P<0.01*; SHAM vs 14 days: 0.30 [IQR, 0.23-0.34], *P<0.05*). A peak was observed at day 7 post-MI which was statistically significant compared with all other time-points (^{19}F MRI=7 days: vs 3 days, *P<0.05*; vs 14 days, *P<0.01*; vs 21 days: 0.18 [IQR, 0.15-0.28], *P<0.01*). At 21 days post-MI the ^{19}F signal was negligible and significantly lower compared with 3 and 7 days post-MI consistent with the resolution of the inflammatory response (^{19}F MRI: 3 vs 21 days, *P<0.05;* 7 vs 21 days, *P<0.01*). ^{19}F signal was also detected at the site where surgical thoracotomy was performed, in the liver and lymph nodes, as these are major sites of macrophage clearance. No background signal from other tissues was observed.

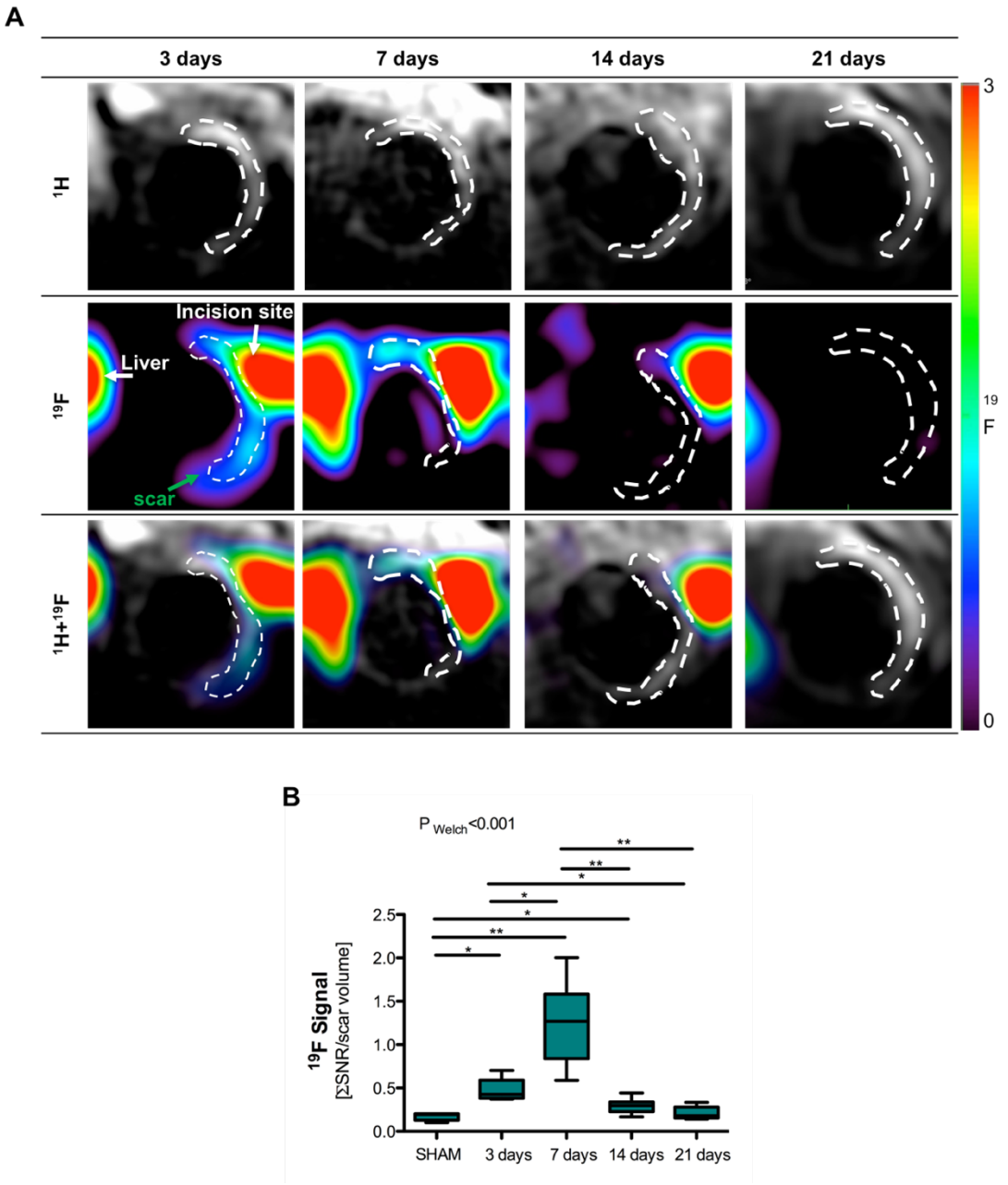

Figure 6.3. Assessment of inflammatory response after induced myocardial infarction in mice using 3T MRI and ^{19}F perfluorocarbon nanoparticles. (A) Representative short-axis views of ^{1}H images (top), ^{19}F images (middle)and with the matching ^{1}H+^{19}F images (bottom) from the heart 3,7,14 and 21 days after MI; (B) *In vivo* ^{19}F MRI signal quantification. N=8 per time-point, N=6 SHAM-operated animals.

To verify the *in vivo* results, *ex vivo* ^{1}H/^{19}F MRI experiments of the excised hearts were performed. ^{1}H/^{19}F overlay images confirmed that PFC accumulation was restricted to the infarcted region and that no signal was detected in the remote myocardium (**Fig.6.4A**). To further quantitate the evolution of the ^{19}F

signal, infarcted and remote areas were separated for *ex vivo* NMR spectroscopy. The NMR spectra corroborated the *in vivo* MRI findings, where infarcted regions showed high ^{19}F PFC signal that was absent in the remote myocardium (**Fig.6.4B&C**). NMR spectra quantification showed a peak of ^{19}F concentration in the infarcted regions at 7 days that was statistically higher compared with day 21 (^{19}F NMR[159]=7 days: 0.12 [IQR, 0.075-0.18] vs 21 days= 0.0063 [IQR, 0.0042-0.020], *P<0.05*). At 7 days post-MI, infarcted and remote myocardium from operated animals and healthy hearts from SHAM-operated animals could be distinguished based on the ^{19}F signal (^{19}F NMR[159]=infarct: 0.12 [IQR, 0.075-0.18] vs remote: 0.026 [IQR, 0.015-0.057] vs SHAM: 0.012 [IQR, 0.0042-0.044], *P<0.05*). At 21 days post-MI, the signal in the remote myocardium from MI-operated animals and myocardium from SHAM-operated animals was statistically different. In SHAM-operated animals injected with PFCE, no ^{19}F signal was detected in the heart. Furthermore, a correlation was observed between *in vivo* MRI measurements and *ex vivo* NMR ^{19}F signal measurements (**Figure 6.5**).

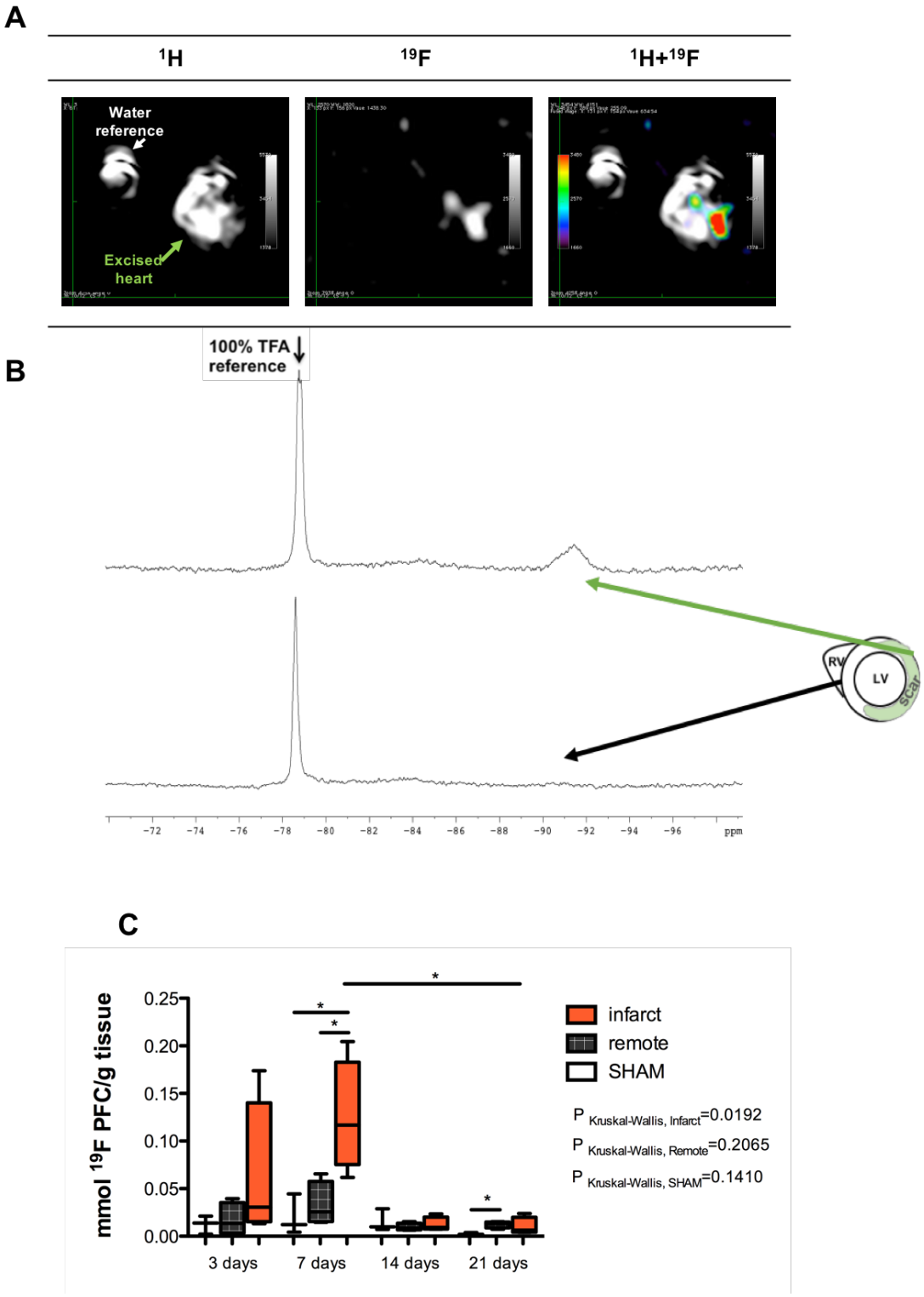

Figure 6.4. Analysis of ^{19}F PFC uptake in the heart. (A) *Ex vivo* MRI of the heart and water tube (as reference). ^{19}F signal is detected in a specific region within the heart. (B) *Ex vivo* NMR spectroscopy of the heart after separating in infarcted and remote, showed that a peak is detected in the infarcted myocardium but not in the remote tissue. (C) *Ex vivo* ^{19}F NMR signal quantification. N=4 per time-point, N=3 SHAM-operated animals.

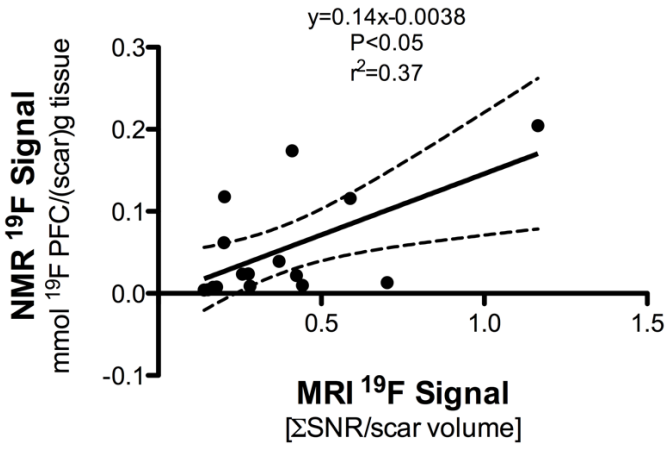

Figure 6.5. Correlation between *in vivo* ^{19}F MRI signal and *ex vivo* NMR ^{19}F signal quantification. Pearson correlation (N=16, r=0.61, *P<0.05*).

MAC-3 IHC for identification of myocardial tissue macrophages is shown in **Figure 6.6A**. IHC showed recruitment of macrophages during the early stages following MI. Macrophages were present within the infarcted area, at 3 and 7 days post-MI, but were absent in the remote myocardium as seen with the ^{19}F PFC imaging findings. The amount of MAC-3 positive macrophages was significantly higher at 3 and 7 days compared with SHAM-operated animals (IHC MAC-3[%]=SHAM: 0.003 [IQR, 0.002-0.004] vs 3 days: 2.12 [IQR, 1.88-2.63], *P<0.05*; and SHAM vs 7 days: 3.65 [IQR, 2.74-4.09], P<*0.01*) and macrophage content was significantly higher at 7 days compared to 21 days post-MI (IHC MAC-3=21 days: 0.13 [IQR, 0.041-0.23], *P<0.05*) (**Fig.6.6B**). There was a significant correlation between the *in vivo* ^{19}F MRI signal and macrophage content as evaluated by IHC (r= 0.84, *P<0.001*, **Fig.6.7**).

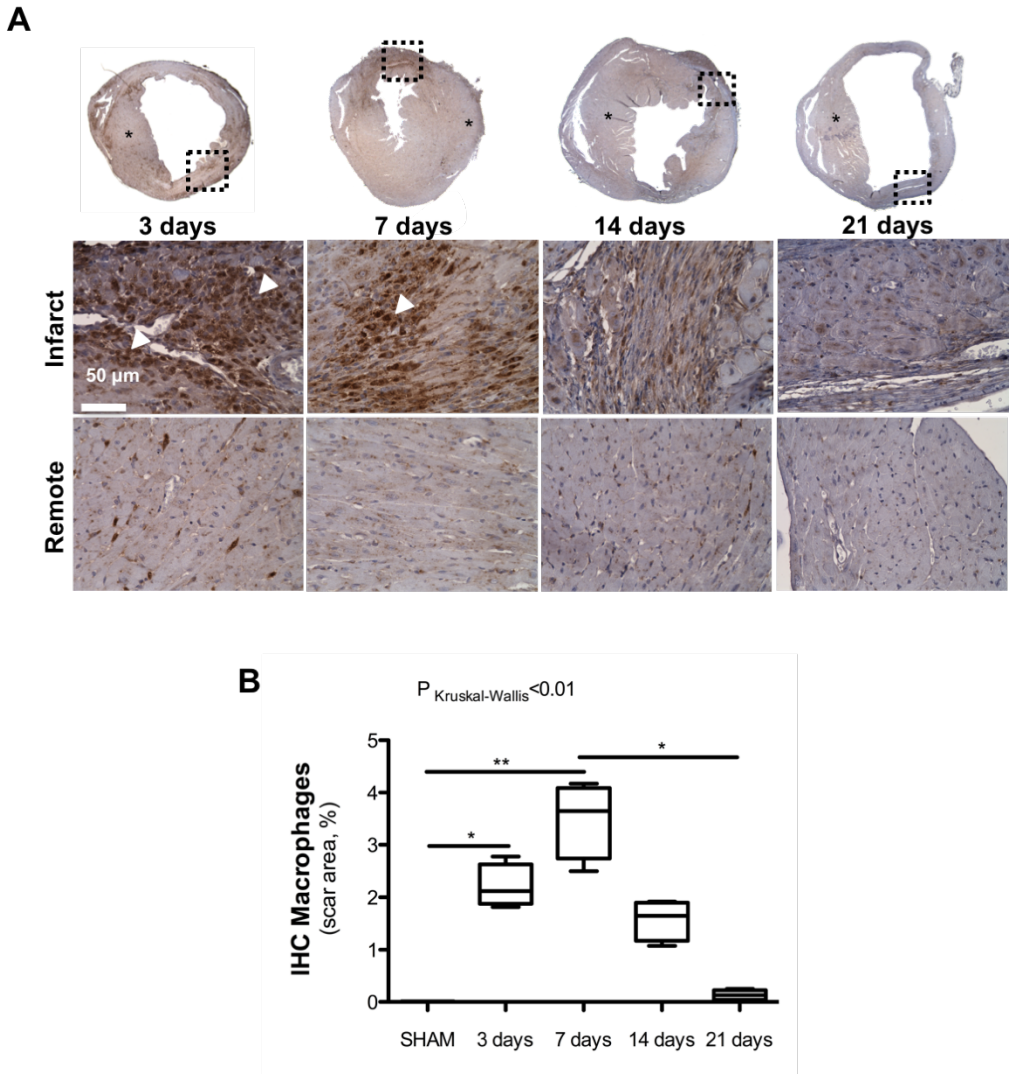

Figure 6.6. Macrophage immunohistochemistry (IHC) of the hearts sections at day 3, 7, 14 and 21 days after MI. (A) Macrophages were identified as MAC-3 positive (brown). (B) IHC quantification shown a significantly decrease between 7 and 21 days after infarct. N=4 per time-point. Scale bar, 50 µm.

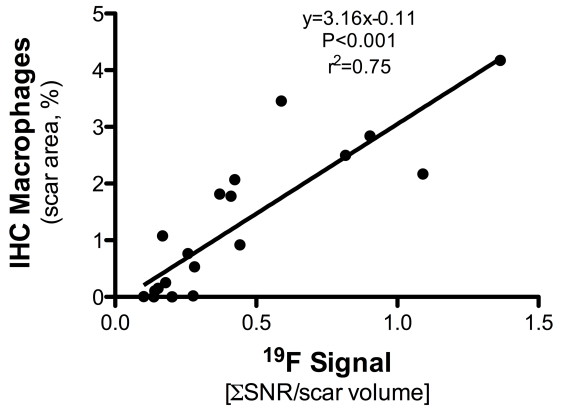

Figure 6.7. Correlation between *ex vivo* macrophage immunohistochemistry (IHC) and *in vivo* ^{19}F MRI signal. Pearson correlation (N=16, r= 0.84*, P<0.0001*).

6.5.3 - Optimization of Gd-ESMA protocol

The kinetics of Gd-ESMA has been studied by Wildgruber and colleagues at 1.5T [164]. The authors showed that the SNR reached its maximum value 1 hour after Gd-ESMA i.v. injection, allowing the distinction between scar, normal myocardium and blood pool in a mouse model of MI [164]. Moreover, Protti and colleagues [251] have shown that 2 hours after Gd-ESMA injection, the contrast is confined to the scar area, without any visible signal in neither remote nor blood pool at 7T.

Here, the effect of i.v. injection of Gd-ESMA was studied using 3T MRI. Two hours after i.v. injection the contrast agent was detected within the scar area, however, it was also observed in the blood pool, making the distinction and segmentation of the scar challenging (**Fig.6.8A**). For this reason, after i.v. injection of Gd-ESMA, the animals were allowed to recover for 45 minutes (to facilitate blood clearance) and LGE images were acquired between 60 and 90 minutes after contrast administration. **Figure 6.8B** shows the effect of this protocol on the LGE images; scar and remote myocardium can be distinguished, and no contrast was seen on the blood pool.

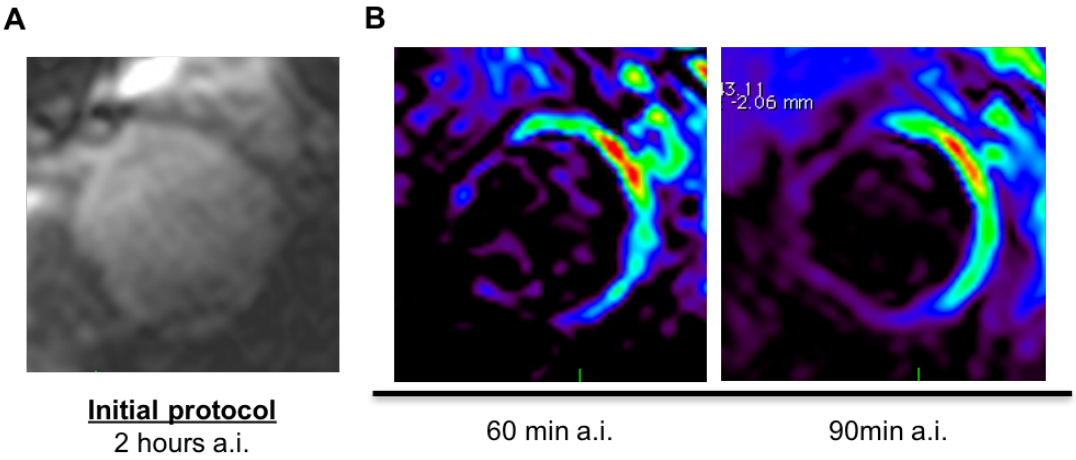

Figure 6.8. Effect of Gd-ESMA intravenous injection on the late-gadolinium enhancement images at 3T MRI. (A) Protocol 1: Immediately after injection of the contrast, the imaging session commenced. Higher amounts of contrast remained in the blood pool and remote myocardium, making the segmentation of the scar challenging. (B) Protocol 2: Allowing the animal to recover for 45 minutes after intravenous injection of Gd-ESMA facilitated delineation of the infarcted myocardium from the blood pool and remote myocardium. a.i. after injection.

6.5.4 - Oedema after myocardial infarction

Early after MI, fluid accumulation can be detected in the interstitial space. Here, oedema was assessed using T_2W sequences at 3 and 7 days post-MI. Myocardial oedema was evident at day 3, and absent at day 7 (**Fig.6.9 top**). To confirm the presence of infarct in this animal, Gd-ESMA was injected and scar tissue appeared enhanced at both 3 and 7 days post-MI (**Fig.6.9 middle and bottom images**).

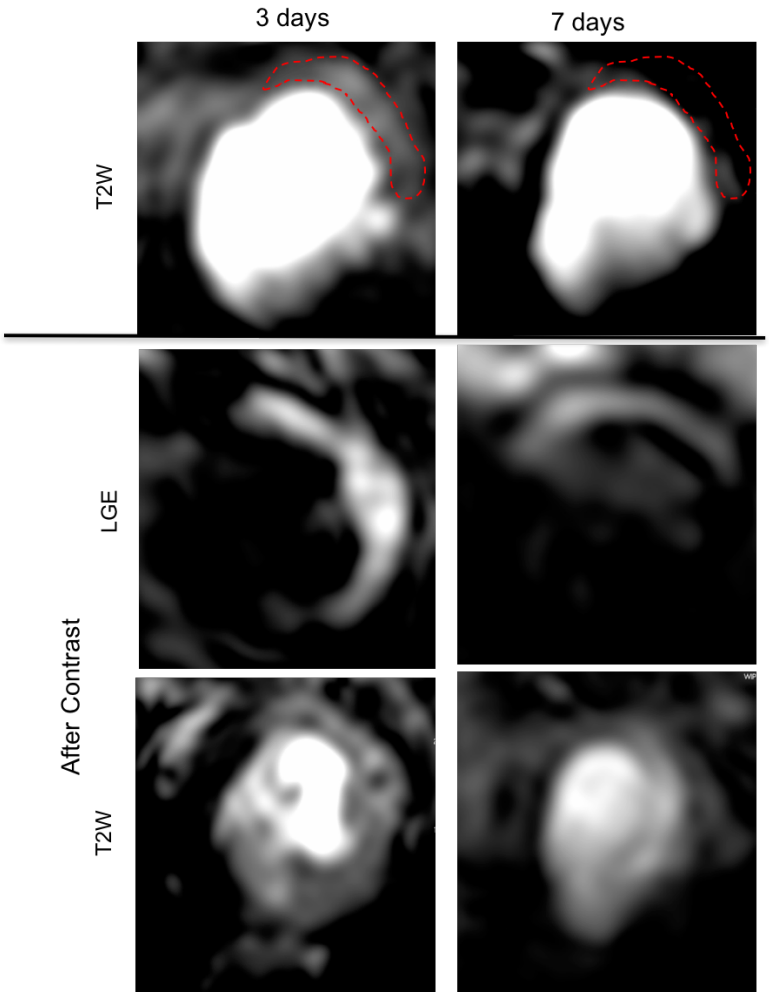

Figure 6.9. Assessment of myocardial oedema in mice with myocardial infarction. T_2-weighted images showing high signal intensity in the lateral wall (top row images); Contrast-enhanced images (late gadolinium enhancement) showing high signal intensity in the infarcted areas (middle row images); and T_2-weighted images after intravenous injection of contrast (lower row images).

6.5.5 - Scar assessment

One hour post-Gd-ESMA injection, infarcted areas showed enhancement at all time-points (3-21 days), allowing quantification of infarct size **(Fig. 6.10A**). Trichrome staining was also performed and used to quantify infarct size *ex vivo*. There was a strong linear correlation between infarct size measured by *in vivo* MRI and histology (r=0.90, *P<0.001*) (**Fig.6.10B**).

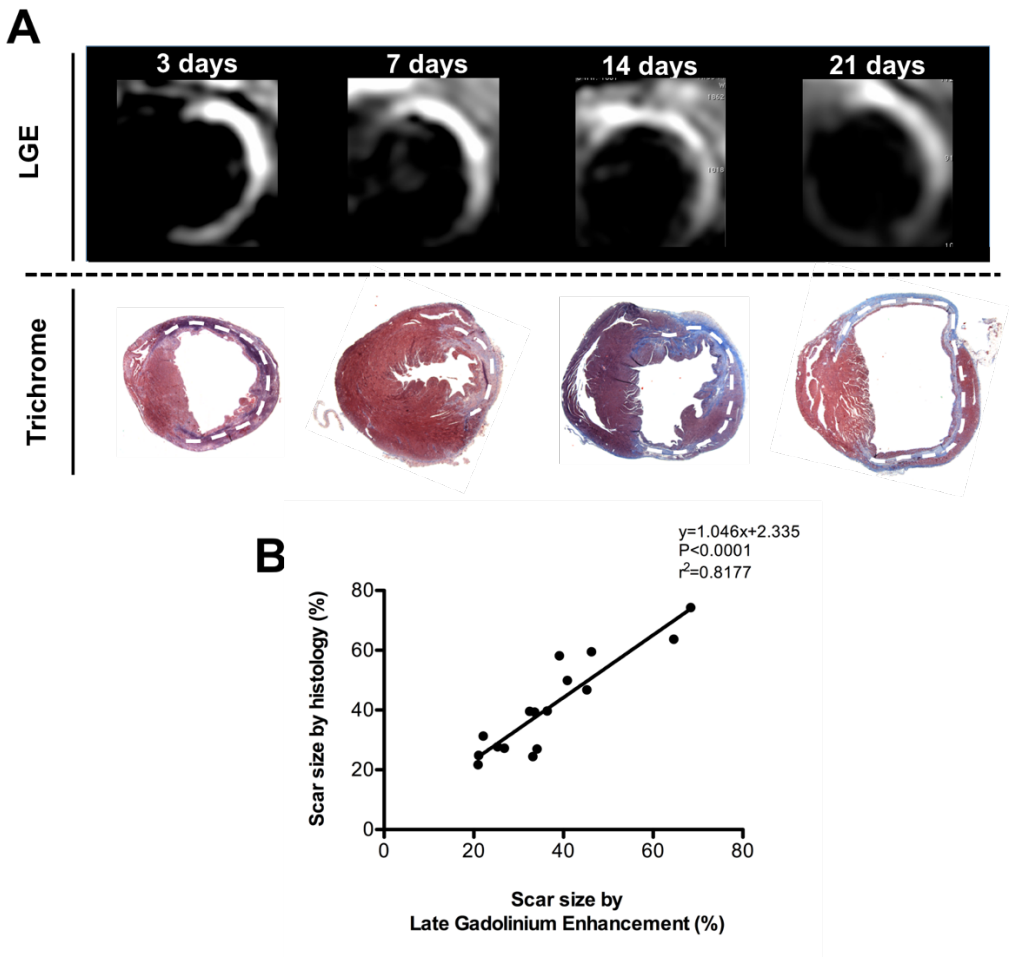

Figure 6.10. Assessment of infarct size *in vivo* by LGE-MRI and *ex vivo* histology using Trichrome staining. (A) *In vivo* delayed-enhancement magnetic resonance imaging (LGE) after intravenous injection of Gd-ESMA (top) and *ex vivo* Trichrome staining (bottom) showing delineation of scar area at 3,7,14 and 21 days post-MI. (B) Good correlation between *in vivo* and *ex vivo* assessment of scar size was observed between MRI and histology. Pearson correlation (N=16, r=0.90, *P<0.0001*).

The high signal intensity on LGE images at 3 days post-MI has been associated with oedema; not reflecting deposition of elastin/tropoelastin but reflecting instead increase of the extracellular volume due to cardiomyocyte death and cell swelling. For this reason, the 3 days time point has not been considered for the R_1 map and histology analysis.

6.5.6 - Assessment of extracellular matrix (ECM) remodelling post-MI using Gd-ESMA

ECM remodelling post-MI was evaluated using Gd-ESMA, a contrast agent that binds specifically to both cross-linked mature elastin and its precursor tropoelastin (immature non-crosslinked elastin). *In vivo* quantification of Gd-ESMA uptake was performed with T_1 mapping. **Figure 6.11A** shows the relaxation rate (R_1) maps after Gd-ESMA administration in animals with MI at 7, 14 and 21 days. R_1 maps showed uptake of Gd-ESMA in the infarcted area at all time points while no enhancement was observed in the remote myocardium. Quantification of R_1 demonstrated that the infarcted myocardium exhibited significantly higher R_1 values compared to remote myocardium at 7, 14, and 21 days and also when compared to SHAM-operated animals (infarct-remote *P<0.01*, infarct-SHAM *P<0.001*, **Fig.6.11B**). R_1 values were also significantly higher within the infarct area between 7 and 21 days ($R_1[s^{-1}]$=7 days: 2.3 [IQR, 2.12-2.5] vs 21 days: 2.83 [IQR, 2.69-3.30], *P<0.01*).

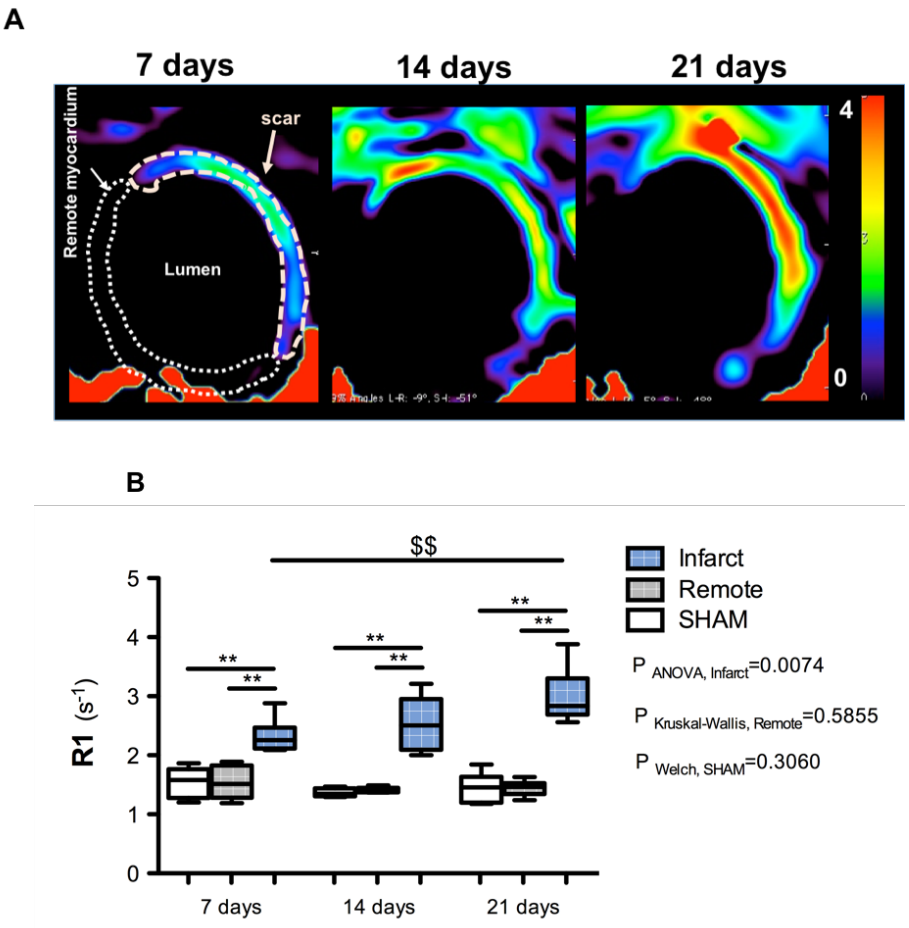

Figure 6.11. *In vivo* imaging of extracellular matrix (ECM) remodelling after myocardial infarction (MI) with a gadolinium-based elastin/tropoelastin-specific contrast agent. (A) Representative short-axis images of relaxation rate (R_1) maps at 7,14 and 21 days post-MI using 3T MRI. (B) Quantification of R_1 values in the infarct, remote myocardium (N=8 per time-point) and on the SHAM-operated animals (N=6 per time-point). R_1 values increased significantly from 7 to 21 days post-MI suggesting ECM remodelling.

In order to analyse the deposition of elastin fibres in the heart after MI, Elastica van Gieson staining was performed. Mature fibres could be visualized; however, quantification was challenging (**Fig.6.12**).

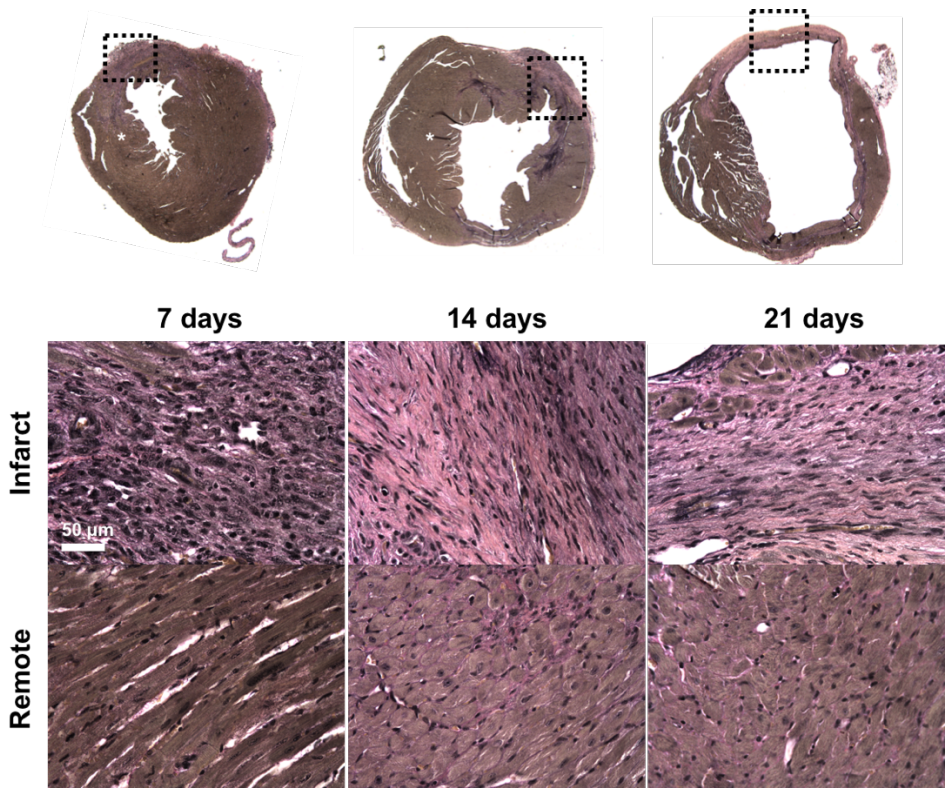

Figure 6.12. Elastica van Gieson staining of infarct and remote myocardium at 3,7,14 and 21 days post-MI. Elastin fibres were identified as black fibre network, specially at 14 and 21 days. Scale bar, 50 µm.

For that reason, quantification of tropoelastin was performed with IHC (**Fig.6.13A**). Tropoelastin IHC revealed a dense fibre network within the infarcted myocardium at 14 and 21 days post-MI but not in the remote myocardium. Tropoelastin deposition was significantly higher at 21 days compared to 7 days post-MI ($IHC_{Tropoelastin}$[%]= 21 days: 3.25 [IQR, 2.87-3.45] vs 7 days: 1.92 [IQR, 1.62-2.31, *P<0.01*). There was a statistically significant correlation between the myocardial R_1 values measured *in vivo* after administration of Gd-ESMA and tropoelastin IHC (r= 0.76, *P<0.01*, **Fig.6.13B)**.

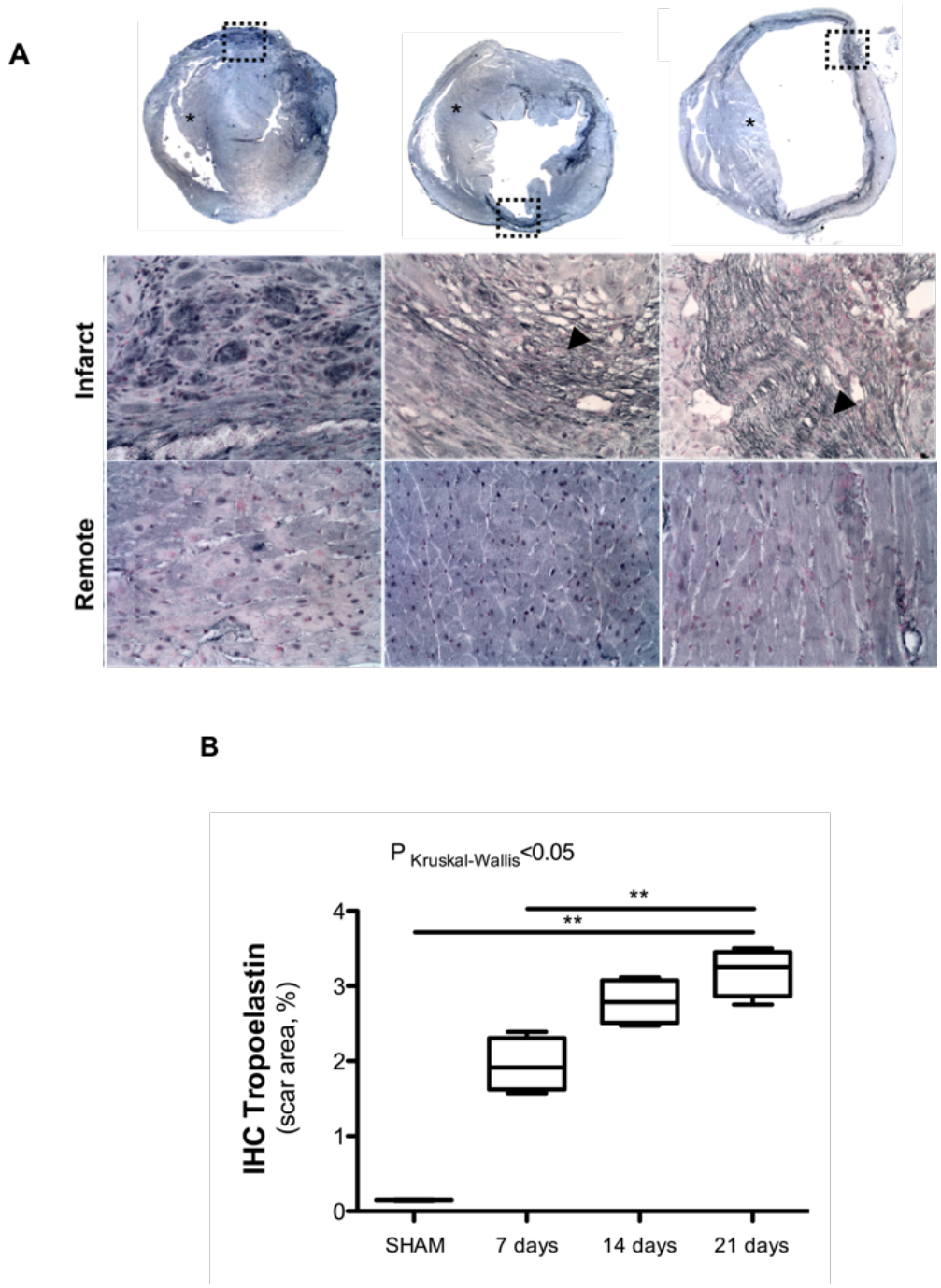

Figure 6.13. Tropoelastin immunohistochemistry (IHC) of heart sections at day 7, 14 and 21 days after MI. (A) Tropoelastin fibres were identified as black fine fibre network (arrow). (B) IHC quantification, showing a significantly increment in tropoelastin fibres between 7 and 21 days post-MI. N=4 per time-point. Scale bar, 50 μm.

There was also statistically significant correlation between the myocardial R1 values measured in vivo after administration of Gd-ESMA and tropoelastin IHC (r=0.90, *P<0.001*, Fig.14).

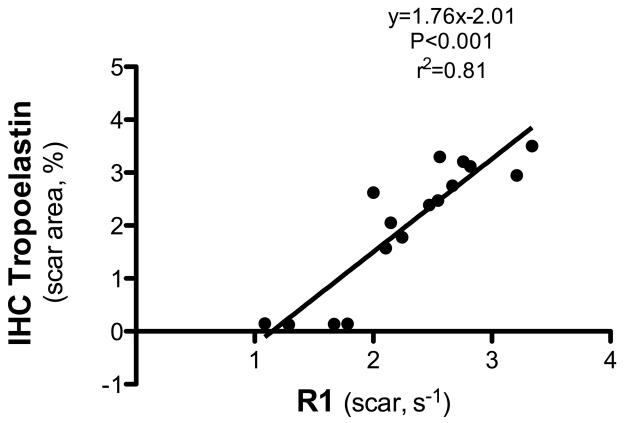

Figure 6.14. Correlation between *ex vivo* measurements of tropoelastin immunohistochemistry (IHC) and R_1 values of the scar. Pearson correlation (N=12, r=0.90, *P<0.001*).

6.5.7 - ^{19}F vs R_1 can be used to predict cardiac output: longitudinal study

Remodelling post-MI is a dynamic and complex process where several factors can influence cardiac outcome (e.g. degree and duration of inflammation, infarct size, and ECM deposition). To understand the potential prognostic value of the *in vivo* ^{19}F and Gd-ESMA MRI measurements, a longitudinal proof-of-principle study was performed. Fifteen animals were scanned twice at days 7 and 21 post-MI. ^{19}F MRI was performed at 7 days (48 hours after 400 μL ^{19}F PFCs were injected at day 5) to quantify the severity of inflammation. Day 7 was chosen as it the inflammatory response was strongest at this time as shown in the pilot studies described above. An elastin scan (1 hour post Gd-ESMA injection) was performed at day 7 and 21 post-MI. No correlation was found between ^{19}F at day 7 post-MI and Gd-ESMA uptake at day 7 (**Fig.6.15A**) and at

day 21 post-MI (**Fig.6.15B**), suggesting that these biological processes are independent/ decoupled from each other.

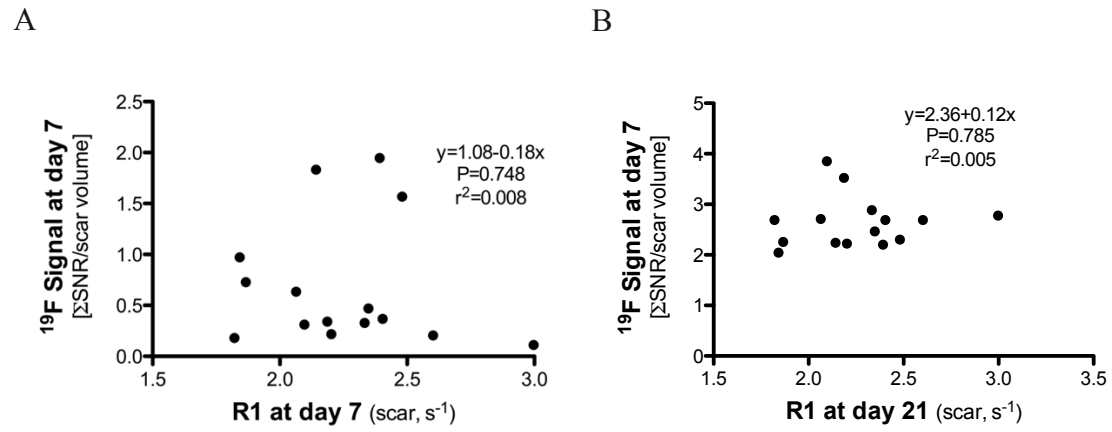

Figure 6.15. There is no correlation between ^{19}F signal at day 7 and (A) Gd-ESMA uptake 7 days after MI and (B) Gd-ESMA uptake in the infarcted myocardium at day 21 post-MI.

In order to analyse the predictive value of each contrast agent the EDV at day 21 was used as an outcome measure of cardiac function post-MI (higher EDV reflects worse cardiac outcome). The presence of elastin at day 7 (measured as R_1 within the infarcted myocardium after Gd-ESMA administration) showed a linear correlation with the EDV measured at day 21, suggesting that early accumulation of elastin/tropoelastin (larger Gd-ESMA uptake at day 7) might not be beneficial for the healing of the myocardium at day 21 (**Fig.6.16A**). Interestingly, the inflammatory process measure at day 7 showed a more complex behaviour with respect to the outcome of EDV at day 21, and was best described with a quadratic regression. ^{19}F PFCs data suggests that an optimal inflammatory response is observed when the ^{19}F signal ranged between [0.55-1.85] (**Fig.6.16B**). Both an excessive (^{19}F>>1.85) or weak (^{19}F<<0.55) inflammatory response at early stages post-MI result in large EDV (EDV>100 µl) at day 21 suggestive of adverse cardiac outcome. Similar results were found when total area MI at day 21 post-MI was used as a cardiac outcome and

compared with ^{19}F signal and R_1 at day 7, however with lower significance as compared with EDV (data not shown).

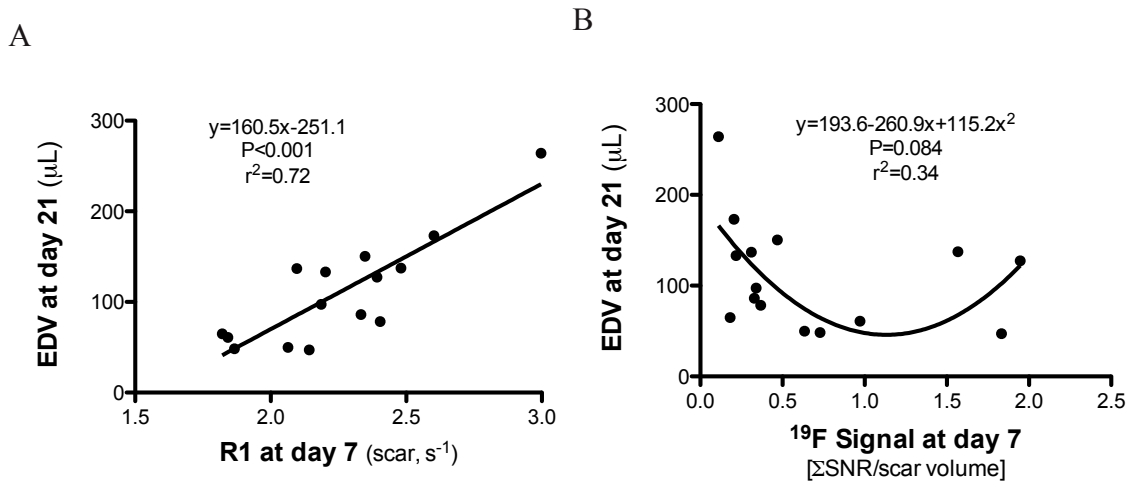

Figure 6.16. (A) Linear correlation between EDV measured at day 21 and R_1 values (Gd-ESMA uptake) at day 7, (B) Quadratic regression between EDV measured at day 21 and ^{19}F SNR at day 7.

The value of ^{19}F signal (^{19}F SNR) and quantitative assessment of elastin/tropoelastin deposition (R_1) in predicting impaired left-ventricular remodelling after MI was also investigated with receiver-operator analysis (**Fig.6.17**). R_1 and ^{19}F MRI showed high sensitivity and specificity for predicting cardiac outcome as summarized in **Table 6.1**. Both measurements carry some predictive value but the combination of the two improves the overall performance of the test in detecting which animals may undergo favourable myocardial remodelling post-MI.

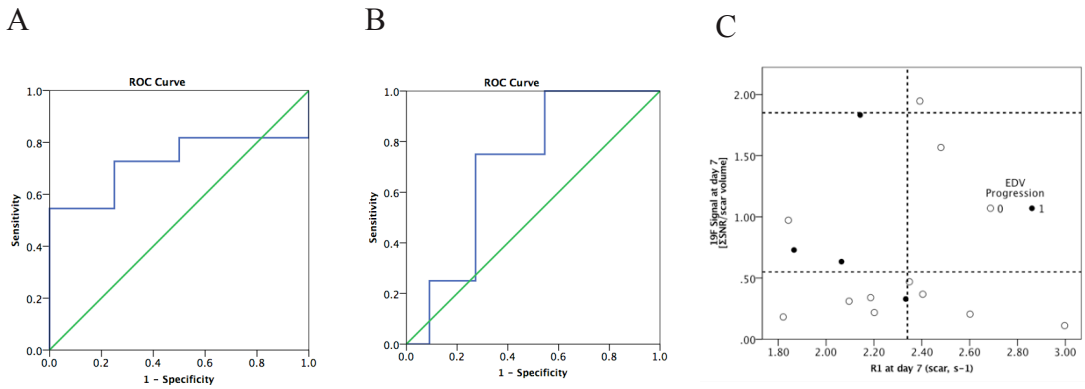

Figure 6.17. (A) R_1 of Gd-ESMA contrast uptake at day 7 (AUC:0.727; 95% CI=0.47-0.98) and (B) ^{19}F uptake at day 7 (AUC:0.705; 95% CI=0.43-0.97) as predictors for beneficial myocardial remodelling (EDV>100µl). (C) Double cut-of-points analysis. 1- good EDV progression; 0- detrimental EDV progression. The "window" of beneficial remodelling is defined by a R_1 value lower than 2.34 s^{-1} and a normalised ^{19}F signal between 0.55 and 1.85. EDV: end-diastolic volume.

Table 6.1. Ability of MRI measurements in predicting beneficial left-ventricular remodelling defined as $R_1 \leq 2.34$ and $0.55 \leq {}^{19}F \leq 1.85$ after MI. When using the information provided by both contrast agents at day 7, the sensitivity and specificity for predicting beneficial LV remodelling at day 21 was 75% and 91%, respectively.

	$R_1 \leq 2.34$	**$0.55 \leq {}^{19}F \leq 1.85$**	**$R_1 \leq 2.34$ $0.55 \leq {}^{19}F \leq 1.85$**
Sensitivity (%)	54.5	50	75
Specificity (%)	100	82	91

6.6 - Discussion

Despite great efforts in preventing MI, its incidence and the subsequent heart failure remain a worldwide health problem. Ongoing research aims at identifying patients with increased risk of adverse left ventricular remodelling in order to more aggressively treat those patients while minimizing usage of drugs and associated side effects in patients deemed to be at lower risk. The outcome of adverse remodelling can be assessed by conventional functional imaging; however, there is a lack of imaging techniques that can detect early adverse

remodelling due to a lack of molecular imaging biomarkers, thus limiting the opportunity for prevention. Molecular imaging of the immune system is an important area of research as it can influence the healing myocardium, where deficient or exacerbated immune responses may adversely contribute to remodelling. Assessing the extent and duration of the inflammatory process *in vivo* post-MI might be a strategy to detect, predict and treat post-MI remodelling. When inflammation dissipates, the infarcted tissue is replaced by scar, which is composed of different proteins which can be visualised and quantified non-invasively using novel imaging targeting e.g. collagen or elastin. As mentioned before, the deposition of these proteins needs to be controlled, as otherwise it can contribute to excessive cardiac remodelling and may lead to heart failure. In this study, we investigated the feasibility of a non-invasive multinuclear $^{1}H/^{19}F$ for the simultaneous assessment of the temporal and spatial course of the inflammatory response and ECM deposition in post-MI remodelling and its predictive values.

In this cross-sectional study, we showed that (1) ^{19}F PFCs MRI can be used to assess and monitor inflammatory cell recruitment *in vivo* into the injured myocardium at clinical field strength, as confirmed by *ex vivo* NMR and histological studies; and (2) Gd-ESMA MRI allows quantification and visualization of scar size, visualization and quantification of elastin/tropoelastin deposition in the myocardium during the scar maturation phase. (3) In a longitudinal proof-of-concept study, we further investigated the merits of both biomarkers in predicting cardiac outcome (measured as end-diastolic volume). We found that at early stages of the healing process an excessive or weak inflammatory response might induce inadequate MI healing, and that excessive tropoelastin deposition within

the scar tissue is not beneficial for cardiac outcome. Our results suggest that multinuclear $^{19}F/^{1}H$ MRI may provide a better understanding of the biological processes underlying post-MI remodelling *in vivo* and that ^{19}F PFCs and Gd-ESMA may serve as new imaging biomarkers for monitoring the progression of cardiac disease and predicting outcome.

Within the first week after MI inflammatory cells are recruited to the site of injury. They are characterized by their phagocytic capacity and thus avidly take up ^{19}F PFCs, which can be imaged by MRI with excellent contrast and without any unwanted background signal. Several studies have shown that ^{19}F MRI allows the *in situ* visualization and quantification of the inflammatory process both *in vivo* and *ex vivo* in the heart post-MI, by targeting monocytes/macrophages [97, 136, 238, 242]. However, no study has described the temporal evolution of ^{19}F signal *in vivo* at clinical field strength and related with the presence of immune cells. Here, we successfully demonstrated the non-invasive visualization and quantification of ^{19}F signal in the infarcted region after LAD ligation by *in vivo* MRI and *ex vivo* validation by NMR. MRI signal intensity measurements demonstrate that ^{19}F is detectable within the first week post-MI, with a peak at 7 days post-MI. Similarly, quantitative *ex vivo* NMR spectroscopy showed higher ^{19}F signal at early stages of MI healing, confirming the same peak at 7 days, and more importantly, PFC accumulation was restricted to the infarcted region with no signal was detected in the remote myocardium. Consistent with these findings, histological analysis showed that monocytes/macrophage populations are significantly increased in the infarct up to 7 days after LAD occlusion as detected by immune positive MAC-3 staining. Furthermore, we found a strong correlation between MAC-3 and ^{19}F MRI signal. Our results are in good agreement with the

resolution of inflammatory cells at later time points (14-21 days) as described in animal models of myocardial infarction [26, 252, 253].

Non-invasive imaging of inflammatory cells has been also achieved using magnetic nanoparticles (MNP) (e.g. iron oxide particles) as shown in models of atherosclerosis [254] and infarct healing [255]. Despite their excellent sensitivity, unlike ^{19}F PFCs which generates a positive signal, iron oxide particles generate negative signal due to the shortening of the T2/T2* relaxation time of nearby water protons. The local deposition of these particles creates hyperintense regions in affected tissues making the differentiation between MNP accumulation and tissue interfaces challenging as both create signal voids. The interest in ^{19}F particles thus increased as they allow avoiding these challenges. Their applications for cell tracking, targeted drug purposes and cell labelling *in vivo* have been extensively explored. ^{19}F PFCs have the advantage of being chemically stable and have the potential for functionalization. Adding fluorochromes to their chemical structure offers the opportunity to multimodal imaging (e.g. combined MRI and fluorescence imaging) while adding cell-specific ligands, could possibly aid the distinction between different cell types (e.g. M1 and M2 macrophages). In this work, we did not differentiate the monocyte/macrophage sub-populations, but for further investigation it would be of great interest to distinguish between Ly6C^{high} and Ly6C^{low} and study their role in post-MI remodelling *in vivo*. ^{19}F MRI may provide an *in vivo* readout for monitoring of treatment-related changes in inflammatory cell infiltration.

As the inflammatory process dissipates, granulation tissue accumulates in the infarcted regions and is then replaced by extracellular matrix proteins. For a long time the ECM was thought to be an inert tissue, however its importance and

role in the remodelling process post-MI has become more evident both in terms of both cell signalling and tissue structure [157, 256]. Scar tissue formation commences as early as 1 week following MI, and is mainly composed of collagen type I but also elastin. Elastin is an insoluble protein and its role in scar formation and stabilization has received more attention recently as it may provide elasticity and help limit scar expansion after infarction [59, 257, 258]. Mature elastin is formed by cross-linking of its soluble precursor, tropoelastin. Here, we investigated the merits of Gd-ESMA contrast agent as an imaging biomarker for the assessment of ECM remodelling. Elastin/tropoelastin was quantified using T_1 mapping to measure the relaxation rate (R_1) after Gd-ESMA injection with 3T MRI. R_1 values significantly increased from 7 to 21 days post-MI, which was in good agreement with the deposition of tropoelastin in the infarcted area measured by immunohistochemistry. No differences were found between remote myocardium and SHAM-operated animals. At 3 days post-MI, T_1 mapping showed a significant increase in R_1 in the infarcted area, however histology showed lack of elastin/tropoelastin at this time point. We hypothesised that Gd-ESMA behaves similarly to other gadolinium-based contrast agents due to its small size [164, 259], and immediately after MI its retention within the infarcted region may be unspecific and attributed to formation of oedema, cellular swelling and rupture, and subsequent increase in extracellular volume, as previously shown in dogs and humans [88, 93, 260]. Consistent with this hypothesis, we observed a high signal intensity on native T_2-weighted images at day 3 (high water content) in the infarcted area, which decreased at day 7 post-MI. Additionally, it has been reported that Gd-ESMA binds not only to tropoelastin and elastin (41%, K_D=9.2±0.7 μM and 40%, K_D=1.0±0.5 μM, respectively) but

also to other proteins including BSA (15%, K_D=ns) and chondroitin sulfates (5%, K_D=ns) [261], collagen type I and III (22%, K_D=7.3±1.3 μM and 13%, K_D=6.8±1.2 μM, respectively) [262] that may be present in small quantities at day 3, thus increasing its retention and tissue relaxation. Elastin fibres were detected by van Gieson staining, however due to their thin shape, segmentation and quantification was challenging. Staining with an anti-tropoelastin antibody demonstrated that tropoelastin molecules significantly increased from 7 to 21 days within the infarct area.

Gd-ESMA has already been used successfully for molecular imaging of vessel wall elastin in atherosclerosis [259, 261, 263], and also generated persistent enhancement of myocardial scar due to binding to elastin/tropoelastin fibres [251]. Whole heart cardiac MRI in concert with Gd-ESMA could provide both scar and coronary plaque burden assessment in a single scan, thereby allowing to risk stratify patients and monitor treatment effects. In addition, it may enable the evaluation of novel cardioprotective therapies. Here, we evaluated ECM remodelling with Gd-ESMA, but alternative contrast agents could be used to monitor collagen deposition [162] another important ECM protein in myocardial remodelling.

We thought to investigate the prognostic value of the inflammatory response and of elastin remodelling on cardiac function in a proof-of-principle longitudinal study. The impact of the inflammatory response on cardiac output was evaluated with ^{19}F PFCs MRI. Excessive or week inflammation (high and low ^{19}F signal) at 3 days post-MI, was associated with a poor cardiac output (at day 21). Conversely, a more balanced inflammatory response at day 3 (intermediate ^{19}F signal) resulted in more beneficial remodelling and better cardiac function at

day 21. Our results are in agreement with other studies that showed that the first hours after MI are crucial and represent a time-window during which restoring blood flow could minimize cardiomyocyte death and drastically attenuate LV remodelling [3]. The healing process is affected by the exposure to and duration of acute inflammation. Prolonged and exacerbated inflammation has been related to worse prognosis and similarly, the lack of inflammation has been associated with thinner infarcts, where the myocardium is more likely to rupture [56, 247]. A certain degree of inflammation and a controlled recruitment of monocyte/macrophages populations seems to be desired for an optimal MI healing.

We have further investigated the prognostic value of Gd-ESMA on cardiac function. In our study, higher R_1 values at 7 days (high elastin/tropoelastin deposition) were associated with an unfavourable prognosis at 21 days as measured by high EDV at day 21 post-MI. In previous work, Gd-ESMA has also been used to assess elastin deposition in the heart in a mouse model of MI [164]. In this cross-sectional study, Wildgruber et al [164] found that a higher contrast-to-noise ratio (CNR) between scar and myocardium at day 21 correlated with a higher ejection fraction at the same time-point, while the CNR at day 7 did not predict outcome at day 21. In contrast, we performed a longitudinal study, using T_1 mapping instead of CNR measurements and EDV as an endpoint for cardiac function and found that a high R_1 signal at day 7 was associated with a poor cardiac outcome at day 21. Other studies showed that modifying the composition of myocardial scar by exogenously increasing elastin content resulted in improvement cardiac function [58, 59, 249] in a rat model of LAD ligation. In addition, increased expression of elastin via cell-based gene therapy improved

cardiac function and survival of ischemic hearts in a rat model of MI [59, 264]. Further studies are now warranted to investigate the role of elastin turnover/metabolism and cross-linking following MI at later time points.

Molecular MRI has great potential for the quantification of inflammatory cell recruitment and extracellular matrix (elastin and collagen) remodelling; two key biological processes underlying the healing of the myocardium post-MI. Multinuclear $^{19}F/^{1}H$ MRI may improve our knowledge of cardiac remodelling *in vivo* by targeting two key biological processes that are responsible for post-MI remodelling. In this work, we studied the feasibility of simultaneously assessing inflammation and extracellular matrix remodelling using ^{19}F PFC nanoparticles and Gd-ESMA contrast agents. Our findings suggest that a weak or exacerbated inflammatory response, and increased deposition of elastin at day 7 in the infarcted myocardium may hamper the healing process. This imaging protocol may be useful for risk stratification or to facilitate the *in vivo* study of the effects of novel therapeutic procedures in disease progression and potentially personalization of therapy.

6.7 - Limitations

This study has shown the feasibility of multinuclear imaging in a murine model of post-MI remodelling via LAD ligation. ^{19}F imaging was performed in a small animal model using a clinical 3T MR scanner, and high amounts of ^{19}F PFCs are required to generate enough signal. The high dosage enabled visualization of ^{19}F PFCs in small structures such as the murine heart. Direct quantification of ^{19}F PFCs from the MRI could not be performed, as a surface coil was used. However, with the use of NMR experiments at 9.4T we were able to

quantify ^{19}F PFCs content both in the remote and infarcted myocardium *ex vivo*. ^{19}F PFCs injection did not show any adverse effects in the animals throughout the period of time animals were monitored. However, PFCs have a long retention time in the body, making it challenge to obtain approval for clinical application. Improvement of PFC clearance while maintaining their specificity for macrophages could facilitate future use in humans. In addition, we used a 2.5 to 5-folder high dose of Gd-ESMA (0.5 mmol/Kg) than usually used in a clinical setting. Future experiments will require dose optimization prior to use humans; however, no toxic effects have been observed in the animals at any time-point. Finally, we utilised a permanent LAD occlusion model to induce a strong acute inflammatory response for proof-of-concept ^{19}F/^{1}H MRI. In future studies, we aim to investigate a reperfusion model, which is clinically more relevant.

6.8 - Conclusions

We successfully demonstrated the feasibility of multinuclear ^{1}H/^{19}F MRI to non-invasively assess and quantify the inflammatory response and elastin turnover following post-MI remodelling in a murine model *in vivo*. We further studied the interplay between these biological processes, and our findings suggest that a balanced inflammatory response may be beneficial for myocardial remodelling, while high amounts of tropoelastin/elastin at day 7 post MI resulted in impaired cardiac function. This novel approach may have potential for monitoring treatments that aim at modulating the inflammatory response or the deposition of ECM proteins *in vivo.* It may also aid the prognosis in patients with myocardial infarction.

Chapter 7

In vivo imaging of monocyte chemoattractant protein-1 role in myocardial remodelling after myocardial infarction

7.1 - Personal Contribution

For this project, René M. Botnar, Ajay Shah, Alkystis Phinikaridou and Isabel Ramos conceived the main idea of the study. IR performed the surgeries, magnetic resonance imaging (MRI) and nuclear magnetic resonance (NMR) spectroscopy scans, histology, fluorescence-activated cell sorting (FACS) and data analysis described in the following study. Markus Henningsson, Begoña Lavin (BL), Thomas R. Eykyn and AP helped with data collection. BL performed the genotyping and helped with FACS analysis. Prof. Ulrich Flögel provided the ^{19}F nanoparticles. A manuscript has been written and is currently being reviewed by all co-authors before submission to a Journal.

Part of this study was submitted for the 25th Scientific Meeting of the International Society for Magnetic Resonance in Medicine conference meeting in Honolulu, Hawaii 2017 and was selected for an e-poster presentation.

Authors List

Isabel Ramos[1,2], Begoña Lavin[1,2], Alkystis Phinikaridou[1,2], Markus Henningsson[1], Thomas Eykyn[1], Ulrich Flögel[3], Ajay M. Shah[2,4], René M. Botnar[1,2,5]

Affiliations

[1]School of Biomedical Engineering and Imaging Sciences, King's College London, London, United Kingdom. [2]Cardiovascular Division, The British Heart Foundation Centre of Excellence, King's College London, London, United Kingdom. [3]Department of Molecular Cardiology, Heinrich Heine University Duesseldorf, Duesseldorf, Germany. [4]Cardiovascular Division, James Black Centre, King's College London, London, United Kingdom. [5]Escuela de Ingeniería, Pontificia Universidad Católica de Chile, Santiago, Chile.

7.2 - Introduction

Adverse ventricular remodelling after myocardial infarction (MI) and subsequent chronic heart failure is a major healthcare problem worldwide [265, 266]. After MI, there is recruitment of inflammatory cells, followed by the formation of granulation tissue and the deposition of extracellular matrix (ECM) [9, 246]. The severity and duration of this healing response may have an important impact on the outcome. A controlled initial immune response is crucial to provide a time window for treatment in order to limit cardiac remodelling [9, 26, 267, 268]. However, several studies have provided evidence that early and persistent inflammation within the infarcted area may promote adverse remodelling and lead to poor prognosis. An extensive inflammatory response within the infarcted myocardium has been related to an increased death of cardiomyocytes and ischemic myocardial injury [269-271].

After MI, the inflammatory response is characterized by an increased expression of chemokines and cytokines, which contributes to immune cell recruitment into the injured area [22, 270]. Monocyte Chemoattractant Protein 1 (MCP-1) is a chemokine which levels are increased in blood after MI in both animal models and patients [62, 272-274]. MCP-1 plays an important role in the recruitment of leukocytes and its lack has been associated with defective recruitment of macrophages into the healing infarct and subsequent replacement of injured myocytes by granulation tissue [32]. In addition, MCP-1 seems to actively participate in the regulation of the maturation phase, by modulating fibroblast phenotype, stimulating extracellular matrix production and metabolism [32, 275, 276]. MCP-1 knockout mice showed an attenuation in left-ventricle (LV) remodelling as a consequence of delay recruitment of leukocytes and delayed replacement of injured cardiomyocytes with granulation tissue [32]. In mice, anti-MCP-1 gene therapy resulted in an attenuation in LV dysfunction, and reduced interstitial fibrosis as measured by collagen staining [277].

In vivo imaging of the remodelling process after MI is important for the understanding of the pathophysiology of myocardial repair. Magnetic resonance imaging (MRI) is a non-invasive imaging technique, with high temporal and spatial resolution that allows to visualise and quantify biological processes by the use of cell or protein specific imaging probes. The purpose of this study was to investigate the role of MCP-1 in myocardial healing *in vivo* in a murine model of MI using a 3T clinical MR scanner. ^{19}F perfluorocarbons (PFCs) that are avidly taken up by macrophages [278] were used to investigate inflammatory cell recruitment into the injured myocardium. To evaluate LV remodelling post-MI, we used a small molecular weight gadolinium-based elastin-specific MR contrast

agent (Gd-ESMA) that enables to non-invasively assess ECM remodelling [164, 251]. *In vivo* imaging of the biological changes in this model may contribute to a better understanding of the role of MCP-1 in post-MI remodelling and may contribute to the development of new therapeutic approaches.

7.3 - Aims

We sought to explore differences in myocardial inflammation and extracellular matrix remodelling in a MCP-1 knockout and wild type murine model of MI *in-vivo* using ^{19}F perfluorocarbon nanoparticles and an elastin specific MR contrast agent, Gd-ESMA.

7.4 - Methods

All animal procedures were performed in accordance with institutional guidelines, following the European Communities Council Directive 2010/ 63/EU on the protection of animals used for scientific purposes, and UK Home Office legislation (The Animals [Scientific Procedures] Act 1986).

7.4.1 - Animal model

Wild-type (WT) C57/BL6 mice (obtained from Charles River Laboratories, United Kingdom) and B6.129S4-*Ccl2*^{tm1Rol}/J knock-down (MCP-1$^{-/-}$) mice (obtained from Jackson laboratories, USA) were used for these experiments. MCP-1$^{-/-}$ animals were genotyped using the polymerase chain reaction protocol advised by Jackson laboratories (section **7.4.2**). MI was induced in WT and MCP-1$^{-/-}$ female mice aged between 10-12 weeks by permanent occlusion of the left anterior descending coronary artery (LAD). Detail description can be found in

Chapter 6, **section 5.3.2.** Survival rates after surgery were similar for both strains (WT 13% vs MCP-$1^{-/-}$ 12% mortality rate).

7.4.2 - Genotyping of MCP-1 animals: sampling, DNA extraction and quantification

Ear samples were taken from the mice after weaning and stored at -20°C until analysis. Ear notches were incubated at 55°C in a lysis buffer containing 10mg/mL proteinase K during 2-3 hours. The supernatant was transferred to a tube containing cold isopropanol and was mixed carefully to precipitate the DNA. After centrifugation at 14,000 rpm for 10 minutes at room temperature, supernatant was discarded and cold 70% ethanol was added to wash the DNA pellets. Then, samples were again centrifuged, supernatant discarded and the sample was left at room temperature until complete evaporation of ethanol. Finally, ultra-pure distilled water was added and samples were stored at -20°C until further analysis.

For genotyping the following primers were used:

- Mutant primer: ‘5’GCCAGAGGCCACTTGTGTAG-3’
- Wild-type forward: 5’TGACAGTCCCCAGAGTCACA-3’
- Common primer: 5’TCATTGGGATCATCTTGCTG-3’

Polymerase chain reaction (PCR) was performed using Illustra Hot Start Master Mix (Ge Healthcare). The reaction mixture for PCR, with a total volume of 12 µL, contained 2 µL of DNA, plus 0.6µL of each primer (20 µM), 1 µL of $MgCl_2$ (25 mM), 1 µL ultrapure deoxynucleotides (dNTPs, 0.2 mM), 1.20 µL of 10X AB PCR Buffer II (1.00X), 2 µL of DNA, 0.09 µL Taq DNA polymerase (5 U/µL) and 3.33 µL of ddH_2O. Initial denaturation at 94°C for 3 minutes was followed by denaturation at 94°C for 30sec, annealing at 61°C for 1 minutes, and extension

at 72°C for 1 minutes, with final extension at 72°C for 10 minutes. Temperature cycling was repeated for 35 cycles, with additionally 2 minutes at 72°C and holding 10°C.

DNA loading buffer (blue) was added into the PCR products and run in a 1.5% agarose gel (Pronadisa) that contained 25ng of gelRed in TBE 1x buffer. Samples were run together with a 1Kb plus DNA ladder (Invitrogen) to determine the size of the PCR products. An example of the genotyping results in shown in **Figure 7.1**.

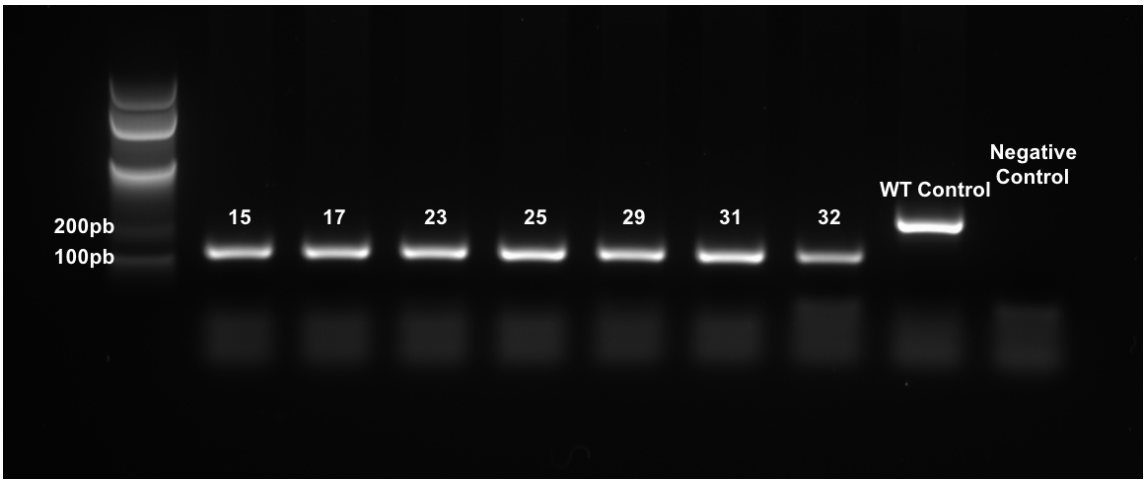

Figure 7.1. Photographs of agarose gels showing the results of amplification by PCR obtained from seven adult MCP-1$^{-/-}$ (animal 15, 17, 23, 25, 29, 31, 32) mice and one wild-type (WT, control) mice ear samples. MCP-1$^{-/-}$=179pb, Wild type (WT control) = 287pb.

7.4.3 - Magnetic Resonance Imaging (MRI) at 3T

In vivo MRI and image analysis were performed as described in **Chapter 6**, **section 6.4.2**. and **Chapter 6**, **section 6.4.3**, respectively.

7.4.4 - Nuclear Magnetic Resonance (NMR) spectroscopy at 9.4T

Ex vivo NMR ^{19}F signal quantification was performed as described in **Chapter 6**, **section 6.4.4**.

7.4.5 - Histology

Trichrome staining was performed as described previously in **Chapter 6**, **section 6.4.5** to measure area of infarct and collagen deposition post-MI. MAC-3 immunohistochemistry (IHC) was performed for detection of macrophages within the infarcted area as described in **Chapter 6**, **section 6.4.5.** Immunohistochemistry for detection and quantification of fibroblasts was performed using a rabbit monoclonal antibody (anti-vimentin ab92547, Abcam; dilution 1:100) using an avidin-biotin-peroxidase method (Vector® SG Peroxidase substrate; Vector Laboratories, Burlingame, CA). Vimentin can be also found in non-epithelial cells (e.g. mesenchymal cells), however because it is highly expressed in fibroblasts, for simplification positive-vimentin-IHC will be referred as fibroblast expression. Digital images were analysed using ImageJ (National Institute of Health, Bethesda, MD). Fibroblast quantification was expressed as percentage of the infarcted myocardium measured by histology using Trichrome staining.

7.4.6 - Fluorescent Activated Cell Sorting (FACS) analysis

For *ex vivo* evaluation of the inflammatory response, animals were sacrificed at 3, 7, 14 and 21 days and blood and hearts were collected. Blood was collected by cardiac puncture using sodium citrate 0.1% as anticoagulant. Hearts were extensively flushed with PBS and then excised. Remote myocardium was separated from infarct and border zone using a dissection microscope. Then, tissues were cut into small pieces to facilitate enzyme digestion and placed in a Dissociation Enzyme Stock solution containing: 0.5% BSA (Sigma Aldrich), collagenase IV (1 mg/mL, C5138, Sigma Aldrich), 1 mM EDTA, DNase I (100 units/mL, D7291, Sigma Aldrich), hyaluronidase IV-S (500 units/mL, C5138,

Sigma Aldrich) at 37ºC for 30 minutes. Hearts were subsequently filtered through a 40 µm nylon mesh (352054, Fisher Scientific). Samples were then stained for 20 minutes with following antibodies: CD3 (Biolegend, clone 100325), B220 (Biolegend, clone 103233), NK1.1 (Biolegend, clone 108725), Ly6C (Biolegend, clone 128007), F4/80 (Biolegend, 123115), CD11b (Biolegend, clone 101225), CD115 (Biolegend, clone 135517), Ly6G (Biolegend, clone 127617), CD45 (Biolegend, 103125). Then, a red blood cell lysis buffer (BD, New Jersey, U.S.) was used to lyse red blood cells and samples were then wash with PBS+2%BSA, fixed with 1% PFA for 15 minutes, and maintained in PBS and 4°C until data acquisition.

Data was acquired on a BD SORP Fortessa™ and analysed with FlowJo (Tree Star, Ashland, OR, USA). Monocytes were identified as $CD45^{+}$, $CD3^{-}$, $B220^{-}$, $NK1.1^{-}$, $F4/80^{+}$, $CD115^{+}$, $Ly6C^{+}$, $Ly6G^{-}$, $CD11b^{+}$. Monocytes subsets were identified as $CD115^{+}$, $F4/80^{+}$ and $Ly6C^{high}$ or $Ly6C^{low}$.

7.4.7 - Statistical analysis

A total of 123 mice were used in this study: 64 animals were subjected to MRI imaging at 3,7,14 and 21 days after MI (32 WT and 32 MCP-$1^{-/-}$, N=8/time-point); 59 were used for FACS analysis, 32 were used for histological validation and 32 mice were used for NMR ^{19}F quantification experiments.

GraphPad Prism 5.00 (GraphPad Software, Inc., La Jolla, California, USA) was used for statistical analysis. Normality was assessed by histogram, Q-Q plots, and the Shapiro-Wilk test, and equal variances was assessed with the Bartlet's test and Levene's test. For normally distributed variables with equal variances, an ANOVA test followed by Bonferroni post hoc analysis for multiple group comparisons (e.g. infarct size) was performed. For normally distributed

variables with unequal variances a Welch test followed by a Games-Howell post hoc test for multiple group comparisons (e.g. LV mass, left-ventricle end-diastolic volume (LVEDV), ^{19}F MRI, R_1) was performed. For non- normally distributed variables, a Kruskal-Wallis test was used for multiple group comparisons (e.g. Ejection fraction (EF), NMR, FACS, IHC MAC-3, IHC Tropoelastin, IHC Vimentin, collagen quantifications) following by Dunn's post-hoc test. *P<0.05* was considered statistically significant. Data are presented as mean ± SEM.

7.5 - Results

7.5.1 - WT mice showed LV expansion during post-MI remodelling, while no significant changes were observed in MCP-1$^{-/-}$ mice.

In order to investigate the role of MCP-1 in cardiac remodelling, several functional and volumetric parameters were compared between MCP-1$^{-/-}$ and WT animals at 3 and 21 days after LAD occlusion. Representative short-axis images of late-gadolinium enhancement (LGE) for assessment of infarct and cine images for estimation of cardiac parameters are shown in **Figure 7.2A**. Infarct sizes were similar in both strains at both time-points (**Fig.7.2B**) and similar EF was observed in both groups (**Fig.7.2C**). No differences were detected between WT and MCP-1$^{-/-}$ at 3 and 21 days time-point for left-ventricular mass and left-ventricle end-diastolic volume. WT mice showed LV expansion during post-MI remodelling (assessed by left ventricular mass) (*P<0.05*, **Fig.7.2D**). LVEDV increased in both WT and MCP-1$^{-/-}$ animals from 3 to 21 days post-MI, however, more significantly in WT mice (LVEDV $WT_{3\text{-}21days}$ [µL]: 62.69±3.14 vs 106.0±9.16, *P<0.01*; LVEDV MCP-1$^{-/-}$ $_{3\text{-}21days}$ [µL]: 67.34±5.96 vs 94.62±13.03, *P<0.05*) (**Fig.7.2E**).

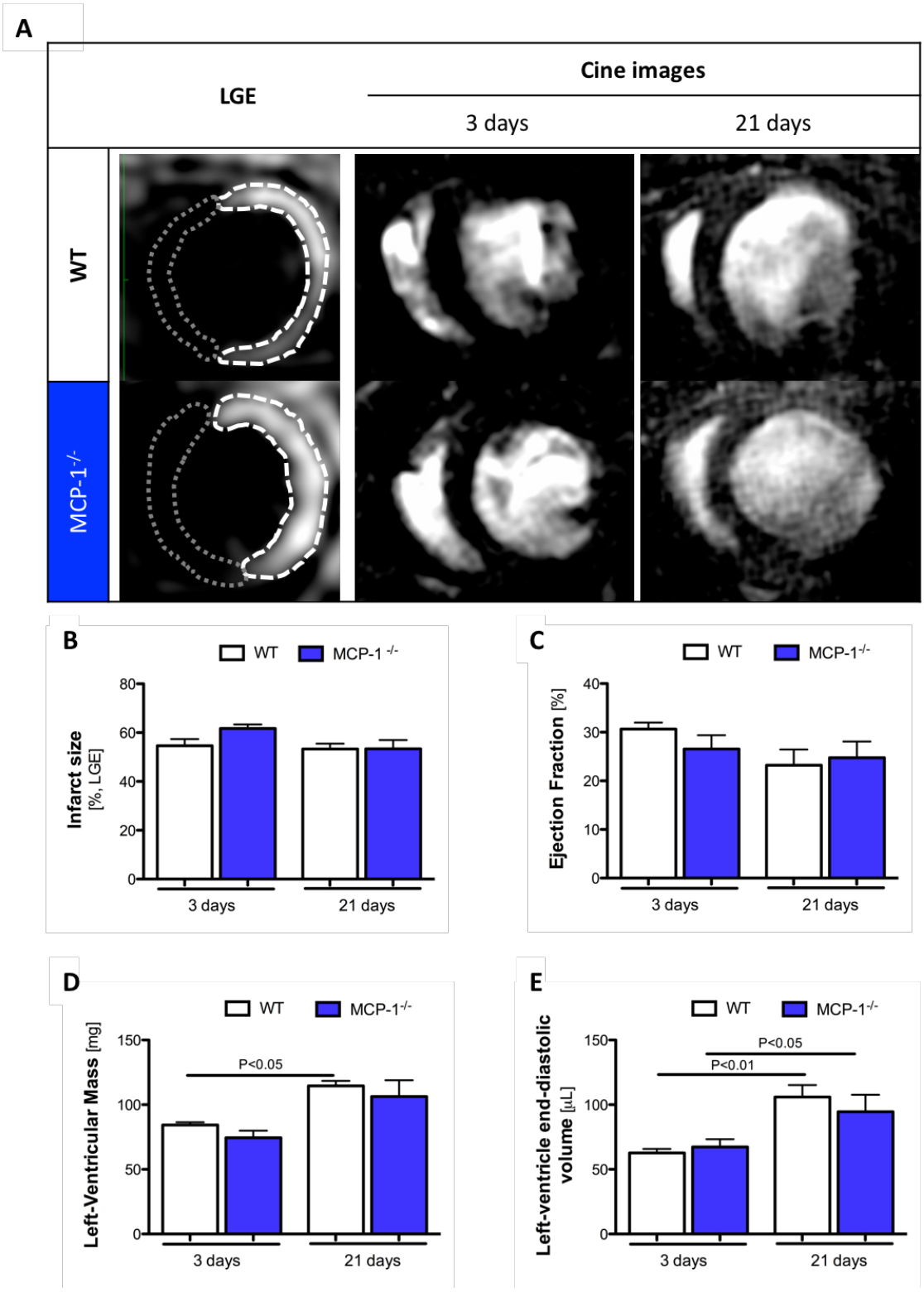

Figure 7.2. Comparison of functional and volumetric cardiac parameters between WT and MCP-1$^{-/-}$ animals 3 and 21 days after LAD occlusion. (A) Representative short-axis views of LGE and end-diastolic cine images. (B) Infarct size (%), (C) Ejection fraction (%), (D) Left-ventricular mass (mg) and (E) Left-ventricular end-diastolic volume (µL). N=8 per time-point. LGE: late-gadolinium enhancement; LAD: left-anterior descending coronary artery; WT: wild-type.

7.5.2 - MPC-1$^{-/-}$ mice exhibited an early ^{19}F signal during post-MI remodelling

To explore the differences in inflammatory cell recruitment in MCP-1$^{-/-}$ and WT non-invasively, animals received a bolus injection of ^{19}F PFCs intravenously 48 hours before the imaging session (to allow phagocytosis of the PFCs and blood clearance). ^{19}F MRI signal was evaluated at 3, 7 and 21 days after LAD occlusion *in vivo*.

Morphologically matching ^{1}H and ^{19}F images enabled the anatomical localization of PFCs (**Fig.7.3A**). **Figure 7.3B** shows ^{19}F MRI signal quantification in WT and MCP-1$^{-/-}$ animals. MCP-1$^{-/-}$ animals high ^{19}F signal at 3 and 7 days, which decreased significantly at 21 days post-MI ($^{19}F_{7\text{-}21days}$=0.53±0.09 vs 0.24±0.01, *P<0.05*). An increasing ^{19}F signal was observed at 3 and 7 days post-MI in WT animals ($^{19}F_{3\text{-}7days}$=0.48±0.05 vs 1.23±0.16, *P<0.01*), which significantly decreased at 21 days ($^{19}F_{21days}$=0.2±0.02; $^{19}F_{3\text{-}21days}$=*P<0.001*; $^{19}F_{7\text{-}21days}$=*P<0.001*). In contrast, ^{19}F signal was highest at day 3 in MCP-1$^{-/-}$ animals and then steadily decreased. At day 7, ^{19}F signal higher in WT compared to MCP-1$^{-/-}$ more suggesting a reduced recruitment of inflammatory cells (*P<0.01*) at this time-point. ^{19}F signal was also detected in the adjacent chest tissue (where the thoracotomy for the LAD ligation was performed), liver and lymph nodes. No background signal from other tissues was detectable (data not shown).

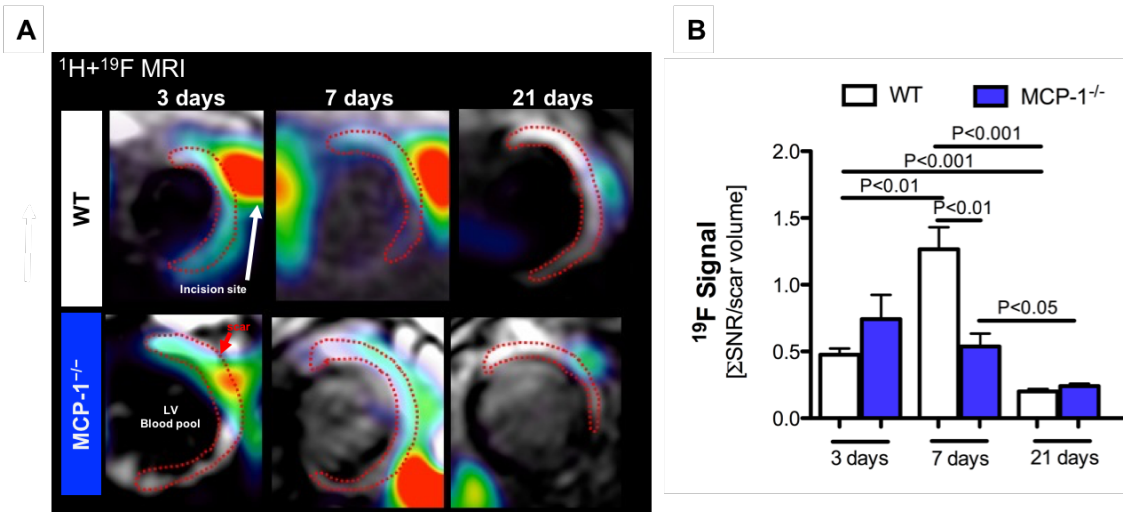

Figure 7.3. Evaluation of ^{19}F MRI uptake at 3, 7 and 21 days post-MI in MCP-$1^{-/-}$ and WT animals. (A) Representative images of anatomically matched and super-imposed ^{1}H and ^{19}F short-axis view images. (B) Quantification of ^{19}F MRI signal at the different time points post-MI. N=8 per time-point.

To validate our *in vivo* findings hearts were collected at the end of imaging session. Infarct and remote areas were then separated and NMR spectroscopy was performed. In agreement with *in vivo* MRI, *ex vivo* NMR showed a peak at 7 days in WT animals, with the ^{19}F signal decreasing significantly at 21 days (^{19}F NMR [159] $_{7\text{-}21\text{days}}$: WT= 0.12±0.03 vs 0.01±0.005, *P<0.05*) (**Fig.7.4A**). MCP-$1^{-/-}$ animals showed a similar signal behaviour as *in vivo* with the highest signal at day 3 and then steadily decreasing towards day 21. The signal changes were however non-significant; no ^{19}F signal was observed in the remote areas throughout the remodelling period (**Fig.7.4B**).

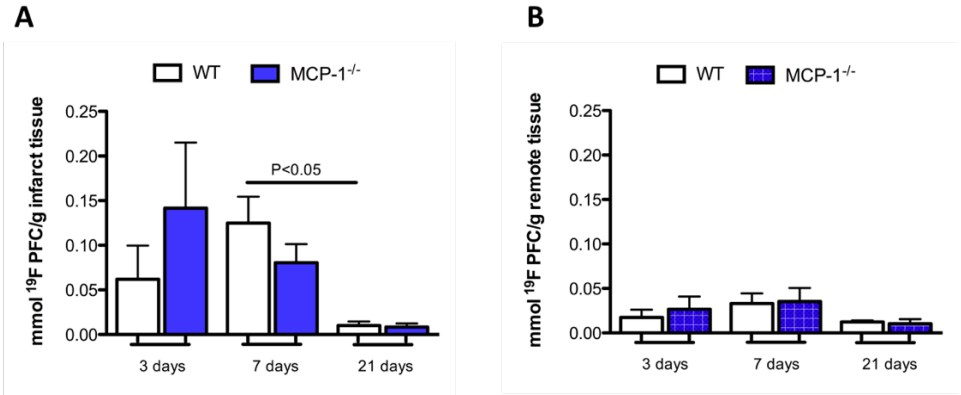

Figure 7.4. ^{19}F signal quantification by NMR spectroscopy at 3, 7 and 21 days post-MI. mmol ^{19}F PFC uptake per gram of A) infarcted tissues and (B) remote areas. N=4 per time-point. WT: wild-type.

7.5.3 - Uptake of ^{19}F PFCs by inflammatory cells: FACS and histological validation

In the absence of injury, both WT and MCP-1$^{-/-}$ SHAM-operated animals showed similar monocyte/macrophage content. However, it is well established that in early stages after MI there is a significant extravasation of monocytes where dead cardiomyocytes and resident macrophages are replaced by monocyte-derived macrophages [7]. The first phase after MI is characterized by the recruitment of inflammatory monocytes Ly6C^{high} to the infarct from the spleen and bone marrow, followed by a second phase dominated by anti-inflammatory Ly6C^{low} monocytes [10]. To examine the role of MCP-1 in the monocyte recruitment into the injured area FACS analysis was performed (**Fig.7.5)**.

As a result of MI, blood levels of inflammatory Ly6C^{high} monocytes increase resulting in an increased and prolonged presence of these cells in the healing infarct during the first week after MI. Blood Ly6C^{high} and Ly6C^{low} were comparable between animal strains at all time-points. A significant increase in Ly6C^{high} was observed in WT animals between SHAM and 3 days post-MI (Ly6C^{high} WT [10^4/mL]: SHAM=0.005±0.002 vs 3 days=1.27±0.36, *P<0.05*). In SHAM-operated WT animals higher amounts of Ly6C^{low} where observed than in

SHAM MCP-1$^{-/-}$ (Ly6C^{low} [10^4/mL]: $SHAM_{WT}$=2.55±0.59 vs $SHAM_{MCP\text{-}1\text{-}/\text{-}}$ =0.59±0.25, *P<0.05*). A significant decrease of Ly6C^{low} was observed between SHAM and 21 days in WT animals (Ly6C^{low} WT [10^4/mL]: SHAM=2.55±0.59 vs 21 days=0.56±0.15, *P<0.05*). In tissue, 3 days after MI, monocyte infiltration was higher in MCP-1$^{-/-}$ compared with WT (Monocytes [10^3/mg] 3 days: WT=31.03±3.08 vs MCP-1$^{-/-}$=57.82±8.44, *P<0.05*). Also, a significant increase in monocytes was observed in MCP1$^{-/-}$ animals compared to SHAM and 3 days time point (Monocytes [10^3/mg] MCP-1$^{-/-}$: SHAM= 2.42±0.60 vs 3 days=57.82±8.44, *P<0.01*). After 7 days, monocytes in MCP-1$^{-/-}$ infarcts were not significantly different than WT and in both strains and had a trend to decrease up to 21 days (*P=ns*). A monocyte subset analysis showed that inflammatory monocytes are present within the infarct tissue during the first days after MI, and after the first week, the tissue is invaded by reparative monocytes. A significant increase of Ly6C^{high} was observed in both WT and MCP1$^{-/-}$ at 3 days post-MI compared with SHAM animals (Ly6C^{high} WT [10^3/mg]: SHAM=1.63±0.49 vs 3 days=29.38±3.83, *P<0.05*; Ly6C^{high} MCP-1$^{-/-}$ [10^3/mg]: SHAM=1.43±0.47 vs 3 days=45.58±6.45, *P<0.01*) and decreased significantly from 3 to 21 days post-MI (Ly6C^{high} WT [10^3/mg]: 3 days=29.38±3.83 vs 21 days=2.53±0.62, *P<0.05*; Ly6C^{high} MCP-1$^{-/-}$ [10^3/mg]: 3 days=45.58±6.45 vs 21 days=3.35±0.56, *P<0.05*). Ly6C^{low} population also behave similarly between animal strains at all time-points post-MI. WT animals shown a significant increase between SHAM and 21days post-MI (Ly6C^{low} WT [10^3/mg]: SHAM=0.96±0.31 vs 21 days=12.69±2.69, *P<0.01*). In MCP-1$^{-/-}$ mice a significant increase was observed in SHAM and 3 days compared with 7 days post-MI (Ly6C^{low} MCP-1$^{-/-}$ [10^3/mg]: SHAM=1.56±0.44 vs 7 days=17.05±1.95, *P<0.01*; 3 days=2.80±1.78 vs 7 days=17.05±1.95, *P<0.01*).

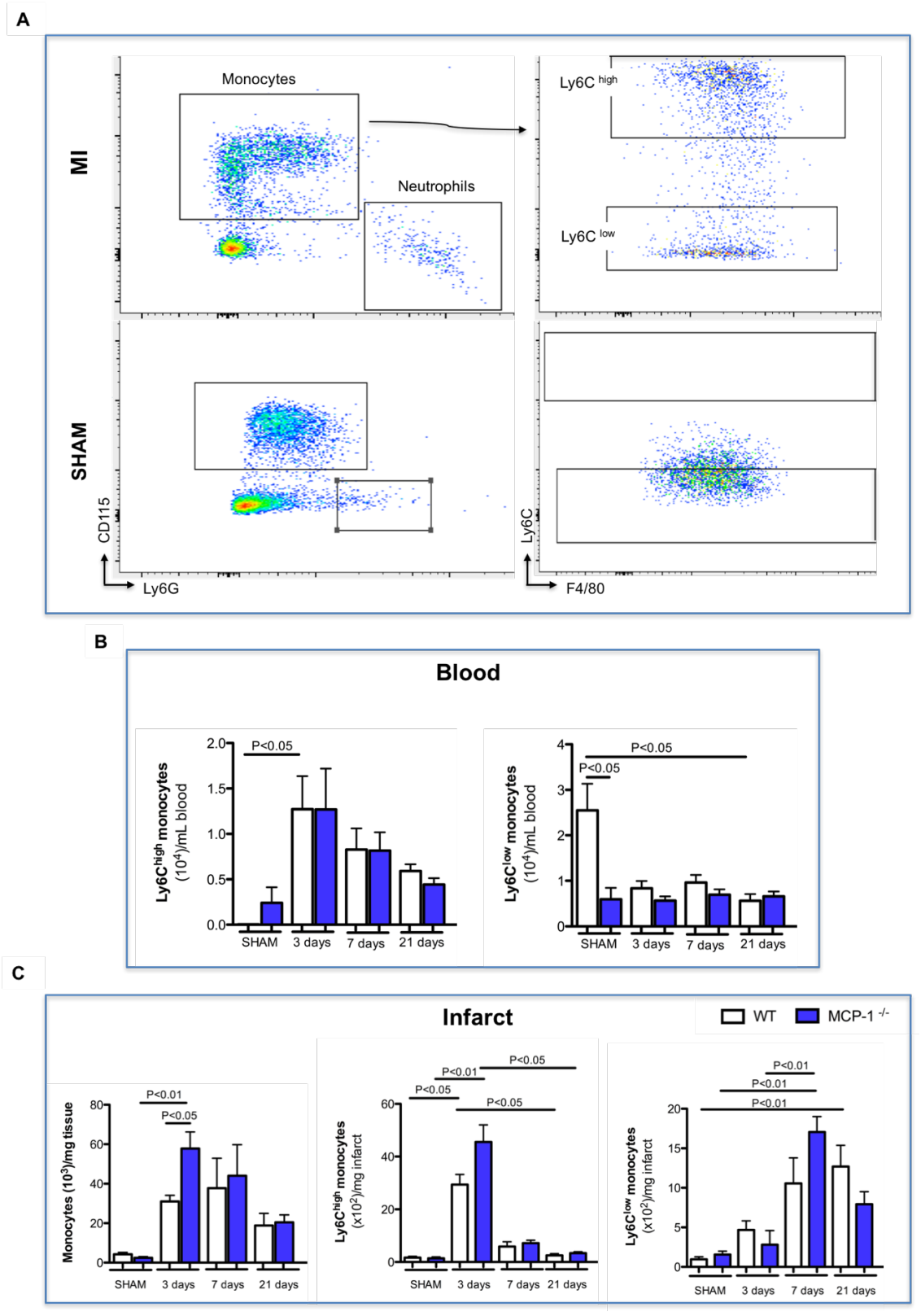

Figure 7.5. FACS analysis of blood and tissue after MI in WT and MCP-1$^{-/-}$ animals. (A) Representative gating strategy for the identification of monocyte sub-populations. (B) Quantitative analysis of blood Ly6C^{high} and Ly6C^{low} monocytes. (C) Quantitative analysis of total monocyte population and sub-monocyte population in WT and MCP-1$^{-/-}$ mice. N=4-6 per group.

Tissue macrophages were analysed by MAC-3 IHC (**Fig.7.6&7.7)**. Macrophages were present in infarcted areas but not in remote areas post-MI (**Fig.7.6**).

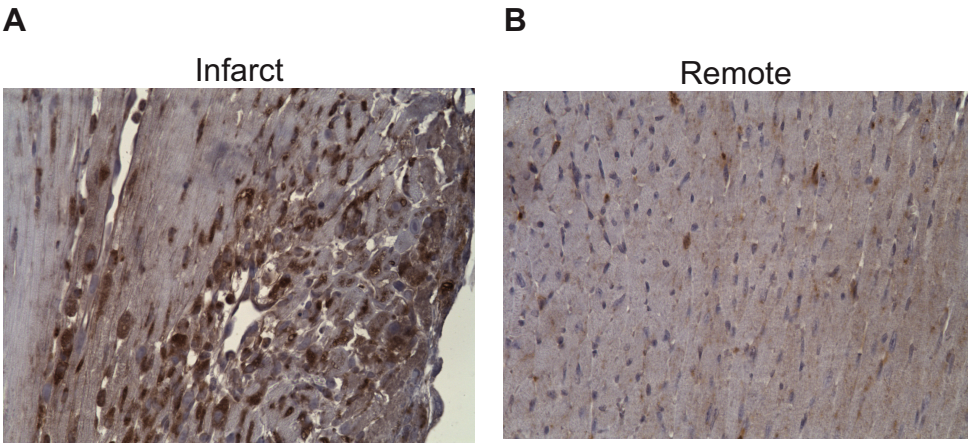

Figure 7.6. Macrophage immunohistochemistry of the heart after MI. Sections of (A) infarcted tissue (MAC-3 positive stained in brown) and (B) remote myocardium.

Figure 7.7 shows MAC-3 quantification. A peak in macrophages content was observed at early stages during acute inflammation. At 3 days, macrophage density was significantly higher in WT compared to MCP-1$^{-/-}$ mice (MAC-3 IHC $_{3days}$: WT= 2.21±0.20 vs MCP-1$^{-/-}$: 1.17± 0.07, *P<0.05*). At day 7 both strains showed an increase in macrophages, consistent with the inflammatory phase, followed by a decrease at day 21 consistent with the resolution of inflammation (MAC-3 IHC $_{7\text{-}21\ days}$ [%]: WT=3.49±0.36 vs 0.13±0.05, *P<0.01*; MCP-1$^{-/-}$= 1.99±0.35 vs 0.55±0.19, *P<0.01*). Overall, macrophage response in MCP-1$^{-/-}$ mice was less pronounced compared with WT.

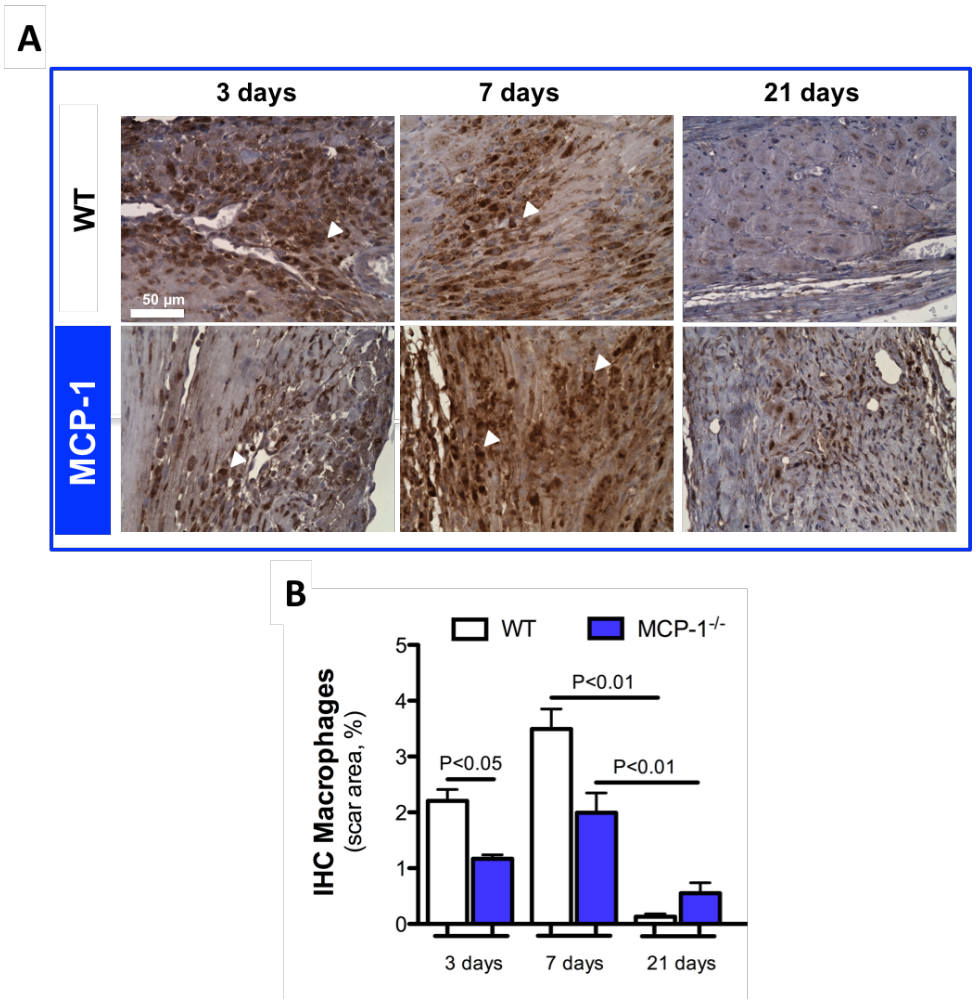

Figure 7.7. Immunohistochemistry analysis of macrophage content in the heart at 3,7 and 21 days after LAD occlusion. (A) Representative sections of infarcted areas in the heart were stained with anti-MAC-3. (B) Quantification of macrophage IHC demonstrating significantly higher macrophage deposition in WT compared to MCP-$1^{-/-}$ mice at day 3 (P<0.05). Macrophage content was highest at 7 days in both strains and thereafter decreasing significantly over time (day 21). N=4 per time-point. WT: wild-type; IHC: immunohistochemistry.

7.5.4 - MCP-$1^{-/-}$ mice show attenuated extracellular matrix deposition post-MI

The potential effect of MCP-1 protein on ECM deposition was assessed with Gd-ESMA, a contrast agent that binds to elastin/tropoelastin proteins, by MRI. **Figure 7.8A** reports relaxation rate (R_1) maps at days 7 and 21 and the *in situ* quantification of Gd-ESMA, 60 minutes after injection. Both WT and MCP-$1^{-/-}$ mice showed similar uptake of Gd-ESMA at day 7 (*P=ns*); however, at day 21, MCP-$1^{-/-}$ animals showed significantly lower R_1 values ($R_1[s^{-1}]$: WT=3.30±0.15 vs

MCP-1$^{-/-}$=2.32±0.09, *P<0.05*), suggesting reduced elastin deposition (**Fig.7.8B**). A significant increase in R_1 between 7 to 21 days was observed in WT animals (R_1[s^{-1}] WT: 7 days=2.33±0.09 vs 21 days=3.30±0.15, *P<0.001*).

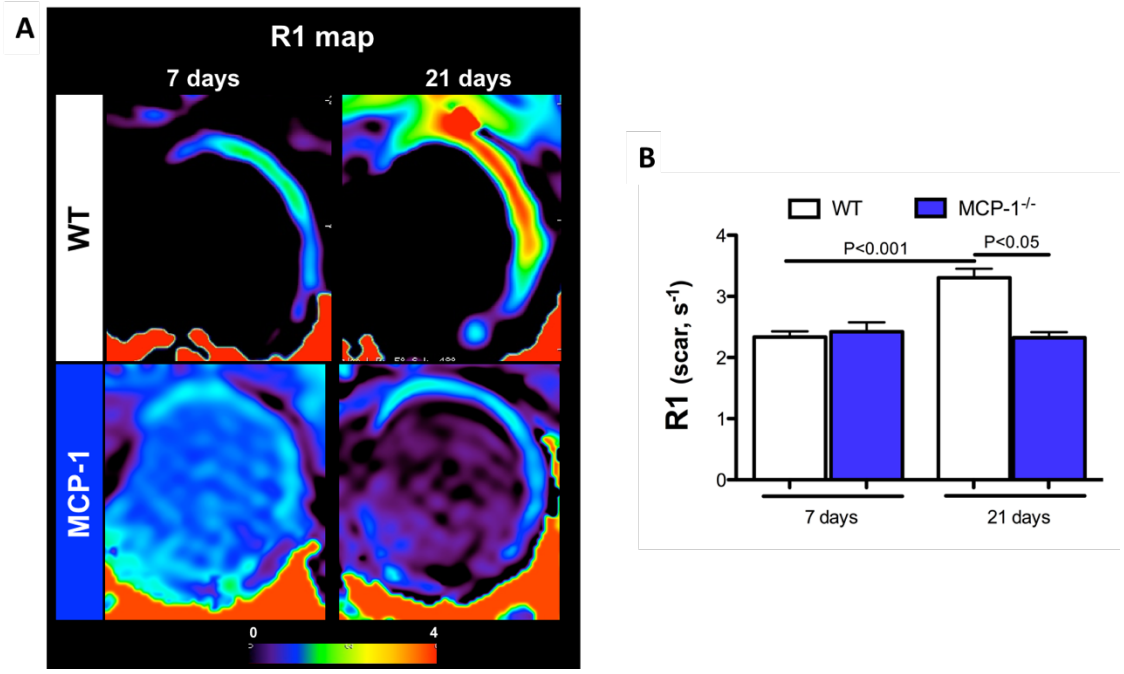

Figure 7.8. Uptake of Gd-ESMA in the heart after 7 and 21 days post LAD occlusion. (A) Relaxation rate (R_1) maps show increased Gd-ESMA uptake in the infarct at day 21 in WT mice. Intense red signal indicates increased Gd-ESMA concentration. (B) Quantitative R_1 values demonstrating an increase at day 21 in WT mice. N=8 per time-point. WT: wild-type.

To examine elastin deposition within the heart, Elastic van Gieson staining was performed. As shown in **Figure 7.9,** elastin quantification was challenging due to its thin shape of the fibres. For this reason, tropoelastin, an elastin precursor was studied with IHC.

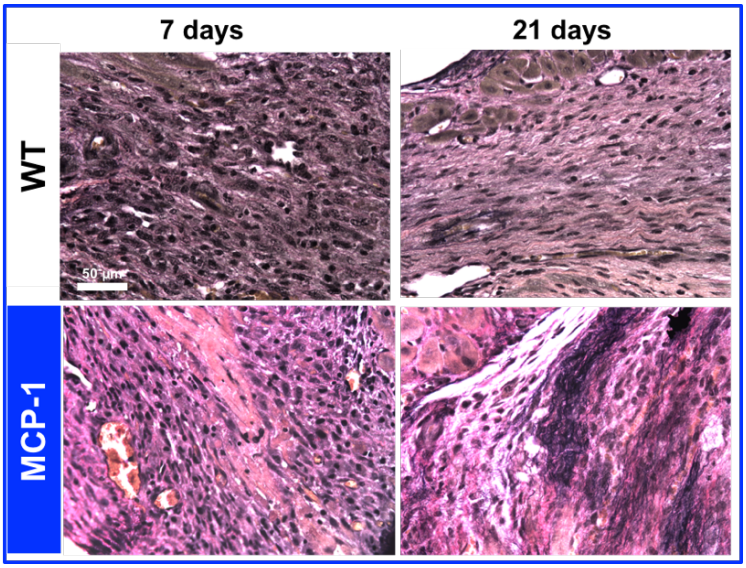

Figure 7.9. Elastica van Gieson staining. Representative images of infarct tissue at 7 and 21 days after ligation of the left-anterior descending coronary artery in MCP-1$^{-/-}$ and wild-type (WT) animals. Elastin is identified as the black fibre deposition.

Tropoelastin IHC revealed a dense fibre network at 21 days post-MI in the infarcted areas in both WT and MCP-1$^{-/-}$ mice. At 7 days, MCP-1$^{-/-}$ and WT mice showed comparable tropoelastin deposition. In agreement with the MRI *in vivo* analysis, tropoelastin IHC showed a significantly lower tropoelastin deposition in the infarcted myocardium of MCP-1$^{-/-}$ mice at 21 days compared to WT mice (Tropoelastin IHC $_{21\ days}$ [%]: WT=3.19±0.16 vs MCP-1$^{-/-}$= 1.31±0.25, $P<0.05$) (**Fig.7.10**). A significant increase of tropoelastin deposition was observed in WT animals overtime at 21 days (Tropoelastin IHC WT: 7 days=1.95±0.18 vs 21 days, $P<0.05$), which was in good agreement with the imaging results.

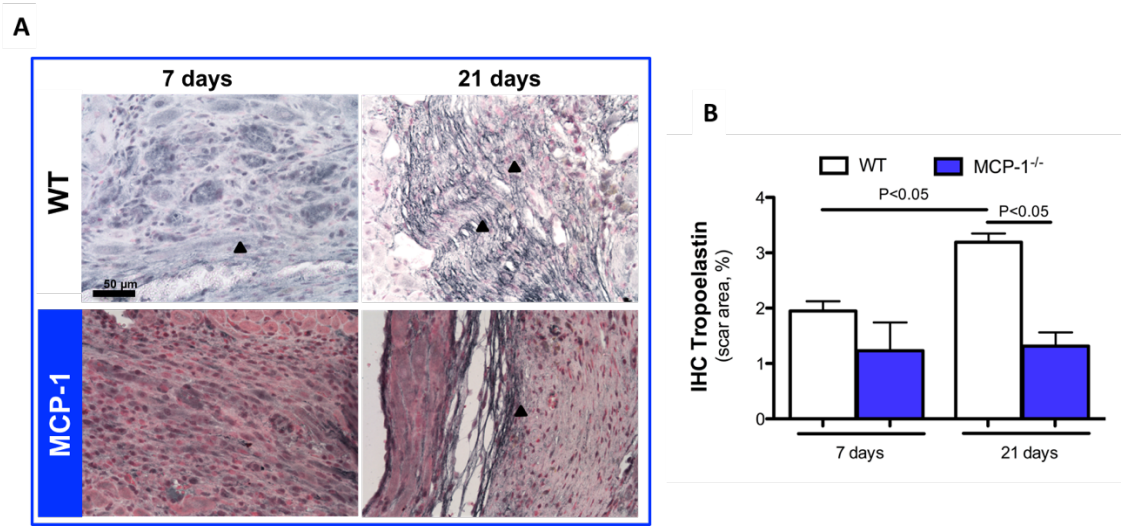

Figure 7.10. Immunohistochemistry analysis of tropoelastin deposition in the heart at 7 and 21 days post-MI. (A) *Ex vivo* tropoelastin IHC revealed deposition of tropoelastin in the infarcted region at 21 days. (B) Quantification of tropoelastin. In MCP-1$^{-/-}$ tropoelastin deposition was significantly lower at both 7 and 21 days when compared to WT animals. N=4 per time-point. WT: wild-type.

7.5.5 - MCP-1$^{-/-}$ Mice Showed Decreased collagen content

To further study ECM composition, collagen content was also evaluated. Trichrome staining was used to analyse infarct size (as shown before) and to evaluate the deposition of collagen-rich proteins that became more evident in the at latter stages post-MI (**Fig.7.11**).

During the acute stage, WT and MCP-1$^{-/-}$ mice showed similar collagen content. At 21 days, WT mice showed significantly higher collagen deposition that at day 7 (collagen[%] WT: 7 days=0.47±0.18 vs 21 days=2.71±0.54, *P<0.05*) and higher collagen content at 21 days compared to MCP-1$^{-/-}$ mice (collagen[%] WT vs MCP-1$^{-/-}{}_{21days}$=2.71±0.54 vs 1.34±0.15, *P<0.05*). These results suggest less collagen formation in MCP-1$^{-/-}$ mice, as a result of the altered inflammatory response.

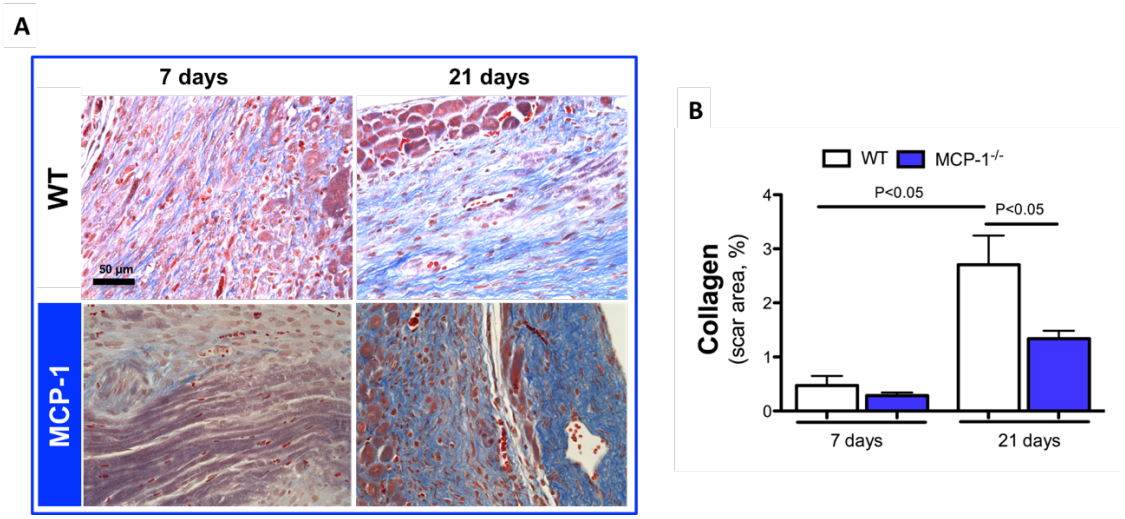

Figure 7.11. *Ex vivo* trichrome staining allowed the differentiation between infarcted and remote areas in the heart. (A) Representative sections of infarct area from MCP-1$^{-/-}$ and WT animals. Blue reveals the deposition of collagen-like proteins in the heart that becomes more evident at later stages post-MI. (B) Collagen quantification. In MCP-1$^{-/-}$ collagen was significantly lower at 21 days compared with WT animals. N=4 per time-point. WT: wild-type.

7.5.6 - Fibroblast infiltration in MCP-1$^{-/-}$ mice

During the inflammatory phase, removal of debris is orchestrated by inflammatory cells followed by the deposition of fibrous tissue. During the phagocytic phase which promotes tissue repair and scar formation, reparative cells are recruited (e.g. fibroblasts and myofibroblasts) to the injury site.

Macrophages regulate fibroblast proliferation through the production of cytokines and growth factors [7]. Fibroblasts then differentiate in myofibroblasts are the predominant source of collagen in MI healing [279-282]. Fibroblasts/myofibroblasts are responsible for the synthesis of the ECM needed to support cell ingrowth and the newly formed blood vessels supplying oxygen and nutrients necessary to sustain cell metabolism. These reparative cells, transiently appear during granulation tissue formation and become apoptotic when scar matures [283, 284].

Early after MI, fibroblasts are predominantly localized in the border-zone area (**Fig.7.12A**). Three days after MI, MCP-1$^{-/-}$ mice showed decreased

fibroblast infiltration compared with WT animals (Vimentin IHC [%] $_{3days}$: WT=3.39±0.16 vs MCP-1$^{-/-}$=1.58±0.16, *P<0.05*) (**Fig.7.12B**). At 7 days post-MI both exhibited similar fibroblasts content (*P*=ns). At later stages, fibroblasts remained in the infarct zone in MCP-1$^{-/-}$, but their content was significantly lower in WT animals (Vimentin IHC [%] $_{21days}$: WT=0.65±0.19 vs MCP-1$^{-/-}$= 2.10±0.14, *P<0.05*). This might suggest a delayed and/or prolonged maturation phase in MCP-1$^{-/-}$ animals.

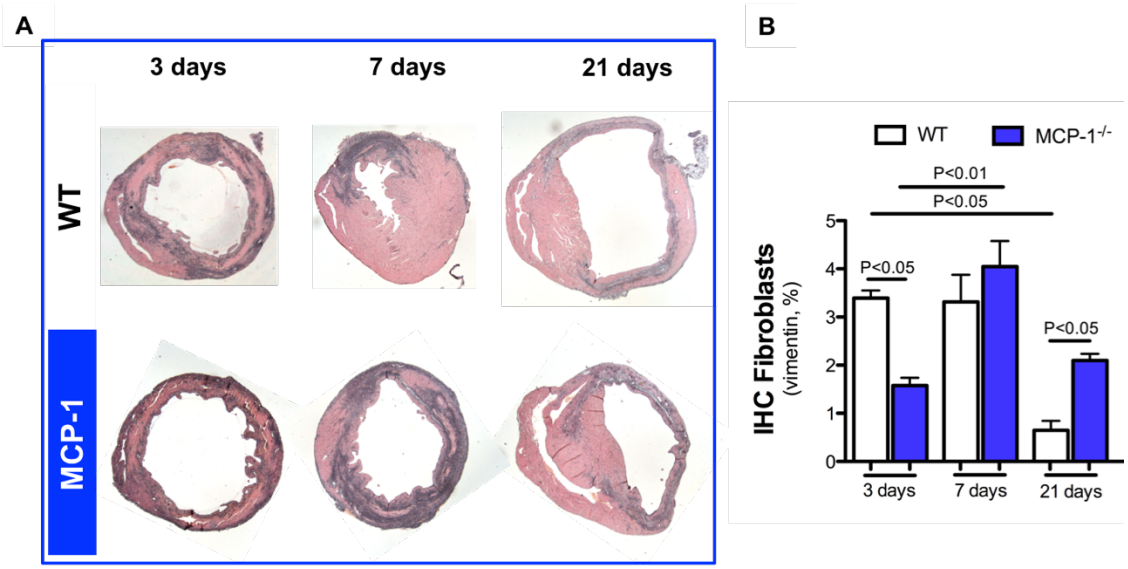

Figure 7.12. Immunohistochemistry analysis of fibroblasts infiltration in the heart after 3,7 and 21 days post-MI in WT and MCP-1$^{-/-}$ mice. Representative sections of the heart stained with anti-vimentin are shown in (A). (A) Both MCP-1$^{-/-}$ and WT fibroblasts expression was predominantly in the border-zone. From acute to later stages of MI fibroblasts migrate from the border-zone to the injured. (B) IHC for vimentin quantification demonstrating that fibroblasts infiltration is significantly higher in WT compared to MCP-1$^{-/-}$ (*P<0.05*) at day 3. Fibroblasts expression in WT mice significantly decreased from 3 to 21 days post-MI (*P<0.05*), while remained elevated in MCP-1$^{-/-}$ mice until 21 days (*P<0.05*). N=4 per time-point. WT: wild-type.

7.6 - Discussion

The MCP-1 protein is overexpressed after MI and is responsible for the recruitment of inflammatory cells into the injured myocardium [9, 22]. After MI, inflammatory cells are recruited from the blood stream to the injured tissue. These cells roll along the lumen, because of the presence of the CCR2 receptor on the membrane of leukocytes, and bind to MCP-1 (also known as CCL2) of the

endothelial cells [285]. The interaction of CCR2 and MCP-1 leads to the diapedesis of monocytes and therefore its extravasation into the myocardium, where monocytes differentiate in macrophages. Macrophages clean the infarct from debris and dead cells, and are also involved in the production of MMPs which degrade the damaged ECM and promote the recruitment of reparative cells [20]. Fibroblasts and myofibroblasts when recruited to the site of injury produce new ECM which will then form the fibrotic tissue [14].

Several studies investigated the role of the MCP-1 protein during wound healing; specifically anti-inflammatory strategies have been implicated with the reduction of infarct size and improved cardiac outcome in preclinical work; however its translation into the clinics has failed [286]. For this reason, new imaging techniques are required to better unravel the molecular and cellular mechanisms that depend on the MCP-1 protein. In this work, we sought to investigate the potential effect of the MCP-1 protein on myocardial remodelling *in vivo* in a murine model of MI. To achieve this objective, we used a $^{19}F/^{1}H$ multi nuclear MRI. ^{19}F MRI has emerged as a new platform to study inflammation, taking advantage of the phagocytic capacity of inflammatory cells in uptaking ^{19}F PFC. To study the effect of MCP-1 in scar formation, an elastin-specific MR contrast agent has been used. Elastin, along with collagen, is upregulated after MI and is one of the main ECM constituent, making it suitable for the study of LV remodelling *in vivo*.

Our study demonstrates that in the absence of the MCP-1 protein, inflammatory cell infiltration is highest at day 3 compared with WT mice, which is in agreement with the presence of high amounts of inflammatory monocytes. However, no significant differences in monocyte population were observed, while

macrophages infiltration was reduced. MCP-1$^{-/-}$ animals also showed a delayed deposition of ECM proteins as assessed both with *in vivo* MRI and *ex vivo* histology, which was associated with the presence of fibroblasts.

Cardiac function

Here we assessed the effect of the MCP-1 protein in cardiac output *in vivo* MRI. While no differences were observed in infarct size and EF between strains, WT animals showed a more evident increase in LV mass and LVEDV, while a moderate increase was observed in MCP-1$^{-/-}$ mice. High levels of MCP-1 protein have been associated with an elevated risk of MI in humans [285]. In CD-1 mice (used for genetic studies instead of WT), anti-MCP-1 gene therapy was shown to attenuate ventricular dilatation and preserved cardiac function after MI [277] and in MCP-1$^{-/-}$ mice of reperfused MI [32].

Assessment of Leukocyte recruitment with ^{19}F MRI

CCL2/MCP-1 has shown to be a potent chemoattractant chemokine for monocytes *in vitro* and critically regulates the recruitment of this cells *in vivo* as shown in different animal models of inflammation [287, 288]. In mice, after reperfused MI, MCP-1 is upregulated followed by prolonged induction of its receptor CCR2 [32]. ^{19}F MRI allows the study of the recruitment of inflammatory cells *in vivo* [97, 135, 238]. To our knowledge, no study has described the temporal evolution of inflammatory cells in MCP-1 deficient mice. Here, we examine the effect of MCP-1 protein in immune cell infiltration *in vivo* after MI, after the injection of ^{19}F PFCs in both WT and MCP-1$^{-/-}$ animals.

We found that permanent occlusion of the LAD resulted in an earlier peak of the ^{19}F signal in MCP-$1^{-/-}$ at 3 days, compared to a peak at day 7 in WT animals. At day 7 MCP-$1^{-/-}$ mice showed a significantly decrease in ^{19}F signal compared with WT. Furthermore, at 21 days post-MI, a more evident decrease in ^{19}F signal was observed in WT (*P<0.001*) compared with MCP-$1^{-/-}$ mice (*P<0.05*). *Ex vivo* ^{19}F signal quantification by NMR showed similar results.

To understand the source of the ^{19}F signal, monocyte populations were analysed by FACS and macrophages with IHC. MI triggers the recruitment of neutrophils and monocytes. Although neutrophils do not express CCR2 and therefore do not respond to MCP-1, some studies reported that MCP-1 might play a role in neutrophil recruitment by an interdependence between monocyte and neutrophil recruitment in pulmonary inflammation. In MI, the disruption of MCP-1 did not affect the time course or density of neutrophils [32]. Similarly, no difference was observed in our study (data not shown). Monocyte recruitment after an acute injury is characterized by a biphasic response where, first an early peak of circulating inflammatory monocytes (Ly6C^{high}) is observed followed by an increase in reparative monocytes (Ly6C^{low}) [10]. Here no differences were observed in blood monocytes between WT and MCP-$1^{-/-}$ mice. In agreement with the *in vivo* MRI findings, MCP-$1^{-/-}$ animals showed an early peak of monocytes in infarcted tissue at day 3, while in WT mice, monocytes were elevated at day 7. Both monocytes subtypes showed a similar recruitment pattern in both strains, with an early recruitment of inflammatory monocytes followed by reparative monocytes. Because of this similarity, it can be speculated that a compensatory process occurs, especially because CCR2 ligands bind not only to MCP-1 but also to MCP-3 and MCP-5. Besides the role of MCP1 in the recruitment of

monocytes, CCL7 also has been shown to be involved in this process [289, 290]. In another study, it was shown that the vasoconstrictive hormone angiotensin II promotes the release of Ly6C^{high} monocytes from the spleen, independently of CCR2 signalling [35] . This compensatory mechanism is not fully understood, and more investigations needs to be performed to better understand the recruitment of monocytes to the site of injury.

The recruitment of macrophages was studied by IHC. We found that MCP-1$^{-/-}$ mice recruited overall less macrophages to the site of injury than WT animals. At day 3 a significant difference was observed in the recruitment of these cells, with WT mice showing higher recruitment than MCP-1$^{-/-}$ mice. However, when comparing 7 and 21 days, despite the lower number of macrophages in MCP-1$^{-/-}$ mice no significant differences were detected compared with WT at each time point. Dewald et al [32], in a reperfused model of MI showed that MCP-1 null mice had a decreased and delayed recruitment of macrophages to the infarct area, compared with WT mice. In their study, macrophages peaked at day 24 after reperfusion in WT animals, and after 72 hours in MCP-1$^{-/-}$ mice.

From our findings, although monocyte response seems to be comparable in both strains, macrophage recruitment behaved differently. In fact, we hypothesized that the MCP-1 protein may influence monocyte differentiation. MCP-1 has been associated with modulating monocyte phenotype and activity *in vitro* [291] and *in vivo [32]*. In the reperfused model of MI, Dewald and colleagues observed that MCP-1$^{-/-}$ mice showed a decreased expression of OPN-1 compared with WT [32]. OPN-1 is a marker of monocyte-to-macrophage differentiation [292], highly expressed in mature macrophages of the healing infarct [293]. However, in this study FACS was not performed, and no

quantification was performed to assess the monocyte populations. Therefore, it is not clear if the decrease in macrophage population is due to the decrease in OPN expression or due to fewer monocytes. In rats, the neutralization of MCP-1 has been also associated with a decrease in adhesion molecule expression and macrophage infiltration [273]. The analysis of macrophage activity would be interesting to assess, e.g. by comparing plasma levels of TNFα and IL-6 between MCP-1$^{-/-}$ and WT.

Effect of MCP-1 in protein deposition assessed with MRI

The effect on the MCP-1 protein in scar formation was assessed with MRI one hour after the injection of Gd-ESMA. Gd-ESMA allows the direct quantification of elastin and tropoelastin proteins *in vivo*. A significant increase of Gd-ESMA uptake was observed between 7 and 21 days post-MI in WT, but not in MCP-1$^{-/-}$ animals. Furthermore, at day 21, MCP-1$^{-/-}$ animals showed a significant lower R1 value compared with WT mice, suggesting less post-infarct myocardial remodelling. The presence of elastin and tropoelastin proteins was analysed by histology. Due to the thinner shape, elastin quantification with Elastic Van Gieson was challenging. Therefore, tropoelastin (elastin precursor) was studied by IHC and used to quantify the presence of this protein within the infarcted areas. In good agreement with the *in vivo* findings, *ex vivo* IHC showed a significant increase in tropoelastin in the WT animals between 7 and 21days, but not in the MCP-1$^{-/-}$ mice. A significant difference in tropoelastin was observed at day 21 post-MI, where WT mice showed a greater amount of tropoelastin compared with MCP-1$^{-/-}$ mice. Apart from tropoelastin also collagen was

downregulated in MCP-1$^{-/-}$ mice. Trichrome staining showed that collagen is significantly reduced in MCP-1$^{-/-}$ animals compared with WT mice.

The production of ECM proteins is regulated by fibroblasts. These cells differentiate in myofibroblasts, and transiently appear during granulation tissue formation and warrants further exploitation.

7.7 - Limitations

As described in **section 6.7**.

7.8 - Conclusions

We demonstrate the feasibility of simultaneous assessment of inflammation and remodelling in a mouse model of MI using ^{19}F PFCs and Gd-ESMA in concert with a ^{1}H/^{19}F multi nuclear coil at 3T. Our results show that MCP-1$^{-/-}$ mice have a prolonged but attenuated inflammatory phase and lower tropoelastin production within the healing myocardium compared to WT mice. Future studies are now warranted to investigate the effects of these differences on cardiac function.

Chapter 8

General discussion & Future directions

Myocardial infarction (MI), and subsequent heart failure, remains a major healthcare problem in the western and developing world and leads to substantial morbidity and mortality worldwide. Diagnosis is currently being performed with conventional diagnostic exams such as the electrocardiograms or blood tests, however often additional information is required not provided by these tests. Imaging techniques such as X-ray angiography, echocardiography or cardiac MR are the mainstay in cardiology and allow the assessment of anatomy, perfusion, function and viability, but do not provide insights into specific biological processes occurring within the heart after MI.

The process of infarct healing after MI consists of three phases: the inflammatory phase where neutrophils and macrophages remove dead cells and extracellular matrix debris, the proliferative phase during which fibroblast proliferation and angiogenesis forms granulation tissue and finally collagen synthesis and cross-linking to form a fibrous scar during the maturation phase (**Chapter 2**). Prognostic outcome is closely dependent upon a balance of the

duration and severity of these phases, resulting in either a stable scar or adverse myocardial remodelling leading to rupture or subsequent heart failure.

Novel non-invasive imaging methods, based on target specific imaging agents, may allow the imaging of the molecular processes underlying the post-MI immune cell response, and subsequent myocardial remodelling (**Chapter 3**). Molecular MRI has proven to be a particularly promising for the assessment of post MI remodelling. It provides high resolution images with intrinsic soft-tissue contrast, in concert with cellular and molecular information (**Chapter 4**). Compared to molecular MRI, other imaging modalities such as PET and SPECT have the advantage of requiring very small doses of the imaging probes, making their clinical translational more straight forward; however, these modalities are associated with ionising radiation and do not provide high spatial resolution, which is important for the evaluation of the cardiovascular system.

For the development and validation of these novel contrast agents, preclinical research plays a very important role. Several animal models, including genetically modified mice (also known as knockout), are available for the study of the different mechanisms underlying cardiac diseases Experimental mouse models provide well controlled experimental conditions and this lend themselves ideally to test the potential of novel imaging probes to visualise and quantify the cellular and molecular events altered during disease onset, progression or complication. One of the challenges of the MI model is the difficulty of reproducibility and the high mortality rate. Reproducibility is highly dependent on the surgeon's skills. Highly experienced surgeons might help maintaining consistency between surgeries however some aspects cannot be controlled such as the physiology of the animal. The induction of infarct requires the intubation of

the animal. A reproducible and robust method for mouse intubation as well as the protocol for the induction of MI in mice by permanent occlusion of the left-anterior descending coronary artery (LAD) has been described in this project in **Chapter 5**.

Molecular imaging often lacks standardization and reliable approaches for obtaining quantitative measurements of disease activity. **Chapter 5** further discusses the development of a MR compatible heating system for the assessment of animal temperature during the imaging sessions. The importance of the heating system, besides allowing the monitoring of the animals throughout the scanning period, is the ability of maintaining a reliable ECG signal (constant body temperature=constant heart rate), which is very important for the all MRI sequence protocols (e.g. T_1 MOLLI with images acquired over several cardiac cycles) as the sequences have to be synchronised with the ECG.

Inflammation plays a central role in MI. Higher amounts of inflammatory cells are observed following MI, making them an excellent biomarker for early and late disease detection and guidance of treatment. Macrophages phagocytose foreign bodies and this behaviour is exploited in the study design that involves the intravenous injection of nanoparticle based contrast agents. These particles can be either phagocytosed by blood-monocytes or by resident macrophages in the infarcted tissue. Non-invasive imaging of inflammatory cells using magnetic nanoparticles (MNPs) during infarct healing has been shown previously. The most widely used magnetic nanoparticles are the ultra-small super-paramagnetic iron oxide (USPIO) particles, which are known as potent T_2/T_2^* MRI contrast agents. In addition to preclinical research, USPIO nanoparticles have been also evaluated in small-scale patient studies and clinical

trials. A drawback of MNP detection, however, is the difficulty in differentiating between MNP accumulation and focal tissue interfaces due to local susceptibility gradients as well as areas of low proton density. An alternative approach is the use of ^{19}F perfluorocarbons (PFCs). ^{19}F MRI has been used in multiple inflammatory disease models in preclinical research, including MI, allowing the selective imaging of inflammatory cells *in vivo* without any contamination from background signal and may also allow for more accurate signal quantification. Different PFCs have been described and its characteristics have been discussed in **Chapter 5**.

In **Chapter 6** the potential of a multinuclear $^{19}F/^{1}H$ MRI for the selective imaging of inflammatory cells after MI was investigated in wild-type (WT) animals. MI was induced after permanent occlusion of the LAD and animals were imaged at 3,7, 14 and 21 days post-MI. ^{19}F PFCs signal was increased in areas of infarction, and absent in remote tissue. This was in agreement with the presence of inflammatory cells in the infarct zone, as confirmed by histology (positive MAC-3 immunohistochemistry (IHC)). Absolute quantification of ^{19}F signal was performed after excision of the heart, and after separating remote and infarcted tissues, with 9.4T NMR spectroscopy. A linear relationship was found between *in vivo* MRI measurements and *ex vivo* NMR signal quantification. The predictive prognostic power of ^{19}F PFCs was also investigated in a longitudinal proof-of-principle study, confirming that a balanced inflammatory response results in a better recovery of the heart.

Fluorine PFCs have shown promising results in cell labelling and in molecular imaging. Some fluorine-based compounds are FDA approved such as blood substitutes and cell tracking applications. More recently, the first ^{19}F MRI

agent has been FDA approved for *in vivo* cell tracking (Celsense Inc., Pittsburgh, USA). Because of the detection limit and SNR challenges, the clinical implementation of $^{1}H/^{19}F$ MRI might be challenging as it requires dedicated MR equipment, such as broadband radiofrequency amplifiers and coils. To improve SNR, usually multiple injections are required for *in vivo* ^{19}F MRI. PFCs accumulate in the liver and spleen for many days to weeks which represents a challenge for clinical translational. Efforts in changing the chemical structure and coating of ^{19}F PFCs might help increasing SNR and decreasing retention time in the body.

During wound healing and subsequent formation of the fibrotic scar the synthesis of extracellular matrix (ECM) proteins is upregulated. Of the specific ECM proteins, collagen type I has been found to be a major constituent of scar formation and stabilization. Besides collagen, elastin has been identified as a key ECM protein decisive for infarct stabilization and preservation of ventricular function. Elastic fibres deposition increases within the myocardial scar in the first weeks following ischemic injury and continues to form a dense network between remaining viable myocytes, myofibroblasts and smooth muscle cells during maturation of the infarct scar. The abundance of elastin within the myocardial scar makes this ECM protein a promising imaging biomarker for molecular MRI. Here, we explore the merits of an elastin-specific MR contrast agent (Gd-ESMA) for the assessment of elastin deposition during left-ventricular (LV) remodelling which is presented in **Chapters 6**. Late-gadolinium enhancement sequence was employed one hour after intravenous administration of Gd-ESMA at 7,14 and 21 days post-MI animals. In the infarcted tissue, Gd-ESMA uptake (measured as R_1 relaxation rate) increased significantly from day 7 to day 21 because of the

synthesis of elastin/tropoelastin. Validation of tropoelastin deposition was confirmed with IHC *ex vivo*. At 3 days post-MI, Gd-ESMA behaved similarly to a conventional gadolinium contrast agent, with non-specific retention being the main mechanisms for accumulation in the infarcted tissue. Its retention in the infarct areas might be attributed to oedema, cellular swelling and rupture and subsequent increase in extracellular volume, as shown in other animal models. Consistent with this, we observed high signal intensity on native T_2-weighted images at day 3 post-MI, which was absent at day 7. We further investigated the prognostic value of Gd-ESMA in a longitudinal proof-of-principle study. The results of this study suggested that deposition of tropoelastin at early stages of MI (day 7) lead to a worse cardiac output (measured as end-diastolic volume) at day 21.

Gd-ESMA has also been used for molecular imaging of vessel wall elastin in atherosclerosis, and was shown to generates persistent enhancement of myocardial scar due to the specific binding to elastin/tropoelastin fibres. Whole heart MRI could potentially provide scar and coronary plaque burden measurement in a single scan. This could potentially enable the early detection of atherosclerosis and the evaluation of novel cardio-protective therapies.

A similar study was performed in Monocyte Chemoattractant Protein 1 knockout (MCP-$1^{-/-}$) animals and is described in **Chapter 7**. The same animal model was used under similar experimental conditions for the *in vivo* experiments of **Chapter 6** and therefore direct comparison can be made between WT and MCP-$1^{-/-}$ animals. MCP-1 levels increased after MI, and is responsible for the recruitment of inflammatory cells into the myocardium. In MCP-$1^{-/-}$ animals, deficient recruitment of macrophages into the healing infarct has been observed,

and its influence in ECM production has also been reported. Here we aimed to evaluate the potential of multinuclear $^{19}F/^{1}H$ MRI to explore the effect of MCP-1 protein during myocardial healing *in vivo*. Monocyte/macrophage recruitment usually occurs during the first weeks after MI; therefore, MRI scans were performed at 3 and 7 days post-MI. A later time-point of 21 days was also investigated in order to study the impact of MCP-1 on ECM protein deposition. Early and strong uptake of ^{19}F-PFCs was observed in the MCP-$1^{-/-}$ hearts at day 3, while ^{19}F signal peaked at day 7 in WT animals. Flow cytometry analysis showed similar recruitment patterns of monocytes in the blood and infarcted tissue in WT and MCP-$1^{-/-}$ mice. Macrophage infiltration was analysed by IHC, and was lower in MCP-$1^{-/-}$ than in WT mice. The ^{19}F signal is a result from the uptake by both monocytes and macrophages, possible justifying the difference in signal from both animal strains. The deposition of elastin/tropoelastin was analysed by T_1 mapping at day 7 and 21 post-MI, and was lower in MCP-$1^{-/-}$ than in WT mice. This finding was confirmed by tropoelastin IHC. Scar formation requires the proliferation of fibroblasts, which have the ability to synthesize ECM proteins. Fibroblasts were identified by vimentin positive by IHC. MCP-$1^{-/-}$ animals showed delayed infiltration of fibroblasts at 3 days post-MI compared with WT, while at 7 days no difference was observed between both animal strains. In contrast, a significant reduction of fibroblasts was observed in WT animals compared to MCP-$1^{-/-}$ mice at day 21, which was consistent with the resolution of the maturation phase. Cine scans allowed the study of LV function. WT showed a significant expansion of the LV, while a more moderate expansion was observed in MCP-$1^{-/-}$ 21 days post-MI. Overall, our results suggests that MCP-$1^{-/-}$ might attenuate LV remodelling by affecting inflammatory cell

recruitment and ECM production, and be beneficial myocardial remodelling. However, more investigations need to be performed to better understand the biology underlying these processes.

In this PhD project, two novel contrast agents, ^{19}F PFCs and Gd-ESMA, were investigated and evaluated for the simultaneous assessment of inflammation and ECM remodelling in a murine model of myocardial infarction. ^{19}F MRI was established as a new platform technology at KCL for imaging inflammation in mouse models of MI. I demonstrated that Gd-ESMA has potential for the quantification of myocardial remodelling at 3T. Further research will focus on how these agents could be used for risk stratification and treatment monitoring in patients post-MI.

Curriculum Vitae

Name	**Isabel Maria da Silva Teixeira Ramos**
Address	King's College London
	Division of Imaging Sciences and Biomedical Engineering
	4th Floor, Lambeth Wing, St Thomas' Hospital
	London SE1 7EH
Phone	+447546876507
Email	isabelmtramos@gmail.com/ isabel.ramos@kcl.ac.uk
Date of birth	03 March 1990
Place of birth	Porto (Portugal)
Nationality	Portuguese

Education

2014- current : PhD candidate in Biomedical Engineering
King's College London (KCL), London, United Kingdom

2008 – 2013: MSc in Bioengineering major of Biomedical Engineering (Hons)
Faculty of Engineering, University of Porto, Portugal

Research and working experience

CAREER EXPERIENCE

2014/15 – 2015/16: Teaching experience
Assisted undergraduate students at Physics modules (lab demonstrator 40 hours).

Feb- Jul 2013: Research Intern (Erasmus placement; Master thesis)
Travelled to Barcelona, Spain to investigate the regenerative process of the heart in a zebrafish model. Placement at Professor Raya's Laboratory, Control of Stem Cell Potency Group, Institute for Bioengineering of Catalonia.

List of publications

Ramos I T, Henningsson M, Nezafat M, Lavin B, Lorrio S, Gebhardt P, Protti A, Eykyn T R, Andia M E, Flögel U, Phinikaridou A, Shah A M, Botnar R M. Molecular imaging of inflammation and extracellular matrix remodelling in a murine model of myocardial infarction. (**in preparation**)

Ramos I T, Lavin B, Phinikaridou A, Henningsson M, Eykyn T R, Flögel U, Shah A M, Botnar R M. In vivo imaging of monocyte chemoattractant protein-1 role in myocardial remodelling after MI. (**in preparation**)

Nezafat M, **Ramos I T**, Henningsson M, Protti A, Basha T, Botnar R M. Improved Segmented Modified Look-Locker Inversion Recovery T_1 Mapping Sequence in Mice. (**in review**)

Abstracts

Ramos I, Henningsson M, Nezafat M, Lavin B, Lorrio S, Phinikaridou A, Flögel U, Shah AM, Botnar RM. Molecular imaging of inflammation and extracellular matrix remodeling in a murine model of myocardial infarction. International Society for Magnetic Resonance in Medicine **(ISMRM),** Hawaii, USA, 2017. (**oral presentation. Summa Cum Laude Merit Award**).

Ramos I, Henningsson M, Lavin B, Lorrio S, Phinikaridou A, Flögel U, Shah AM, Botnar RM. Molecular Imaging of the effects of monocyte chemoattractant protein-1 (MCP-1) on extracellular matrix remodelling following myocardial infarction. Category: Applications of Molecular Imaging & Hyperpolarized MRI. **ISMRM**, Hawaii, USA, 2017 (**E-poster**).

Ramos I, Henningsson M, Nezafat M, Lavin B, Lorrio S, Eykyn T, Phinikaridou A, Flögel U, Shah A, Botnar R. Molecular imaging of inflammation and extracellular matrix remodelling after myocardial infarction. **King's BHF Centre of Research Excellence Annual Symposium**. London, January 2017 (**Poster**).

Ramos I, Henningsson M, Lavin B, Gebhardt P, Protti A, Nezafat M, Lacerda S, Lorrio S, Phinikaridou A, Shah A, Botnar RM. Molecular imaging of inflammation and extracellular matrix remodelling after myocardial infarction. **ISMRM**, Singapore,2016 (**oral presentation. Magna Cum Laude Merit Award**).

Ramos I, Henningsson M, Lavin B, Gebhardt P, Protti A, Nezafat M, Lacerda S, Lorrio S, Phinikaridou A, Shah A, Botnar RM. Molecular imaging of inflammation and extracellular matrix remodelling after myocardial infarction. **Divisional Symposium Imaging Sciences & Biomedical Engineering** Department King's College London, London, UK, 2015 (**oral presentation. Top 10 abstracts**).

Bibliography

1. Cannon, B., *Cardiovascular disease: Biochemistry to behaviour.* Nature, 2013. **493**(7434): p. S2-3.
2. Lewis, E.F., et al., *Predictors of late development of heart failure in stable survivors of myocardial infarction: the CARE study.* J Am Coll Cardiol, 2003. **42**(8): p. 1446-53.
3. Aaronson, P. and J.P.T. Ward, *The cardiovascular system at a glance*. 1999, Malden, Mass.: Blackwell Science.
4. Murry, C.E., H. Reinecke, and L.M. Pabon, *Regeneration gaps: observations on stem cells and cardiac repair.* J Am Coll Cardiol, 2006. **47**(9): p. 1777-85.
5. Gheorghiade, M. and R.O. Bonow, *Chronic heart failure in the United States: a manifestation of coronary artery disease.* Circulation, 1998. **97**(3): p. 282-9.
6. St John Sutton, M., et al., *Cardiovascular death and left ventricular remodeling two years after myocardial infarction: baseline predictors and impact of long-term use of captopril: information from the Survival and Ventricular Enlargement (SAVE) trial.* Circulation, 1997. **96**(10): p. 3294-9.
7. Frangogiannis, N.G., *The mechanistic basis of infarct healing.* Antioxid Redox Signal, 2006. **8**(11-12): p. 1907-39.
8. Frangogiannis, N.G., *The immune system and cardiac repair.* Pharmacol Res, 2008. **58**(2): p. 88-111.
9. Frangogiannis, N.G., *The inflammatory response in myocardial injury, repair, and remodelling.* Nat Rev Cardiol, 2014. **11**(5): p. 255-65.
10. Nahrendorf, M., et al., *The healing myocardium sequentially mobilizes two monocyte subsets with divergent and complementary functions.* J Exp Med, 2007. **204**(12): p. 3037-47.
11. Swirski, F.K. and M. Nahrendorf, *Leukocyte behavior in atherosclerosis, myocardial infarction, and heart failure.* Science, 2013. **339**(6116): p. 161-6.
12. Epelman, S., P.P. Liu, and D.L. Mann, *Role of innate and adaptive immune mechanisms in cardiac injury and repair.* Nat Rev Immunol, 2015. **15**(2): p. 117-29.
13. Gordon, S. and P.R. Taylor, *Monocyte and macrophage heterogeneity.* Nat Rev Immunol, 2005. **5**(12): p. 953-64.
14. Camelliti, P., T.K. Borg, and P. Kohl, *Structural and functional characterisation of cardiac fibroblasts.* Cardiovasc Res, 2005. **65**(1): p. 40-51.
15. Kusachi , S. and Y. Ninomiya, *Myocardial Infarction and Cardiac Fibrogenesis*. 2003: Springer US.
16. Wynn, T.A., *Cellular and molecular mechanisms of fibrosis.* J Pathol, 2008. **214**(2): p. 199-210.
17. van den Borne, S.W., et al., *Myocardial remodeling after infarction: the role of myofibroblasts.* Nat Rev Cardiol, 2010. **7**(1): p. 30-7.

18. Frangogiannis, N.G., *Matricellular proteins in cardiac adaptation and disease.* Physiol Rev, 2012. **92**(2): p. 635-88.
19. Fan, D., et al., *Cardiac fibroblasts, fibrosis and extracellular matrix remodeling in heart disease.* Fibrogenesis Tissue Repair, 2012. **5**(1): p. 15.
20. van der Laan, A.M., M. Nahrendorf, and J.J. Piek, *Healing and adverse remodelling after acute myocardial infarction: role of the cellular immune response.* Heart, 2012. **98**(18): p. 1384-90.
21. Weber, K.T., et al., *Remodeling and reparation of the cardiovascular system.* J Am Coll Cardiol, 1992. **20**(1): p. 3-16.
22. Frangogiannis, N.G. and M.L. Entman, *Targeting the chemokines in myocardial inflammation.* Circulation, 2004. **110**(11): p. 1341-2.
23. Blankesteijn, W.M., et al., *Dynamics of cardiac wound healing following myocardial infarction: observations in genetically altered mice.* Acta Physiol Scand, 2001. **173**(1): p. 75-82.
24. Cleutjens, J.P., et al., *The infarcted myocardium: simply dead tissue, or a lively target for therapeutic interventions.* Cardiovasc Res, 1999. **44**(2): p. 232-41.
25. Ertl, G. and S. Frantz, *Healing after myocardial infarction.* Cardiovasc Res, 2005. **66**(1): p. 22-32.
26. Frangogiannis, N.G., *Regulation of the inflammatory response in cardiac repair.* Circ Res, 2012. **110**(1): p. 159-73.
27. Birdsall, H.H., et al., *Complement C5a, TGF-beta 1, and MCP-1, in sequence, induce migration of monocytes into ischemic canine myocardium within the first one to five hours after reperfusion.* Circulation, 1997. **95**(3): p. 684-92.
28. Dreyer, W.J., et al., *Kinetics of C5a release in cardiac lymph of dogs experiencing coronary artery ischemia-reperfusion injury.* Circ Res, 1992. **71**(6): p. 1518-24.
29. Granger, C.B., et al., *Pexelizumab, an anti-C5 complement antibody, as adjunctive therapy to primary percutaneous coronary intervention in acute myocardial infarction: the COMplement inhibition in Myocardial infarction treated with Angioplasty (COMMA) trial.* Circulation, 2003. **108**(10): p. 1184-90.
30. Faxon, D.P., et al., *The effect of blockade of the CD11/CD18 integrin receptor on infarct size in patients with acute myocardial infarction treated with direct angioplasty: the results of the HALT-MI study.* J Am Coll Cardiol, 2002. **40**(7): p. 1199-204.
31. Colotta, F., et al., *Modulation of granulocyte survival and programmed cell death by cytokines and bacterial products.* Blood, 1992. **80**(8): p. 2012-20.
32. Dewald, O., et al., *CCL2/Monocyte Chemoattractant Protein-1 regulates inflammatory responses critical to healing myocardial infarcts.* Circ Res, 2005. **96**(8): p. 881-9.
33. Takahashi, T., et al., *Relationship of admission neutrophil count to microvascular injury, left ventricular dilation, and long-term outcome in patients treated with primary angioplasty for acute myocardial infarction.* Circ J, 2008. **72**(6): p. 867-72.
34. Horckmans, M., et al., *Neutrophils orchestrate post-myocardial infarction healing by polarizing macrophages towards a reparative phenotype.* Eur Heart J, 2016.

35. Swirski, F.K., et al., *Identification of splenic reservoir monocytes and their deployment to inflammatory sites.* Science, 2009. **325**(5940): p. 612-6.
36. Panizzi, P., et al., *Impaired infarct healing in atherosclerotic mice with Ly-6C(hi) monocytosis.* J Am Coll Cardiol, 2010. **55**(15): p. 1629-38.
37. Hansson, G.K. and P. Libby, *The immune response in atherosclerosis: a double-edged sword.* Nat Rev Immunol, 2006. **6**(7): p. 508-19.
38. Robbins, C.S., et al., *Extramedullary hematopoiesis generates Ly-6C(high) monocytes that infiltrate atherosclerotic lesions.* Circulation, 2012. **125**(2): p. 364-74.
39. Phinikaridou, A., et al., *Molecular MRI of atherosclerosis.* Molecules, 2013. **18**(11): p. 14042-69.
40. Doughty, R.N., et al., *Effects of carvedilol on left ventricular remodeling after acute myocardial infarction: the CAPRICORN Echo Substudy.* Circulation, 2004. **109**(2): p. 201-6.
41. Zouggari, Y., et al., *B lymphocytes trigger monocyte mobilization and impair heart function after acute myocardial infarction.* Nat Med, 2013. **19**(10): p. 1273-80.
42. Hofmann, U., et al., *Activation of CD4+ T lymphocytes improves wound healing and survival after experimental myocardial infarction in mice.* Circulation, 2012. **125**(13): p. 1652-63.
43. Anzai, A., et al., *Regulatory role of dendritic cells in postinfarction healing and left ventricular remodeling.* Circulation, 2012. **125**(10): p. 1234-45.
44. Weirather, J., et al., *Foxp3+ CD4+ T cells improve healing after myocardial infarction by modulating monocyte/macrophage differentiation.* Circ Res, 2014. **115**(1): p. 55-67.
45. Chen, W. and N.G. Frangogiannis, *Fibroblasts in post-infarction inflammation and cardiac repair.* Biochim Biophys Acta, 2013. **1833**(4): p. 945-53.
46. Willems, I.E., et al., *The alpha-smooth muscle actin-positive cells in healing human myocardial scars.* Am J Pathol, 1994. **145**(4): p. 868-75.
47. Cleutjens, J.P., et al., *Collagen remodeling after myocardial infarction in the rat heart.* Am J Pathol, 1995. **147**(2): p. 325-38.
48. Sun, Y. and K.T. Weber, *Infarct scar: a dynamic tissue.* Cardiovasc Res, 2000. **46**(2): p. 250-6.
49. Erlebacher, J.A., et al., *Late effects of acute infarct dilation on heart size: a two dimensional echocardiographic study.* Am J Cardiol, 1982. **49**(5): p. 1120-6.
50. White, H.D., et al., *Left ventricular end-systolic volume as the major determinant of survival after recovery from myocardial infarction.* Circulation, 1987. **76**(1): p. 44-51.
51. Kim, S.H., J. Turnbull, and S. Guimond, *Extracellular matrix and cell signalling: the dynamic cooperation of integrin, proteoglycan and growth factor receptor.* J Endocrinol, 2011. **209**(2): p. 139-51.
52. Díez, J., et al., *Losartan-dependent regression of myocardial fibrosis is associated with reduction of left ventricular chamber stiffness in hypertensive patients.* Circulation, 2002. **105**(21): p. 2512-7.
53. Narula, J. and H.W. Strauss, *The popcorn plaques.* Nat Med, 2007. **13**(5): p. 532-4.

54. Jeremias, A., et al., *Coronary artery compliance and adaptive vessel remodelling in patients with stable and unstable coronary artery disease.* Heart, 2000. **84**(3): p. 314-9.
55. Medugorac, I., *Characterization of intramuscular collagen in mammalian left ventricle.* Basic Res Cardiol, 1982. **77**(6): p. 589-98.
56. Pfeffer, M.A. and E. Braunwald, *Ventricular remodeling after myocardial infarction. Experimental observations and clinical implications.* Circulation, 1990. **81**(4): p. 1161-72.
57. Bassett, E.G. and J.S. Wakefield, *Elastic fibers in myocardial scars in rats: development teraction with other components.* Connect Tissue Res, 2008. **49**(5): p. 321-7.
58. Mizuno, T., et al., *Overexpression of elastin fragments in infarcted myocardium attenuates scar expansion and heart dysfunction.* Am J Physiol Heart Circ Physiol, 2005. **288**(6): p. H2819-27.
59. Mizuno, T., et al., *Elastin stabilizes an infarct and preserves ventricular function.* Circulation, 2005. **112**(9 Suppl): p. I81-8.
60. Hinek, A. and M. Rabinovitch, *67-kD elastin-binding protein is a protective "companion" of extracellular insoluble elastin and intracellular tropoelastin.* J Cell Biol, 1994. **126**(2): p. 563-74.
61. Clarke, A.W., et al., *Coacervation is promoted by molecular interactions between the PF2 segment of fibrillin-1 and the domain 4 region of tropoelastin.* Biochemistry, 2005. **44**(30): p. 10271-81.
62. Dewald, O., et al., *Of mice and dogs: species-specific differences in the inflammatory response following myocardial infarction.* Am J Pathol, 2004. **164**(2): p. 665-77.
63. Wu, J.C., et al., *Influence of sex on ventricular remodeling after myocardial infarction in mice.* J Am Soc Echocardiogr, 2003. **16**(11): p. 1158-62.
64. Brilla, C.G., J.S. Janicki, and K.T. Weber, *Cardioreparative effects of lisinopril in rats with genetic hypertension and left ventricular hypertrophy.* Circulation, 1991. **83**(5): p. 1771-9.
65. Klocke, R., et al., *Surgical animal models of heart failure related to coronary heart disease.* Cardiovasc Res, 2007. **74**(1): p. 29-38.
66. Hood, W.B., B. McCarthy, and B. Lown, *Myocardial infarction following coronary ligation in dogs. Hemodynamic effects of isoproterenol and acetylstrophanthidin.* Circ Res, 1967. **21**(2): p. 191-9.
67. Kuhlmann, M.T., et al., *G-CSF/SCF reduces inducible arrhythmias in the infarcted heart potentially via increased connexin43 expression and arteriogenesis.* J Exp Med, 2006. **203**(1): p. 87-97.
68. Iwanaga, K., et al., *Effects of G-CSF on cardiac remodeling after acute myocardial infarction in swine.* Biochem Biophys Res Commun, 2004. **325**(4): p. 1353-9.
69. Chimenti, S., et al., *Myocardial infarction: animal models.* Methods Mol Med, 2004. **98**: p. 217-26.
70. Vandervelde, S., et al., *Increased inflammatory response and neovascularization in reperfused vs. non-reperfused murine myocardial infarction.* Cardiovasc Pathol, 2006. **15**(2): p. 83-90.
71. Saraste, A., S.G. Nekolla, and M. Schwaiger, *Cardiovascular molecular imaging: an overview.* Cardiovasc Res, 2009. **83**(4): p. 643-52.
72. Naresh, N.K., et al., *Molecular Imaging of Healing After Myocardial Infarction.* Curr Cardiovasc Imaging Rep, 2011. **4**(1): p. 63-76.

73. Jivraj, N., et al., *Molecular imaging of myocardial infarction.* Basic Res Cardiol, 2014. **109**(1): p. 397.
74. McMurray, J.J. and M.A. Pfeffer, *Heart failure.* Lancet, 2005. **365**(9474): p. 1877-89.
75. Beeres, S.L., et al., *Role of imaging in cardiac stem cell therapy.* J Am Coll Cardiol, 2007. **49**(11): p. 1137-48.
76. Dobrucki, L.W. and A.J. Sinusas, *PET and SPECT in cardiovascular molecular imaging.* Nat Rev Cardiol, 2010. **7**(1): p. 38-47.
77. Phelps, M.E., *PET: the merging of biology and imaging into molecular imaging.* J Nucl Med, 2000. **41**(4): p. 661-81.
78. Mulder, W.J., et al., *Imaging and nanomedicine in inflammatory atherosclerosis.* Sci Transl Med, 2014. **6**(239): p. 239sr1.
79. Dobrucki, L.W. and A.J. Sinusas, *Molecular imaging. A new approach to nuclear cardiology.* Q J Nucl Med Mol Imaging, 2005. **49**(1): p. 106-15.
80. Arrighi, J.A. and V. Dilsizian, *Multimodality imaging for assessment of myocardial viability: nuclear, echocardiography, MR, and CT.* Curr Cardiol Rep, 2012. **14**(2): p. 234-43.
81. Jaarsma, C., et al., *Diagnostic performance of noninvasive myocardial perfusion imaging using single-photon emission computed tomography, cardiac magnetic resonance, and positron emission tomography imaging for the detection of obstructive coronary artery disease: a meta-analysis.* J Am Coll Cardiol, 2012. **59**(19): p. 1719-28.
82. Beller, G.A. and R.C. Heede, *SPECT imaging for detecting coronary artery disease and determining prognosis by noninvasive assessment of myocardial perfusion and myocardial viability.* J Cardiovasc Transl Res, 2011. **4**(4): p. 416-24.
83. Ghosh, N., et al., *Assessment of myocardial ischaemia and viability: role of positron emission tomography.* Eur Heart J, 2010. **31**(24): p. 2984-95.
84. Mendoza, D.D., et al., *Viability imaging by cardiac computed tomography.* J Cardiovasc Comput Tomogr, 2010. **4**(2): p. 83-91.
85. Feuchtner, G., et al., *Adenosine stress high-pitch 128-slice dual-source myocardial computed tomography perfusion for imaging of reversible myocardial ischemia: comparison with magnetic resonance imaging.* Circ Cardiovasc Imaging, 2011. **4**(5): p. 540-9.
86. Constantine, G., et al., *Role of MRI in clinical cardiology.* Lancet, 2004. **363**(9427): p. 2162-71.
87. Ugander, M., et al., *Myocardial edema as detected by pre-contrast T1 and T2 CMR delineates area at risk associated with acute myocardial infarction.* JACC Cardiovasc Imaging, 2012. **5**(6): p. 596-603.
88. Abdel-Aty, H., et al., *Edema as a very early marker for acute myocardial ischemia: a cardiovascular magnetic resonance study.* J Am Coll Cardiol, 2009. **53**(14): p. 1194-201.
89. Friedrich, M.G., et al., *The salvaged area at risk in reperfused acute myocardial infarction as visualized by cardiovascular magnetic resonance.* J Am Coll Cardiol, 2008. **51**(16): p. 1581-7.
90. Alam, S.R., et al., *Ultrasmall superparamagnetic particles of iron oxide in patients with acute myocardial infarction: early clinical experience.* Circ Cardiovasc Imaging, 2012. **5**(5): p. 559-65.

91. Kok, M.B., et al., *Cellular compartmentalization of internalized paramagnetic liposomes strongly influences both T1 and T2 relaxivity.* Magn Reson Med, 2009. **61**(5): p. 1022-32.
92. Strijkers, G.J., et al., *MRI contrast agents: current status and future perspectives.* Anticancer Agents Med Chem, 2007. **7**(3): p. 291-305.
93. Dall'Armellina, E., et al., *Dynamic changes of edema and late gadolinium enhancement after acute myocardial infarction and their relationship to functional recovery and salvage index.* Circ Cardiovasc Imaging, 2011. **4**(3): p. 228-36.
94. Yan, A.T., et al., *Characterization of the peri-infarct zone by contrast-enhanced cardiac magnetic resonance imaging is a powerful predictor of post-myocardial infarction mortality.* Circulation, 2006. **114**(1): p. 32-9.
95. Choi, K.M., et al., *Transmural extent of acute myocardial infarction predicts long-term improvement in contractile function.* Circulation, 2001. **104**(10): p. 1101-7.
96. Kwong, R.Y., et al., *Impact of unrecognized myocardial scar detected by cardiac magnetic resonance imaging on event-free survival in patients presenting with signs or symptoms of coronary artery disease.* Circulation, 2006. **113**(23): p. 2733-43.
97. Flögel, U., et al., *In vivo monitoring of inflammation after cardiac and cerebral ischemia by fluorine magnetic resonance imaging.* Circulation, 2008. **118**(2): p. 140-8.
98. Kwong, R.Y. and E.K. Yucel, *Cardiology patient pages. Computed tomography scan and magnetic resonance imaging.* Circulation, 2003. **108**(15): p. e104-6.
99. Kanal, E., et al., *American College of Radiology White Paper on MR Safety.* AJR Am J Roentgenol, 2002. **178**(6): p. 1335-47.
100. Shellock, F.G., *Magnetic resonance safety update 2002: implants and devices.* J Magn Reson Imaging, 2002. **16**(5): p. 485-96.
101. Villanueva, F.S. and W.R. Wagner, *Ultrasound molecular imaging of cardiovascular disease.* Nat Clin Pract Cardiovasc Med, 2008. **5 Suppl 2**: p. S26-32.
102. Gessner, R. and P.A. Dayton, *Advances in molecular imaging with ultrasound.* Mol Imaging, 2010. **9**(3): p. 117-27.
103. Levin, C.S., *Primer on molecular imaging technology.* Eur J Nucl Med Mol Imaging, 2005. **32 Suppl 2**: p. S325-45.
104. Judenhofer, M.S., et al., *Simultaneous PET-MRI: a new approach for functional and morphological imaging.* Nat Med, 2008. **14**(4): p. 459-65.
105. Nahrendorf, M., et al., *Nanoparticle PET-CT imaging of macrophages in inflammatory atherosclerosis.* Circulation, 2008. **117**(3): p. 379-87.
106. Garcia-Dorado, D. and J. Oliveras, *Myocardial oedema: a preventable cause of reperfusion injury?* Cardiovasc Res, 1993. **27**(9): p. 1555-63.
107. Sasaguri, S., et al., *Early change of myocardial water during acute cardiac allograft rejection.* Jpn Circ J, 1986. **50**(11): p. 1113-9.
108. Higgins, C.B., et al., *Nuclear magnetic resonance imaging of acute myocardial infarction in dogs: alterations in magnetic relaxation times.* Am J Cardiol, 1983. **52**(1): p. 184-8.
109. Aletras, A.H., et al., *Retrospective determination of the area at risk for reperfused acute myocardial infarction with T2-weighted cardiac magnetic resonance imaging: histopathological and displacement encoding with*

stimulated echoes (DENSE) functional validations. Circulation, 2006. **113**(15): p. 1865-70.
110. Tilak, G.S., et al., *In vivo T2-weighted magnetic resonance imaging can accurately determine the ischemic area at risk for 2-day-old nonreperfused myocardial infarction.* Invest Radiol, 2008. **43**(1): p. 7-15.
111. Cury, R.C., et al., *Cardiac magnetic resonance with T2-weighted imaging improves detection of patients with acute coronary syndrome in the emergency department.* Circulation, 2008. **118**(8): p. 837-44.
112. Hotchkiss, R.S., et al., *Cell death.* N Engl J Med, 2009. **361**(16): p. 1570-83.
113. Berry, N.C. and D.E. Sosnovik, *Cardiomyocyte death: insights from molecular and microstructural magnetic resonance imaging.* Pediatr Cardiol, 2011. **32**(3): p. 290-6.
114. Fonge, H., et al., *Preliminary in vivo evaluation of a novel 99mTc-labeled HYNIC-cys-annexin A5 as an apoptosis imaging agent.* Bioorg Med Chem Lett, 2008. **18**(13): p. 3794-8.
115. Hofstra, L., et al., *Visualisation of cell death in vivo in patients with acute myocardial infarction.* Lancet, 2000. **356**(9225): p. 209-12.
116. Dumont, E.A., et al., *Real-time imaging of apoptotic cell-membrane changes at the single-cell level in the beating murine heart.* Nat Med, 2001. **7**(12): p. 1352-5.
117. Sosnovik, D.E., et al., *Magnetic resonance imaging of cardiomyocyte apoptosis with a novel magneto-optical nanoparticle.* Magn Reson Med, 2005. **54**(3): p. 718-24.
118. Sosnovik, D.E., et al., *Molecular MRI of cardiomyocyte apoptosis with simultaneous delayed-enhancement MRI distinguishes apoptotic and necrotic myocytes in vivo: potential for midmyocardial salvage in acute ischemia.* Circ Cardiovasc Imaging, 2009. **2**(6): p. 460-7.
119. Kajstura, J., et al., *Apoptotic and necrotic myocyte cell deaths are independent contributing variables of infarct size in rats.* Lab Invest, 1996. **74**(1): p. 86-107.
120. Reutelingsperger, C.P., et al., *Visualization of cell death in vivo with the annexin A5 imaging protocol.* J Immunol Methods, 2002. **265**(1-2): p. 123-32.
121. Nahrendorf, M., M.J. Pittet, and F.K. Swirski, *Monocytes: protagonists of infarct inflammation and repair after myocardial infarction.* Circulation, 2010. **121**(22): p. 2437-45.
122. Frantz, S., et al., *Monocytes/macrophages prevent healing defects and left ventricular thrombus formation after myocardial infarction.* FASEB J, 2013. **27**(3): p. 871-81.
123. Iiyama, K., et al., *Patterns of vascular cell adhesion molecule-1 and intercellular adhesion molecule-1 expression in rabbit and mouse atherosclerotic lesions and at sites predisposed to lesion formation.* Circ Res, 1999. **85**(2): p. 199-207.
124. Nahrendorf, M., et al., *18F-4V for PET-CT imaging of VCAM-1 expression in atherosclerosis.* JACC Cardiovasc Imaging, 2009. **2**(10): p. 1213-22.
125. AMAG Pharmaceuticals®, I., *FERAHEME® (ferumoxytol) Injection*. 2009.
126. Spinale, F.G., *Matrix metalloproteinases: regulation and dysregulation in the failing heart.* Circ Res, 2002. **90**(5): p. 520-30.

127. Phatharajaree, W., A. Phrommintikul, and N. Chattipakorn, *Matrix metalloproteinases and myocardial infarction.* Can J Cardiol, 2007. **23**(9): p. 727-33.
128. de Haas, H.J., et al., *Molecular imaging of the cardiac extracellular matrix.* Circ Res, 2014. **114**(5): p. 903-15.
129. Sahul, Z.H., et al., *Targeted imaging of the spatial and temporal variation of matrix metalloproteinase activity in a porcine model of postinfarct remodeling: relationship to myocardial dysfunction.* Circ Cardiovasc Imaging, 2011. **4**(4): p. 381-91.
130. Chen, J., et al., *Near-infrared fluorescent imaging of matrix metalloproteinase activity after myocardial infarction.* Circulation, 2005. **111**(14): p. 1800-5.
131. Nahrendorf, M., et al., *Dual channel optical tomographic imaging of leukocyte recruitment and protease activity in the healing myocardial infarct.* Circ Res, 2007. **100**(8): p. 1218-25.
132. Ravichandran, L.V., R. Puvanakrishnan, and K.T. Joseph, *Influence of isoproterenol-induced myocardial infarction on certain glycohydrolases and cathepsins in rats.* Biochem Med Metab Biol, 1991. **45**(1): p. 6-15.
133. Tsuchida, K., et al., *Degradation of myocardial structural proteins in myocardial infarcted dogs is reduced by Ep459, a cysteine proteinase inhibitor.* Biol Chem Hoppe Seyler, 1986. **367**(1): p. 39-45.
134. Ge, J., et al., *Enhanced myocardial cathepsin B expression in patients with dilated cardiomyopathy.* Eur J Heart Fail, 2006. **8**(3): p. 284-9.
135. Bönner, F., et al., *Monocyte imaging after myocardial infarction with 19F MRI at 3 T: a pilot study in explanted porcine hearts.* Eur Heart J Cardiovasc Imaging, 2015. **16**(6): p. 612-20.
136. Temme, S., et al., *19F magnetic resonance imaging of endogenous macrophages in inflammation.* Wiley Interdiscip Rev Nanomed Nanobiotechnol, 2012. **4**(3): p. 329-43.
137. Bulte, J.W. and D.L. Kraitchman, *Monitoring cell therapy using iron oxide MR contrast agents.* Curr Pharm Biotechnol, 2004. **5**(6): p. 567-84.
138. Yang, Y., et al., *Temporal and noninvasive monitoring of inflammatory-cell infiltration to myocardial infarction sites using micrometer-sized iron oxide particles.* Magn Reson Med, 2010. **63**(1): p. 33-40.
139. Weissleder, R., M. Nahrendorf, and M.J. Pittet, *Imaging macrophages with nanoparticles.* Nat Mater, 2014. **13**(2): p. 125-38.
140. Tian, J., M.F. Smith, and T. Dickfeld, *Clinical Application of FDG-PET Imaging for Three-Dimensional Myocardial Scar and Left Ventricular Anatomy During Ventricular Tachycardia Ablation.* PET Clin, 2011. **6**(4): p. 393-402.
141. Berr, S.S., et al., *Images in cardiovascular medicine. Serial multimodality assessment of myocardial infarction in mice using magnetic resonance imaging and micro-positron emission tomography provides complementary information on the progression of scar formation.* Circulation, 2007. **115**(17): p. e428-9.
142. Lee, W.W., et al., *PET/MRI of inflammation in myocardial infarction.* J Am Coll Cardiol, 2012. **59**(2): p. 153-63.
143. Saha, J.K., et al., *Acute hyperglycemia induced by ketamine/xylazine anesthesia in rats: mechanisms and implications for preclinical models.* Exp Biol Med (Maywood), 2005. **230**(10): p. 777-84.

144. Thackeray, J.T. and F.M. Bengel, *Translational Molecular Nuclear Cardiology.* Cardiol Clin, 2016. **34**(1): p. 187-98.
145. Spahn, D.R., *Blood substitutes. Artificial oxygen carriers: perfluorocarbon emulsions.* Crit Care, 1999. **3**(5): p. R93-7.
146. Sosnovik, D.E., et al., *Fluorescence tomography and magnetic resonance imaging of myocardial macrophage infiltration in infarcted myocardium in vivo.* Circulation, 2007. **115**(11): p. 1384-91.
147. Montet-Abou, K., et al., *In vivo labelling of resting monocytes in the reticuloendothelial system with fluorescent iron oxide nanoparticles prior to injury reveals that they are mobilized to infarcted myocardium.* Eur Heart J, 2010. **31**(11): p. 1410-20.
148. Protti, A., et al., *Assessment of inflammation with a very small iron-oxide particle in a murine model of reperfused myocardial infarction.* J Magn Reson Imaging, 2014. **39**(3): p. 598-608.
149. Küstermann, E., et al., *Stem cell implantation in ischemic mouse heart: a high-resolution magnetic resonance imaging investigation.* NMR Biomed, 2005. **18**(6): p. 362-70.
150. Meoli, D.F., et al., *Noninvasive imaging of myocardial angiogenesis following experimental myocardial infarction.* J Clin Invest, 2004. **113**(12): p. 1684-91.
151. Dimastromatteo, J., et al., *In vivo molecular imaging of myocardial angiogenesis using the alpha(v)beta3 integrin-targeted tracer 99mTc-RAFT-RGD.* J Nucl Cardiol, 2010. **17**(3): p. 435-43.
152. Higuchi, T., et al., *Assessment of alphavbeta3 integrin expression after myocardial infarction by positron emission tomography.* Cardiovasc Res, 2008. **78**(2): p. 395-403.
153. Makowski, M.R., et al., *In vivo molecular imaging of angiogenesis, targeting alphavbeta3 integrin expression, in a patient after acute myocardial infarction.* Eur Heart J, 2008. **29**(18): p. 2201.
154. Rodriguez-Porcel, M., et al., *Imaging of VEGF receptor in a rat myocardial infarction model using PET.* J Nucl Med, 2008. **49**(4): p. 667-73.
155. Oostendorp, M., et al., *Molecular magnetic resonance imaging of myocardial angiogenesis after acute myocardial infarction.* Circulation, 2010. **121**(6): p. 775-83.
156. Badylak, S.F., *The extracellular matrix as a biologic scaffold material.* Biomaterials, 2007. **28**(25): p. 3587-93.
157. Ozbek, S., et al., *The evolution of extracellular matrix.* Mol Biol Cell, 2010. **21**(24): p. 4300-5.
158. Mascherbauer, J., et al., *Cardiac magnetic resonance postcontrast T1 time is associated with outcome in patients with heart failure and preserved ejection fraction.* Circ Cardiovasc Imaging, 2013. **6**(6): p. 1056-65.
159. Broberg, C.S., et al., *Quantification of diffuse myocardial fibrosis and its association with myocardial dysfunction in congenital heart disease.* Circ Cardiovasc Imaging, 2010. **3**(6): p. 727-34.
160. Zeng, M., et al., *Histological validation of cardiac magnetic resonance T1 mapping for detecting diffuse myocardial fibrosis in diabetic rabbits.* J Magn Reson Imaging, 2016. **44**(5): p. 1179-1185.

161. Jugdutt, B.I., M.J. Joljart, and M.I. Khan, *Rate of collagen deposition during healing and ventricular remodeling after myocardial infarction in rat and dog models.* Circulation, 1996. **94**(1): p. 94-101.
162. Helm, P.A., et al., *Postinfarction myocardial scarring in mice: molecular MR imaging with use of a collagen-targeting contrast agent.* Radiology, 2008. **247**(3): p. 788-96.
163. Muzard, J., et al., *Non-invasive molecular imaging of fibrosis using a collagen-targeted peptidomimetic of the platelet collagen receptor glycoprotein VI.* PLoS One, 2009. **4**(5): p. e5585.
164. Wildgruber, M., et al., *Assessment of myocardial infarction and postinfarction scar remodeling with an elastin-specific magnetic resonance agent.* Circ Cardiovasc Imaging, 2014. **7**(2): p. 321-9.
165. Nahrendorf, M., et al., *Transglutaminase activity in acute infarcts predicts healing outcome and left ventricular remodelling: implications for FXIII therapy and antithrombin use in myocardial infarction.* Eur Heart J, 2008. **29**(4): p. 445-54.
166. Nahrendorf, M., et al., *Factor XIII deficiency causes cardiac rupture, impairs wound healing, and aggravates cardiac remodeling in mice with myocardial infarction.* Circulation, 2006. **113**(9): p. 1196-202.
167. Phinikaridou, A., et al., *Advances in molecular imaging of atherosclerosis and myocardial infarction: shedding new light on in vivo cardiovascular biology.* Am J Physiol Heart Circ Physiol, 2012. **303**(12): p. H1397-410.
168. *Basic Principles of Cardiovascular MRI*. 2015: Springer. 338.
169. McRobbie, D., et al., *MRI: From Picture to Proton*. Second edition ed. 2007: Cambridge University Press. 393.
170. MCRobbie, D., et al., *MRI from picture to proton*. Cambridge: Cambridge University Press.
171. Westbrook, C. and C. Kaut, *MRI in practice*, ed. B.P. Company. 1998.
172. Caravan, P., et al., *Gadolinium(III) Chelates as MRI Contrast Agents: Structure, Dynamics, and Applications.* Chem Rev, 1999. **99**(9): p. 2293-352.
173. Kellman, P. and A.E. Arai, *Cardiac imaging techniques for physicians: late enhancement.* J Magn Reson Imaging, 2012. **36**(3): p. 529-42.
174. Ahrens, E.T. and J.W. Bulte, *Tracking immune cells in vivo using magnetic resonance imaging.* Nat Rev Immunol, 2013. **13**(10): p. 755-63.
175. Small, W.C., R.C. Nelson, and M.E. Bernardino, *Dual contrast enhancement of both T1- and T2-weighted sequences using ultrasmall superparamagnetic iron oxide.* Magn Reson Imaging, 1993. **11**(5): p. 645-54.
176. Ruiz-Cabello, J., et al., *Fluorine (19F) MRS and MRI in biomedicine.* NMR Biomed, 2011. **24**(2): p. 114-29.
177. Schweighardt, F.K. and J.A. Rubertone, *Perfluoro-crown ethers in fluorine magnetic resonance imaging*. 1989.
178. Yu, J.X., et al., *19F: a versatile reporter for non-invasive physiology and pharmacology using magnetic resonance.* Curr Med Chem, 2005. **12**(7): p. 819-48.
179. Yu, J.X., et al., *New frontiers and developing applications in 19F NMR.* Prog Nucl Magn Reson Spectrosc, 2013. **70**: p. 25-49.
180. Pan, D., et al., *Manganese-based MRI contrast agents: past, present and future.* Tetrahedron, 2011. **67**(44): p. 8431-8444.

181. Weissleder, R., et al., *Ultrasmall superparamagnetic iron oxide: characterization of a new class of contrast agents for MR imaging.* Radiology, 1990. **175**(2): p. 489-93.
182. Scholz, T.D., J.B. Martins, and D.J. Skorton, *NMR relaxation times in acute myocardial infarction: relative influence of changes in tissue water and fat content.* Magn Reson Med, 1992. **23**(1): p. 89-95.
183. Biro, G.P. and P. Blais, *Perfluorocarbon blood substitutes.* Crit Rev Oncol Hematol, 1987. **6**(4): p. 311-74.
184. Clark, L.C. and F. Gollan, *Survival of mammals breathing organic liquids equilibrated with oxygen at atmospheric pressure.* Science, 1966. **152**(3730): p. 1755-6.
185. Janjic, J.M. and E.T. Ahrens, *Fluorine-containing nanoemulsions for MRI cell tracking.* Wiley Interdiscip Rev Nanomed Nanobiotechnol, 2009. **1**(5): p. 492-501.
186. Kromen, W., et al., *Correlation of left ventricular wall thickness, heart mass, serological parameters and late gadolinium enhancement in cardiovascular magnetic resonance imaging of myocardial inflammation in an experimental animal model of autoimmune myocarditis.* Int J Cardiovasc Imaging, 2012. **28**(8): p. 1983-97.
187. Elster, A. *Questions and Answers in MRI* 2017 [cited 2017; Available from: http://www.mri-q.com/why-is-t1--t2.html.
188. Ganame, J., et al., *Impact of myocardial haemorrhage on left ventricular function and remodelling in patients with reperfused acute myocardial infarction.* Eur Heart J, 2009. **30**(12): p. 1440-9.
189. Ichikawa, Y., et al., *Late gadolinium-enhanced magnetic resonance imaging in acute and chronic myocardial infarction. Improved prediction of regional myocardial contraction in the chronic state by measuring thickness of nonenhanced myocardium.* J Am Coll Cardiol, 2005. **45**(6): p. 901-9.
190. Simonetti, O.P., et al., *An improved MR imaging technique for the visualization of myocardial infarction.* Radiology, 2001. **218**(1): p. 215-23.
191. Bohl, S., et al., *Advanced methods for quantification of infarct size in mice using three-dimensional high-field late gadolinium enhancement MRI.* Am J Physiol Heart Circ Physiol, 2009. **296**(4): p. H1200-8.
192. Geelen, T., et al., *Contrast-enhanced MRI of murine myocardial infarction - part I.* NMR Biomed, 2012. **25**(8): p. 953-68.
193. Strich, G., et al., *Tissue distribution and magnetic resonance spin lattice relaxation effects of gadolinium-DTPA.* Radiology, 1985. **154**(3): p. 723-6.
194. Messroghli, D.R., et al., *Modified Look-Locker inversion recovery (MOLLI) for high-resolution T1 mapping of the heart.* Magn Reson Med, 2004. **52**(1): p. 141-6.
195. Kellman, P. and M.S. Hansen, *T1-mapping in the heart: accuracy and precision.* J Cardiovasc Magn Reson, 2014. **16**: p. 2.
196. Roujol, S., et al., *Accuracy, precision, and reproducibility of four T1 mapping sequences: a head-to-head comparison of MOLLI, ShMOLLI, SASHA, and SAPPHIRE.* Radiology, 2014. **272**(3): p. 683-9.
197. Wolters, M., et al., *Clinical perspectives of hybrid proton-fluorine magnetic resonance imaging and spectroscopy.* Invest Radiol, 2013. **48**(5): p. 341-50.

198. Chen, J., G.M. Lanza, and S.A. Wickline, *Quantitative magnetic resonance fluorine imaging: today and tomorrow.* Wiley Interdiscip Rev Nanomed Nanobiotechnol, 2010. **2**(4): p. 431-40.
199. Jacoby, C., et al., *Probing different perfluorocarbons for in vivo inflammation imaging by 19F MRI: image reconstruction, biological half-lives and sensitivity.* NMR Biomed, 2014. **27**(3): p. 261-71.
200. Keupp, J., et al., *Simultaneous dual-nuclei imaging for motion corrected detection and quantification of 19F imaging agents.* Magn Reson Med, 2011. **66**(4): p. 1116-22.
201. Tirotta, I., et al., *(19)F magnetic resonance imaging (MRI): from design of materials to clinical applications.* Chem Rev, 2015. **115**(2): p. 1106-29.
202. Brockmann, M.A., A. Kemmling, and C. Groden, *Current issues and perspectives in small rodent magnetic resonance imaging using clinical MRI scanners.* Methods, 2007. **43**(1): p. 79-87.
203. Brockmann, M.A., *Use of clinical MR scanners for small rodent imaging.* Methods, 2007. **43**(1): p. 1.
204. Gilson, W.D. and D.L. Kraitchman, *Cardiac magnetic resonance imaging in small rodents using clinical 1.5 T and 3.0 T scanners.* Methods, 2007. **43**(1): p. 35-45.
205. Beuf, O., F. Jaillon, and H. Saint-Jalmes, *Small-animal MRI: signal-to-noise ratio comparison at 7 and 1.5 T with multiple-animal acquisition strategies.* MAGMA, 2006. **19**(4): p. 202-8.
206. Herold, V., et al., *In vivo quantitative three-dimensional motion mapping of the murine myocardium with PC-MRI at 17.6 T.* Magn Reson Med, 2006. **55**(5): p. 1058-64.
207. Nezafat, M., et al., *A segmented modified look-locker inversion recovery (MOLLI) sequence for high heart rate T1 mapping of mice*, in *18th Annual SCMR Scientific Sessions*, J.o.C. Magnetic and Resonance, Editors. 2015: Nice, France.
208. Daire, J.L., et al., *Cine and tagged cardiovascular magnetic resonance imaging in normal rat at 1.5 T: a rest and stress study.* J Cardiovasc Magn Reson, 2008. **10**: p. 48.
209. Delattre, B.M., et al., *Myocardial infarction quantification with Manganese-Enhanced MRI (MEMRI) in mice using a 3T clinical scanner.* NMR Biomed, 2010. **23**(5): p. 503-13.
210. Lovell, D.P., *Variation in barbiturate sleeping time in mice. 3. Strain X environment interactions.* Lab Anim, 1986. **20**(4): p. 307-12.
211. van Bogaert, M.J., et al., *Mouse strain differences in autonomic responses to stress.* Genes Brain Behav, 2006. **5**(2): p. 139-49.
212. van den Borne, S.W., et al., *Mouse strain determines the outcome of wound healing after myocardial infarction.* Cardiovasc Res, 2009. **84**(2): p. 273-82.
213. Lovell, D.P., *Variation in pentobarbitone sleeping time in mice. 1. Strain and sex differences.* Lab Anim, 1986. **20**(2): p. 85-90.
214. Roth, D.M., et al., *Impact of anesthesia on cardiac function during echocardiography in mice.* Am J Physiol Heart Circ Physiol, 2002. **282**(6): p. H2134-40.
215. Brown, R.H., et al., *A method of endotracheal intubation and pulmonary functional assessment for repeated studies in mice.* J Appl Physiol (1985), 1999. **87**(6): p. 2362-5.

216. Das, S., et al., *A simple method of mouse lung intubation.* J Vis Exp, 2013(73): p. e50318.
217. Wang, J., et al., *A simple and fast experimental model of myocardial infarction in the mouse.* Tex Heart Inst J, 2006. **33**(3): p. 290-3.
218. Hamacher, J., et al., *Microscopic wire guide-based orotracheal mouse intubation: description, evaluation and comparison with transillumination.* Lab Anim, 2008. **42**(2): p. 222-30.
219. Kolk, M.V., et al., *LAD-ligation: a murine model of myocardial infarction.* J Vis Exp, 2009(32).
220. Bohl, S., et al., *Refined approach for quantification of in vivo ischemia-reperfusion injury in the mouse heart.* Am J Physiol Heart Circ Physiol, 2009. **297**(6): p. H2054-8.
221. Theye, R.A. and J.D. Michenfelder, *Whole-body and organ Vo2 changes with enflurane, isoflurane, and halothane.* Br J Anaesth, 1975. **47**(8): p. 813-7.
222. Taylor, D.K., *Study of two devices used to maintain normothermia in rats and mice during general anesthesia.* J Am Assoc Lab Anim Sci, 2007. **46**(5): p. 37-41.
223. Ando, S., et al., *Effects of intravenous amino acids on anesthesia-induced hypothermia in ovariectomized rats.* J Nutr Sci Vitaminol (Tokyo), 2012. **58**(2): p. 143-8.
224. Murase, K., et al., *A simple and inexpensive system for controlling body temperature in small animal experiments using MRI and the effect of body temperature on the hepatic kinetics of Gd-EOB-DTPA.* Magn Reson Imaging, 2013. **31**(10): p. 1744-51.
225. Instruments, S. *MR-compatible Small Rodent Heater System*. 2009 [cited 2017.
226. Riess, J.G., *Oxygen carriers ("blood substitutes")--raison d'etre, chemistry, and some physiology.* Chem Rev, 2001. **101**(9): p. 2797-920.
227. Brateman, L., *Chemical shift imaging: a review.* AJR Am J Roentgenol, 1986. **146**(5): p. 971-80.
228. Giraudeau, C., et al., *A new paradigm for high-sensitivity 19F magnetic resonance imaging of perfluorooctylbromide.* Magn Reson Med, 2010. **63**(4): p. 1119-24.
229. Ozdemirel, B. and O. Nalcioglu, *Correction of chemical-shift artifacts in multislice F-19 imaging with perfluorooctyl bromide.* Magn Reson Med, 1992. **23**(2): p. 324-32.
230. Behan, M., et al., *Perfluorooctylbromide as a contrast agent for CT and sonography: preliminary clinical results.* AJR Am J Roentgenol, 1993. **160**(2): p. 399-405.
231. Ramaesh, K., et al., *Corneal epithelial toxic effects and inflammatory response to perfluorocarbon liquid.* Arch Ophthalmol, 1999. **117**(10): p. 1411-3.
232. Castro, C.I. and J.C. Briceno, *Perfluorocarbon-based oxygen carriers: review of products and trials.* Artif Organs, 2010. **34**(8): p. 622-34.
233. Partlow, K.C., et al., *19F magnetic resonance imaging for stem/progenitor cell tracking with multiple unique perfluorocarbon nanobeacons.* FASEB J, 2007. **21**(8): p. 1647-54.

234. Srinivas, M., et al., *Customizable, multi-functional fluorocarbon nanoparticles for quantitative in vivo imaging using 19F MRI and optical imaging.* Biomaterials, 2010. **31**(27): p. 7070-7.
235. Ahrens, E.T., et al., *In vivo imaging platform for tracking immunotherapeutic cells.* Nat Biotechnol, 2005. **23**(8): p. 983-7.
236. Srinivas, M., et al., *(19)F MRI for quantitative in vivo cell tracking.* Trends Biotechnol, 2010. **28**(7): p. 363-70.
237. Jacoby, C., et al., *Visualization of immune cell infiltration in experimental viral myocarditis by (19)F MRI in vivo.* MAGMA, 2014. **27**(1): p. 101-6.
238. Ebner, B., et al., *Early assessment of pulmonary inflammation by 19F MRI in vivo.* Circ Cardiovasc Imaging, 2010. **3**(2): p. 202-10.
239. Ahrens, E.T., et al., *Clinical cell therapy imaging using a perfluorocarbon tracer and fluorine-19 MRI.* Magn Reson Med, 2014. **72**(6): p. 1696-701.
240. Kok, M.B., et al., *Quantitative (1)H MRI, (19)F MRI, and (19)F MRS of cell-internalized perfluorocarbon paramagnetic nanoparticles.* Contrast Media Mol Imaging, 2011. **6**(1): p. 19-27.
241. Kadayakkara, D.K., et al., *(19)F spin-lattice relaxation of perfluoropolyethers: Dependence on temperature and magnetic field strength (7.0-14.1T).* J Magn Reson, 2014. **242**: p. 18-22.
242. Flögel, U., et al., *Noninvasive detection of graft rejection by in vivo (19) F MRI in the early stage.* Am J Transplant, 2011. **11**(2): p. 235-44.
243. van Heeswijk, R.B., et al., *Fluorine-19 magnetic resonance angiography of the mouse.* PLoS One, 2012. **7**(7): p. e42236.
244. Keipert, P.E., *Use of Oxygent, a perfluorochemical-based oxygen carrier, as an alternative to intraoperative blood transfusion.* Artif Cells Blood Substit Immobil Biotechnol, 1995. **23**(3): p. 381-94.
245. WHO. *Cardiovascular diseases (CVDs)*. 2016.
246. Virag, J.I. and C.E. Murry, *Myofibroblast and endothelial cell proliferation during murine myocardial infarct repair.* Am J Pathol, 2003. **163**(6): p. 2433-40.
247. Solomon, S.D., et al., *Recovery of ventricular function after myocardial infarction in the reperfusion era: the healing and early afterload reducing therapy study.* Ann Intern Med, 2001. **134**(6): p. 451-8.
248. Whittaker, P., D.R. Boughner, and R.A. Kloner, *Role of collagen in acute myocardial infarct expansion.* Circulation, 1991. **84**(5): p. 2123-34.
249. Lichtenauer, M., et al., *Intravenous and intramyocardial injection of apoptotic white blood cell suspensions prevents ventricular remodelling by increasing elastin expression in cardiac scar tissue after myocardial infarction.* Basic Res Cardiol, 2011. **106**(4): p. 645-55.
250. Protti, A., et al., *Late gadolinium enhancement of acute myocardial infarction in mice at 7T: cine-FLASH versus inversion recovery.* J Magn Reson Imaging, 2010. **32**(4): p. 878-86.
251. Protti, A., et al., *Assessment of Myocardial Remodeling Using an Elastin/Tropoelastin Specific Agent with High Field Magnetic Resonance Imaging (MRI).* J Am Heart Assoc, 2015. **4**(8): p. e001851.
252. Frangogiannis, N.G., *Targeting the inflammatory response in healing myocardial infarcts.* Curr Med Chem, 2006. **13**(16): p. 1877-93.
253. Jaffer, F.A., et al., *Molecular imaging of myocardial infarction.* J Mol Cell Cardiol, 2006. **41**(6): p. 921-33.

254. Makowski, M.R., et al., *Noninvasive assessment of atherosclerotic plaque progression in ApoE-/- mice using susceptibility gradient mapping.* Circ Cardiovasc Imaging, 2011. **4**(3): p. 295-303.
255. A., P., et al., *Imaging of inflammation using vsop at multiple time points in a mouse model of myocardial infarction.* 2011, ISMRM.
256. Frantz, C., K.M. Stewart, and V.M. Weaver, *The extracellular matrix at a glance.* J Cell Sci, 2010. **123**(Pt 24): p. 4195-200.
257. Yanagisawa, H., et al., *Fibulin-5 is an elastin-binding protein essential for elastic fibre development in vivo.* Nature, 2002. **415**(6868): p. 168-71.
258. Kielty, C.M., M.J. Sherratt, and C.A. Shuttleworth, *Elastic fibres.* J Cell Sci, 2002. **115**(Pt 14): p. 2817-28.
259. Makowski, M.R., et al., *Assessment of atherosclerotic plaque burden with an elastin-specific magnetic resonance contrast agent.* Nat Med, 2011. **17**(3): p. 383-8.
260. Willerson, J.T., et al., *Abnormal myocardial fluid retention as an early manifestation of ischemic injury.* Am J Pathol, 1977. **87**(1): p. 159-88.
261. von Bary, C., et al., *MRI of coronary wall remodeling in a swine model of coronary injury using an elastin-binding contrast agent.* Circ Cardiovasc Imaging, 2011. **4**(2): p. 147-55.
262. Botnar, R.M., et al., *In vivo assessment of aortic aneurysm wall integrity using elastin-specific molecular magnetic resonance imaging.* Circ Cardiovasc Imaging, 2014. **7**(4): p. 679-89.
263. Phinikaridou, A., et al., *Vascular remodeling and plaque vulnerability in a rabbit model of atherosclerosis: comparison of delayed-enhancement MR imaging with an elastin-specific contrast agent and unenhanced black-blood MR imaging.* Radiology, 2014. **271**(2): p. 390-9.
264. Li, S.H., et al., *Elastin overexpression by cell-based gene therapy preserves matrix and prevents cardiac dilation.* J Cell Mol Med, 2012. **16**(10): p. 2429-39.
265. van Riet, E.E., et al., *Epidemiology of heart failure: the prevalence of heart failure and ventricular dysfunction in older adults over time. A systematic review.* Eur J Heart Fail, 2016. **18**(3): p. 242-52.
266. Redfield, M.M., et al., *Burden of systolic and diastolic ventricular dysfunction in the community: appreciating the scope of the heart failure epidemic.* JAMA, 2003. **289**(2): p. 194-202.
267. Heusch, G., et al., *Cardiovascular remodelling in coronary artery disease and heart failure.* Lancet, 2014. **383**(9932): p. 1933-43.
268. Lin, L. and A.A. Knowlton, *Innate immunity and cardiomyocytes in ischemic heart disease.* Life Sci, 2014. **100**(1): p. 1-8.
269. Baumgarten, G., et al., *Myocardial injury modulates the innate immune system and changes myocardial sensitivity.* Basic Res Cardiol, 2006. **101**(5): p. 427-35.
270. Frangogiannis, N.G., *The immune system and the remodeling infarcted heart: cell biological insights and therapeutic opportunities.* J Cardiovasc Pharmacol, 2014. **63**(3): p. 185-95.
271. Kain, V., S.D. Prabhu, and G.V. Halade, *Inflammation revisited: inflammation versus resolution of inflammation following myocardial infarction.* Basic Res Cardiol, 2014. **109**(6): p. 444.

272. Kumar, A.G., et al., *Induction of monocyte chemoattractant protein-1 in the small veins of the ischemic and reperfused canine myocardium.* Circulation, 1997. **95**(3): p. 693-700.
273. Ono, K., et al., *Prevention of myocardial reperfusion injury in rats by an antibody against monocyte chemotactic and activating factor/monocyte chemoattractant protein-1.* Lab Invest, 1999. **79**(2): p. 195-203.
274. Boyle, A.J., et al., *Myocardial production and release of MCP-1 and SDF-1 following myocardial infarction: differences between mice and man.* J Transl Med, 2011. **9**: p. 150.
275. Gharaee-Kermani, M., E.M. Denholm, and S.H. Phan, *Costimulation of fibroblast collagen and transforming growth factor beta1 gene expression by monocyte chemoattractant protein-1 via specific receptors.* J Biol Chem, 1996. **271**(30): p. 17779-84.
276. Yamamoto, T., et al., *Monocyte chemoattractant protein-1 enhances gene expression and synthesis of matrix metalloproteinase-1 in human fibroblasts by an autocrine IL-1 alpha loop.* J Immunol, 2000. **164**(12): p. 6174-9.
277. Hayashidani, S., et al., *Anti-monocyte chemoattractant protein-1 gene therapy attenuates left ventricular remodeling and failure after experimental myocardial infarction.* Circulation, 2003. **108**(17): p. 2134-40.
278. Flogel, U., et al., *In vivo monitoring of inflammation after cardiac and cerebral ischemia by fluorine magnetic resonance imaging.* Circulation, 2008. **118**(2): p. 140-8.
279. Weber, K.T., et al., *Connective tissue and repair in the heart. Potential regulatory mechanisms.* Ann N Y Acad Sci, 1995. **752**: p. 286-99.
280. Weber, K.T., Y. Sun, and J.P. Cleutjens, *Structural remodeling of the infarcted rat heart.* EXS, 1996. **76**: p. 489-99.
281. Cleutjens, J.P., et al., *Regulation of collagen degradation in the rat myocardium after infarction.* J Mol Cell Cardiol, 1995. **27**(6): p. 1281-92.
282. Squires, C.E., et al., *Altered fibroblast function following myocardial infarction.* J Mol Cell Cardiol, 2005. **39**(4): p. 699-707.
283. Darby, I., O. Skalli, and G. Gabbiani, *Alpha-smooth muscle actin is transiently expressed by myofibroblasts during experimental wound healing.* Lab Invest, 1990. **63**(1): p. 21-9.
284. Desmoulière, A., et al., *Apoptosis mediates the decrease in cellularity during the transition between granulation tissue and scar.* Am J Pathol, 1995. **146**(1): p. 56-66.
285. Niu, J. and P.E. Kolattukudy, *Role of MCP-1 in cardiovascular disease: molecular mechanisms and clinical implications.* Clin Sci (Lond), 2009. **117**(3): p. 95-109.
286. Roberts, R., V. DeMello, and B.E. Sobel, *Deleterious effects of methylprednisolone in patients with myocardial infarction.* Circulation, 1976. **53**(3 Suppl): p. I204-6.
287. Lu, B., et al., *Abnormalities in monocyte recruitment and cytokine expression in monocyte chemoattractant protein 1-deficient mice.* J Exp Med, 1998. **187**(4): p. 601-8.
288. Tesch, G.H., et al., *Monocyte chemoattractant protein-1 promotes macrophage-mediated tubular injury, but not glomerular injury, in nephrotoxic serum nephritis.* J Clin Invest, 1999. **103**(1): p. 73-80.

289. Tsou, C.L., et al., *Critical roles for CCR2 and MCP-3 in monocyte mobilization from bone marrow and recruitment to inflammatory sites.* J Clin Invest, 2007. **117**(4): p. 902-9.
290. Jia, T., et al., *Additive roles for MCP-1 and MCP-3 in CCR2-mediated recruitment of inflammatory monocytes during Listeria monocytogenes infection.* J Immunol, 2008. **180**(10): p. 6846-53.
291. Jiang, Y., et al., *Monocyte chemoattractant protein-1 regulates adhesion molecule expression and cytokine production in human monocytes.* J Immunol, 1992. **148**(8): p. 2423-8.
292. Krause, S.W., et al., *Differential screening identifies genetic markers of monocyte to macrophage maturation.* J Leukoc Biol, 1996. **60**(4): p. 540-5.
293. Frangogiannis, N.G., et al., *Cytokines and the microcirculation in ischemia and reperfusion.* J Mol Cell Cardiol, 1998. **30**(12): p. 2567-76.